

# Table of Contents

Abstract.....	iii
Acknowledgement.....	vi
Table of Contents.....	x
List of Figures.....	xiv
List of Tables.....	xviii
1. Introduction.....	1
1.1. General.....	1
1.2. Research needs.....	2
1.3. Research objectives.....	3
1.4. Organisation of thesis.....	4
2. Literature Review.....	7
2.1. Introduction.....	7
2.1.1. The shake table testing method.....	7
2.1.2. The quasi-static testing method.....	8
2.2. The hybrid simulation method.....	10
2.3. Numerical errors.....	14
2.4. Systematic experimental errors.....	15
2.4.1. Transducer calibration error.....	16
2.4.2. Actuator displacement calibration error.....	17
2.4.3. Friction error.....	18
2.4.4. Conversion error.....	19
2.4.5. Support movement.....	20
2.4.6. Inconsistent actuator motion.....	21
2.5. Random experimental errors.....	21
2.6. Implementation of the hybrid simulation method.....	22
2.6.1. The servo-valve.....	23
2.6.2. The actuator.....	25
2.6.3. The internal displacement transducer.....	26
2.6.4. The servo-controller.....	26
2.7. Numerical integration method.....	31
2.8. Hybrid simulation with substructuring.....	35

2.8.1.	Hybrid simulation with substructures algorithm .....	35
2.8.2.	Advantages and limitations.....	37
2.9.	Notable development in the hybrid simulation method .....	37
2.9.1.	Effective force testing .....	38
2.9.2.	Unconditionally stable integration methods .....	40
3.	Delay Compensation for Fast hybrid simulation.....	45
3.1.	Introduction .....	45
3.2.	Prior research.....	46
3.3.	Systematic displacement control errors and their effect on energy content .....	50
3.4.	Computation of energy error.....	53
3.4.1.	Modification in energy computation .....	54
3.4.2.	Proposed error compensation algorithm utilising artificial viscous damping .....	56
3.5.	Numerical verification.....	59
3.6.	Experimental validation .....	68
3.7.	Stability .....	78
3.8.	Summary .....	81
4.	Improving hybrid simulation through Kalman filter .....	83
4.1.	Introduction .....	83
4.2.	Kalman filter.....	85
4.3.	Influence of DOF coupling.....	90
4.3.1.	Case 1: weak DOF coupling .....	91
4.3.2.	Case 2: strong DOF coupling .....	94
4.4.	Increasing simulation stability through Kalman filter .....	96
4.4.1.	Increasing simulation stability without modified command generation method .....	97
4.4.2.	Increasing simulation stability with modified command generation method .....	101
4.5.	Effectiveness of Kalman filter algorithm for inelastic systems .....	105
4.5.1.	Numerical simulations of inelastic system.....	105
4.5.2.	Stability assessment for inelastic system.....	115
4.6.	Summary .....	118
5.	Multi-axial Actuator Control .....	121
5.1.	Introduction .....	121
5.2.	Prior research.....	121
5.3.	Quasi-static tests on RC walls .....	125
5.3.1.	Experiment setup.....	126

5.3.2.	Loading protocol .....	127
5.3.3.	Transformation procedure.....	129
5.3.4.	Experiment results .....	134
5.4.	Hybrid simulations on RC column .....	138
5.4.1.	Experiment setup.....	139
5.4.2.	Transformation procedure.....	139
5.5.	Study on error accumulation .....	143
5.6.	Summary .....	148
6.	Displacement paths effect in hybrid simulations considering nonlinear responses .....	151
6.1.	Introduction .....	151
6.2.	Test setup and specimen .....	153
6.3.	Displacement tracking strategies.....	156
6.4.	Loading regime.....	157
6.5.	Experiment results and discussions .....	161
6.6.	Summary .....	181
7.	Hybrid testing on concrete wall .....	183
7.1.	Introduction .....	183
7.2.	Methodology.....	184
7.2.1.	Experimental specimen.....	184
7.2.2.	Loading protocol .....	186
7.2.3.	Discrete parameters for the hybrid simulation with and without substructuring .....	188
7.3.	Test setup.....	191
7.4.	Instrumentations .....	193
7.5.	Implementation problems during tests .....	195
7.5.1.	Faulty coordinate transformation algorithm .....	195
7.5.2.	Actuator behaviour .....	198
7.6.	Results and discussions on global responses.....	199
7.6.1.	Comparison of displacement time histories .....	199
7.6.2.	Comparison of force deformation relationships.....	201
7.6.3.	Replications of boundary conditions .....	202
7.6.4.	Comparison of energy dissipation characteristics .....	203
7.7.	Results and discussions on local responses .....	208
7.7.1.	Comparison of damage patterns .....	208
7.7.2.	Comparison of deformation components .....	209

7.7.3.	Comparison of curvature distributions .....	211
7.7.4.	Comparison of average tensile strains.....	212
7.7.5.	Comparison of plastic hinge lengths.....	214
7.8.	Numerical validations .....	215
7.8.1.	Modelling of the wall from the hybrid simulation without substructuring.....	215
7.8.2.	Modelling of the wall from the hybrid simulation with substructuring .....	219
7.9.	Summary .....	221
8.	Conclusions .....	224
8.1.	Future work.....	229
	References .....	232
	Appendix A.....	240
A.	Implementation for numerical verification.....	240
	Appendix B.....	247
B.	Bouc-Wen equation solver.....	247
	Appendix C.....	251
C.	NEM Extended Kalman Filter (EKF) state matrices .....	251
	Appendix D.....	252
D.	Bidirectional rocking column testing .....	252
D.1.	Material testing samples.....	252
D.2.	Specimen construction .....	254
	Appendix E.....	261
E.	Wall testing .....	261
E.1.	Material testing samples.....	261
E.2.	Specimen construction .....	263

# List of Figures

Figure 2-1 The shake table facility at The University of Auckland .....	8
Figure 2-2 Example of standard loading protocol used in quasi-static cyclic testing [3].....	9
Figure 2-3 A schematic diagram of a displacement-controlled hybrid simulation.....	12
Figure 2-4 The effect of transducer calibration error .....	16
Figure 2-5 The effect of actuator displacement calibration error .....	18
Figure 2-6 The effect of friction .....	19
Figure 2-7 The effect of conversion error .....	20
Figure 2-8 The effect of support movement.....	21
Figure 2-9 Dual-loop architecture of a hybrid simulation.....	22
Figure 2-10 Ramp-hold hybrid simulation technique .....	23
Figure 2-11 The relationship between system supply pressure and no-load flow [11] .....	24
Figure 2-12 Relationship between oil flow and actuator load pressure.....	25
Figure 2-13 The effect of different proportional gains .....	28
Figure 2-14 The effect of integral controller.....	29
Figure 2-15 The effect of derivative controller .....	30
Figure 2-16 Typical result of optimally tuned PID controller.....	30
Figure 2-17 Typical tuning process of a PID controller for dynamic testing .....	31
Figure 2-18 Accuracy of Newmark Explicit Method (NEM) .....	35
Figure 3-1 Idealised force-deformation response of system with displacement control errors [48] ..	52
Figure 3-2 Graphical representation of energy error in Equation 3-4.....	53
Figure 3-3 Displacement control error and the associated energy error .....	55
Figure 3-4 Graphical illustration of the energy error calculation outlined in Equation 3-9 to 3-11 .....	56
Figure 3-5 SDOF structure.....	59
Figure 3-6 Numerical simulation of a hybrid simulation using block diagram .....	60
Figure 3-7 Ground acceleration records for numerical simulations .....	61
Figure 3-8 Displacement responses without displacement error and with uncompensated systematic displacement error.....	62
Figure 3-9 Cumulative energy error as calculated using the proposed method, Thewalt and Roman [46], and [47].....	63
Figure 3-10 Displacement response without displacement error and with compensated systematic displacement error.....	65
Figure 3-11 Additional variable damping ratio to compensate for energy error in the responses.....	66
Figure 3-12 Relationship between components of Equation 3-13 .....	66
Figure 3-13 Relationship between the sum of velocities and the incremental displacement of the response to 1995 Kobe earthquake.....	67
Figure 3-14 Steel moment resisting frame specimen (MRF) used in the experimental validations ....	69
Figure 3-15 Displacement response of the MRF specimen during experimental validations .....	71
Figure 3-16 Measured displacement and fore time histories during Tabas experimental validation..	72
Figure 3-17 $G_v$ in displacement response due to 1995 Kobe earthquake excitation .....	75
Figure 3-18 Measured restoring force in frequency domain from the experimental validation using Tabas earthquake record for the first 5 seconds of the simulation .....	76

Figure 3-19 Numerical simulations using polynomial extrapolation method without simulated measurement noises.....	77
Figure 3-20 Numerical simulations using polynomial extrapolation method with simulated measurement noises.....	77
Figure 3-21 Normalised residual energy ratio for selected critical damping ratio values.....	79
Figure 4-1 Schematic drawing of the two DOF shear frame.....	91
Figure 4-2 Unscaled ground acceleration record from the 1999 Duzce earthquake (Turkey).....	92
Figure 4-3 Case 1 simulation results without Kalman filter.....	93
Figure 4-4 Case 1 simulation results with Kalman filter.....	94
Figure 4-5 Case 2 simulation results without Kalman filter.....	95
Figure 4-6 Case 2 simulation results with Kalman filter.....	96
Figure 4-7 Simulated displacement response with combined delay compensation and Kalman filter application in the presence of actuator delay.....	98
Figure 4-8 Simulation result using combined algorithms without tangent stiffness estimation update.....	100
Figure 4-9 Displacement response from numerical simulations with delay utilising combined polynomial extrapolation-Kalman filter algorithm.....	101
Figure 4-10 The relationship between normalised residual energy error and delay magnitude from parametric simulations with Kalman filter.....	104
Figure 4-11 Resulting behaviour from Bouc-Wen relationship using parameters in Table 4-1.....	106
Figure 4-12 Inelastic simulation result with combined proposed delay compensation and EKF algorithm.....	111
Figure 4-13 Inelastic simulation result with combined polynomial extrapolation and EKF algorithm.....	112
Figure 4-14 Inelastic simulation result with combined delay compensation and EKF algorithm: storey shear time histories.....	114
Figure 4-15 Parametric study result from inelastic simulations: dissipated energy rate of change ..	116
Figure 4-16 Parametric study result from inelastic simulations: maximum drift error ratio.....	116
Figure 4-17 Parametric study result from inelastic simulations: dissipated energy error ratio.....	117
Figure 5-1 Geometric error due to finite actuator length in non-planar hybrid simulation [66].....	122
Figure 5-2 Schematic drawing of internal forces in the wall at a) full height and b) lower half of equivalent full height.....	125
Figure 5-3 Schematic drawing of the quasi-static test setup.....	126
Figure 5-4 Translational displacement protocol for quasi-static experiments.....	127
Figure 5-5 Free-body diagram of the wall-actuators setup.....	129
Figure 5-6 Typical displaced wall position during experiment.....	130
Figure 5-7 Last three cycles of actual wall displacement.....	135
Figure 5-8 Wall drift and number of iteration required.....	136
Figure 5-9 Actual axial force applied to the wall.....	136
Figure 5-10 Actual aspect ratio of the wall.....	137
Figure 5-11 Change in the actuators' orientations during the wall cyclic displacement, a) horizontal and b) vertical actuators.....	138
Figure 5-12 Schematic drawing of the bidirectional hybrid simulation setup plan view.....	139
Figure 5-13 Schematic drawing of bidirectional hybrid simulation setup.....	140
Figure 5-14 Typical displaced configuration of the column during experiment.....	141

Figure 5-15 The time history of $R_{er}$ for a selected hybrid simulation result along both axes of the column .....	144
Figure 5-16 Fourier transformation of $u_{er}$ in the weak axis direction.....	147
Figure 6-1 Multi-span bridge prototype .....	154
Figure 6-2 Bidirectional hybrid simulation setup as viewed from above .....	155
Figure 6-3 Column base detailing .....	156
Figure 6-4 Plausible displacement paths for applying an in-plane displacement .....	157
Figure 6-5 Scaled spectra of acceleration records used in test series A.....	158
Figure 6-6 Quasi-static displacement patterns for test series B.....	160
Figure 6-7 Quasi-static force-displacement response of the column under different loading patterns .....	164
Figure 6-8 Quasi-static force-displacement envelope of the column under different loading patterns .....	164
Figure 6-9 PT force-displacement history under different loading patterns.....	165
Figure 6-10 hybrid simulation result using 1979 El Centro earthquake record.....	167
Figure 6-11 hybrid simulation result using 1999 Chichi earthquake record.....	168
Figure 6-12 hybrid simulation result using 1999 Duzce earthquake record.....	169
Figure 6-13 hybrid simulation result using 1978 Tabas earthquake record.....	170
Figure 6-14 hybrid simulation result using 1999 Yarımcı earthquake record .....	171
Figure 6-15 Buckled EMD.....	172
Figure 6-16 Distribution of normalised displacement and force amplitude differences from the hybrid simulations.....	175
Figure 6-17 Biaxial moment trajectory and interaction surface at decompression .....	177
Figure 6-18 Component of dissipated energy during hybrid simulations .....	179
Figure 6-19 Comparison of hysteretic responses between experiments using quasi-static and hybrid simulation methods .....	180
Figure 7-1 Schematic drawing of the wall specimens.....	186
Figure 7-2 Comparison between the original (CHHC) and synthetic earthquake record.....	187
Figure 7-3 5% damped elastic response spectra for input ground motion .....	188
Figure 7-4 Idealised MDOF representation of the hybrid simulation without substructuring specimen .....	188
Figure 7-5 Idealised MDOF representation of the hybrid simulation with substructuring specimen..	190
Figure 7-6 Schematic drawing of test setup .....	192
Figure 7-7 Photos from actual test setup .....	193
Figure 7-8 Schematic drawing of instrumentations arrangement.....	195
Figure 7-9 Actuator coordinate system .....	196
Figure 7-10 Comparison between physically measured, expected, and incorrectly fed back bending moment.....	198
Figure 7-11 Comparison of displacement time histories at top of the wall (top figure) and at the location of interface node (bottom figure).....	200
Figure 7-12 Wall base moment vs top of wall displacement for the test without and with substructuring.....	201
Figure 7-13 Axial load time histories from the hybrid simulation without substructuring (left) and the hybrid simulation with substructuring (right).....	202

Figure 7-14 Bending moment time histories at interface node the hybrid simulation without substructuring (left) and the hybrid simulation with substructuring (right) .....	203
Figure 7-15 Example of force maxima and zero force point selections.....	204
Figure 7-16 Comparison of dissipated energy between the wall M6 (left figure) and wall M7 (right figure).....	205
Figure 7-17 Relationship between $\zeta_{eq}$ and $u_{max}/u_{yield}$ for the hybrid simulation without substructuring (wall M6) .....	207
Figure 7-18 Relationship between $\zeta_{eq}$ and $u_{max}/u_{yield}$ the hybrid simulation with substructuring (wall M7).....	207
Figure 7-19 Final state of the hybrid simulated wall (left) and the hybrid tested wall (right) .....	209
Figure 7-20 Deformation component contributions between a) wall M6 (without substructuring) and b) wall M7 (with substructuring) .....	210
Figure 7-21 Curvature distributions obtained from a) wall M6 (without substructure) and b) wall M7 (with substructure) .....	212
Figure 7-22 Average tensile strains from a) wall M6 (without substructuring) and b) wall M7 (with substructuring).....	213
Figure 7-23 Comparison of plastic hinge lengths between wall M6 (without substructuring) and wall M7 (with substructuring).....	215
Figure 7-24 Schematic drawing of numerical model representing wall M6 (without substructuring) .....	216
Figure 7-25 Schematic drawing of Pivot hysteresis rules parameters [92] .....	217
Figure 7-26 Time histories of $u$ from the SAP2000 model and the hybrid simulation .....	218
Figure 7-27 Time histories of $u$ from the SAP2000 model with negative damping and the hybrid simulation .....	219
Figure 7-28 Schematic drawing of numerical model representing wall M7 (without substructuring) .....	220
Figure 7-29 Time histories of $u_l$ from the SAP2000 model and the hybrid simulation.....	221
Figure A-1 Root model .....	243
Figure A-2 “NEM integration” subsystem.....	244
Figure A-3 “Experimental structure and compensation” subsystem .....	245
Figure A-4 Delay compensation subsystem .....	246
Figure B-1 2-DOF shear frame for Bouc-Wen MATLAB verification .....	249
Figure B-2 Comparison of force and displacement for Bouc-Wen MATLAB verification .....	250
Figure D-1 Stress-strain curve from concrete compressive test.....	252
Figure D-2 Stress-strain curve from Grade 300E D10 tension test.....	253
Figure D-3 Stress-strain curve from Grade 300E D16 tension test.....	254
Figure D-4 Photographs showing the construction sequence of the unbonded PT column.....	255
Figure D-5 Photographs showing the column foundation construction sequence .....	256
Figure E-1 Stress-strain curve from concrete compressive test of wall M6 .....	261
Figure E-2 Stress-strain curves from grade 300E R6 tension tests .....	262
Figure E-3 Stress-strain curves from Grade 300E D10 tension tests .....	263
Figure E-4 Tested walls construction process.....	264

# List of Tables

Table 3-1 SDOF structure properties .....	59
Table 3-2 Summary of stability limit of the proposed delay compensation method with different simulation parameters.....	80
Table 4-1 The values of Bouc-Wen parameters for inelastic simulations .....	106
Table 5-1 Parameters of the specimens and numerical integrations used during hybrid simulations .....	147
Table 5-2 Summary of computation to determine total $u_i + 1er, Rmax$ on both column axes .....	148
Table 6-1 Properties of prototype and model of bridge pier .....	155
Table 6-2 Seismic hazard parameters for earthquake record scaling .....	158
Table 6-3 Quasi-static displacement patterns for test series B .....	160
Table 6-4 Equivalent viscous damping (%).....	163
Table 6-5 Normalised maximum displacement amplitude difference (%) .....	172
8. Table 7-1 Summary of wall detailing.....	185
Table 7-2 Summary of wall specimen for each test.....	185
Table 7-3 Comparison between $u$ (without substructuring) and $u_N$ (with substructuring).....	200
Table 7-4 Comparison of $u_I$ .....	200
Table 7-5 Parameter values for Thin Takeda hysteresis rules .....	206
Table 7-6 Regression parameters for experimentally derived $\zeta_{eq}$ .....	207
Table 7-7 Comparisons of F1 and F2 between the wall M6 (without substructuring) and wall M7 (with substructuring) .....	210
Table 7-8 Average curvatures at maximum drifts of the hybrid simulation without and with substructuring.....	211
Table 7-9 Longitudinal reinforcement strains at maximum drifts from the hybrid simulation without and with substructuring.....	213
Table 7-10 Nonlinear moment-rotation relationships for Link element in M6 numerical model.....	216
Table 7-11 Parameters for Pivot hysteresis rules in wall M6 (without substructuring) numerical modelling .....	217
Table 7-12 Parameters for Pivot hysteresis rules in M6 numerical modelling.....	220
Table A-1 Bouc-Wen parameters in MATLAB verification .....	250
Table D-1 Specified material properties for bidirectional hybrid simulation specimen.....	252
Table D-2 Concrete compressive test summary .....	253
Table E-1 Wall M6 concrete compressive tests summary .....	262
Table E-2 Wall M7 concrete compressive tests summary .....	262





# Chapter 1

## Introduction

---

### 1.1. General

In the last 40 years, the hybrid simulation method has emerged as a useful and convenient method to simulate the dynamic response of civil engineering structures subjected to earthquake. The benefit of the method lies in its capability to simulate accurate dynamic response of a specimen as in a shake table test by only applying quasi-static or dynamic loads at reduced speed.

Experimental errors have more serious implications in a hybrid simulation than in a shake table or a quasi-static test. These errors commonly result from inaccurate measurements and inability to exactly apply actuation, physically and temporally. Although these sources of errors are not exclusive to the hybrid simulation method, they are inevitably used inside computation cycles during a hybrid simulation such that they propagate and accumulate during the test leading to inaccurate result, or in the worst case leading to test instability. The development of real-time hybrid simulation method to simulate structural systems with rate-dependent behaviour also brings new challenges to the task of ensuring a stable and accurate experiment.

The introduction of the substructuring technique to the hybrid simulation method increases its efficiencies as it eliminates the need to build and test complete structures. One of the challenges in a hybrid simulation with substructuring is to ensure compatibility between the

physically tested specimen and the rest of the structure which does not experience physical testing.

## **1.2. Research needs**

Experimental errors influence the reliability of a hybrid simulation to simulate seismic response. Shing and Mahin [1] was the first to compile some of the experimental error sources in a hybrid simulation. They proposed mitigation techniques to tackle the issues at the sources. Since the report, a number of challenges still needs to be addressed to improve the hybrid simulation method, including:

- Complexities in a large number of existing delay compensation methods to compensate the effect of actuator delay that is critical in real time hybrid simulation method. In depth knowledge of control theory and system identification are sometimes required yet most structural engineers are not familiar with them.
- The effect of measurement noises during hybrid simulations. Measurement noises are typically considered less detrimental compared to the more systematic type of errors. However, unusually high noise magnitudes will degrade the quality of a hybrid simulation result significantly. Delay compensation method that utilises measurements can also become less effective in the presence of large measurement noises.
- The effect of geometric nonlinearity in multi-axial testing is rarely considered. Geometric nonlinearity occurs in multi-axial testing since actuating in more than one loading axis will lead to systematic position error of the specimen due to rotating actuation devices. A nonlinear transformation subroutine that accounts for these rotations using continuous measurements on the dimensions of the overall test setup

must be incorporated in multi-axial testing, including hybrid simulation. The subroutine must be able to account for geometric changes while maintaining correct boundary conditions in the test setup.

- hybrid simulation with substructuring where there is an incompatible behaviour between the physical substructure and the prototype structure. There is a need to investigate whether the hybrid simulation with substructuring can “manipulate” the physical substructure to simulate the prototype structure when the two typically demonstrate different behaviours.

### **1.3. Research objectives**

The aim of this study is to improve the hybrid simulation method to increase accuracy and applicability by reducing the barriers of physical and temporal inaccuracies. This will accommodate experiments that will not be possible using the shake table or the quasi-static methods. The following objectives will address the research needs outlined earlier:

- Develop an intuitive delay compensation method that only requires understanding of structural engineering principles and little knowledge of control system theory.
- Apply smart filtering approach to tackle high noise level in measurements. Also, to utilise the smart filtering to improve the proposed delay compensation method performance.
- Extend the hybrid simulation capability in the University of Auckland structural testing laboratory to multi-axial testing. This requires subroutines that enforce accurate boundary conditions and handling of geometric changes in the test setup due to actuators-specimen interaction.

- Validate the concept of hybrid simulation with substructuring. This is achieved by replicating failure mechanism of a structural system where the physical substructure is known to exhibit different behaviour from the complete system.

#### **1.4. Organisation of thesis**

The thesis is divided into eight chapters. A brief outline is as follows:

- Chapter 2 provides a detailed literature review of recent hybrid simulation method research and an overview of the basic implementation of a hybrid test, common sources of experimental errors, numerical integration methods adapted for hybrid simulations, the concept of substructuring in hybrid simulations, as well as more recent developments regarding the testing method.
- Chapter 3 presents a new intuitive method for compensating delay in fast hybrid simulations. This chapter presents the theoretical derivation, numerical and experimental validations, and a parametric study on the stability of the proposed method.
- Chapter 4 presents the integration of the Kalman filter algorithm into the hybrid simulation method, in particular its effect on the proposed delay compensation method presented in Chapter 3. The combined delay compensation-Kalman filter method produces stable simulations even when the delay magnitude is beyond the stability limit derived in Chapter 3. Application of the proposed delay compensation to nonlinear simulations is also presented and the effect of the Kalman filter in producing stable simulations for higher delay magnitude is demonstrated.
- Chapter 5 presents a development in multi-axial hybrid simulations with a focus on nonlinear coordinate transformation to account for systematic displacement error

due to geometric effect of the test setup and to enforce accurate boundary conditions simultaneously.

- Chapter 6 presents bidirectional seismic response simulation tests using different displacement patterns and actuator displacement tracking strategies. The effect of the different actuation strategies to the inelastic behaviour of the specimen is demonstrated.
- Chapter 7 presents hybrid simulations without and with substructuring using concrete wall specimens. The behaviour of the wall specimen used in the test with substructuring is shear-dominant while in the test without substructuring is flexure dominant. The capability of the hybrid simulation method to generate similar behaviours regardless of the specimen's inherent behaviour will be demonstrated in this chapter.
- Chapter 8 summarises and presents conclusions from the current study as well as presenting recommendations for future studies.

[Bestpfe.com](http://Bestpfe.com)

# Chapter 2

## Literature Review

---

### 2.1. Introduction

Structural analysis software has improved significantly over time. It is now possible to accurately simulate the seismic response of many specialist features in very high details. Yet, physical experiments remain important to help understanding the cause of structural failure. Experimental testing is crucial for verifying design assumptions and rules adopted in design codes and structural analysis software.

Prior to the invention of the hybrid simulation method, the shake table and the quasi-static methods are the two most commonly used experimental techniques to simulate the seismic responses of structures.

#### 2.1.1. The shake table testing method

A shake table test is often regarded as the most accurate seismic simulation method. In these tests, a specimen is placed on top of a platform that is accurately controlled to move in the same manner as the moving ground during an earthquake. Most shake tables for structural engineering purpose are powered by hydraulic actuators. For illustration, Figure 2-1 shows the shake table in the University of Auckland Structural Testing Laboratory (STL). Accurate control of the shake table accounting for stiffness of the table, table-specimen interaction and oil column characteristics are important to accurately replicate the ground displacement, velocity and acceleration. This is important to ensure the correct velocity and inertia dependent effects are replicated.

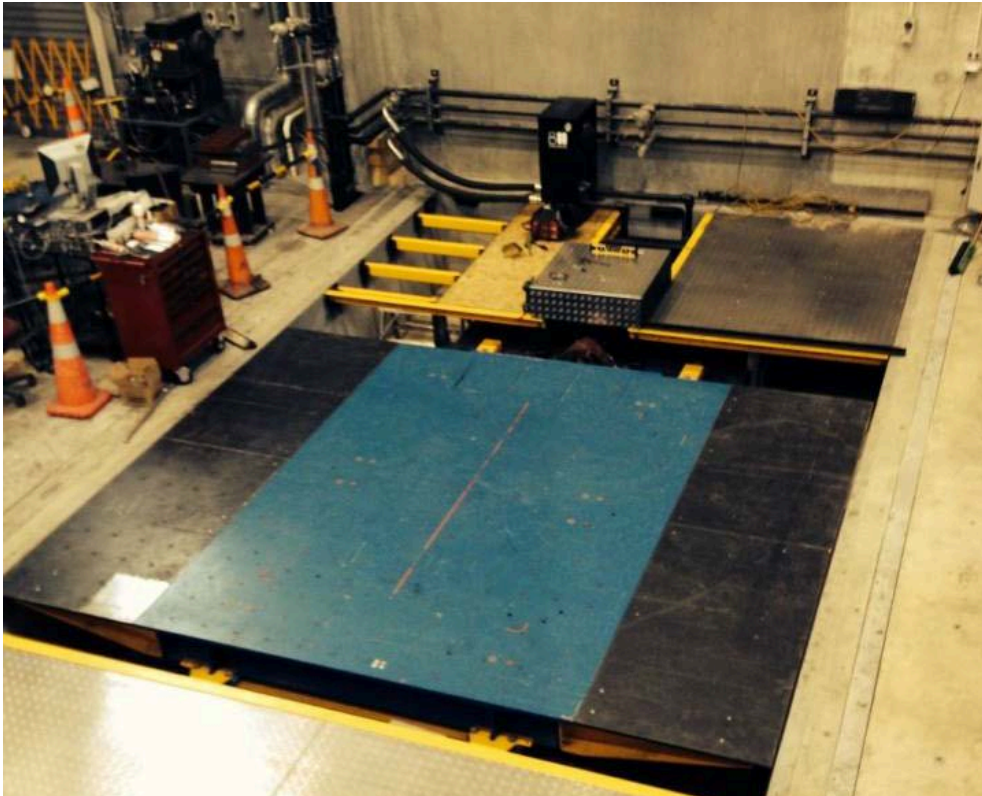


Figure 2-1 The shake table facility at The University of Auckland

The shake table method imposes large force and velocity demand during testing. Test specimens are often scaled down due to equipment constraints. This is not ideal as complete similitude compliant in scaling is often not possible in structural engineering experiments. Certain failure mode may not be replicated properly, such as brittle shear failure in a squat reinforced concrete (RC) wall structure due to material, fabrication or loading challenges [2].

### **2.1.2. The quasi-static testing method**

The name of the method suggests that the load is applied slowly to the structure. Depending on the loading protocols, the quasi-static testing method has three main sub-categories:

- Monotonic testing to failure, where the structure is loaded in one direction only. The load to the structure is gradually increased up to a certain magnitude or failure of the

structure. Definition of structural failure varies among practices for example when the lateral load carrying capacity drops by more than 20% from the maximum load sustained during the test [3].

- Cyclic testing to a predefined loading cycle that neither simulates specific displacement history nor the strain rate of an earthquake. Instead the structure is subjected to a number of loading cycles up to a predetermined ductility levels [3]. Researchers worldwide have used a range of loading patterns, as well as various definitions of yield and ultimate deformations, making comparison of results from different investigations difficult. Figure 2-2 shows a cyclic loading pattern which has been used in USA and Japan [3]. In the pattern, the yield displacement (i.e.  $\mu = \pm 1$ ) is taken as the displacement at first yield of the outer longitudinal reinforcing bars. Ductility level is increased one step at a time and the number of symmetrical loading cycles per ductility level varies between 2 in the US and 10 in Japan.
- Cyclic testing to a predefined loading history, where the loading protocol is generated from a time history analysis. This type of test is more suitable for validations of the numerical model in the time history itself.

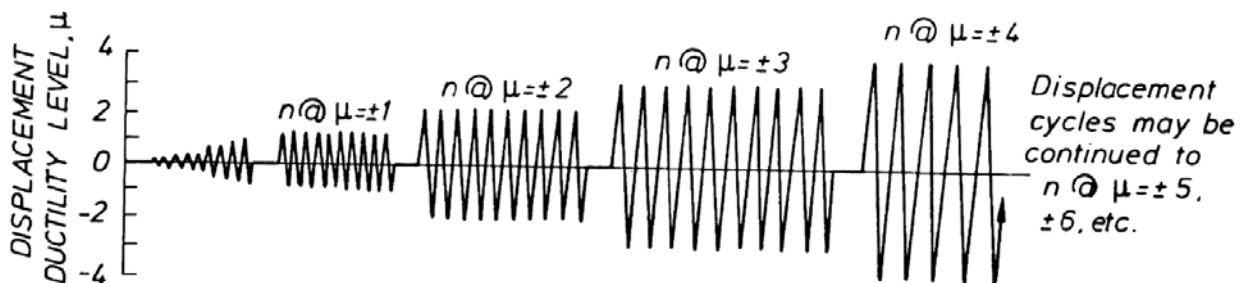


Figure 2-2 Example of standard loading protocol used in quasi-static cyclic testing [3]

The quasi-static testing method reveals conservative estimate of the strength of the structure because the load is applied slowly, since the increase in strain rate due to dynamic loading

results in increase material strength [3]. Additionally, the ductility level in quasi-static cyclic loading protocol is often more severe than the demand in reality. Yet, criticisms toward the method have been mostly directed to the fact that the method does not reveal any information about the dynamic properties of a structure, that have a large contribution to structural degradation. Interpreting energy dissipation characteristic from a quasi-static test is also difficult since inelastic behaviour is history dependent. Dissipated energies due to symmetric loading protocol such as in cyclic testing and due to random vibration such as earthquake will differ significantly [4].

## **2.2. The hybrid simulation method**

The hybrid simulation method is an experimental method to replicate seismic load acting on a structure using experimental techniques involving actuating devices combined with numerical simulations. The hybrid simulation method accounts for dynamic effects on the structure using mathematical method and thus, the loading history can be imposed on the structure quasi-statically.

The finite element (FE) method is a method to obtain approximate solutions to boundary value problem based upon the weak (variational) statements of the problem [5]. The variational formulations are discretised into finite-dimensional approximations using the Galerkin method. In structural dynamics problem, the Galerkin approximation method leads to linear differential equation form of the variational problem, formulated as

$$M\ddot{u}_i + C\dot{u}_i + Ku_i = F_i \tag{2-1}$$

Equation 2-1 is referred to as the equation of motion. In the equation,  $M$ ,  $C$ , and  $K$  are matrices representing the mass, damping, and stiffness properties. The vectors  $\ddot{u}$ ,  $\dot{u}$ , and  $u$  are

the acceleration, velocity, and displacement responses respectively at the designated degree of freedom.  $F$  is the vector of external forces; for earthquake excitation, it is equal to  $-M\iota\ddot{u}_g$ , where  $\iota$  is the influence vector and  $\ddot{u}_g$  is a ground acceleration value. The previous terminologies are frequently applied, especially when the problem under consideration pertains to a mechanical or structural system [3]. Depending on the nature of the external excitations, closed-form solutions of Equation 2-1 may not always be available and numerical approximation through time-stepping algorithm is employed to derive the responses which satisfy the equilibrium in Equation 2-1. A number of time-stepping or numerical integration methods are available and will be elaborated in detail in Section 2.7.

The distinction between a hybrid simulation and conventional numerical finite element analysis is that the stiffness matrix is not formulated, instead the equilibrium in Equation 2-1 is satisfied using restoring force directly measured from a physical specimen. The equation of motion to be solved during a hybrid simulation can thus be formulated as

$$M\ddot{u}_i + C\dot{u}_i + R_i^m = F_i \quad 2-2$$

where  $R_i^m$  is the vector of measured restoring forces from the specimen.

Figure 2-3 shows a schematic figure of a displacement-controlled hybrid simulation. Beginning with an initial displacement  $u_0$ , velocity  $\dot{u}_0$ , and acceleration  $\ddot{u}_0$ , in each subsequent time step  $i$ , the following steps are executed:

- Obtain the ground acceleration  $\ddot{u}_{g,i}$ .
- Calculate the next target displacement  $u_i$  using numerical integration.
- Apply the target displacement  $u_i$  to the specimen.
- Measure the developed restoring force  $R_i^m$ .

- Solve the equation of motion using  $R_i^m$  to obtain the current acceleration  $\ddot{u}_i$  and velocity  $\dot{u}_i$ .
- Set  $i = i + 1$  and repeat.

This highlights that the loading history of a hybrid simulation is not predefined but it is interactively determined from the experimental results as the test is conducted.

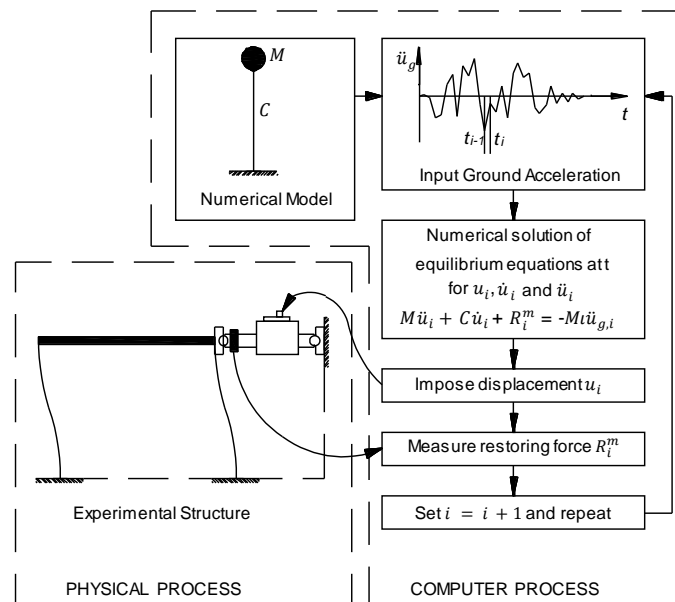


Figure 2-3 A schematic diagram of a displacement-controlled hybrid simulation

Some of the advantages of the hybrid method includes,

- Various types of external loads can be simulated as long as the loads can be defined analytically. While a shake-table test can only simulate mechanical base, a hybrid simulation can replicate loading from many other sources such as wind and blast loads, traffic loads from moving train, hydrodynamic load such as tsunami, or load from pounding between structures. An interesting application by Whyte et al. [6] reported the use of the hybrid simulation method to replicate fire loading to structures.

- The hybrid simulation method directly obtains the nonlinear behaviour of a specimen that are often too complex to be adequately modelled numerically.
- The hybrid simulation method conceptually requires no more specialised equipment than that required for a quasi-static test [7].
- The hybrid simulation method allows an experiment to be conducted in any time scale. More commonly, tests are conducted order of magnitudes slower than real time, thus allowing more careful observation of any degradation during experiment.
- The hybrid simulation method accounts for dynamic effects numerically through the equation of motion.
- The loading history for a hybrid simulation is not predetermined. Instead it is continually determined based on the current state of the specimen. This enables a simulation to reflect the actual response including any sudden failure or change in structural characteristics.
- The hybrid simulation method allows experiment on large specimen since testing can be conducted at a reduced loading rate. This substantially reduces the demand on the actuating systems and removes the barrier to testing full scale specimen and circumvents issues of similitude requirement violations on small scale testing that are common place in shake table tests.
- The hybrid simulation method can also readily replicate multi-directional earthquake excitation, whereas only few facilities around the world accommodate shake table facilities capable of simulating multidirectional earthquake excitations. The hybrid simulation method achieves this simply through accurately replicating the expected coupled boundary conditions on the structures in a quasi-static manner.

The hybrid simulation method is also not without limitations. Within the scope of this research, some of these limitations include:

- The conventional hybrid simulation method is not suitable for testing structures with dominant rate dependent characteristics. Although this is generally not significant for most typical construction, it is not the case for some new structural systems such as those with visco-elastic dampers, shape memory alloy dampers or base isolation. The nonlinear behaviours of such structures are highly influenced by the rate of loading applied. The conventional hybrid simulation method is unfortunately unsuitable for these types of structure as loading rates are not accurately replicated.
- The hybrid simulation method is arguably complex and the accuracy is sensitive to experimental and numerical errors. Moreover, errors in hybrid simulations compound cumulatively since the test is history dependent and cannot simply be corrected offline after test. The validity of a hybrid simulation highly depends on the efforts to minimise these errors. Certain types of experimental errors can even result in instability and premature termination of the experiment if not properly addressed during the experiment.

### **2.3. Numerical errors**

In a hybrid simulation, errors are inevitably introduced during numerical and experimental processes. The reliability of the result is therefore dependant to the magnitude and propagation characteristics of these errors. Numerical errors are the first source of inaccuracy in a hybrid simulation, arising from computation and modelling processes. For example, discrete parameters idealisation is only an approximate representation of a continuous specimen. Shing and Mahin [8] investigated the effect of structural idealisations in a hybrid

simulation environment and concluded that the method is more suitable for structures whose significant portion of their masses are concentrated at limited number of degree-of-freedom (DOF). Much like a computer simulation, the method is less reliable if the mass is distributed evenly in the prototype structure or the discretisation assumption is not valid.

Another source of numerical error is the numerical integration method used to solve the equation of motion. The selected parameters for the integration as well as the time step size must be able to accurately capture the dynamic response of the structure.

However, it should be noted that the numerical errors are inherent in any numerical analysis, and arguably more important in a hybrid simulation setting. Well recognised strategies exist to minimise these through appropriate modelling assumptions and analysis parameters.

There are also experimental errors, where previous research has shown that these can have significant effects on the accuracy of hybrid simulation results. Based on observations from their propagation characteristics, Shing and Mahin [1] classified experimental errors into random and systematic errors. Sections 2.4 and 2.5 present numerically simulated hybrid simulations of a single-degree-of-freedom (SDOF) structure under free vibration to demonstrate the effect of these errors. The SDOF structure has a natural period  $T_n$  of 0.16 s and an equivalent viscous damping  $\zeta$  of 5%. The structure is subjected to an impulse excitation of 1 g. The resulting displacement amplitude of the structure is close to 10 mm.

#### **2.4. Systematic experimental errors**

Systematic errors in a hybrid simulation are those that have recurrence patterns and significantly affect the test result [1]. The most cases of systematic errors arise from position errors, i.e. the difference between the actual position of the structure and the value specified

in the numerical model. Position errors may result from miscalibration of measurement transducers, digitisation error in signal conversions, poor actuator tuning, and actuator support deformation.

#### 2.4.1. Transducer calibration error

Specimen displacements and forces are monitored using displacement transducer and load cell in a hybrid simulation, respectively. Converting the electrical voltage into physical measurement of force or displacement requires calibration factors. Although there are different possible combinations between miscalibrations in the force and displacement transducers, the following example simulates the case when both transducers are miscalibrated to a 5% increase in each calibration factor from the correct value. The result is presented in Figure 2-4 including the ideal solution of the simulation without simulated miscalibrations. The specific examples of the miscalibrations result in a higher apparent stiffness of the structure to the hybrid simulation coordinator as indicated in Figure 2-4a. The effect is also illustrated in the displacement time history in Figure 2-4b that shows faster amplitude decay in the simulation with miscalibrations.

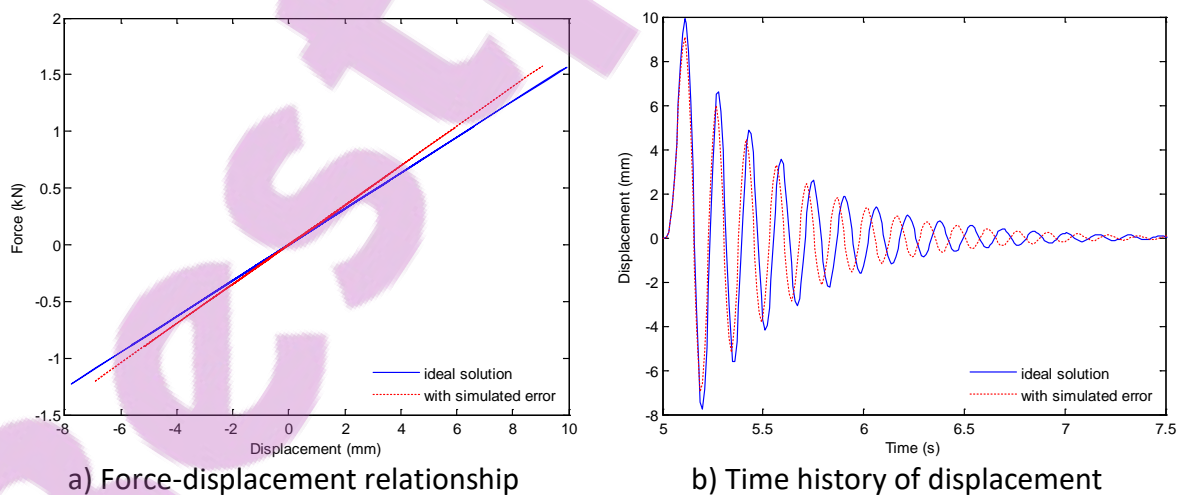


Figure 2-4 The effect of transducer calibration error

Additionally, calibration factors are typically only valid for a certain range of measurements due to inherent nonlinearity of the transducers. Reducing nonlinearity in the transducers can be achieved by calibrating over the expected range of response for each test rather over the entire useful range of the transducer. It is also important to ensure transducers in the test setup accommodates or compensates for potential misalignment, large structural deformation and other possible source of geometric nonlinearities.

#### **2.4.2. Actuator displacement calibration error**

Another opportunity for miscalibration arises when converting the computed displacement from the integration algorithm to the actuator command displacement. The actual position of the structure can either exceed (overshoot) or fall behind (undershoot) the desired displacement.

Figure 2-5 shows the simulation results including the ideal response and the case where the calibration factor for the actuator displacement transducer is 10% above the true value. The simulated miscalibration causes the actual position of the structure to constantly overshoot the desired value, resulting in additional energy being dissipated from the structure. Figure 2-5a indicates that, as opposed to the expected linear relationship, the force-deformation curve exhibits hysteretic behaviour which dissipates energy from the structure in addition to that from numerically specified viscous damping. This results in an overdamped response indicated by faster amplitude decay compared to the ideal solution in Figure 2-5b. This type of error however does not change the dynamic behaviour of the structure as opposed to the effect of transducer calibration error.

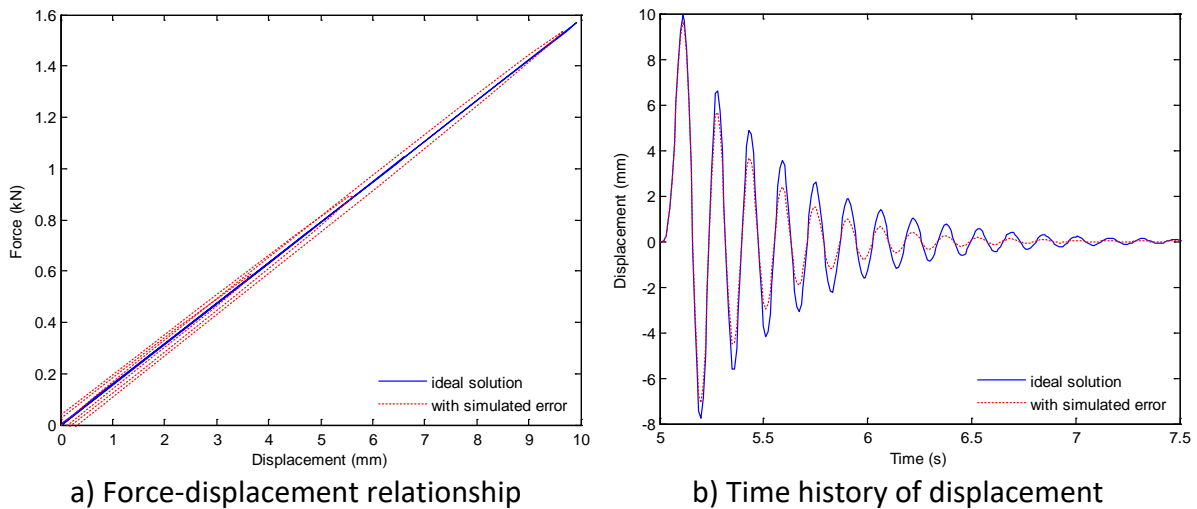


Figure 2-5 The effect of actuator displacement calibration error

### 2.4.3. Friction error

Frictions occur in various locations during a hybrid simulation, for example at the connections between the test equipment and the specimen. These frictions are considered contaminations to the load cell readings since they do not exist in real seismic event.

Figure 2-6 presents the result of simulations considering constant friction force representing the total friction during each cycle of a hybrid simulation as well as an ideal simulation result. The friction force magnitude is 2% of the maximum force developed in an ideal simulation. Figure 2-6a indicates hysteretic behaviour from an otherwise linear elastic structure as a result of this friction which dissipates energy from the structure. Figure 2-6b shows the displacement amplitudes decay faster due the to extra energy dissipation.

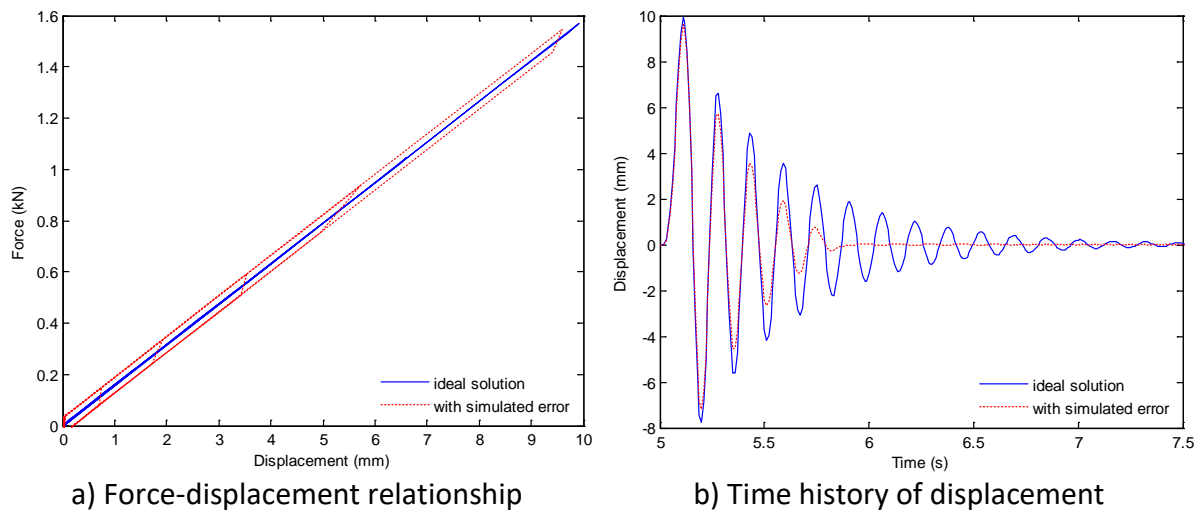


Figure 2-6 The effect of friction

It should be noted that frictions also exist in structural connections and contribute to hysteretic energy dissipation in an actual structure. This type of friction is related to Coulomb damping in structural response and should not be considered an error.

#### 2.4.4. Conversion error

In a hybrid simulation, the target displacement computed by the numerical integration algorithm must first be converted to a voltage signal required to move the actuators through a digital-to-analogue or D/A converter. The voltages in the displacement transducer and load cell must in turn be converted to a digital form through an analogue-to-digital (A/D) converter. Both converters utilise microprocessors that determine the resolution of the information the converter can handle. Problem arises when the actuator is calibrated to a significantly larger range than the maximum expected displacement in an actual test, such that small displacement increments are beyond the converter resolution. Figure 2-7 shows the simulation response where the D/A and A/D conversions are carried out by truncation such that the incremental displacements applied to the structure are consistently less than that specified by the numerical integration. Figure 2-7a indicates a hysteretic behaviour of an

otherwise linear elastic structure. The hysteretic loop is counter-clockwise resulting in additional energy. Figure 2-7b shows time histories of displacements where the displacement amplitudes from simulation with truncation decay slower than those from the ideal simulation due to the additional energy.

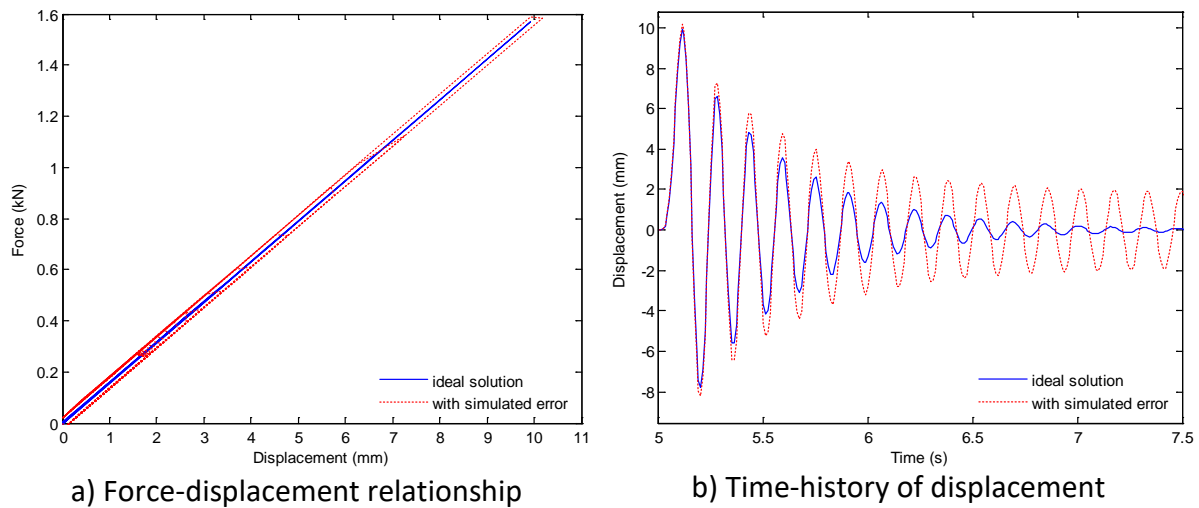


Figure 2-7 The effect of conversion error

Where possible, operations carried out by D/A and A/D converter should utilise rounding off instead of truncation, such that error becomes random and the effect of the error propagation is significantly reduced [1].

#### 2.4.5. Support movement

If displacements of the specimen are measured relative to its support, support movement will result in incorrect displacements to the structure, in turn returning erroneous force measurement. Deformation of the reaction frame supporting the actuator will produce the same effect. Support movement can be idealised as slip in the direction of the actuator movement. In the numerical simulation, slip is assumed constant at 0.5 mm and occurs at every time step. Figure 2-8a shows that the force-deformation curve of the structure contains discontinuity when the force changes sign, with no energy effect observed. Figure 2-8b shows

that slip at the support causes permanent shift in the original zero position indicated by the black dashed line. Support movement increases the apparent flexibility of the structure, indicated by the increase in natural period in Figure 2-8b.

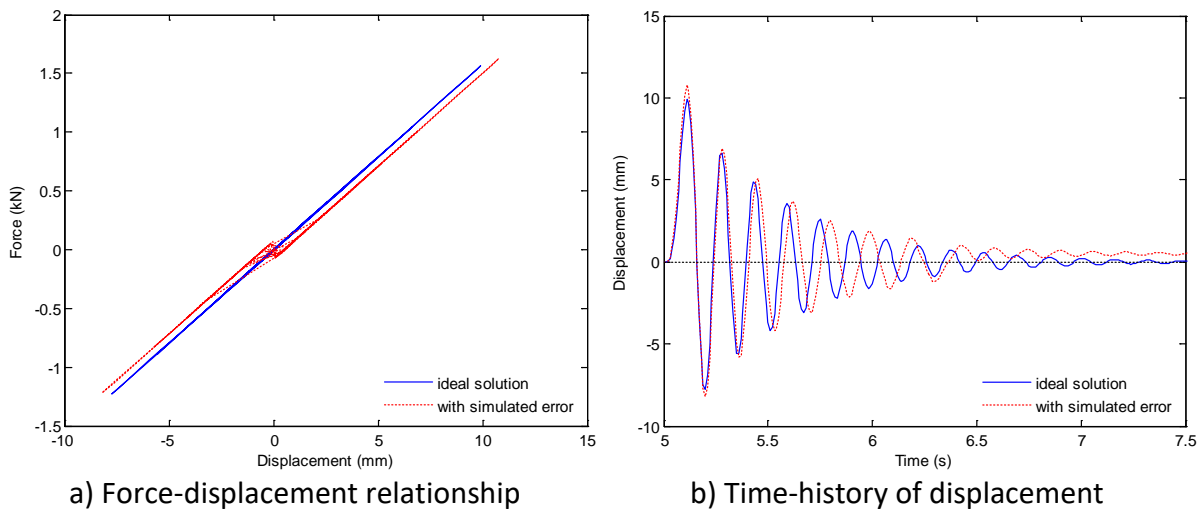


Figure 2-8 The effect of support movement

#### 2.4.6. Inconsistent actuator motion

An actuator sensitivity to command signals depends on the gain settings of its controller. Low gain causes the actuator to respond sluggishly and lags the command signals while high gain causes the actuator to be too sensitive and overshoot the desired positions. Both behaviours result in position errors and introduces energy effect into the structure. Section 2.6.4 elaborates in detail the effect of different gain settings in the actuator controller.

#### 2.5. Random experimental errors

Random errors in a hybrid simulation come from many sources such as electrical noise in wires and electronic systems, rounding-off in D/A and A/D conversions, as well as mechanical disturbance in measurement transducers due to inadequate support fixity. Unlike systematic errors, random errors have no reproducible pattern that no physical effect can be anticipated.

## 2.6. Implementation of the hybrid simulation method

Figure 2-9 illustrates a dual-loop architecture of the hybrid simulation method containing outer and inner loops. The outer loop is the test coordinator containing FE discretisation of the specimen and the hybrid simulation algorithm. The inner loop is a closed-loop control system responsible for accurately imposing the computed loading history to the specimen. Although it is assumed that the hybrid simulation system in Figure 2-9 is conducted in displacement-control, a similar system architecture also applies for a load-control.

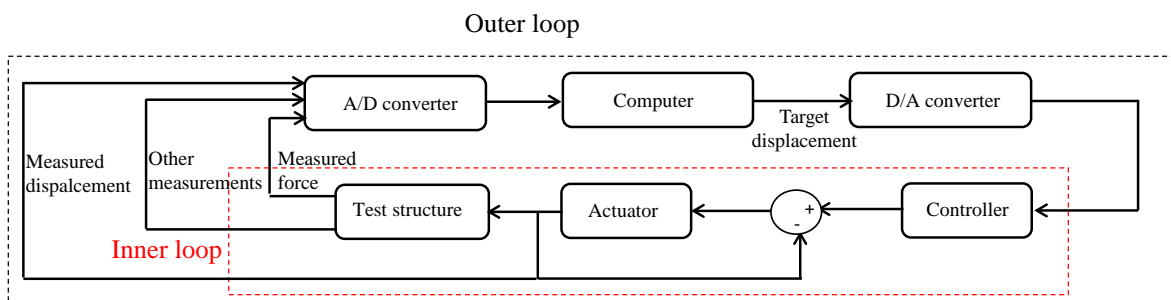


Figure 2-9 Dual-loop architecture of a hybrid simulation

The inner loop is a closed-loop control system responsible for accurately imposing the computed target displacements. In a conventional hybrid simulation after a new target displacement has been computed the outer-loop generates a ramp-type command signal to the inner-loop such as shown in Figure 2-10. During the “ramp” phase the actuator moves the specimen toward the target displacement. The “hold” phase follows where the actuator is held steady and the restoring force and other physical behaviours are measured and sent back to the test coordinator via a data acquisition system.

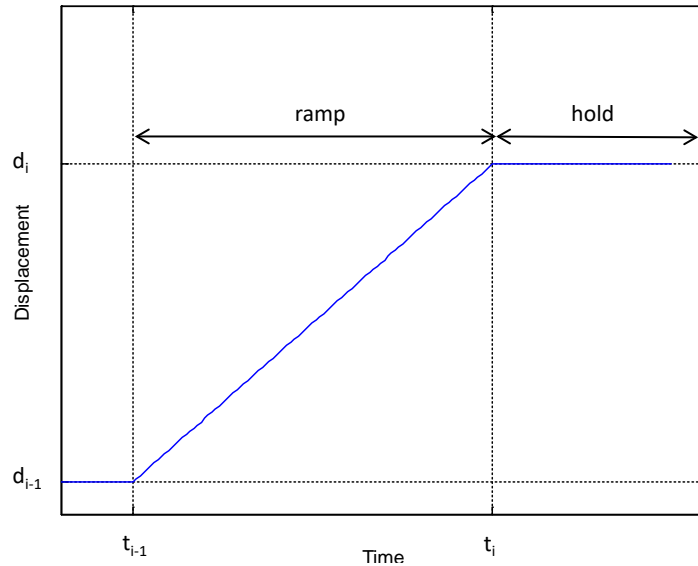


Figure 2-10 Ramp-hold hybrid simulation technique

The inner loop behaviour directly relates to stability of a hybrid simulation and has a significant influence on errors propagation. Thewalt and Mahin [9] provided a detailed description of the four components of a closed-loop control system in a hybrid simulation: servo-valve, servo-controller, actuator, and internal displacement transducer. Their findings are summarised in the following section.

### 2.6.1. The servo-valve

The servo-valve directs oil flow to either end of a double acting actuator as input currents with varying directions and magnitudes excites a magnetic coil inside the valve [10]. The servo-valve is normally specified as a rated flow at 1000 psi valve pressure-drop and the frequency of the servo-valve  $90^\circ$  phase lag (in Hz) [11]. The relationship is formulated as

$$Q_{NL} = Q_R \sqrt{\frac{P_s}{1000}} \quad 2-3$$

$Q_R$  is the rated flow capacity (gpm) and  $P_s$  is the system supply pressure (psi). The flow under no load condition,  $Q_{NL}$ , will vary with supply pressure as shown in Figure 2-11.

When the actuator is loaded, the flow through the servo-valve control ports is given by the following relationship

$$Q_L = Q_{NL} \sqrt{\frac{P_s - P_L}{P_s}} \quad 2-4$$

where  $Q_L$  is the flow capacity when the actuator is under load (gpm) and  $P_L$  is the load over the actuator piston area (psi).

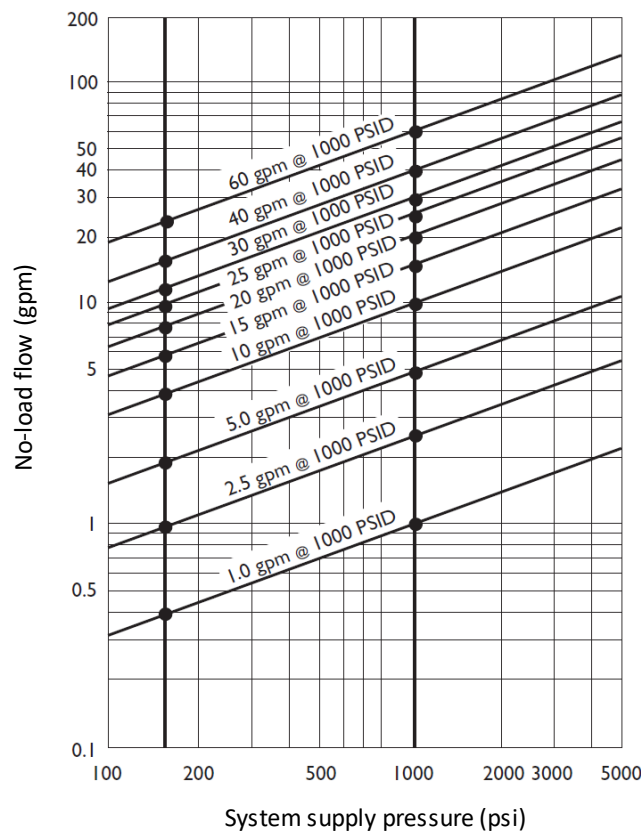


Figure 2-11 The relationship between system supply pressure and no-load flow [11]

Figure 2-12 shows a typical flow-load relationship given in Equation 2-4. The flow changes with various combinations of load pressure drop  $P_L$  and input current. The flow increases with increasing current and increasing pressure drop across the valve.

Another characteristic of a servo-valve is its internal leakage across both the valve spool and the actuator seal which reduces the overall flow capacity. This characteristic is also shown in Figure 2-12 where the servo-valve is assumed to have a supply pressure of 3000 psi and 10 gpm rated flow at 1000 psi valve pressure-drop. Due to leakage, at load pressure drop  $P_L$  equals to 2000 psi the oil flow will be less than the rated 10 gpm flow.

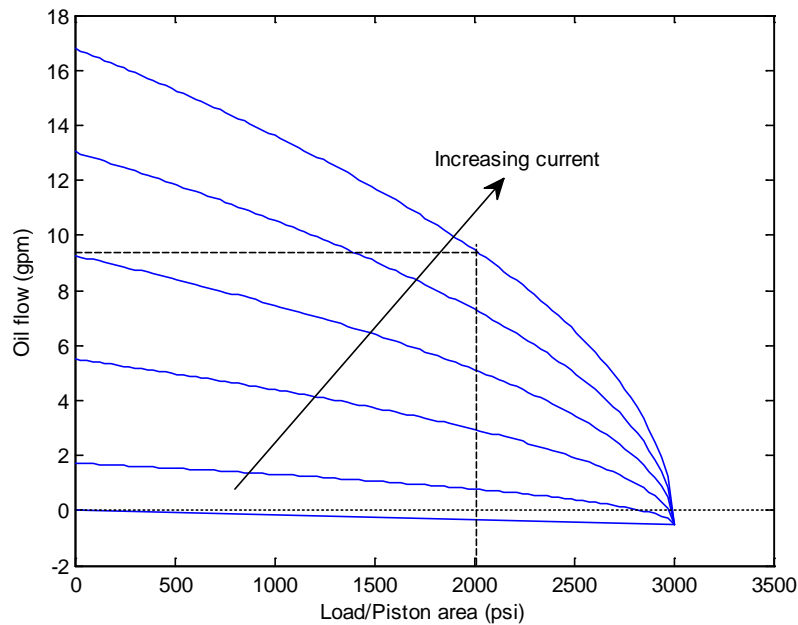


Figure 2-12 Relationship between oil flow and actuator load pressure

### 2.6.2. The actuator

An actuator is described in term of its total stroke and static force capacity, which is the product of the system supply pressure and the actuator piston area. Inside the actuator chamber, the oil column acts like a spring with its stiffness is given by

$$k_{oil} = \frac{4A_p \beta_{oil}}{L_s} \quad 2-5$$

$A_p$  is actuator piston area,  $\beta_{oil}$  is the bulk modulus of hydraulic fluid, and  $L_s$  is the total stroke of the actuator. The oil column stiffness acts in series with the total mass of the actuator and

the attached specimen and thus resulting in the oil column resonance frequency, also known as the cut-off frequency since the actuator does not respond to command frequencies beyond it [12]. Although oil column frequency is most of the time well beyond the operational frequency range for most structures, it can be excited by systematic experimental errors resulting in spurious higher mode frequencies contamination in a hybrid simulation [13].

### **2.6.3. The internal displacement transducer**

The internal displacement transducer provides the necessary structural displacement feedback for the actuator servo-controller to update the command signals. Beside calibration, the accuracy of the feedback is influenced by the deformation of the actuator support. Support deformation will reduce the actual displacement of the structure in the incremental level and as demonstrated before will have energy effect on the structure. Deformations of the structure should ideally be measured with respect to an isolated, stationary reference frame that will not be affected by any deformation of the actuator support. However, using an external displacement transducer inside the closed-loop control system may adversely affect the stability of the control system [14]. A dual displacement control using both external and internal displacement transducers [14] can be employed to provide accurate measurements of structural deformation and stable system.

### **2.6.4. The servo-controller**

The servo-controller determines the overall closed-loop stability and accuracy through its gain settings. The servo-controller amplifies the difference between the current measured displacement of the actuator piston and the command signal, giving rise to electrical current which drives the servo-valve and causes oil to flow into the actuator chamber. In turn, the

actuator piston moves to eliminate the difference. The gain settings inside the servo-controller determine the sensitivity of the actuator to the command signals.

The most common type of controller used in conjunction with servo-hydraulic actuators is the Proportional-Integral-Derivative (PID) controllers. Ideally, the tuning process of a PID controller should be done with the specimen attached to the actuator [13]. However, when there is a risk of damaging the specimen during tuning, the following procedures of offline tuning can be used.

An offline tuning process of a PID controller involves using a step function command (reference) signal to the actuator. The proportional, integration, and derivative gains are adjusted separately until the measured response closely follow the signals. The following parameters should be optimised in the measured response when tracking the command signals:

- Rise time or the time required for the actuator to reach the new reference signal.
- Overshoot or the magnitude at which the actuator exceeds the reference position. Overshoot is followed by oscillation of the response about a new stable position.
- Settling time or the time it takes for the actuator to settle around a new stable point as the oscillation damps out.
- Steady-state error or the difference between the reference position and the actual position at which the actuator stabilises.

An optimal controller setting should minimise these parameters simultaneously. The following numerical simulations demonstrate the effect of adjusting each type of gain in a PID controller to the actuator response using a unit step input as the reference signal.

- *Proportional (P) control*: the input (reference signal) to the actuator from a proportional controller comes from multiplication between the position error and a constant factor. Figure 2-13 shows the effect of two different proportional gains in the measured response. Using only proportional controller however leaves significant steady state error as the actuator stabilises. Increasing the gain reduces steady state error and decreases rise time but potentially destabilises the system as increasing the gain also increases overshoot and oscillation in the response.

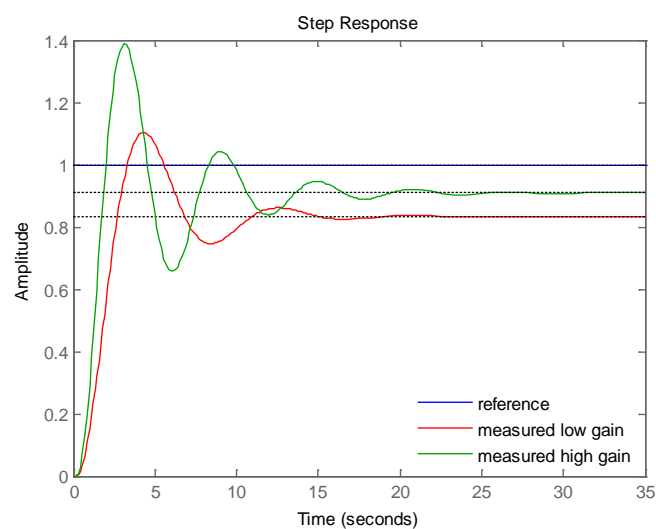


Figure 2-13 The effect of different proportional gains

- *Proportional-Integral (PI) controller*: adding integral controller into an existing proportional controller will remove the steady-state error. The integral controller averages the error over a certain duration then adds them to the reference signal. Since the proportional controller alone results in oscillatory response and steady state error, adding a portion of the averaged error will reduce the average difference between the reference and measured signal. Figure 2-14 shows the result of adding the *I* controller into the simulations presented in Figure 2-13, eliminating steady-state error such that the measured signal stabilises about the desired reference signal.

Oscillation and steady-state error can be further reduced by decreasing the P gain, raising stability margin of the closed-loop control system at the expense of slightly increased rise time.

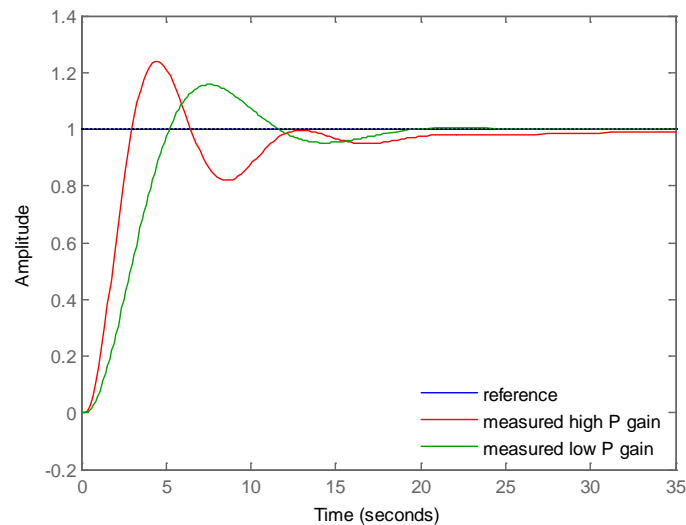


Figure 2-14 The effect of integral controller

- *Proportional-Derivative (PD) controller*: the derivative controller anticipates the change in the servo-controller output using the first derivatives of the position errors over time, for example closing the servo-valve in anticipation of reaching the desired position to minimise overshooting. Figure 2-15 presents the result of adding derivative gain into the simulation with high proportional gain presented in Figure 2-13, reducing overshoot magnitude and settling time which increases stability of the closed-loop control. Adding derivative gain however does not eliminate steady-state error.

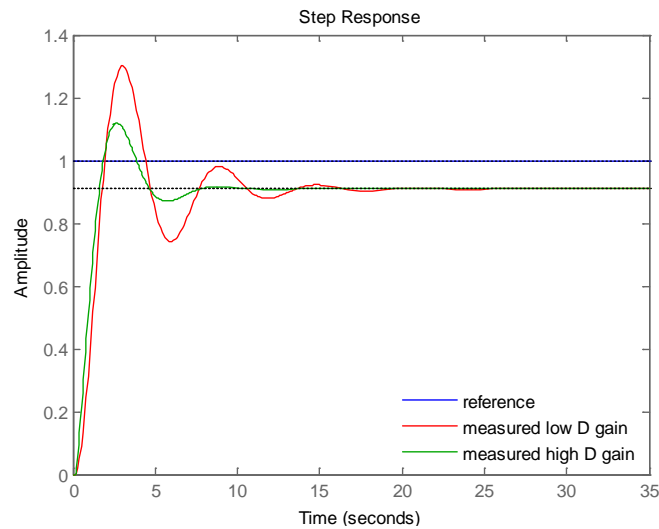


Figure 2-15 The effect of derivative controller

Figure 2-16 presents the result of combining the three controllers with optimum setting for each type of controller. The measured signal traces the reference relatively well with slight overshoot and negligible oscillation, in addition to zero steady-state error.

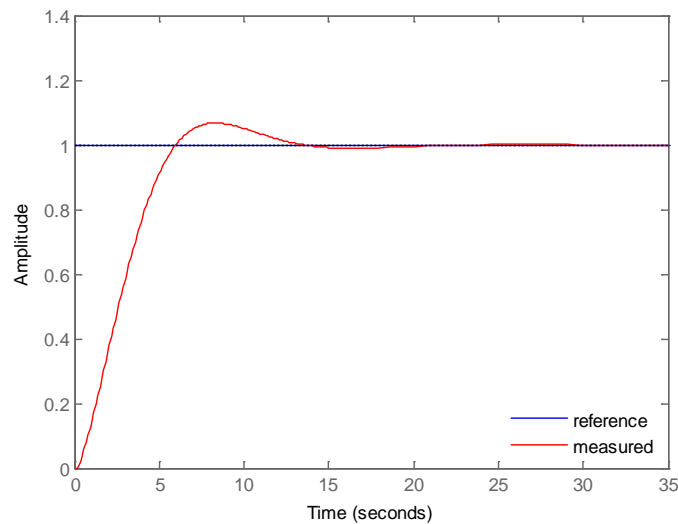


Figure 2-16 Typical result of optimally tuned PID controller

The tuning process described above is suitable for static testing due to a relatively long settling time (in the order of 15 s). The tuning process for dynamic testing is similar but requires higher gains to ensure accurate tracking within a small time-window. Tuning for dynamic tests can be done using a square wave as the command signals, such as shown in Figure 2-17 which

presents a numerical simulation of a PID tuning process using square wave signal of a 10-mm amplitude and a 5-second period. The total rise and settling time for dynamic test tuning is considerably shorter.

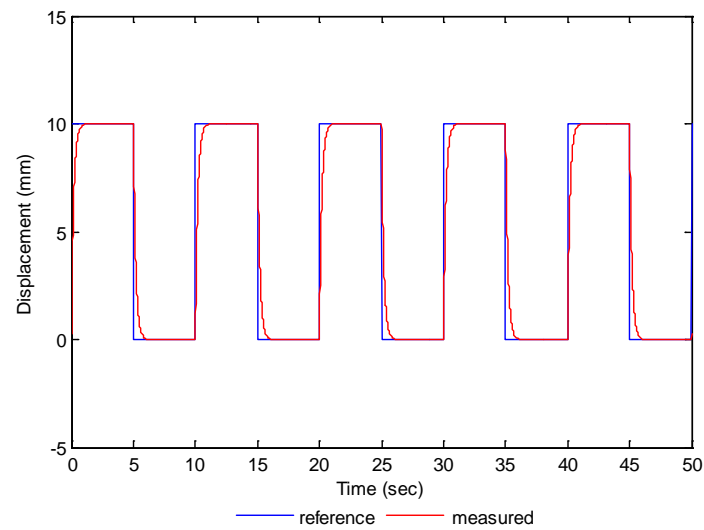


Figure 2-17 Typical tuning process of a PID controller for dynamic testing

## 2.7. Numerical integration method

The hybrid simulation method utilises numerical integration methods to determine the target displacement in each time step. Numerical integration methods can be classified according to: 1) the instance at which the information on the states of the system is required, and 2) the number of function calls required to advance the solution to the next time step [15].

The first group can be further divided into the explicit and implicit integration methods. A numerical integration method is explicit if it only requires the information of the system states from the previous time step or steps. Equation 2-6 presents a general form of an explicit integration method in a hybrid simulation environment; the specimen displacement response at the current time step  $i$  is a function of displacement, velocity, and acceleration responses at  $n$  previous steps.

$$u_i = f(u_{i-1}, \dot{u}_{i-1}, \ddot{u}_{i-1}, \dots, u_{i-n}, \dot{u}_{i-n}, \ddot{u}_{i-n}) \quad 2-6$$

Explicit integration methods are usually conditionally stable that to yield a bounded result, the size of the time step  $\Delta t$  must be sufficiently small. On the other hand, implicit integration methods require not only the states of the system at the previous time steps but also those at the current time step. Equation 2-7 presents a general form of the implicit integration method

$$u_i = f(u_i, \dot{u}_i, \ddot{u}_i, \dots, u_{i-n}, \dot{u}_{i-n}, \ddot{u}_{i-n}) \quad 2-7$$

Implicit integration methods are unconditionally stable that any size of  $\Delta t$  will yield bounded results, making them suitable for stiff structures.

The second group of numerical integration methods can be further divided into iterative and non-iterative methods. The non-iterative methods require only one function call to advance the solution to the next time step, while non-iterative methods require more. From Equation 2-7, implicit integration methods require iterative process since the current state of the specimen appears on both sides of the equation, while an explicit method is non-iterative since all required information is already available from the previous time steps. However, Schellenberg et al. [15] demonstrated that implicit integration methods do not always require iterations.

Both explicit and implicit integration methods have been successfully applied in hybrid simulations. The most widely used integration method in hybrid simulations belongs to the Newmark family of integration methods, expressed in a general form as

$$u_i = u_{i-1} + \Delta t \dot{u}_{i-1} + \Delta t^2 \left( \left( \frac{1}{2} - \beta \right) \ddot{u}_{i-1} + \beta \ddot{u}_i \right) \quad 2-8$$

$$\dot{u}_i = \dot{u}_{i-1} + \Delta t \left( (1 - \gamma) \ddot{u}_{i-1} + \gamma \ddot{u}_i \right) \quad 2-9$$

Selection of the integral parameters  $\beta$  and  $\gamma$  determines the stability and accuracy of the method. For example, setting  $\beta = 1/4$  and  $\gamma = 1/2$  results in constant average acceleration method [16] which is unconditionally stable but requires iterations. Iterative solutions in a hybrid simulation potentially introduce spurious loading and unloading cycle if the incremental displacements during iterations are not strictly increasing or decreasing. The nonlinear response of a physical structure is path dependent and spurious loading-unloading cycles potentially introduce unexpected behaviour.

Non-iterative explicit methods are the preferred integration methods in hybrid simulations. From the Newmark family, setting  $\beta = 0$  and  $\gamma = 1/2$  results in the Newmark Explicit Method (NEM). In a hybrid simulation, the NEM can be employed following these steps

- Assuming the mass and viscous damping matrices are constant throughout the test, assemble an effective mass matrix  $M_{eff}$ .

$$M_{eff} = M + \frac{\Delta t}{2} C \quad 2-10$$

- Calculate the new target displacement  $u_i$ .

$$u_i = u_{i-1} + \Delta t \dot{u}_{i-1} + \frac{1}{2} \Delta t^2 \ddot{u}_{i-1} \quad 2-11$$

- Impose  $u_i$  to the specimen and measure the developed restoring force  $R_i$ .
- Assemble the effective force  $P_{eff}$ .

$$P_{eff} = F_i - R_i - C \left( \dot{u}_{i-1} + \frac{\Delta t}{2} \ddot{u}_{i-1} \right) \quad 2-12$$

- Calculate acceleration  $\ddot{u}_i$ .

$$\ddot{u}_i = M_{eff}^{-1} P_{eff} \quad 2-13$$

- Calculate velocity  $\dot{u}_i$ .

$$\dot{u}_i = \dot{u}_{i-1} + \frac{1}{2} \Delta t (\ddot{u}_{i-1} + \ddot{u}_i) \quad 2-14$$

- Set  $i = i + 1$  and repeat.

Shing and Mahin [8] numerically analysed the stability limit of the NEM using a linear elastic SDOF structure and a recursive form of the integration algorithm. They found that  $\omega_n \Delta t \leq 2$  yields bounded result, where  $\omega_n$  is the highest natural frequency of the structure and  $\Delta t$  is the size of the time step. The accuracy of the NEM can be assessed in term of the difference between the natural frequency of the SDOF structure computed by the algorithm,  $\bar{\omega}$ , and the true natural frequency  $\omega_n$  [1]. Figure 2-18 shows the normalised difference for different values of  $\omega_n \Delta t$  up to its stability limit. At  $\omega_n \Delta t \approx 1.4$  there is a sudden increase in the normalised error. It can be concluded that for NEM, the requirement for the size of  $\Delta t$  is more restrictive than that for stability.

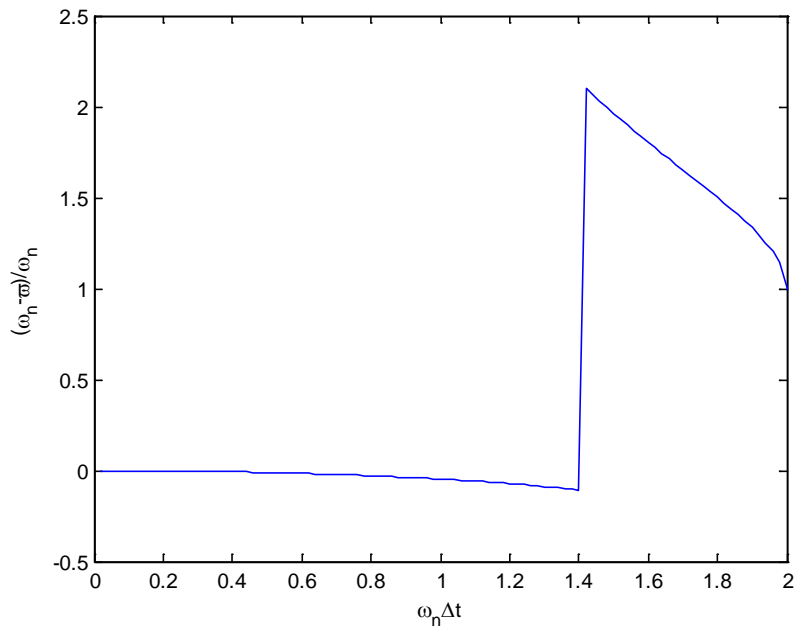


Figure 2-18 Accuracy of Newmark Explicit Method (NEM)

## 2.8. Hybrid simulation with substructuring

During seismic event, it is often found that significant damage is concentrated only at certain parts while the rest of the structure remains well integrated. It is then inefficient to build and test a complete structure for each experiment when only the behaviour of these critical parts is of interest. Since hybrid simulation integrates numerical model and physical specimen during experiment, Dermitzakis and Mahin [17] suggested employing the substructuring technique. The complete specimen is divided into numerical and physical substructures. The physical substructure is normally selected as parts of the complete structure expected to sustain major damage and thus are difficult to be modelled mathematically. The numerical substructure, on the other hand, should be selected as those well understood behaviour such as those expected to stay elastic.

### 2.8.1. Hybrid simulation with substructures algorithm

The discretised form of equation of motion solved during a hybrid testing can be formulated as follow:

$$M\ddot{u}_i + C\dot{u}_i + K^N u_i + R_i^P = F_i \quad 2-15$$

The superscripts N and P denote numerical and physical substructures, respectively.

Considering a MDOF structure with  $m$  total number of DOF and  $n$  total number of physical substructure DOF, the stiffness of the numerical substructure  $[K]^N$  can be formulated as [17]:

$$[K]^N = \begin{bmatrix} 0 & \cdots & 0 \\ \vdots & \ddots & \vdots \\ \vdots & k_{n,n}^N & \cdots & k_{n,m}^N \\ \vdots & \vdots & \ddots & \vdots \\ 0 & k_{m,n}^N & \cdots & k_{m,m}^N \end{bmatrix} \quad 2-16$$

On the other hand, the force measured from the physical substructure is assembled into the vector  $R_i^P$  defined as

$$R_i^P = [R_1^P \quad \cdots \quad R_n^P \quad \cdots \quad 0]^T \quad 2-17$$

Equation 2-16 and Equation 2-17 indicate that at the interface DOF  $n$ , both numerical and physical substructures contribute to the total restoring force. The numerical substructure contribution is proportional to the stiffness matrix element  $k_{n,n}^N$  while the physical substructure contribution  $R_i^P$  is directly measured from the specimen. Equation 2-15 to 2-17 illustrate how the basic equation of motion can be modified to incorporate numerical substructure in a hybrid simulation.

### **2.8.2. Advantages and limitations**

Since the hybrid simulation method with substructures is an extension to the conventional hybrid simulation method, it inherits its advantages and limitations. Some of the advantages are

- hybrid simulation with substructures offers even bigger economical advantage since it eliminates the need to test complete structures, reducing fabrication and installation cost.
- hybrid simulation with substructures offers modularity since multiple tests can be conducted with identical numerical substructure combined with different physical substructure.
- further reduction in the size of the specimen means that the full capacity of the actuator and hydraulic system may be utilised, allowing full scale test on the physical substructure or performing tests at higher loading rates.

The hybrid simulation with substructures method, however, also suffers from the stability consideration associated with the numerical integration method utilised during testing. Since typically more DOF are involved during hybrid simulations with substructures, conditionally stable explicit integration method (e.g. NEM) can only be employed using very small time steps due to the high natural frequencies of the specimen. The test will become impractical.

### **2.9. Notable development in the hybrid simulation method**

Although the hybrid simulation method can be considered relatively novel to the shake table [18] or the quasi-static testing methods, it has seen several major developments. The most important one was probably the development of real-time hybrid simulation method. The development allowed testing on structures or structural components whose behaviours are

directly dependent to the rate of loading, such as supplemental dampers in low-damage buildings. Chapter 3 of this thesis specifically deals with hybrid simulation conducted at high rate of loading.

The following sections summarises different aspects from the hybrid simulation method that have been developed beside real-time testing methods. They specifically deal with the developments on the numerical integration methods for hybrid simulations and the effective force testing method.

### **2.9.1. Effective force testing**

The hybrid simulation method presented so far has exclusively focused on displacement-controlled test where target displacement to be imposed on a specimen is determined at every time step by solving Equation 2-2. Advancement in control system engineering that allows force-control actuation introduces the effective force testing (EFT) method in the family of experimental methods on earthquake response simulation. In EFT, rather than solving Equation 2-2 for target displacements, the right-hand side of the equilibrium can be directly used as the command signals for the actuator operating in force-control.

The concept of EFT was first suggested by Thewalt and Mahin [9]. The forcing function at the right-hand side of Equation 2-2, the effective force, can be completely predefined once the mass matrix has been chosen. In theory, with high oil flow capacity and high system supply pressure, one should be able to conduct the EFT method in real-time since there is no need to perform numerical integrations. The resulting displacement, velocity, and acceleration responses should be identical with that obtained from displacement-controlled hybrid simulation if the effective earthquake forces can be accurately applied.

In reality, the implementation of a real-time EFT is more complicated. Dyke et al. [19] found that due to the control-specimen interaction, the actuator is unable to apply forces near the natural frequencies of the attached test specimen. They referred to this behaviour as the “natural velocity feedback” phenomenon. Murcek [20] developed a feedback loop to negate the effect of the natural velocity feedback using a model of the servo-hydraulic system. Dimig et al. [21] proposed incorporating the servo-valve flow model and the actuator pressure nonlinearities when the system is operated near the force-capacity of the servo-hydraulic actuator. Timm [22] proposed to use directly measured velocities instead of precomputed ones in the velocity feedback compensation procedure, as well as using a phase lead compensator for delay in the velocity measurements. Zhao et al. [23] extended the EFT method into nonlinear testing on SDOF structures undergoing large deformations. They proposed nonlinear natural velocity feedback compensation scheme utilising nonlinear flow-spool opening relationship and a phase-lead network to adjust the compensation signals, since they lag the command signals due to servo-system dynamics.

Chen [24] recognises that to generate proper inertial forces in the test structure, the full structural mass must be included in the experimental setup which may poses difficulties in the laboratory and raise safety issue. He proposes the use of virtual mass to reduce the total mass required by the specimen to produce the correct inertial forces. However, the effective force history to be applied is no longer predefined since the relative acceleration term now appears on both sides of the equation of motion, i.e.

$$M^P \ddot{u}_i + C \dot{u}_i + R_i^m = F_i - M^V \ddot{u}_i \quad 2-18$$

In Equation 2-18  $M^P$  is the physically installed mass on the specimen and  $M^V$  is the portion of the total mass defined virtually. He proposed two methods to conduct EFT with virtual mass;

using direct predicted accelerations or using fixed number of sub-step iterations of predicted accelerations. It is found that the fixed number of sub-step iterations method provides larger stability limit for any virtual mass ratio (the ratio of  $M^V$  to  $M^P$ ) and that the accuracy of the method is insensitive to the values of the virtual mass ratios.

Nakata [25] designed a robust controller for the EFT method using the loop-shaping method; a frequency domain technique for designing feedback control system based on the loop transfer function and the Nyquist stability criterion. Based on theoretical and experimental investigations of actuator dynamics, the loop-shaping method shows favourable characteristics over the proportional control in a PID driven EFT due to the following reasons: 1) it compensates for the control-structure interaction while the proportional controller is unable to apply the required force at the natural frequency of the mass-spring system, 2) it suppresses the oil-column resonance while the proportional controller is unable to, and 3) it shows more robustness against input and measurement noises over the entire frequency range while the performance of the proportional controller is very sensitive to these noises at the oil-column resonance frequency.

The EFT method is still in its early development stage but it certainly opens possibilities for new experimental methods in earthquake engineering that are not possible without force control [25].

### **2.9.2. Unconditionally stable integration methods**

Conditionally stable numerical integration methods may render a hybrid simulation impractical when many DOFs are involved since the resulting time step size may be too small to satisfy the stability requirement. Unconditionally stable integration methods address this limitation. Dermitzakis and Mahin [17] proposed a combined explicit-implicit integration

method that relaxed the stability limit criterion compared to NEM in hybrid tests. In the proposed method, the target displacements for the physical substructure are computed based on an explicit relationship. Measured restoring forces are sent back to the test coordinator to solve the equation of motion. The explicit displacements and velocities are then updated using the computed accelerations at the current time step. Experimental validation of the method demonstrated significant reduction in the error propagation compared to the fully explicit method and correlated well with numerical analysis.

To achieve unconditional stability however the implicit integration methods must be applied to the complete specimen (including the physical substructures in hybrid simulations with substructures). Thewalt and Mahin [9] modifies the implicit integration methods from the Newmark family (i.e.  $\beta \neq 0$ ) for hybrid simulation applications. The target displacements are computed as the total between the explicit and implicit terms from the restoring forces developed as the specimen is loaded. Both hardware and software requires slight modification to allow summing between the D/A output of the explicit term and the force signal analogue voltage. Since the method does no modification to the integration procedure, the stability criteria are identical to the implicit Newmark method, which in this case is unconditionally stable. The drawback of the method is that the final displacement of the specimen is not known to the test coordinator at the beginning of a step and can only be measured at the end.

Another variation of the Newmark method adapted for hybrid simulations is proposed by [26], called the  $\alpha$ -method. The method possesses numerically dissipative properties to damp out spurious higher mode participations excited by the experimental errors during MDOF hybrid simulations, while maintaining low numerical damping for lower modes. The

numerically dissipative properties of the method are controlled by the variable  $\alpha$ . For a general MDOF system, the  $\alpha$ -method is formulated as

$$M\ddot{u}_i + (1 + \alpha)C\dot{u}_i - \alpha C\dot{u}_{i-1} + (1 + \alpha)R_i - \alpha R_{i-1} = (1 + \alpha)F_i - \alpha F_{i-1} \quad 2-19$$

The variation of displacement and velocity between time steps can be defined as

$$u_i = u_{i-1} + \Delta t \dot{u}_{i-1} + \Delta t^2 \left( \left( \frac{1}{2} - \beta \right) \ddot{u}_{i-1} + \beta \ddot{u}_i \right) \quad 2-20$$

$$\dot{u}_i = \dot{u}_{i-1} + \Delta t ((1 - \gamma) \ddot{u}_{i-1} + \gamma \ddot{u}_i) \quad 2-21$$

For unconditional stability and dissipative properties, it is recommended that  $-\frac{1}{3} \leq \alpha \leq 0$ ,  $\beta = (\frac{1}{4} - \alpha)^2$  and  $\gamma = \frac{1}{2}(1 - 2\alpha)$ . When  $\alpha = 0$ , the method becomes identical to the constant average acceleration method that has no numerically dissipative properties. Unlike the implicit Newmark integration proposed by [9], the final target displacement value of the  $\alpha$ -method is known to the test coordinator at the expense of iteration requirement. The application of the original  $\alpha$ -method is thus not directly suitable for a hybrid simulation due to the concern of introducing spurious loading-unloading cycle to the specimen. Shing et al. [14] suggested the use a reduction factor for the incremental displacements between iterations to ensure that they are either strictly increasing or strictly decreasing within a time step. Additionally, since it is difficult to determine accurate and reliable tangent stiffness matrix from a physical specimen, the tangent stiffness matrix is replaced by the initial stiffness matrix during the iteration process. Shing et al. [14] have shown that using the initial stiffness matrix also reduces the chance of overshooting during iterations thus avoiding the spurious loading-unloading cycles. The final modification suggested for the  $\alpha$ -method is related to the position errors of the specimen relative to the converged target displacement from the test

coordinator. Equilibrium is numerically enforced after the last iteration within a time step using the initial stiffness matrix. Through numerical simulation, Shing et al. [14] demonstrated that by enforcing equilibrium, the  $\alpha$ -method shows superior error propagation characteristics in the lower modes compared to the NEM.

Another noteworthy development in the numerical integration methods for hybrid simulations is the CR integration algorithm by Chen and Ricles [27]. While most derivations and analyses of numerical integrations are typically carried out in the time domain, Chen and Ricles [27] employed discrete control theory to derive an unconditionally stable, explicit numerical integration algorithm that requires no iteration. Aside from being unconditionally stable and does not require iteration, the finite difference equations defining the variation of displacements and velocities between time steps in the CR algorithm are explicit, opening new possibilities for velocity control in the closed-loop control system for a real-time test.



# Chapter 3

## Delay Compensation for Fast hybrid simulation

---

### 3.1. Introduction

The conventional hybrid simulation method is unable to simulate the response of structure or structural component with rate-dependant behaviour, such as structures equipped with viscoelastic dampers or base isolation. Energy dissipation characteristics of these devices are highly sensitive to the rate of loading and evaluating these devices using the conventional hybrid simulation method will lead to inaccurate result.

The development of the fast (and real-time) hybrid simulation method [28-30] addresses the shortcoming by replicating the rate of loading the structure will experience in real earthquake. Dynamic interactions between the servo-valve, the actuator piston, and the specimen in fast hybrid simulation result in actuator delay. Actuator delay is the difference in time between the sampling rate of the actuator servo-controller and the instant the actuator physically realises the desired displacement. The time needed for computation and data communication add further delay into the system. Thus assuming all instruments have been properly calibrated, it is almost impossible to achieve the desired displacement within a restricted time limit, such as the sampling rate of the servo-controller, in a fast or real-time hybrid simulation since actuator delay cannot be completely eliminated [31].

Actuator delay in a hybrid simulation system introduces additional energy into the system, analogous to the effect of negative damping [32]. If the rate of energy dissipation, from

viscous damping and hysteretic action, is less than the rate of energy addition resulting from response delay, the response of the specimen will grow without bound and the experiment result will be meaningless. Therefore, it is imperative to properly compensate the effect of actuator delay.

### **3.2. Prior research**

Existing delay compensation methods were largely based on predicting the response of the specimen using known information of the specimen in previous time steps. Horiuchi et al. [32] proposed utilising simple polynomial prediction using Lagrangean extrapolation. Using computed displacements at current and several integration time steps before, the method predicts required actuator displacement several integration time steps ahead to account for the delay.

An improvement of the displacement extrapolation method was proposed using linear extrapolation of acceleration over the expected time delay, which gave a third-order displacement prediction [33]. The improved method increased the stability limit both with respect to stiffness and mass of the specimen.

Darby et al. [34] showed that constant time delay used in the polynomial extrapolation method may not give satisfactory result if there was a large variation in the magnitudes of delay. Actuator delay is a function of the overall system stiffness thus its magnitude can vary significantly when the stiffness changes, for example due to specimen's yielding. They proposed a method to estimate the delay on-the-fly during testing. The estimated delay was assumed proportional to the difference between the actual position of the specimen and the target displacement value specified in the test coordinator at every time step. Parameters of

the delay estimation equation must be tuned for rapid convergence with relatively low oscillations.

Carrion and Spencer [35] proposed a model based prediction that considered physical characteristics of the system by incorporating known information about the specimen and the loading regime. These included the mass, damping, and external excitations to the specimen, as well as an estimate of the restoring force. Compared to the polynomial extrapolation method, the model based prediction method accommodated longer prediction time frame either due to larger time delay or higher natural frequencies.

Ahmadizadeh et al. [36] presented a different technique to estimate and compensate actuator delay. In their method time delay was estimated using polynomial fit to a few desired and measured displacement data points. Displacement command was modified to account for actuator delay using the same kinematic equations formulated in the Newmark direct integration method assuming constant acceleration variation over the expected time delay. Meanwhile, the measured restoring force was also compensated using polynomial fitting technique by seeking the time at which the desired displacement was achieved.

More complex methods regarding actuator delay compensation have also been developed using control and system identification theories. Conceptually, the compensation methods in this category utilised additional outer loop controller between the test coordinator and the closed-loop control system in the dual-loop implementation of the hybrid simulation method illustrated in Figure 2-9. Before being sent to the actuator servo-controller, the additional outer loop modified the target displacement computed by test coordinator to compensate for the anticipated delay. Zhao et al. [23] employed a first-order phase lead compensator to adjust the target displacement and the generated restoring force to account for a total time

delay as large as 81 milliseconds (ms). Carrion et al. [37] adopted a feedforward-feedback compensation procedure as the additional outer-loop controller. Chen [24] used the inverse of a simplified model of servo-hydraulic system using first order discrete transfer function to compensate for actuator delay, known as the Inverse Compensation method.

Due to inherent nonlinearity in the servo-hydraulic system as well as the specimen, the performances of the delay compensation methods may become less effective when delay magnitude varies due to the nonlinearities. In this case it is preferable to use compensators with adaptive gains that seamlessly adjust their parameters in response to changes in the system dynamics. Wallace et al. [38] utilised adaptive parameters to minimise the error in estimating the magnitude of time delay, analogous to the method proposed by Darby et al. [34], and to control the magnitude of forward prediction. These adaptive parameters accommodate possible large variations in dynamic responses of the test specimen.

Chen and Ricles [39] incorporated adaptive parameters based on proportional and integral gains applied to the Tracking Indicator (TI) procedure [40] to improve the Inverse Compensation method [24] by minimising the effect of delay estimation error.

Bonnet et al. [41] adopted a versatile outer loop controller adaptable to changes in the system dynamics called Minimal Control Synthesis with modified demand (MCSmd). In the MCSmd approach, the input to the inner loop PID servo-controller is the sum of the compensated desired displacement from numerical integration and the actuator displacement, multiplied by adaptive gains. The adaptive gains aim to minimise the difference between the desired displacement from numerical integration and the actuator displacement.

Chae et al. [42] proposed an adaptive outer loop controller in time domain. The method was identified as the adaptive time series compensator (ATS), which minimise the sum of square difference between the compensated target displacement and the estimate of compensated target displacement over a certain period. The ATS method utilised adaptive coefficients from the Taylor series expansion determined using standard least square regression method.

Other delay compensation methods that have been identified included the virtual coupling method by Christenson et al. [43] and the 'hockey-stick' method by Elkhoraibi and Mosalam [44]. The virtual coupling method provided an attractive feature from an inherent trade-off between performance and stability depending on the restoring force of the specimen, and was suitable for testing specimens with large dynamic range and highly nonlinear behaviour. The 'hockey-stick' model was particularly of interest because the delay compensation procedure was based on observed relationship between displacement actuation errors and actuator velocity demands, without the need of displacement prediction or system identification.

Additionally, Liu et al. [45] presented an effort to integrate the methods by Darby et al. [34], Horiuchi et al. [33], and Carrion et al. [37]. The integrated method achieved better displacement tracking compared to the performance of each constituting method considered separately.

The chapter presents the development of an error compensation technique that does not require actuator displacement prediction or system identification. Instead of improving actuator tracking by predicting the actuator displacement to minimise the effect of delay, the proposed technique simply compensates the actuator displacement errors after they occurred. The compensation is performed by introducing additional damping in the numerical

integration and exploiting the properties of the errors, using measurements that are readily present or collected during a typical hybrid simulation.

### 3.3. Systematic displacement control errors and their effect on energy content

Actuator delay is an example of systematic displacement actuation error due to its reproducible recurrence pattern [1]. Beside actuator delay, systematic displacement actuation error happens if the actuator exhibits constant undershoot or overshoot errors, in which the actuator moves in phase with the command displacement signal but exceeds or falls behind at peak values, mainly due to the dynamics between the actuator and the servo-controller [34]. In a fast to real time hybrid simulation, the two mechanisms of displacement actuation errors occur simultaneously and are difficult to distinguish between one another. However, both mechanisms affect the energy balance in the system and can thus be compensated using a single algorithm [1, 46].

The change in mechanical energy content in a structural system is the sum of the work done by the inertial, dissipative and elastic restoring components. This balances with the work done by the external forces in lieu of any errors. This can be expressed mathematically in Equation 3-1, which is simply the governing equation of motion integrated with respect to displacements. The following relationship assumes the structural system is initially at rest and the system is elastic.

$$\int_0^u (M\ddot{u})^T du + \int_0^u (C\dot{u})^T du + \int_0^u R^T du = \int_0^u F^T du \quad 3-1$$

The third term in Equation 3-1 represents the strain energy content. In a hybrid simulation, this quantity depends on the measured restoring force from the test specimen. Any displacement actuation errors will result in erroneous displacements and hence erroneous

measured restoring forces. This in turn distorts the energy balance in the system described by Equation 3-1. The perceived energy content is expressed mathematically as,

$$\int_0^u (M\ddot{u})^T du + \int_0^u (C\dot{u})^T du + \int_0^u (R^m)^T du = \int_0^u F^T du \quad 3-2$$

$$R^m = R^d + R^{er} \quad 3-3$$

In Equation 3-2 and 3-3,  $R^m$  is the restoring forces vector measured from the specimen,  $R^d$  is the restoring forces vector at the same time step had the desired displacements been correctly applied, and  $R^{er}$  is the vector of restoring force errors due to the displacement actuation errors. Thus, the energy error across a time-step,  $E^{er}$ , is equal to

$$E^{er} = \int_0^u (R^{er})^T du \quad 3-4$$

Equation 3-4 is a general form of the formula proposed by other researchers [47-49] which does not treat numerical and experimental substructures in a hybrid simulation separately.

In a hybrid simulation, it is common for the numerical integration algorithm to calculate the time history response using the measured restoring forces and the computed (target) displacements. This leads to an interesting conundrum as the command and measured displacements are not necessarily the same due to the presence of experimental errors. Consequently, the measured restoring force is not a corresponding quantity to the commanded displacement. Consider a linear-elastic structure evaluated using hybrid simulation, Figure 3-1 shows a perceived force-deformation relationship of a linear-elastic structure where consistent displacement actuation errors are present. The behaviour of the test structure as observed by the integration algorithm can be thought as a vertical departure of the restoring forces from the true linear elastic response. The departure occurs as the result

of time difference between when the displacement is commanded and when the structure reaches the target displacement. In the case of consistent time delay depicted in Figure 3-1a, the measured forces lag the command displacement, which leads to a perceived counter-clockwise hysteretic response. This behaviour adds energy into the test specimen, represented by the shaded area inside the plot. Conversely, Figure 3-1b depicts the perceived response under consistent time lead. In this case, the perceived clockwise hysteretic response represents additional energy dissipation from the system [47]. Time delay errors are more common in fast hybrid simulations due to the dynamic interactions between the specimen and the test apparatus (servo-controller, servo-valve and the hydraulic actuator).

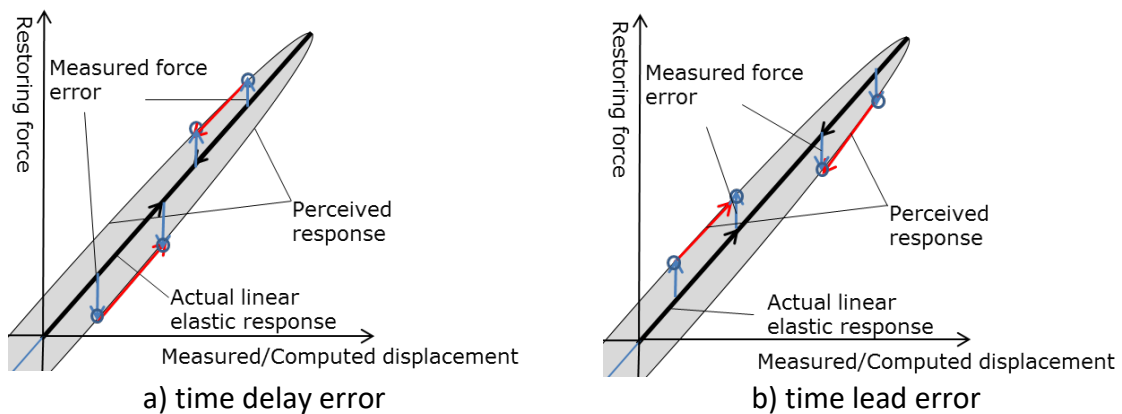


Figure 3-1 Idealised force-deformation response of system with displacement control errors [48]

The energy addition behaviour of time delay error as illustrated in Figure 3-1 can also be illustrated in Figure 3-2, which is a graphical representation of Equation 3-4 for the case of time delay error. Figure 3-2 shows a time histories of computed displacement, restoring force error due to time delay error, as well as the increments of the computed displacement in a normalised scale. The restoring force error is in phase with the incremental displacement, which is always  $90^{\circ}$  out-of-phase with the computed displacement, but with opposite sign. The cumulative energy error, defined as the integration of restoring force error with respect

to the incremental displacement (Equation 3-4) therefore will always be negative. Moving  $E^{er}$  to the right-hand side in Equation 3-2 is equivalent to introducing additional input energy into the structure.

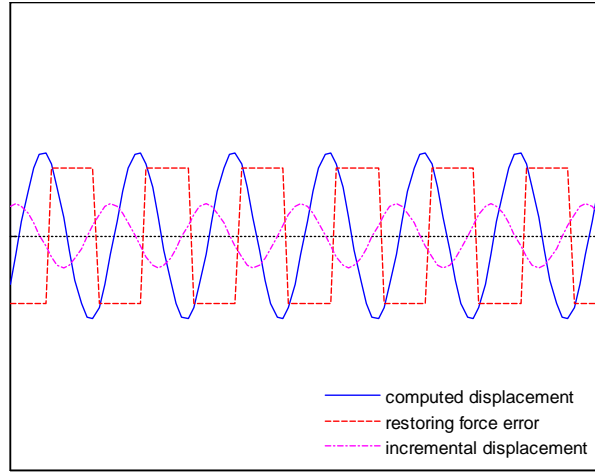


Figure 3-2 Graphical representation of energy error in Equation 3-4

### 3.4. Computation of energy error

The amount of energy error across a time step during a hybrid simulation is approximately equal to the quadrilateral area between the true and perceived force-displacement response over the displacement increment magnitude [46]. This energy error can be estimated using the trapezoidal rule, at time step  $i$ , as,

$$E_i^{er} = \frac{1}{2} (K_{i-1}^t u_{i-1}^{er} + K_{i-1}^t u_i^{er})^T \Delta u_i^c \quad 3-5$$

$K^t$  is the tangent stiffness matrix,  $u_i^{er}$  is the displacement errors at a time step  $i$  given by  $u_i^{er} = u_i^m - u_i^c$ , where superscript  $m$  and  $c$  denote measured and commanded quantities respectively; and  $\Delta u_i^c$  is the target incremental displacements across a time step given by  $\Delta u_i^c = u_i^c - u_{i-1}^c$ .

A drawback of this process is that it requires estimating the tangent stiffness of the specimen. If it is undesirable to estimate the tangent stiffness, the energy error across time step  $i$  ( $E_i^{er}$ ) can also be defined as the difference between the change in strain energy as perceived by the numerical integration ( $E_i^E$ ) and the actual change in strain energy as the specimen deforms ( $E_i^{BE}$ ).

$$E_i^{er} = E_i^{BE} - E_i^E \quad 3-6$$

Equations 3-7 and Equation 3-8 present the description for  $E_i^E$  and  $E_i^{BE}$  respectively.

$$E_i^E = \frac{1}{2}(R_{i-1}^m + R_i^m)^T (u_i^c - u_{i-1}^c) \quad 3-7$$

$$E_i^{BE} = \frac{1}{2}(R_{i-1}^m + R_i^m)^T (u_i^m - u_{i-1}^m) \quad 3-8$$

The above expressions provide a means to monitor in real time the accumulation of energy error in a hybrid simulation. These are the central equations for an error monitoring scheme called Hybrid Simulation Error Monitoring (HSEM) [47]. This scheme provides a timely warning when the accumulation of energy error in a hybrid simulation exceeds a certain threshold, when the final result of the test would no longer be reliable and the test should be terminated, or continued only after corrective measures have been taken [48]. The simplicity of the HSEM method is evident as it requires only quantities that are readily available at every time step during a fast hybrid simulation.

### 3.4.1. Modification in energy computation

Due to the difference between the commanded incremental displacements ( $\Delta u^c$ ) and the measured incremental displacements ( $\Delta u^m$ ), the computations of energy error described in

Equation 3-6 to 3-8 are modified. Consider a linear elastic structure with a force-deformation relationship as shown in Figure 3-3.

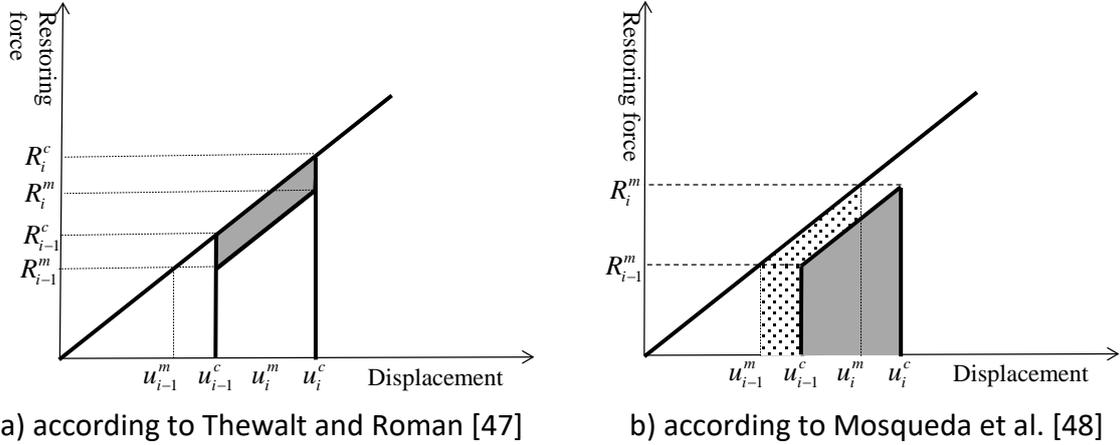


Figure 3-3 Displacement control error and the associated energy error

The energy error as computed by Equation 3-5 is highlighted by the bold area in Figure 3-3a. While the energy error as computed by Equation 3-6 is the difference in areas between the bold and dotted trapezoid.

The energy error calculated using Equation 3-6 is an approximate of the true energy error represented in Figure 3-3a. Despite the inexact nature, it is a more practical measure as it does not require knowledge of the instantaneous stiffness of the system.

It is further proposed that displacements are integrated with respect to restoring forces to compute energy error instead of restoring forces with respect to displacements. Adopting this modification, Equation 3-6 to 3-8 are now expressed as

$$E_i^{E'} = \frac{1}{2}(u_{i-1}^c + u_i^c)^T (R_i^m - R_{i-1}^m) \quad 3-9$$

$$E_i^{BE'} = \frac{1}{2}(u_{i-1}^m + u_i^m)^T (R_i^m - R_{i-1}^m) \quad 3-10$$

$$E_i^{er'} = E_i^{BE'} - E_i^{E'}$$

3-11

This modification in calculating energy error can be perceived as using complementary quadrilateral area and is analogous with the actuator tracking indicator method [40]. A graphical explanation of Equation 3-9 to 3-11 is depicted in Figure 3-4.

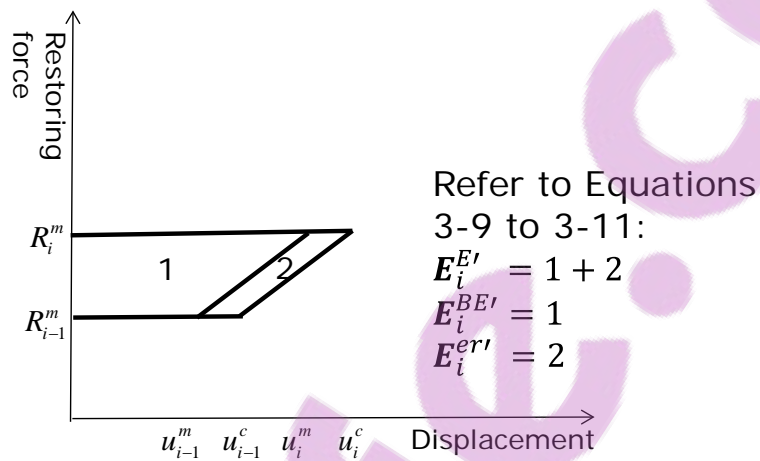


Figure 3-4 Graphical illustration of the energy error calculation outlined in Equation 3-9 to 3-11

### 3.4.2. Proposed error compensation algorithm utilising artificial viscous damping

The HSEM method alone does not provide a means of correcting the error during simulation. The proposed scheme complements the HSEM method to intuitively compensate for errors interactively during a simulation, at or near real-time. This is achieved by introducing a variable amount of artificial viscous damping proportional to the energy error at each time step.

The amount of energy dissipated by viscous damping mechanism is given by the second term on the left-hand side of Equation 3-1. Using the trapezoid rule, this integration can be approximated as

$$E_i^D = \frac{1}{2}(C\dot{u}_{i-1} + C\dot{u}_i)^T \Delta u_i^c \quad 3-12$$

where  $E_i^D$  is the energy dissipated through viscous damping across time step  $i$ . It is assumed that the viscous damping matrix  $C$  is constant throughout the simulation. For clarity, this constant viscous damping is called the initial viscous damping matrix. The variable viscous damping matrix, represented by a new variable  $C_i^{cor}$ , compensates for energy error  $E_i^{er}$  across the same step and can thus be derived by substituting  $E_i^D$  with  $E_i^{er}$  in Equation 3-12, which yields

$$C_i^{cor} = \frac{-2E_i^{er}}{(\dot{u}_{i-1} + \dot{u}_i)(u_i^c + u_{i-1}^c)} \quad 3-13$$

Incorporating this into Equation 3-2, the energy balance becomes,

$$\int (M\ddot{u})^T du + \int (C\dot{u})^T du + \int (R^m)^T du + \int (C_i^{cor}\dot{u})^T du = \int F^T du \quad 3-14$$

The term  $\int (C_i^{cor}\dot{u})^T du$  in Equation 3-14 compensates for the energy error defined by Equation 3-4, which is inherent in the vector of restoring forces  $R^m$ . Two things to note:

1. The negative sign preceding  $E_i^{er}$  in Equation 3-13 indicates that the amount of additional viscous damping to compensate the energy error across a time step is the opposite amount introduced into the system due to the energy error. For instance, if the energy error across a time step introduces negative damping into the structure, then the additional viscous damping  $C_i^{cor}$  is a positive definite matrix.
2. When an explicit numerical integration method such as the NEM method is used to solve the equation of motion, the velocity at the current time step  $\dot{u}_i$  can not be determined before solving the equation of motion. To avoid solving Equation 3-13

with iteration, the current velocity  $\dot{u}_i$  in Equation 3-13 is replaced by the predictor velocity  $\tilde{\dot{u}}_i$  which is expressed as

$$\tilde{\dot{u}}_i = \dot{u}_{i-1} + \Delta t \ddot{u}_{i-1} \quad 3-15$$

The proposed compensation method is readily extensible for MDOF system as will be shown in Chapter 4. Equation 3-13 can be computed for each experimental as well as interface DOF of in hybrid simulation with substructuring. The following points are important for multiple experimental substructures implementation:

- Coordinate transformation, if the global DOF does not coincide with the actuator DOF.

In this case, the transformation  $[T]$  between the global and actuator DOF is defined as

$$d_{act} = [T]d_{global} \quad 3-16$$

Thus Equation 3-9 should be modified into

$$E_{i,global}^{E'} = \frac{1}{2}(u_{i-1,global}^c + u_{i,global}^c)^T [T]^T (R_{i,act}^m - R_{i-1,act}^m) \quad 3-17$$

and Equation 3-10 should be modified into

$$E_{i,global}^{BE'} = \frac{1}{2}(u_{i-1,act}^m + u_{i,act}^m)^T [T^{-1}]^T [T]^T (R_{i,act}^m - R_{i-1,act}^m) \quad 3-18$$

- In real time hybrid simulation (RTHS), the highest natural frequency of the system can be quite high due to multiple DOFs involved, such that delay magnitude becomes critical since the proposed method has limited stability range. In Chapter 4, it will be shown that such limitation can be overcome by the addition of Kalman filter.

### 3.5. Numerical verification

This section presents numerical simulations to verify the proposed compensation algorithm, for fast hybrid simulations with systematic errors. The simulations utilised a linear elastic SDOF structure shown in Figure 3-5, subjected to recorded earthquake excitations. The dynamic properties of the structure are listed in Table 3-1. To study the sole effect of displacement control errors, other common sources of errors in a hybrid simulation, for examples systematic truncation errors in digital to analogue (D/A) and analogue to digital (A/D) conversions, random electronic noises and miscalibration in transducers were not simulated at this stage. Details of the numerical simulation, implemented in MATLAB, can be found in Appendix A.

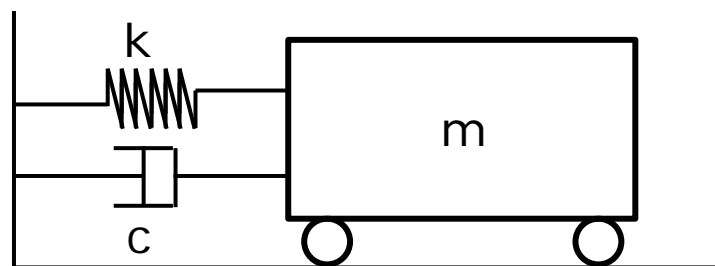


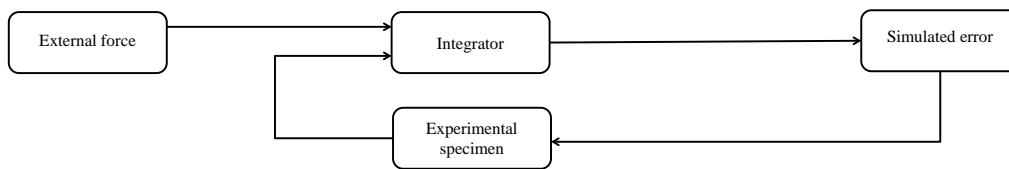
Figure 3-5 SDOF structure

Dynamic properties	
Mass (kg)	1000
Stiffness (kN/m)	158
Damping ratio	0.02
Natural period (s)	0.5

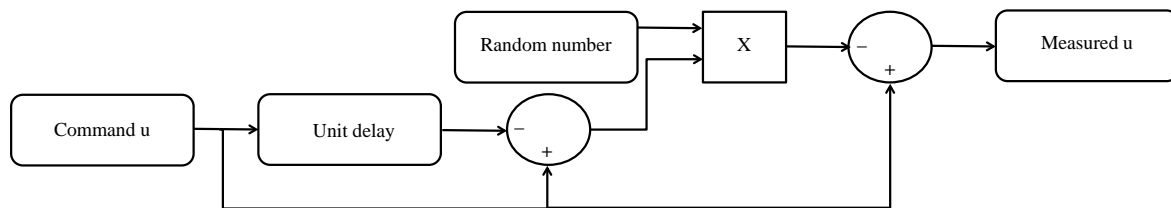
Table 3-1 SDOF structure properties

It should be noted that since the main purpose of these simulations is to demonstrate the simplicity of the proposed scheme, the behaviour of the structure was limited to linear elastic, without considering any nonlinearity such as yielding, softening, or deterioration, among others.

A block diagram describing simulation process is shown in Figure 3-6. The "Integrator" block in Figure 3-6a performs the numerical integration process using the NEM, and the "Experimental specimen" block returns the ideal restoring force of a specimen using a simulated stiffness, representing a test specimen in the laboratory.



a) Complete block diagram of a numerical simulation of a hybrid simulation



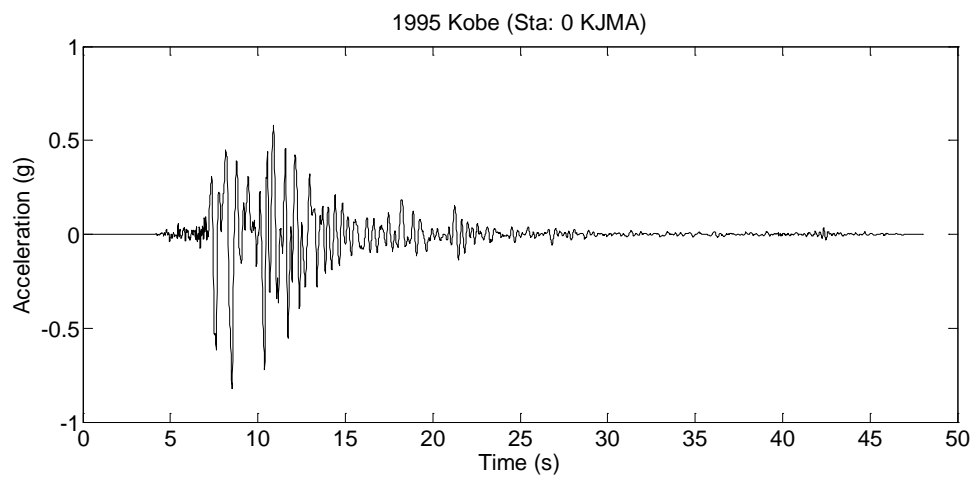
b) simulation of systematic undershooting error inside the "Systematic error" block

Figure 3-6 Numerical simulation of a hybrid simulation using block diagram

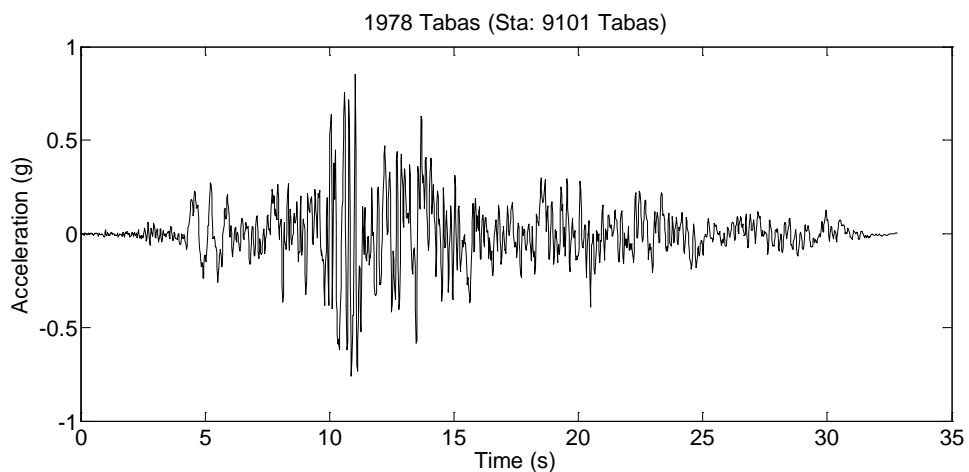
The "Simulated error" is given in detail in Figure 3-6b. The block modifies the command signal from the "Integrator" to emulate systematic actuator delays. This is achieved by introducing a normally distributed random multiplier for the displacement increment at every time step. The mean of the random multiplier is set to negative, resulting in the restoring force lagging the command displacement and reproduces the effect of systematic time delay [36]. Thus, the magnitude of displacement error due to actuator delay is proportional to the magnitude of displacement increment. In the numerical verification, the selected mean of the random number resulted in a 4 ms time delay. This delay magnitude was particularly small compared to the magnitudes present in actual experiments. To the author knowledge, the smallest delay

magnitude reported in an actual experiment was 8 ms [32], however for the purpose of the numerical verification the 4 ms magnitude was deemed appropriate.

Two earthquake records were used in these simulations, from the 1978 Tabas earthquake (Iran) and 1995 Kobe earthquake (Japan). The records of both earthquakes are shown in Figure 3-7.



a) 1995 Kobe (Sta: 0 KJMA)



b) 1978 Tabas (Sta: 9101 Tabas)

Figure 3-7 Ground acceleration records for numerical simulations

Figure 3-8a and Figure 3-8b show the displacement responses of the SDOF structure with and without simulated displacement errors subjected to the two earthquake records. The results

are shown for the first 20 seconds of each excitation, when instabilities start to occur. These figures clearly show that the simulated actuator lag manifested in additional energy into the system resulting in the large erroneous response. This highlights the importance of compensating actuator delay to avoid such instabilities in real experiments.

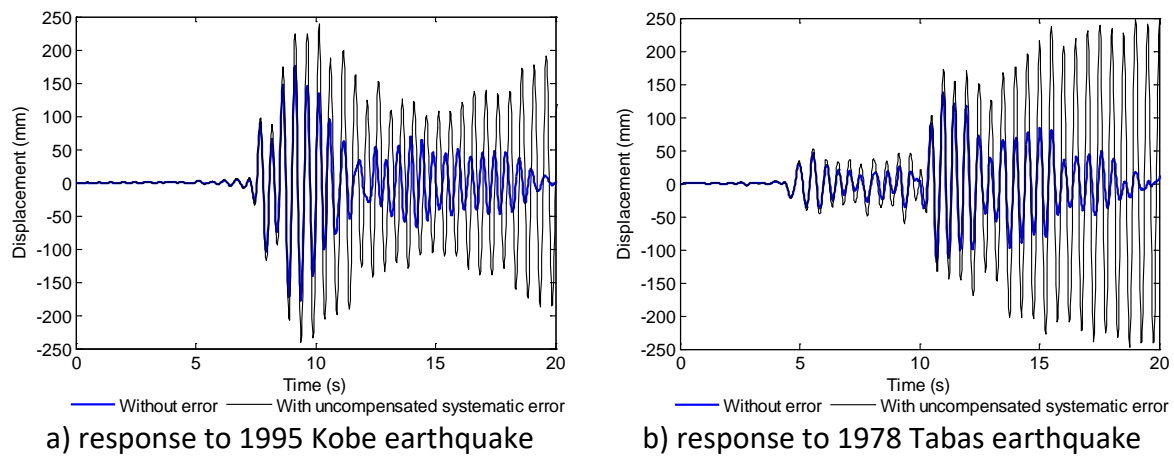


Figure 3-8 Displacement responses without displacement error and with uncompensated systematic displacement error

Figure 3-9 shows a comparison of cumulative energy error according to the three expressions described in this paper (Equation 3-5, 3-6, and 3-11). The three methods produced similar error magnitudes, however upon closer inspection the energy error calculated from Equation 3-6 visibly differed from the rest, while the energy error calculated from Equation 3-11 was very close to that from Equation 3-5. It is a good indication of the accuracy of the proposed method since the formula in Equation 3-5 is the most accurate to approximate the strain energy in a continuous structure albeit requires deriving the constantly changing tangent stiffness.

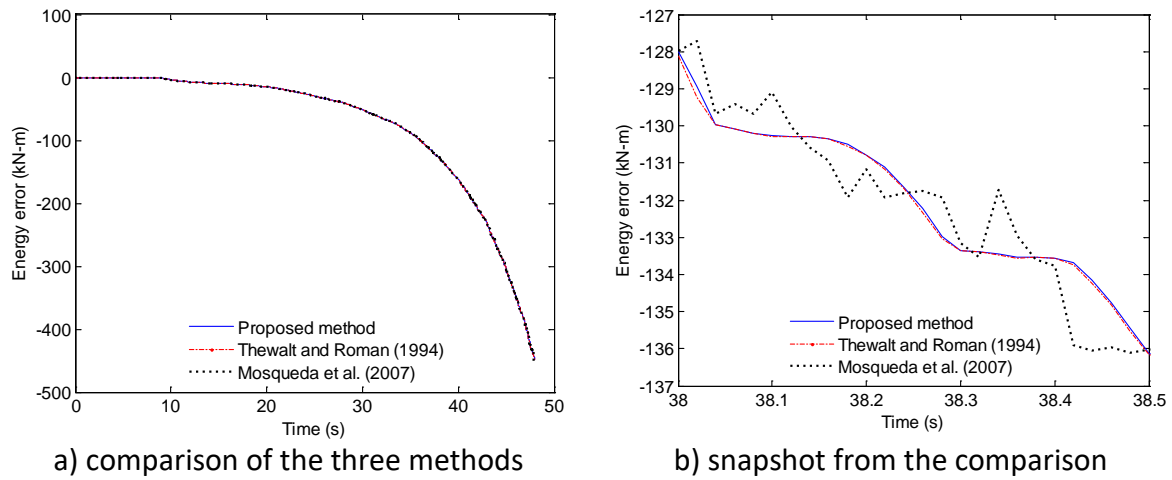
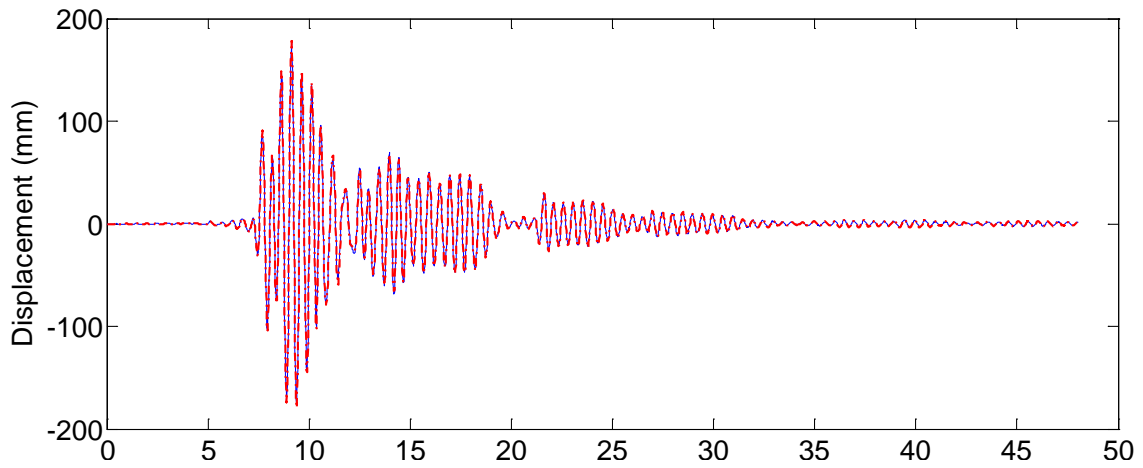
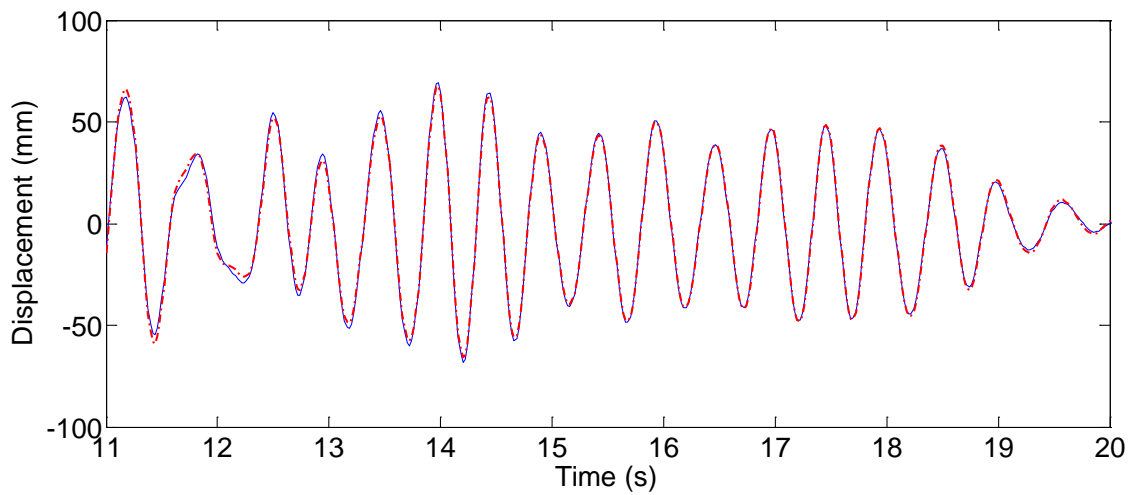


Figure 3-9 Cumulative energy error as calculated using the proposed method, Thewalt and Roman [46], and [47]

The displacement responses of the structure under the same excitations utilising the proposed error compensation scheme applied are shown in Figure 3-10a and Figure 3-10c for the Kobe and Tabas earthquakes respectively. The compensated responses accurately match the ideal responses for both excitations. Figure 3-10b and Figure 3-10d show snapshots of these compensated displacement responses for the Kobe and Tabas earthquakes respectively. These snapshots highlight minor discrepancies between the response with the proposed error compensation and the ideal response, caused by 1) the energy error used to derive the correcting variable viscous damping (Equation 3-11) was only an approximation to the energy error represented by Equation 3-5; and 2) predictor velocity (Equation 3-15) was used for practicality of implementation.

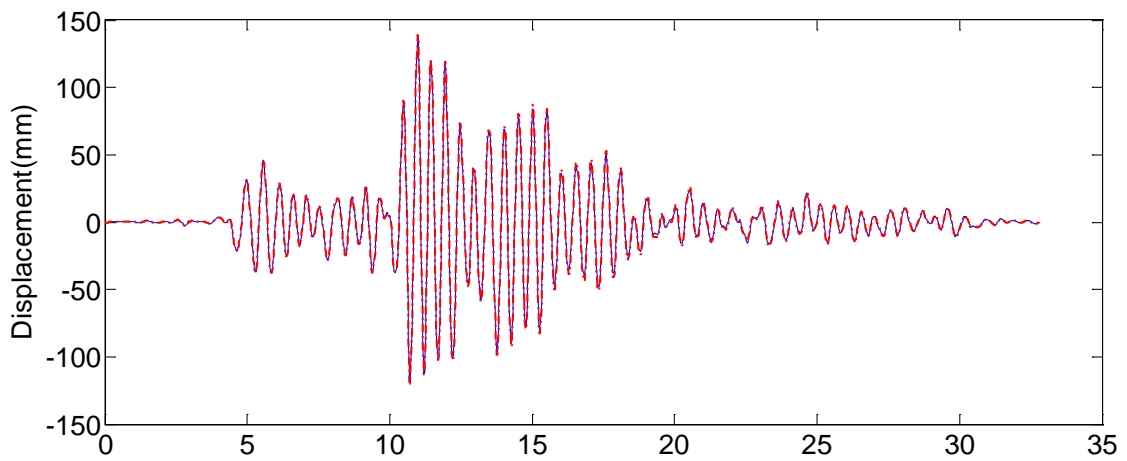


a) response to 1995 Kobe earthquake

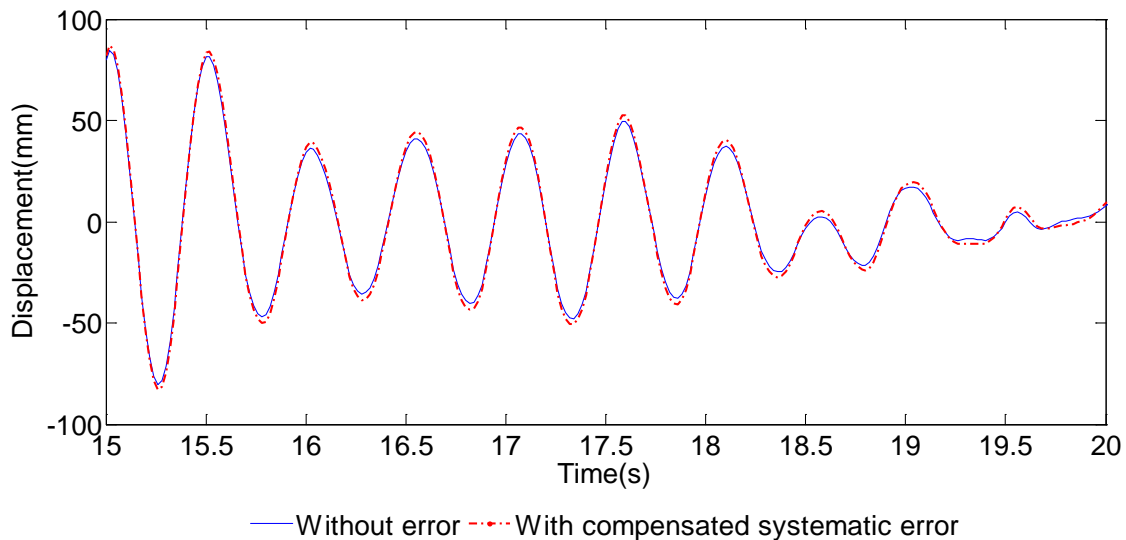


— Without error - - - With compensated systematic error

b) response to 1995 Kobe earthquake (zoomed in)



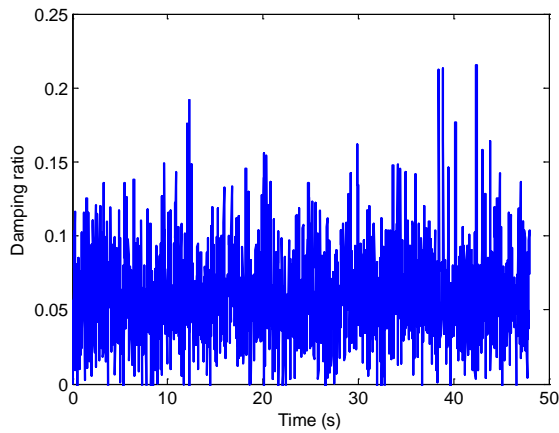
c) response to 1978 Tabas earthquake



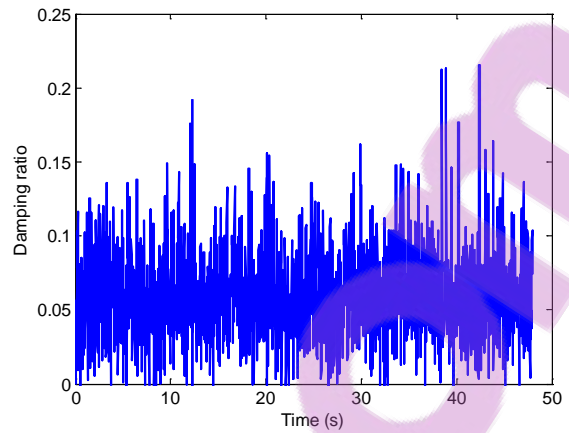
d) response to 1978 Tabas earthquake (zoomed in)

Figure 3-10 Displacement response without displacement error and with compensated systematic displacement error

Figure 3-11 shows the equivalent variable viscous damping ratio introduced into the system to compensate for the energy error at each time step. The amount of artificial viscous damping needed for compensation reached as high as 22% and 12% for the response to the Kobe (Figure 3-11a) and Tabas (Figure 3-11b) earthquakes, respectively. Considering that inherent viscous damping in typical structures are approximately 5% of critical damping, these results demonstrate that even under a relatively small delay (4 ms), the negative damping introduced to the system (the opposite of added damping required to compensate for the response) can exceed the magnitude inherent in the system and hence produces unstable response.



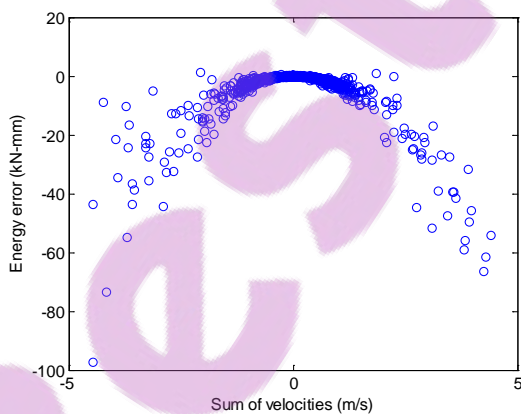
a) response to 1995 Kobe earthquake



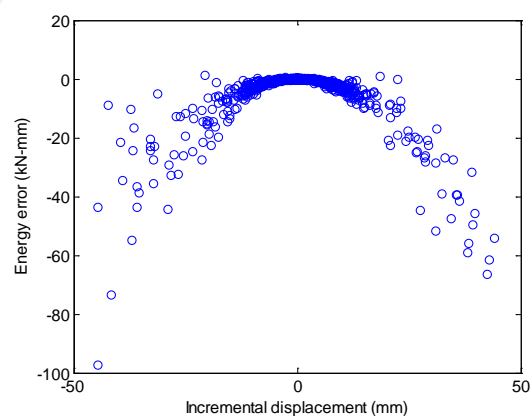
b) response to 1978 Tabas earthquake

Figure 3-11 Additional variable damping ratio to compensate for energy error in the responses

In the calculation of the variable viscous damping presented in Equation 3-13, a strategy is needed to mitigate the asymptotic mathematical error when the denominator in the Equation 3-13 becomes very small and results in erroneously large amount of viscous damping compensation which reduces the effectiveness of the proposed scheme. Figure 3-12 shows the relationships between the energy error and the two bracketed terms in the denominator in Equation 3-13, the “sum of velocities” and “incremental displacement”. For brevity, only the relationships in the response to Kobe earthquake are presented, but similar trend is also observed in the other simulation.



a) energy error and sum of velocities relationship



b) energy error and incremental displacement relationship

Figure 3-12 Relationship between components of Equation 3-13

From Figure 3-12a, as the sum of velocities approaches zero from either direction, the energy error also approaches zero. Similar trend can be observed for the incremental displacement presented in Figure 3-12b, which is expected as incremental displacement is a first order approximation of velocity. Consequently, the sum of velocities and incremental displacements approaches zero simultaneously and explains how Equation 3-13 may result in an erroneously large viscous damping compensator. Exploiting the linear relationship between incremental displacements and sum of velocities as demonstrated by Figure 3-13, it is proposed that when sum of velocities in Equation 3-13 approaches zero, the variable viscous damping at the current time step takes the same value as that from the previous time step. This strategy was implemented in the simulation and produced satisfactory results as presented in Figure 3-10.

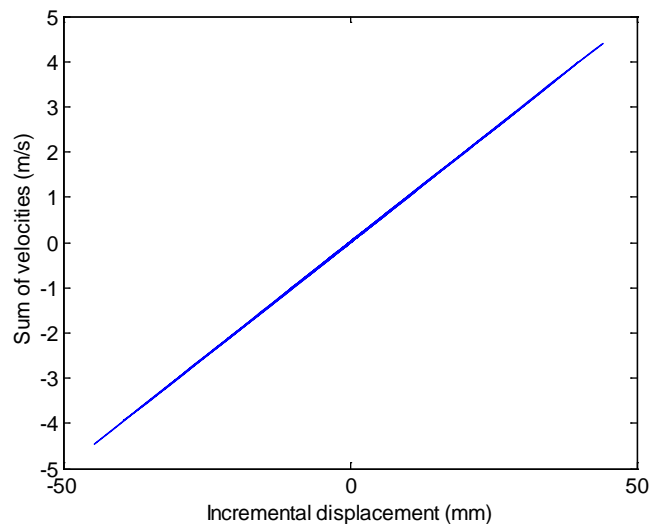


Figure 3-13 Relationship between the sum of velocities and the incremental displacement of the response to 1995 Kobe earthquake

For completeness, the accuracy of the proposed method is quantified in terms of normalized maximum error,  $\varepsilon^{max}$ , and normalized root-mean-square of error,  $\varepsilon^{rms}$  [48]. They are expressed as,

$$\varepsilon^{max} = \frac{\max |u^{sim} - u^{ideal}|}{\max |u^{ideal}|} \quad 3-19$$

$$\varepsilon^{rms} = \frac{rms |u^{sim} - u^{ideal}|}{\max |u^{ideal}|} \quad 3-20$$

In these equations,  $u^{sim}$  is the displacement response of the structure from simulation with simulated experimental errors, and  $u^{ideal}$  is the ideal displacement response from identical simulation without errors.  $\varepsilon^{max}$  measures the peak error while  $\varepsilon^{rms}$  provides a measure of the degree of match throughout the simulations.  $\varepsilon^{max}$  and  $\varepsilon^{rms}$  from the simulation using Kobe earthquake were 0.0349 and 0.007 respectively, and from the simulation using Tabas earthquake were 0.0265 and 0.095. The relatively small values indicate that the proposed compensation scheme performed well.

### 3.6. Experimental validation

The proposed compensation scheme was validated experimentally using a steel moment resisting frame (MRF) as shown in Figure 3-14. Concrete blocks with a total mass of 1.158 tons were attached on the steel beam at the top of the frame, to ensure the frame was in the same stress state as in-service prototype structure. The structure was idealised as a SDOF system.

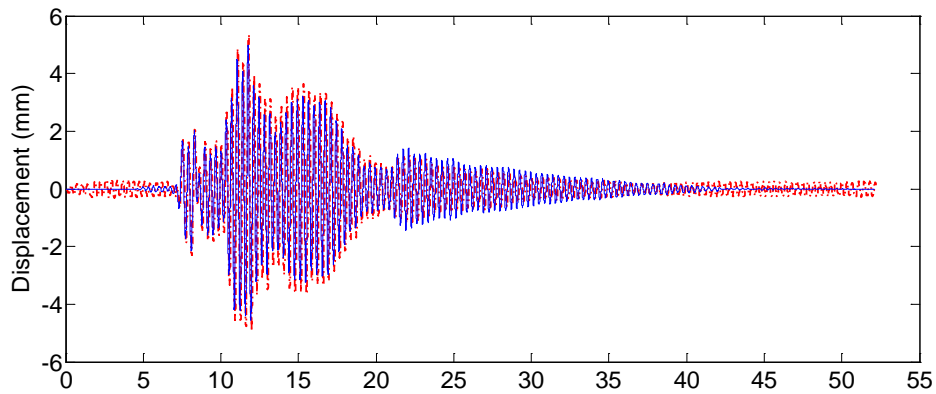


Figure 3-14 Steel moment resisting frame specimen (MRF) used in the experimental validations

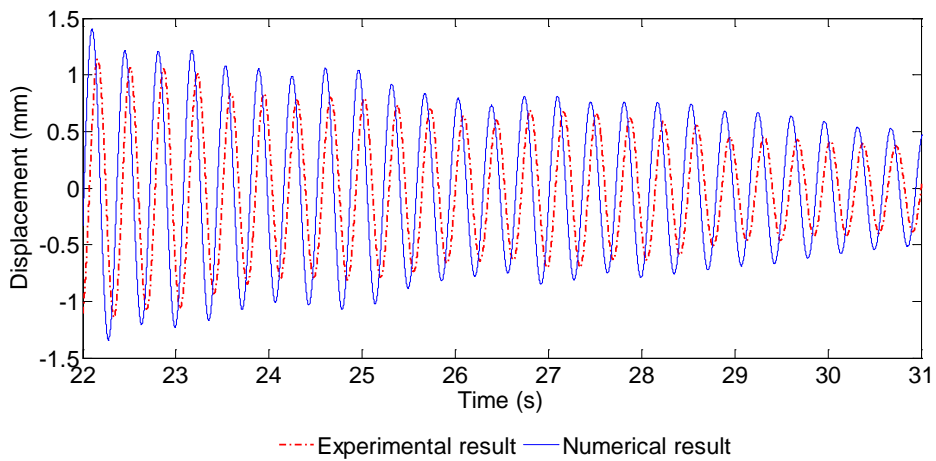
From a low-amplitude cyclic test the elastic stiffness of the frame was found to be 358.5 kN/m, which yielded an elastic natural period of 0.36 s. A hydraulic actuator with  $\pm 150$  mm stroke and  $\pm 300$  kN load capacity applied the target displacements at the top of the frame. A characterisation test found that there was 33.5 ms delay in the actuator response. With due consideration of the time delay magnitude and the natural frequency of the specimen, a time scale of 10 was selected for the testing to avoid instability.

The Kobe and Tabas earthquake records were also used during the experimental validations. The ground motion amplitudes were scaled such that displacement responses of the steel MRF did not exceed 6 mm to keep the specimen within the elastic range. Figure 3-15a and Figure 3-15c shows the displacement response of the steel frame subjected to Tabas and Kobe earthquake records respectively. Figure 3-15b and Figure 3-15d provide snapshots of Figure 3-15a and Figure 3-15b for certain time windows. The differences between the experimental and the ideal numerical simulation results can be attributed to the following factors:

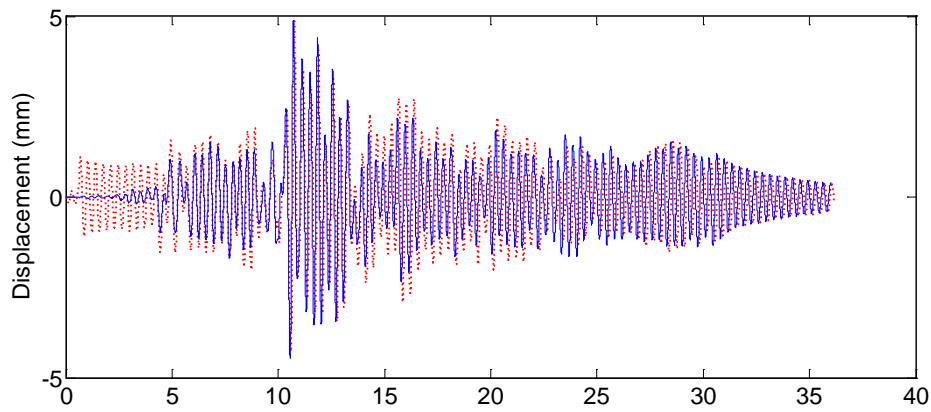
- the proposed compensation method only compensates approximate amount of energy error (Equation 3-11), resulting in residual energy error not compensated by the method in each time step.
- small differences between the dynamic parameters of the MRF assumed in the numerical simulations and the experiments.
- measurement noises.



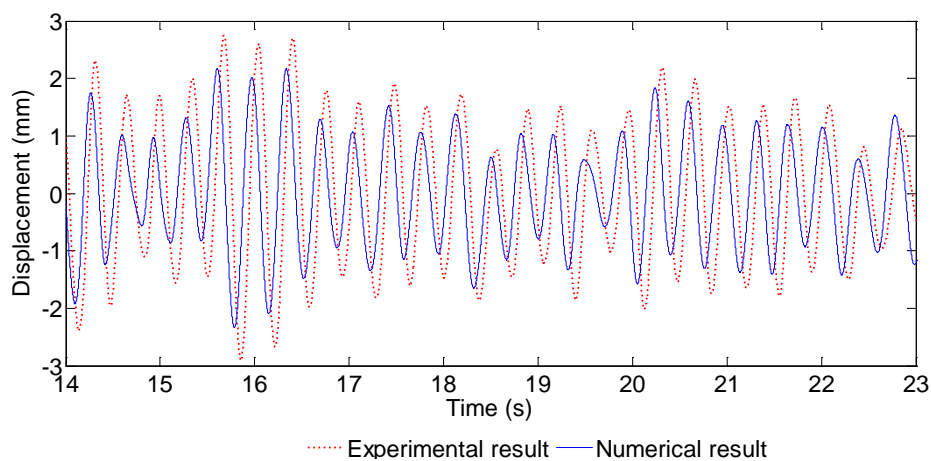
a) response to 1995 Kobe earthquake



b) response to 1995 Kobe earthquake (zoomed in)



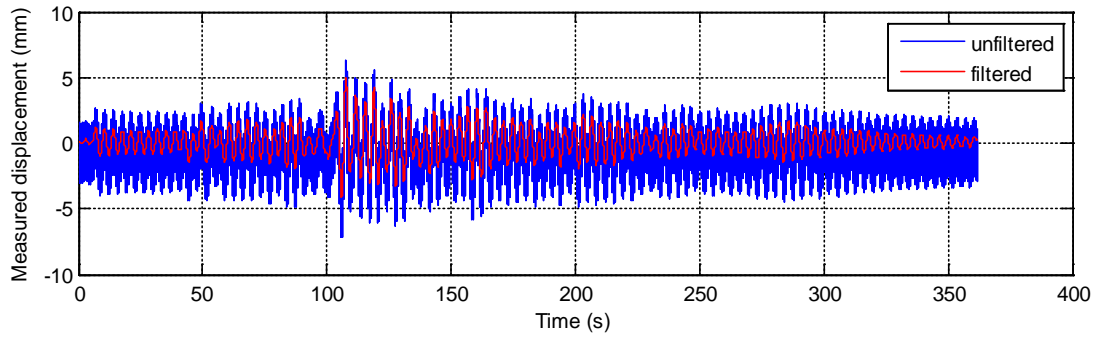
c) response to 1978 Tabas earthquake



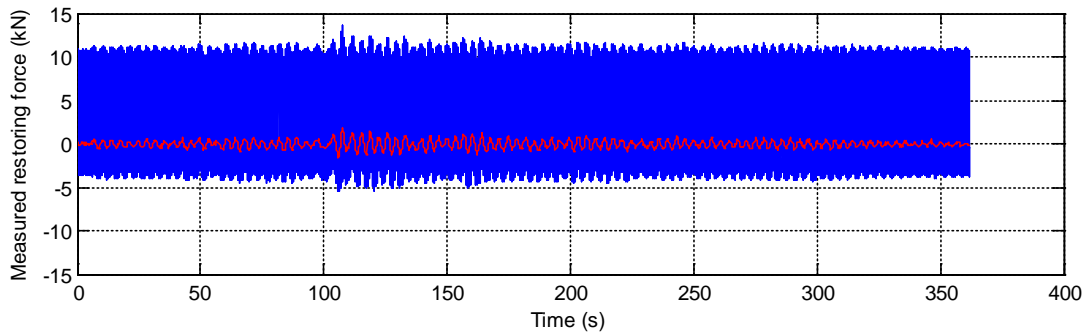
d) response to 1978 Tabas earthquake (zoomed in)

Figure 3-15 Displacement response of the MRF specimen during experimental validations

The presence of measurement noises is particularly important during experimental validations. In real experiments, measurements from force and displacement transducers are invariably affected by noise. As measurement noises are typically randomly distributed [1], this is likely to lead to uncorrelated force and displacement increment readings, which would be misinterpreted as energy error. Figure 3-16 shows measured force and displacement time histories from the experimental validations using Tabas earthquake record. The unfiltered data was recorded directly from corresponding measurement channels, while the filtered data was the result of applying zero-phase digital filter to indicate the true magnitude of the measurements, but was not performed during the actual experiments.



a) Measured displacement from Tabas experimental validation



b) Measured restoring force from Tabas experimental validation

Figure 3-16 Measured displacement and fore time histories during Tabas experimental validation

The effect of noise is particularly important in fast and continuous hybrid simulation as the equations of motion are solved at the very high sampling rate of the actuator servo-controller. During the experimental validations, the test coordinator generated command displacements at 1 kHz, the sampling rate of the actuator controller. At this rate, the commanded displacement increments at each time step in some instances were smaller than the resolution of the actuator servo-controller such that the actuators would theoretically stay on hold as it did not see any change in the displacement reference signal. Consequently, the force feedback would also stay constant until the incremental displacement exceeds the threshold governed by the actuator controller's resolution. However, due to the presence of measurement noises, which in this case are larger than the actual displacement actuation errors, the proposed compensation would detect changes in the measured restoring forces

and generated viscous damping compensations, negating the efficacy of the algorithm. The noise level in displacement and restoring force measurements were reduced during the experimental validation using a combination of two methods described in the next paragraphs.

The first method was to implement signal-smoothing procedure such as digital lowpass filter on both the displacement and force measurements. As conventional filtering introduces unavoidable time delay in the filtered response and further increase the time delay from actuator dynamics alone, a model-based filtering scheme called the Kalman filter algorithm was applied to the measured displacement and force responses. A detailed discussion on the use of Kalman filter can be found in a report by Carrion and Spencer [50] and will be presented in detail in Chapter 4.

The second method took advantage of the relationship between systematic displacement control error and the amount of energy error. Since systematic displacement control errors have direction and magnitude proportional to the displacement increments [46], the amount of energy error introduced at a given time step is dependant on the magnitude of incremental displacement. This relationship can be observed from Figure 3-12, where approaching peak displacement, indicated by small velocities or small displacement increment, the magnitudes of energy errors are close to zero representing small displacement errors. While at these small displacement increments there is little energy error due to actuator delay, the presence of noise or uncorrelated force and displacement readings will mislead the delay compensation algorithm to believe there is large energy error requiring correction. Based on this observation, an additional gain multiplier is added to the numerator of Equation 3-13. The gain multiplier deactivates the compensation when the incremental displacement is small,

and becomes as close as possible to unity when the incremental displacement is within the normal operating range. The gain multiplier can be viewed as an “ON/OFF” switch which controls the appropriate timing for the compensation scheme to work. A hyperbolic secant function of the ratio between the displacement and velocity of the structure is found to satisfy these requirements. This form of the gain multiplier is analogous to the velocity gain constant used in delay estimation procedure proposed by Darby et al. [34] and is defined as

$$G_{v_i} = \left( \operatorname{sech} \left( \frac{\omega_n u_i}{\dot{u}_{i-1}} \right) \right)^\gamma \quad 3-21$$

The parameter  $\gamma$  should be selected as  $0 < \gamma \leq 1$ , this controls the transition steepness between of  $G_{v_i}$ . For the experimental validations,  $\gamma$  was selected to be 0.05. The complete expression for the modified additional variable damping matrix becomes,

$$C_i^{cor} = \frac{-2E_i^{er} G_{v_i}}{(\dot{u}_{i-1} + \dot{u}_i)(u_i^c + u_{i-1}^c)} \quad 3-22$$

Figure 3-17 illustrates the “ON/OFF” switching behaviour of  $G_{v_i}$  for Tabas excitation. It suggests that not all energy error was corrected at every time step due to the smooth transition of  $G_{v_i}$ . It is important that the parameter  $\gamma$  be tuned so that  $G_{v_i}$  is as steep as possible to balance the effects of noise and accurate actuator delay compensation.

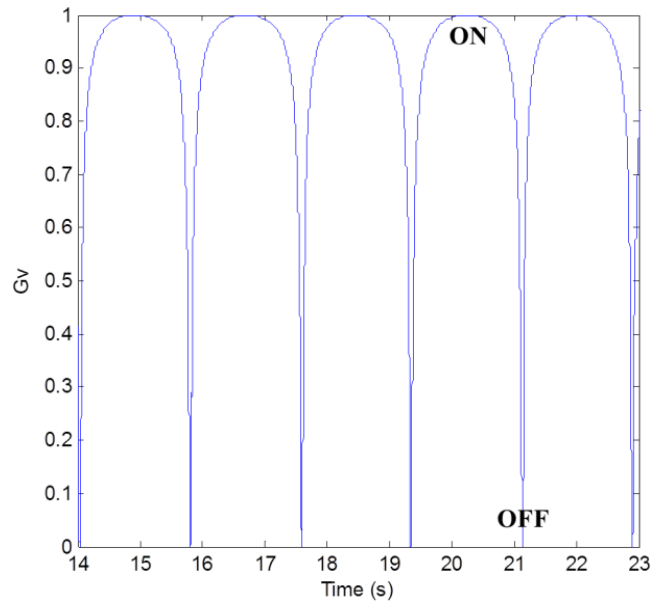
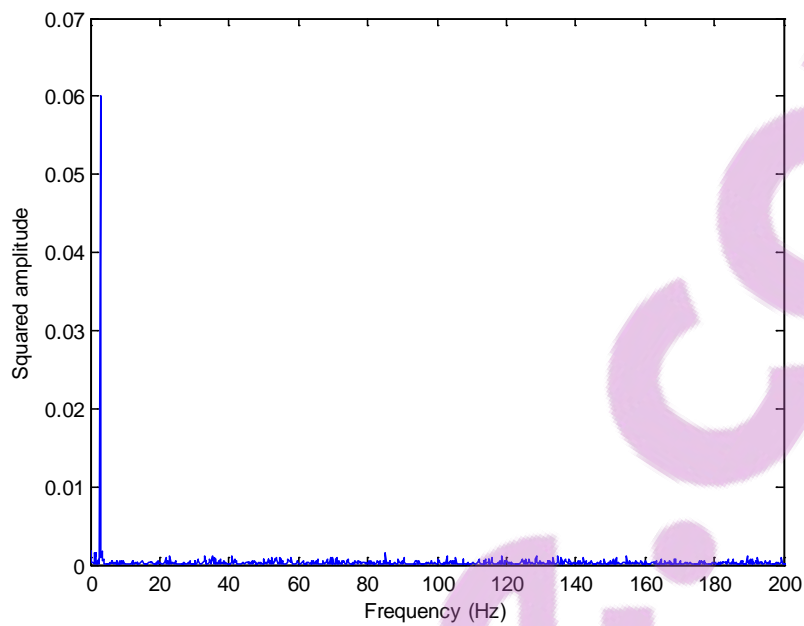


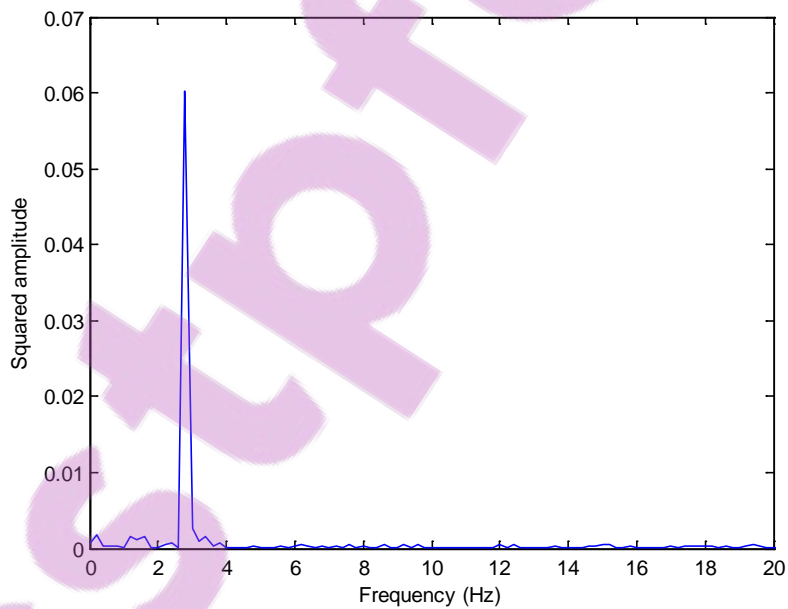
Figure 3-17  $G_v$  in displacement response due to 1995 Kobe earthquake excitation

In the beginning of the simulation, however, since excitation was small, measurement noises were too dominant to be effectively eliminated by both the Kalman filter and the gain  $G_v$ . Figure 3-15 indicates that in the beginning of the simulation, there was erroneous displacement excitation of  $\pm 1$  mm. It is of interest to investigate if there were any other sources of the erroneous excitation during the experiment beside measurement noises. Hashemi [51] utilised the frequency domain transformation of the force feedback to investigate the possible sources. Figure 3-18 shows the Fourier transformation of the force feedback from the first 5 seconds of the experimental validation using the Tabas earthquake record. The transformation used the original time scale of the earthquake record. It can be seen that there is only a single dominant frequency at around 2.8 Hz, which corresponded to the natural frequency of the steel MRF in real time scale. Unlike the research by Hashemi [51], the frequency domain plot does not reveal any other peaks that may correspond to, amongst others, the natural frequency of the actuator-reaction frame system, and the oil column frequency of the actuator-specimen system. It can be concluded that the erroneous

displacement excitation during this time was due to measurement noises in the force feedbacks that caused to the steel MRF to vibrate at its natural frequency.



a) Full frequency range

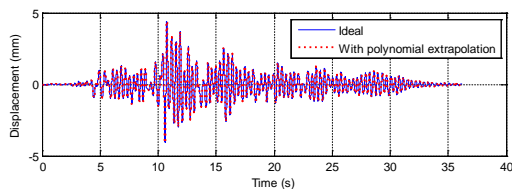


b) snapshot of 0 – 20 Hz

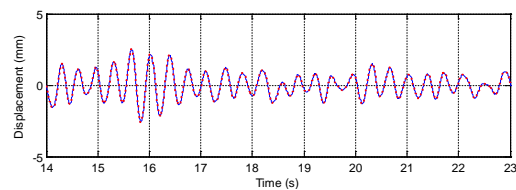
Figure 3-18 Measured restoring force in frequency domain from the experimental validation using Tabas earthquake record for the first 5 seconds of the simulation

It can be shown that unusually large measurement noises such as shown in Figure 3-16, are not only problematic for the proposed delay compensation method but can also degrade the

effectiveness of real time hybrid simulations using a more established delay compensation algorithm. Figure 3-19 and Figure 3-20 show numerical simulation results evaluating the response of the steel MRF using third order polynomial extrapolation method [52] to compensate simulated delay. Parameters for the numerical simulations are adjusted to replicate the conditions during experimental validations as close as possible, such as adopting a time scale of 10 and 33.5 ms simulated delay magnitude. The time axis in Figure 3-19 and Figure 3-20 are brought back to the original time scale of the earthquake record. Figure 3-19 shows that without simulated measurement noises, the polynomial extrapolation method performs well to compensate delay, as also demonstrated by the proposed delay compensation. On the other hand, measurement noises also seem to have similar detrimental effect to the performance of the polynomial extrapolation method as they do on the proposed delay compensation scheme, as demonstrated in the degradation of simulation accuracy shown in Figure 3-20.

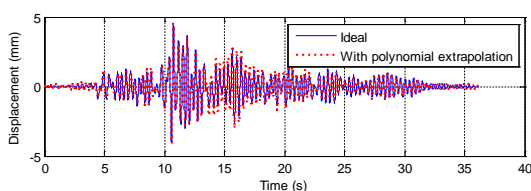


a) response to 1978 Tabas earthquake

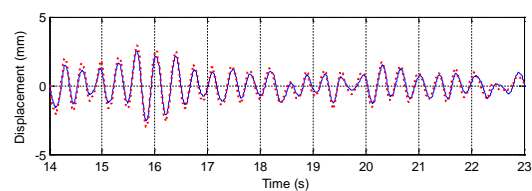


b) snapshot of a)

Figure 3-19 Numerical simulations using polynomial extrapolation method without simulated measurement noises



a) response to 1978 Tabas earthquake



b) snapshot of a)

Figure 3-20 Numerical simulations using polynomial extrapolation method with simulated measurement noises

### 3.7. Stability

The proposed compensation method compensates additional energy from the actuator delay proportional only to an approximation of the magnitude of this additional energy (Equation 3-11) instead of the ideal one (Equation 3-5). The difference between the ideal and the approximated magnitude is the residual energy error not corrected through the proposed algorithm that will build up during the experiment and may become larger than the amount of energy that can be dissipated through the inherent viscous damping of the specimen. Thus, the stability of the proposed delay compensation method is dependent to the magnitude of the inherent viscous damping.

In an ideal situation without delay, an underdamped free vibration response of a SDOF structure will decay toward zero amplitude due to material damping and energy dissipation from frictions at all connections in the whole test setup. Depending on the delay magnitude however, the free vibration response amplitudes may continue growing instead if the rate of energy addition is larger than the rate of energy dissipation. The magnitude of delay beyond which the underdamped free vibration response grows unbounded is the stability limit of the proposed method.

In the proposed compensation method, the residual energy errors propagate throughout the simulation. The equivalent viscous damping ratio becomes a function of time defined as the total between the constant equivalent viscous damping ratio assumed for the specimen and a time-varying, equivalent amount of negative damping ratio from the residual energy error. This complicates deriving a closed-form solution of the stability limit since the time varying equivalent viscous damping term appears in the underdamped displacement response equation of the freely vibrating structure. In the research, a more practical approach to derive

the stability limit is taken through parametric simulations with increasing delay magnitude while keeping all other simulation parameters constant until instability occurs.

The parametric simulations were conducted on a SDOF structure with a natural period  $T_n$  of 0.1 s and an equivalent viscous damping ratio  $\zeta$  of 5%. The structure was subjected to an impulse ground acceleration of 1 g amplitude and duration of  $0.5T_n$ . Normalised residual energy error  $\hat{E}^{res}$  was defined as the difference between Equation 3-5 and 3-11, normalised by the energy from viscous damping, Equation 3-12. Instability occurs when the normalised residual energy error  $\hat{E}^{res}$  became smaller than -1, implying that the residual energy accumulates at a higher rate than the dissipated energy from viscous damping.

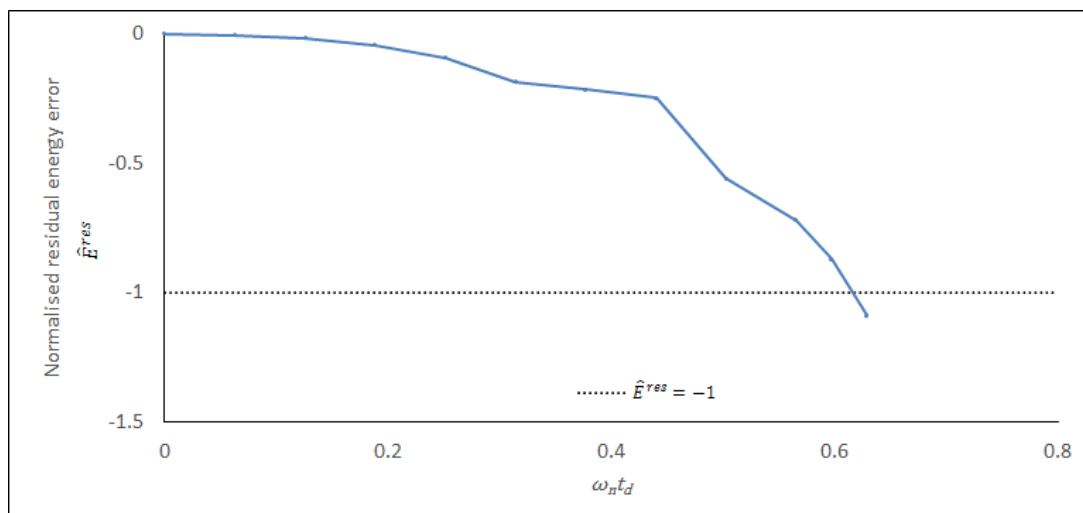


Figure 3-21 Normalised residual energy ratio for selected critical damping ratio values

Figure 3-21 shows the relationship between the residual energy error and the stability criteria, defined by a unitless parameter  $\omega_n t_d$ , where  $\omega_n$  is the natural frequency of the structure. Figure 3-21 shows that the stability limit of the proposed delay compensation method is  $\omega_n t_d \approx 0.59$ , since larger  $\omega_n t_d$  results in a normalised residual energy error smaller than -1. This stability limit is relatively smaller than the stability limit of existing delay compensation methods, for example the polynomial extrapolation method is 1.571 [32] The actual stability

of the proposed method will vary in a case-to-case basis. Table 3-2 summarises the result of two different sets of parametric studies investigating the stability limit of the proposed compensation method. In the first set the numerical integration time step  $\Delta t$  was decreased to 0.0025 s while keeping the other simulation parameters constant. In the second set the natural period of the structure  $T_n$  was increased to 0.2 s while keeping the other simulation parameters from the original set constant.

$\Delta t$	Stability limit ( $\omega_n t_d$ )
0.005 (initial)	0.59
0.0025	0.47
$T_n$	Stability limit ( $\omega_n t_d$ )
0.1 (initial)	0.59
0.2	0.53

Table 3-2 Summary of stability limit of the proposed delay compensation method with different simulation parameters

Table 3-2 shows that both decreasing the integration time step size as well as increasing the natural period of the structure result in a lower stability limit compared to the simulation using the initial set of parameters. This seems counter intuitive at first since decreasing time step size means decreasing displacement increment between time steps and increasing natural period decreases velocity which also decreases displacement increment. Figure 3-6b indicates that smaller displacement increment introduces smaller displacement error to the simulation. However, it should be noted that in the case where the integration time step size is halved, one simulation consists of twice as many integration points as the original one, thus the number of displacement error introduced is also doubled, resulting in larger cumulative energy error at the end of simulation. In the second case, the decreasing stability limit could be due to two causes. For the same time step size, a model with longer natural periods will have more integration points than the shorter one, thus will amplify the cumulative energy

error at the end of simulation. Another reason would be although longer natural period results in smaller displacement error, the total dissipated energy through viscous damping is also smaller due to smaller velocity, and the residual energy can exceed this at smaller  $\omega_n t_d$  than that of the original simulation.

### **3.8. Summary**

A new method to compensate for actuator delay in a fast to real-time hybrid simulation has been presented. It is recognised that actuator delay introduces additional energy into the structure equivalent to the effect of negative damping and can potentially destabilize a hybrid simulation. The method works through quantifying the amount of additional energy at every integration step and transforms it into an equivalent positive damping which provides extra energy dissipation to negate the additional energy. The method is more intuitive than other existing delay compensation procedures since it neither requires stiffness estimation nor prediction of next displacement target, instead the method simply utilises readily available measurements from a test specimen.

It was found during experimental validation that the method is very sensitive to measurement noises. These noises are the most dominant cause of discrepancies between the ideal numerical simulations and experimental results, since the frequency domain transformation of the measured restoring force reveals that the proposed compensation does excite any other peaks that correspond to either the specimen-reaction wall system, or the oil column. It was also shown through numerical simulations that measurement noises had similar deteriorating effect to the polynomial extrapolation method. These show that the noises contributed the most to degrading the experimental performance of the proposed compensation algorithm. Two techniques were utilised to mitigate the effect of the noises;

the Kalman filter algorithm and an adaptive gain that controlled the timing at which the proposed scheme compensated the additional energy.

The stability limit of the proposed method is assessed through parametric study employing a linear elastic SDOF structure. It was found that the stability limit of the proposed method is relatively smaller than those of existing delay compensation procedures.

# Chapter 4

## Improving hybrid simulation through Kalman filter

---

### 4.1. Introduction

Measurement from transducers in experiments inherently come with noise., which is unwanted signal that interferes with the original (or desired) signals of a given physical quantity (voltage, current, resistance) [53]. Measurement noises come external sources such as electromagnetic interference from currents in cables or cross-talk between cables separated by small distance as well as come from internal imperfections in the measurement devices. Noise magnitude may be amplified by ground loop, a condition where there are multiple paths for electricity flow to the ground. Measurement noises can be physically observed in a recorded data as high frequency fluctuations about the actual measurement value.

Although it has been shown the errors of the systematic type have a more severe propagation characteristic [1], random errors, such as measurement noises, can degrade the accuracy of a hybrid simulation if not mitigated properly. The effect is more pronounced in a MDOF system due to DOF coupling, represented by the off-diagonal term in the stiffness matrix. Due to coupling, any experimental errors occurring in one DOF can affect the others, amplifying the effect of experimental errors in any DOF.

The presence of measurement noises is critical in a fast hybrid simulation. In the conventional hybrid simulation method, which utilises the “ramp-and-hold” technique, restoring force

measurements are averaged over the duration of the “hold” phase which reduces measurement noises’ magnitude. In fast hybrid simulation however, the integration algorithm utilises the restoring force measurements at the instant they are measured as actuators are moving continuously during experiment [54]. If the measured restoring forces are substantially in error due to noise the numerical integration may produce premature command displacement to the structure that may lead to unexpected failure.

Traditionally, measurement noises are reduced using lowpass filters. Lowpass filters passes signals with frequencies lower than the cut-off relatively unmodified while attenuating those higher. It is a desirable attribute since measurement noises generally have much higher frequencies than the signals of interest. However, classical lowpass filters, such as Butterworth, Chebyshev, or Elliptic filter, impose time delay (phase shift) in the filtered signals. While this shortcoming is inconsequential for offline data processing, it is highly undesirable in an online, closed-loop system such as hybrid simulation, since time delay introduces negative damping effect. Chapter 3 has illustrated the potentially destabilising effect of time delay in fast hybrid simulations. A more sophisticated filtering algorithm that does not introduce time delay is thus required for hybrid simulations.

The Kalman filter algorithm is a model-based filtering technique that estimates the states of a dynamic system by implementing predictor and corrector steps based on observations obtained from measurements with noises. The filter algorithm uses information such as previously estimated states, the dynamic model of the system, and the statistical distributions of the noises. Unlike classical lowpass filters, the Kalman filter does not introduce time delay in the filtered signals.

This chapter presents a set of numerical simulations focusing on the application of Kalman filters to reduce excessive noises in measurements during hybrid simulations. It will also be shown that the same filtering technique can be used to ensure stability in fast hybrid simulations with actuator delay.

## 4.2. Kalman filter

The first application of Kalman filter in a hybrid simulation was proposed by Carrion and Spencer [50]. They conducted a series of hybrid tests on a small scale, two-bay steel frame structure. The stiffness of the numerical beam substructure was varied to investigate the effect of different signal-to-noise ratio values to the accuracy of the tests. The research showed that when the magnitudes of the desired measurement signals were small compared to the noises, the experiments showed tendencies to become unstable.

The Kalman filter algorithm for a discrete system is implemented in predictor and corrector steps. The standard equations are formulated as

$$\hat{z}_i^- = \mathbf{A}\hat{z}_{i-1} + \mathbf{B}\bar{u}_i + w_i \quad 4-1$$

$$y_i^m = \mathbf{C}\hat{z}_i^- + v_i \quad 4-2$$

Equation 4-1 can be understood as follows. At time step  $i$ , the Kalman filter algorithm predicts the actual state of the system  $z_i$  as  $\hat{z}_i^-$  using information from the estimated state of the specimen at the previous time step,  $\hat{z}_{i-1}$ , the dynamic model of the system in the state transition matrix  $\mathbf{A}$ , and the input at the current time step  $\bar{u}_i$  to the system.  $\mathbf{B}$  is the matrix that relates the input to the corresponding state according to the dynamic model of the system. The algorithm considers measurements  $y_i^m$  to correct the predicted states  $\hat{z}_i^-$  to obtain the new estimated state  $\hat{z}_i$ .  $\mathbf{C}$  is the sensor matrix that relates the predicted states to

the predicted measurements. The new estimated state  $\hat{z}_i$  can be understood as the best approximation to the actual (yet unknown) value of the current state  $z_i$ . Just as the actual measurement  $y_i^m$  is contaminated by the measurement noise  $v$ , the input to the system is also contaminated by the process noise  $w$ . A step-by-step procedure for implementation the Kalman filter algorithm in a discrete-time system can be found in [50] and is repeated here for convenience.

Initialisation:

- Define initial estimated state:  $E[z_0]$  4-3
- Define initial error covariance:  $\mathbf{P}_0 = E[(z_0 - \hat{z}_0)(z_0 - \hat{z}_0)^T]$  4-4

For  $i = 1, 2, \dots$

- State prediction:  $\hat{z}_i^- = \mathbf{A}\hat{z}_{i-1} + \mathbf{B}\bar{u}_i$  4-5
- Error covariance prediction:  $\mathbf{P}_i^- = \mathbf{A}\mathbf{P}_{i-1}\mathbf{A}^T + \mathbf{Q}_{i-1}$  4-6
- Filter gain computation:  $\mathbf{L}_i = \mathbf{P}_i^- \mathbf{C}^T (\mathbf{C}\mathbf{P}_i^- \mathbf{C}^T + \mathbf{R}_i)^{-1}$  4-7
- Estimate state (update prediction):  $\hat{z}_i = \hat{z}_i^- + \mathbf{L}_i (y_i - \mathbf{C}\hat{z}_i^-)$  4-8
- Estimate error covariance (update prediction):  $\mathbf{P}_i = (\mathbf{I} - \mathbf{L}_i \mathbf{C}) \mathbf{P}_i^-$  4-9

where  $E[p]$  represents the expected (mean) value of  $p$ . In a hybrid simulation,  $\mathbf{A}$ ,  $\mathbf{B}$ , and  $\mathbf{C}$  in Equation 4-1 to Equation 4-9 are specific to the numerical integration method employed as well as the way actuators imposes target displacement to the experimental structure.

In Equation 4-6 and 4-7,  $\mathbf{Q}$  and  $\mathbf{R}$  are the noise covariance matrices, namely,

$$\mathbf{Q} = E[w_i w_i^T] \quad 4-10$$

$$\mathbf{R} = E[v_i v_i^T] \quad 4-11$$

Considering  $v$  as the vector of measurement noises,

$$\mathbf{R} = \begin{bmatrix} \mathbf{S}_x & \mathbf{0} \\ \mathbf{0} & S_f \end{bmatrix} \quad 4-12$$

Pertaining to the number of DOF controlled using the actuators,  $\mathbf{S}_x$  is a diagonal matrix of the displacement transducer noise variances while  $\mathbf{S}_f$  is a diagonal matrix of the load transducer noise variances.

The input  $\bar{u}_i$  to the Kalman filter equation in a hybrid simulation is the ground acceleration record. It is deterministic and contains no input noise. Therefore, the process noise covariance is selected as fictitious noise to represent modelling uncertainties [50]. Carrion and Spencer demonstrated that the exact values of  $\mathbf{Q}$  and  $\mathbf{R}$  need not be exactly known and it was sufficient to consider the relative value between the two as in the following expression,

$$\mathbf{RQ}^{-1} = \rho \begin{bmatrix} \mathbf{I} & \mathbf{0} \\ \mathbf{0} & \boldsymbol{\alpha}_v \end{bmatrix} \quad 4-13$$

In Equation 4-13, the  $\boldsymbol{\alpha}_v$  is a diagonal matrix of the load to displacement transducer noise variances ratio. The performance of Kalman filter can be tuned by selecting different values of  $\rho$ , the ratio between the measurement and process noise covariances, to give the most accurate simulation results.

The Kalman filter parameter matrices,  $\mathbf{A}$ ,  $\mathbf{B}$  and  $\mathbf{C}$ , depend on the numerical integration method employed in the hybrid simulation algorithm. For the NEM employed in Chapter 3, these matrices are defined considering the following variables

- The number of experimentally controlled DOFs,  $N_{\text{dof}}$  such that

$$\mathbf{K}^t = \begin{bmatrix} k_{1,1} & \cdots & k_{1,N_{\text{dof}}} \\ \vdots & \ddots & \vdots \\ k_{N_{\text{dof}},1} & \cdots & k_{N_{\text{dof}},N_{\text{dof}}} \end{bmatrix} \quad 4-14$$

$$M = \begin{bmatrix} \mathbf{m}_{1,1} & \cdots & 0 \\ \vdots & \ddots & \vdots \\ 0 & \cdots & \mathbf{m}_{N_{\text{dof}},N_{\text{dof}}} \end{bmatrix} \quad 4-15$$

where  $K^t$  and  $M$  is the tangent stiffness and the diagonal mass matrices. The viscous damping matrix can also be defined in the same way.

$$C = \begin{bmatrix} \mathbf{c}_{1,1} & \cdots & \mathbf{c}_{1,N_{\text{dof}}} \\ \vdots & \ddots & \vdots \\ \mathbf{c}_{N,1} & \cdots & \mathbf{c}_{N_{\text{dof}},N_{\text{dof}}} \end{bmatrix} \quad 4-16$$

This results in an effective mass matrix.

$$M^* = M + \frac{\Delta t}{2} C = \begin{bmatrix} \mathbf{m}_{1,1}^* & \cdots & \mathbf{m}_{1,N_{\text{dof}}}^* \\ \vdots & \ddots & \vdots \\ \mathbf{m}_{N_{\text{dof}},1}^* & \cdots & \mathbf{m}_{N_{\text{dof}},N_{\text{dof}}}^* \end{bmatrix} \quad 4-17$$

- The number of specimen states,  $N_{\text{state}}$ : 3 (displacement, velocity, and acceleration).
- The number of measurements:  $N_{\text{msr}}$ .

Equation 4-1 to 4-14 are put together to formulate the Kalman filter parameter vectors and matrices specific to the NEM scheme. These are defined as

$$\mathbf{A} = \begin{bmatrix} \mathbf{a}_{m=1,n=1}^1 & \cdots & \mathbf{a}_{m=1,n=N_{\text{dof}}}^2 \\ \vdots & \ddots & \vdots \\ \mathbf{a}_{m=N_{\text{dof}},n=1}^2 & \cdots & \mathbf{a}_{m=N_{\text{dof}},n=N_{\text{dof}}}^1 \end{bmatrix}_{(N_{\text{state}} \times N_{\text{dof}}) \times (N_{\text{state}} \times N_{\text{dof}})} \quad 4-18$$

$$\mathbf{a}_{m,n}^1 = \begin{bmatrix} 1 & \Delta t & 0.5\Delta t^2 \\ 0 & 1 - \frac{\Delta t c_{m,n}}{2m_{m,n}^*} & \frac{\Delta t}{2} \left( 1 - \frac{\Delta t c_{m,n}}{2m_{m,n}^*} \right) \\ 0 & -\frac{c_{m,n}}{m_{m,n}^*} & -\frac{\Delta t}{2} \frac{c_{m,n}}{m_{m,n}^*} \end{bmatrix} \quad 4-19$$

$$\mathbf{a}_{m,n}^2 = \begin{bmatrix} 0 & 0 & 0 \\ 0 & 1 - \frac{\Delta t c_{m,n}}{2m_{m,n}^*} & \frac{\Delta t}{2} \left( 1 - \frac{\Delta t c_{m,n}}{2m_{m,n}^*} \right) \\ 0 & -\frac{c_{m,n}}{m_{m,n}^*} & -\frac{\Delta t}{2} \frac{c_{m,n}}{m_{m,n}^*} \end{bmatrix} \quad 4-20$$

Superscript 1 indicates the position of the inner matrices on the main diagonal of the complete matrix  $\mathbf{A}$  while superscript 2 indicates the position on the off-diagonal elements.

$$\mathbf{B} = \begin{bmatrix} b_{m=1,n=1} & \cdots & b_{m=1,n=N_{\text{dof}}} & -b_{m=1,n=1} & \cdots & -b_{m=1,n=N_{\text{dof}}} \\ \vdots & \ddots & \vdots & \vdots & \ddots & \vdots \\ b_{m=N_{\text{dof}},n=1} & \cdots & b_{m=N_{\text{dof}},n=N_{\text{dof}}} & -b_{m=N_{\text{dof}},n=1} & \cdots & -b_{m=N_{\text{dof}},n=N_{\text{dof}}} \end{bmatrix}_{(N_{\text{state}} \times N_{\text{dof}}) \times (N_{\text{msr}} \times N_{\text{dof}})} \quad 4-21$$

$$b_{m,n} = \begin{bmatrix} 0 & \frac{\Delta t}{2m_{m,n}^*} & \frac{1}{m_{m,n}^*} \end{bmatrix}^T \quad 4-22$$

$$\mathbf{C} = \begin{bmatrix} \mathbf{c}_{m=1,n=1}^1 & \cdots & \mathbf{c}_{m=1,n=N_{\text{dof}}}^2 \\ \vdots & \ddots & \vdots \\ \mathbf{c}_{m=N_{\text{dof}},n=1}^2 & \cdots & \mathbf{c}_{m=N_{\text{dof}},n=N_{\text{dof}}}^1 \\ \hat{\mathbf{k}}_{m=1,n=1} & \cdots & \hat{\mathbf{k}}_{m=1,n=N_{\text{dof}}} \\ \vdots & \ddots & \vdots \\ \hat{\mathbf{k}}_{m=N_{\text{dof}},n=1} & \cdots & \hat{\mathbf{k}}_{m=N_{\text{dof}},n=N_{\text{dof}}} \end{bmatrix}_{(N_{\text{msr}} \times N_{\text{dof}}) \times (N_{\text{state}} \times N_{\text{dof}})} \quad 4-23$$

$$\mathbf{c}_{m,n}^1 = [1 \ 0 \ 0] \quad 4-24$$

$$\mathbf{c}_{m,n}^2 = \mathbf{0}_{N_{\text{state}} \times 1} \quad 4-25$$

Superscript 1 indicates the position of the inner matrices on the main diagonal of the upper half of  $\mathbf{C}$  while superscript 2 indicates the position on the off-diagonal elements, and

$$\hat{\mathbf{k}}_{m,n} = [k_{m,n} \ 0 \ 0] \quad 4-26$$

The state,  $z$ , and input,  $\bar{u}$ , vectors into the Kalman filter equation are

$$z = [\mathbf{u}_m \ \dot{\mathbf{u}}_m \ \ddot{\mathbf{u}}_m \ \cdots \ \mathbf{u}_{N_{\text{DOF}}} \ \dot{\mathbf{u}}_{N_{\text{DOF}}} \ \ddot{\mathbf{u}}_{N_{\text{DOF}}}]^T \quad 4-27$$

$$\bar{u} = [\mathbf{F}_m \ \cdots \ \mathbf{F}_{N_{\text{DOF}}} \ \mathbf{R}_m \ \cdots \ \mathbf{R}_{N_{\text{DOF}}}]^T \quad 4-28$$

### 4.3. Influence of DOF coupling

Different sets of simulations demonstrating the advantage of applying the Kalman filter algorithm in a hybrid simulation will be presented next. All simulations utilise a two-storey shear building. The structure is shown schematically in Figure 4-1.

The first set of simulations demonstrates the influence of measurement noises on the accuracy of hybrid simulations considering different extent of couplings between DOF, since the extent of the errors in MDOF system depend not only on the magnitude of the errors themselves but also on the degree of coupling between DOF.

The effect of measurement noises in a hybrid simulation environment is replicated by adding fictitious noise from a Gaussian random number generator to the simulated displacement and force measurements. The random number distribution has a zero mean and a standard

deviation that is adjusted to give the desired noise level [47]. The Kalman filter algorithm works optimally if the distributions of the process and measurement noises are Gaussian, which is considered representative to real noise distributions [1]. In the numerical simulations, the fictitious displacement transducer noise is set to have a zero mean and a standard deviation of 7.97E-5 m, while the force transducer noise is set to a zero mean and a standard deviation of 0.0797 kN. Considering the actuator transducers used during experimental validations in Chapter 3, the standard deviations are equal to 0.026% of the full measurement ranges of the displacement and load transducers. These values are considered representative for the modern servo-hydraulic actuators.

The properties of the frame are varied for different purposes of the numerical simulation. The basic properties are:

- The stiffness at each storey,  $k_{top}$  and  $k_{bottom}$ , is the total stiffness of the columns at each storey. The stiffness matrix (initial/tangent) is formulated as

$$\begin{bmatrix} k_{top} + k_{bottom} & -k_{top} \\ -k_{top} & k_{top} \end{bmatrix}$$

- Identical concentrated mass  $m$  is assumed located on the rigid beam on each storey. The mass stiffness matrix is formulated as

$$\begin{bmatrix} m & 0 \\ 0 & m \end{bmatrix}$$

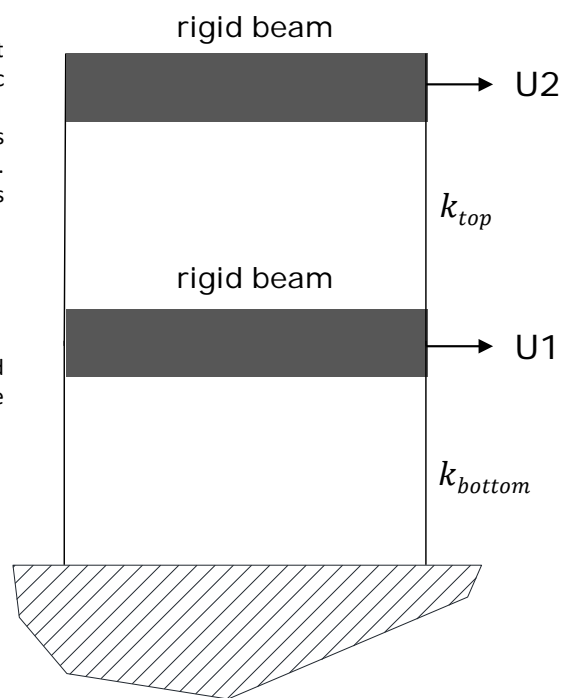


Figure 4-1 Schematic drawing of the two DOF shear frame

#### 4.3.1. Case 1: weak DOF coupling

In Case 1, the top storey stiffness ( $k_{top}$ ) is set to one-fifth of the bottom storey stiffness ( $k_{bottom}$ ). The resulting initial stiffness (with superscript “I” to distinguish with the tangent stiffness) and mass matrices are

$$K' = \begin{bmatrix} 34.11 & -5.68 \\ -5.68 & 5.68 \end{bmatrix} kN / m \quad 4-29$$

$$M = \begin{bmatrix} 500 & 0 \\ 0 & 500 \end{bmatrix} kg \quad 4-30$$

Equation 4-29 shows that the off-diagonal terms in the stiffness matrix are significantly smaller than the diagonal ones, implying limited coupling in the restoring forces developed on both stories of the shear frame structure [1]. The resulting natural frequencies of the numerical model are 0.48 and 1.34 Hz. An equivalent viscous damping ratio of 5% is assumed for both modes.

The numerical structure is subjected to 40% of the 1999 Duzce earthquake ground motion record where the original unscaled record is shown in Figure 4-2. The response of the structure is linear elastic.

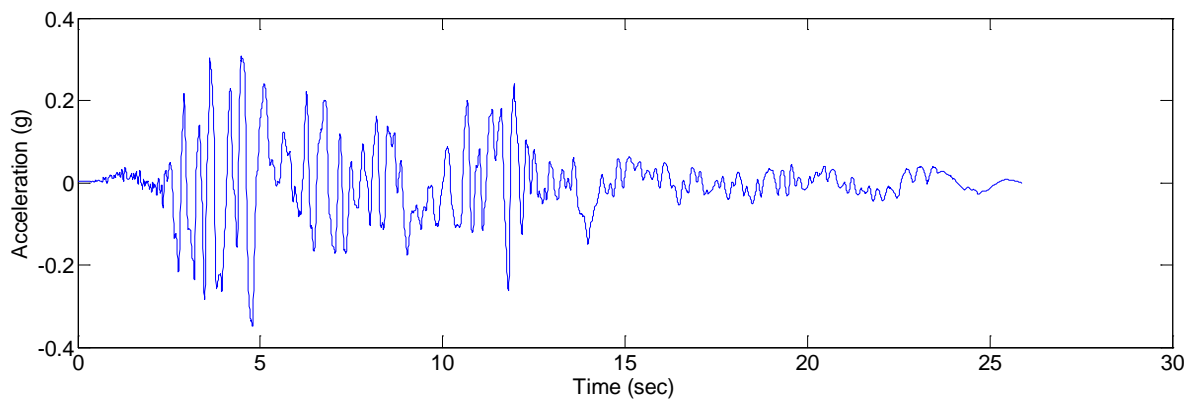


Figure 4-2 Unscaled ground acceleration record from the 1999 Duzce earthquake (Turkey)

Figure 4-3 shows the simulation result without Kalman filter for the first 15 seconds of the earthquake excitation. An ideal simulation result without fictitious noise is also shown for force and displacement responses at each storey. Figure 4-3a and Figure 4-3b show that the effect of measurement noises in the case of limited coupling between DOF is negligible since

there are only small amplitude and phase mismatches in the displacement responses with fictitious noise compared to the ideal case.

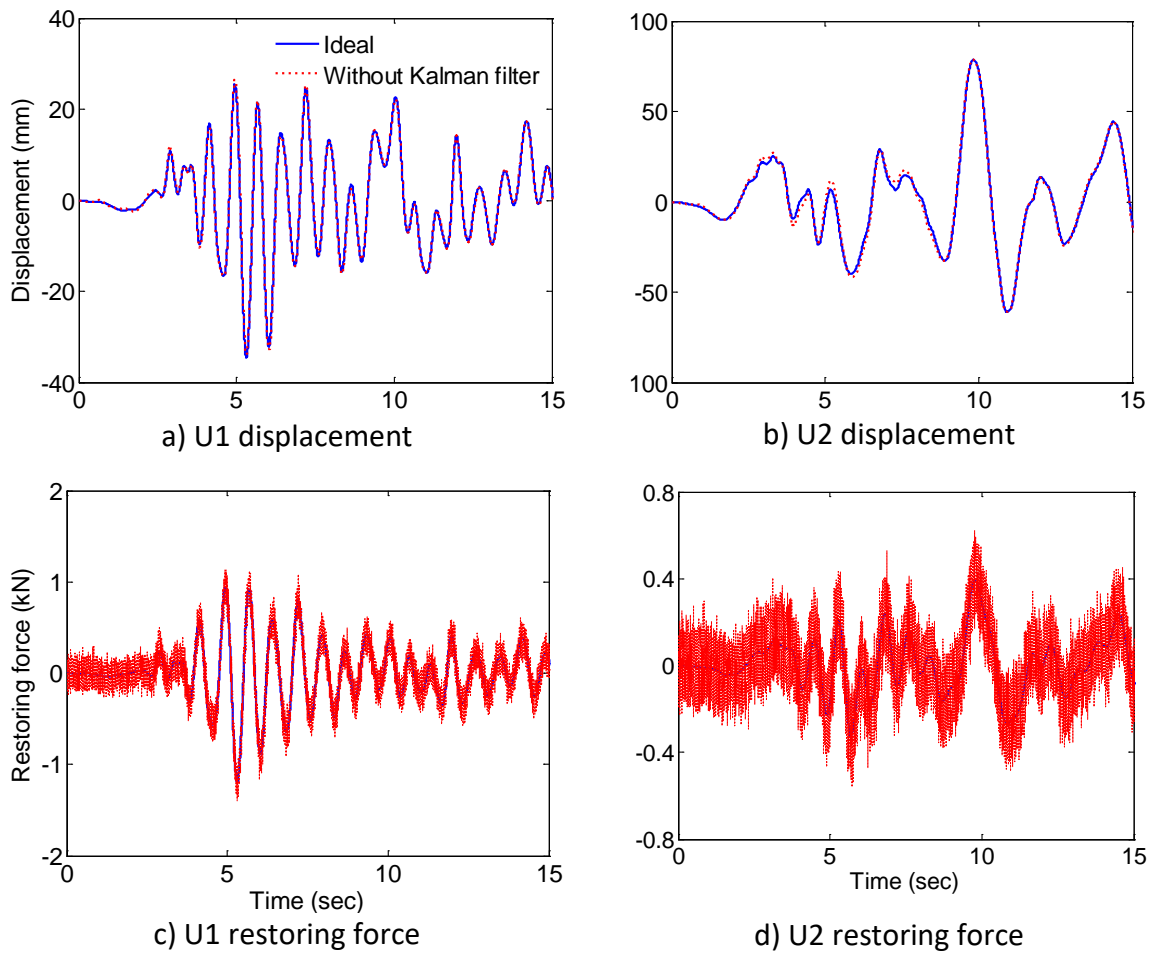


Figure 4-3 Case 1 simulation results without Kalman filter

Figure 4-4 shows the simulation result with Kalman filter for the first 15 seconds of excitation. The displacement responses of both stories show improved accuracy compared to the results without Kalman filter. A significant improvement can be seen in the force responses where the magnitudes of the ideal results are accurately replicated with no phase differences.

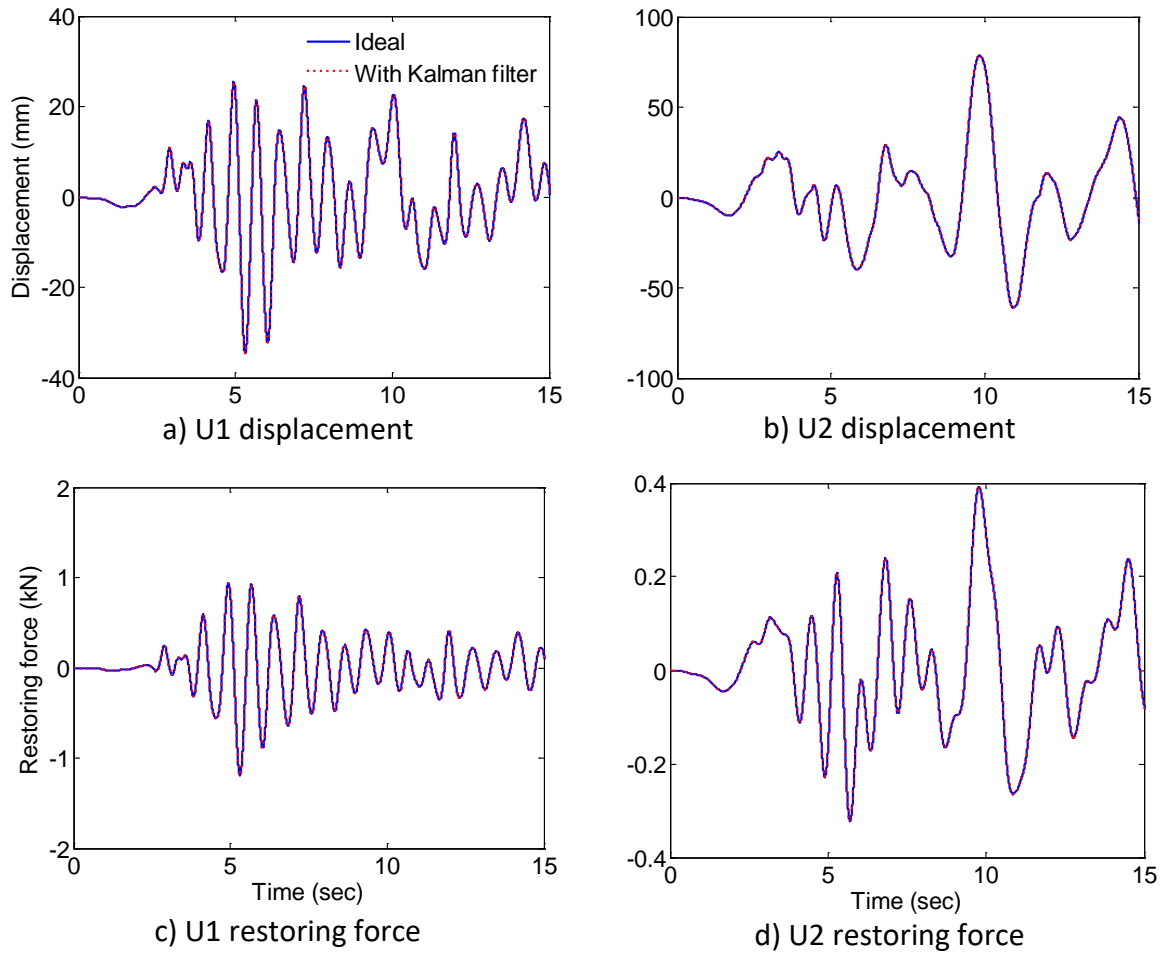


Figure 4-4 Case 1 simulation results with Kalman filter

#### 4.3.2. Case 2: strong DOF coupling

A strong coupling case between the first and second storey DOF is simulated by setting the top storey stiffness to five times the stiffness of the bottom storey. The total stiffness of each storey is adjusted while preserving the mass so that the resulting fundamental frequency is identical to Case 1. The resulting initial stiffness matrix is

$$K^I = \begin{bmatrix} 57.97 & -48.31 \\ -48.31 & 48.31 \end{bmatrix} kN / m \quad 4-31$$

The natural frequencies of this numerical model are 0.48 and 2.27 Hz. The highest natural frequency is now nearly five times the fundamental frequency because of the higher degree of coupling. All other aspects of the simulations are kept identical to Case 1.

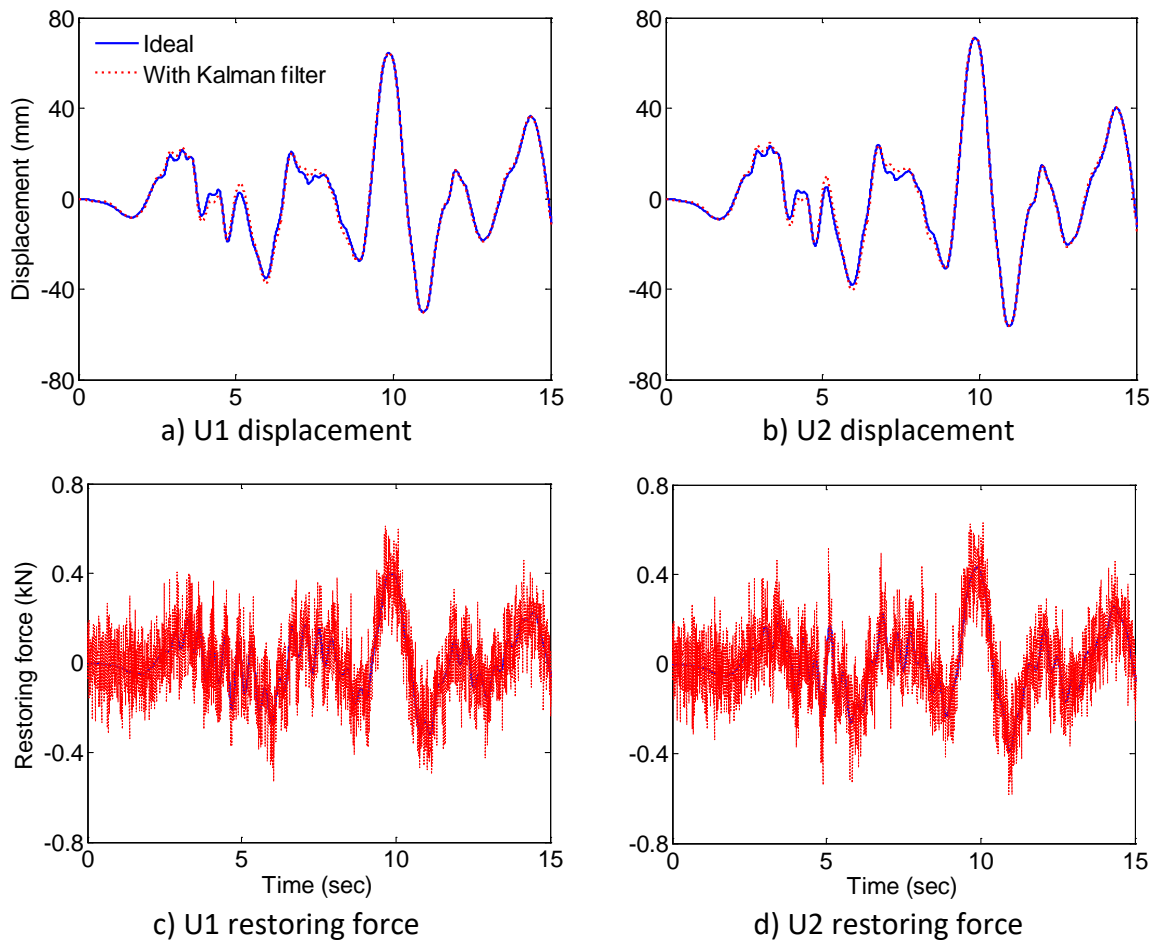


Figure 4-5 Case 2 simulation results without Kalman filter

Figure 4-5 shows the simulation result without Kalman filter for the first 15 seconds of the earthquake excitation. An ideal simulation result without fictitious noise is also shown for each storey force and displacement responses. The effect of measurement noises in the case of stronger coupling between DOF is more significant than in the case of weaker coupling, since both stories now show comparable inaccuracies compared to the ideal results.

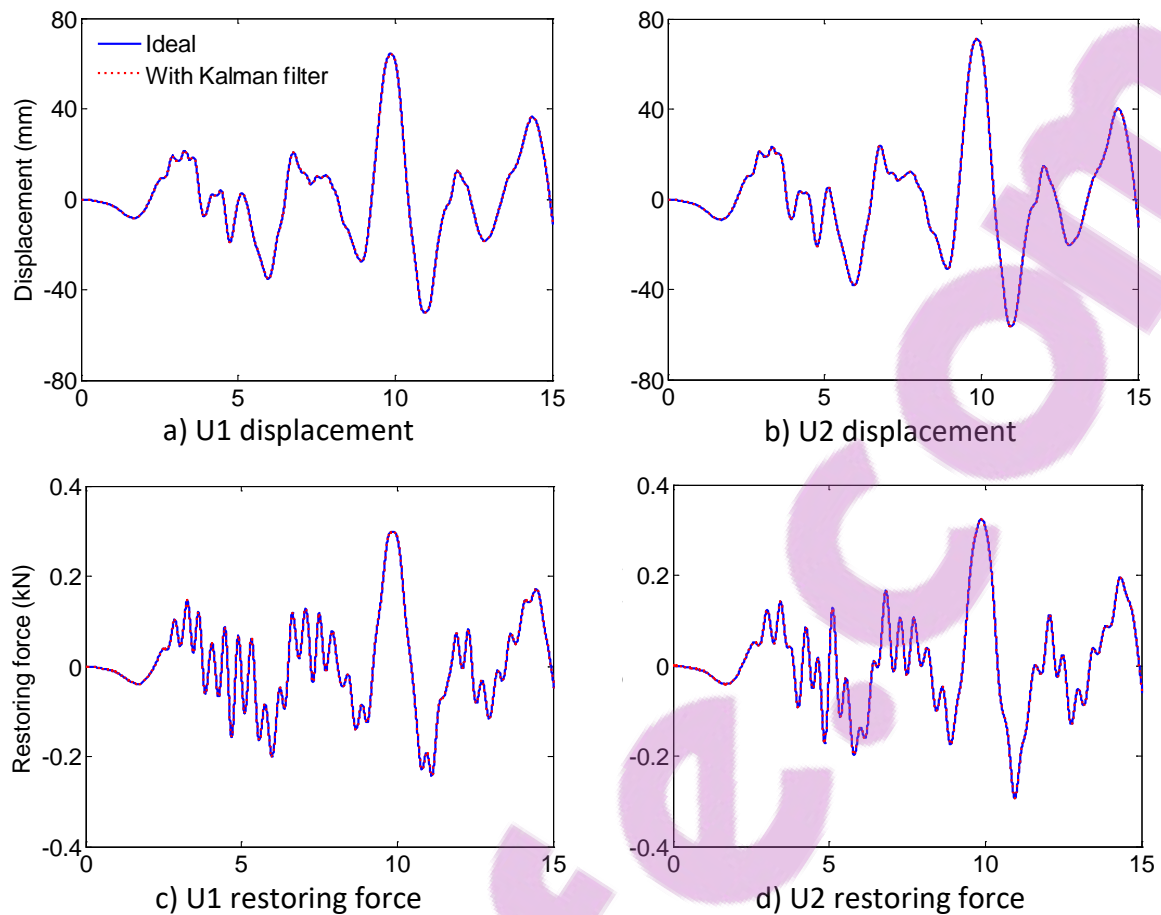


Figure 4-6 Case 2 simulation results with Kalman filter

Figure 4-6 shows the simulation result with Kalman filter for the first 15 seconds of excitation. The application of Kalman filter again improved the accuracy of the simulation results with fictitious noise in comparison with the ideal results, particularly in the force responses.

#### 4.4. Increasing simulation stability through Kalman filter

In Chapter 3, a new method is proposed to compensate additional energy resulting from actuator delay in fast hybrid simulations. During experimental validations, it was discovered that measurement noises degraded the effectiveness of the compensation method. The Kalman filter was one of the method adopted to remove these noises without introducing additional delay in the restoring force measurements.

Two numerical verifications of a combined algorithm between the proposed delay compensation and the Kalman filter will be presented. In the first validation, there is no modification in command signal generation algorithm from the hybrid simulation procedure presented in Section 3.6, where the equation of motion is solved at the sampling rate of the actuator servo-controller (1 kHz). In the second method, a modified approach to synchronise the different time step sizes used to solve the equation of motion and to control the actuator will be presented.

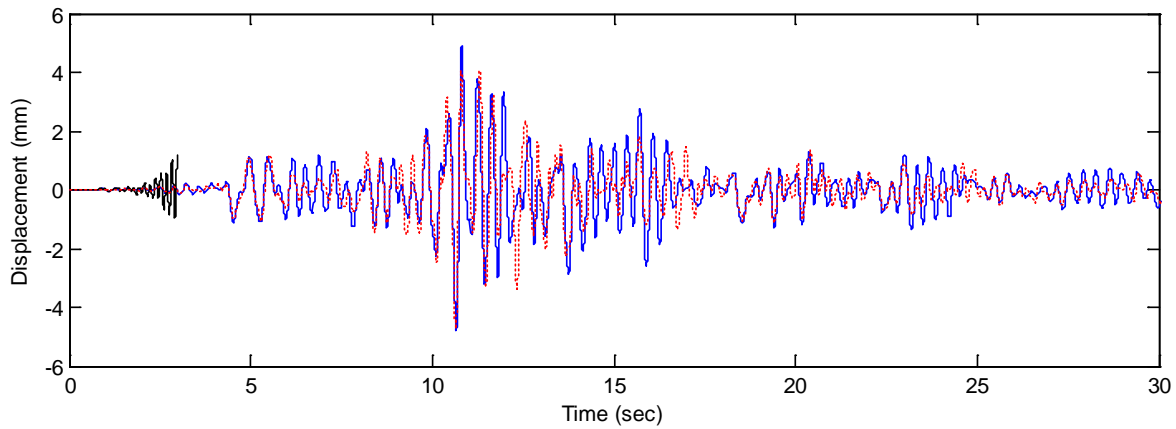
#### **4.4.1. Increasing simulation stability without modified command generation method**

In the following set of simulations, the properties of the two-storey shear frame are calibrated from the steel MRF used in experimental validations presented in Section 3.6. The initial stiffness matrix of the two-storey shear frame becomes

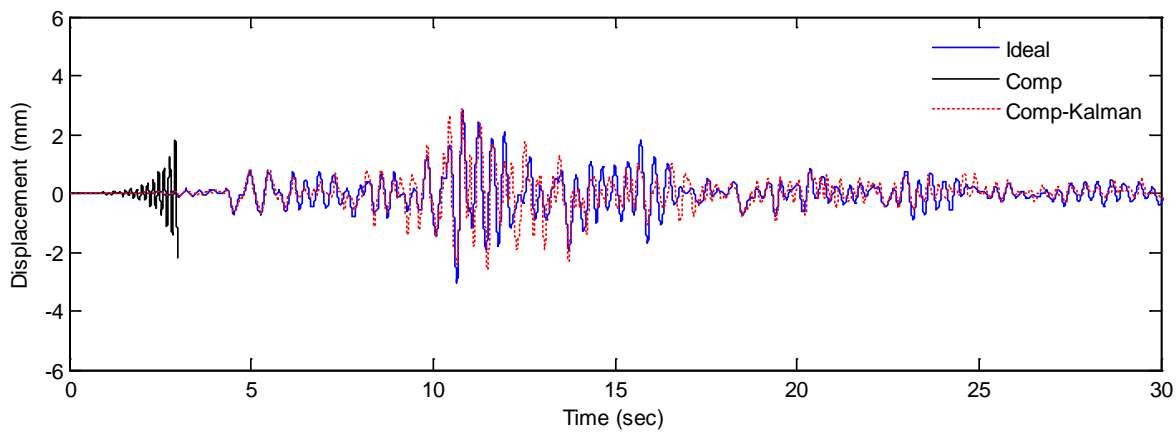
$$K^I = \begin{bmatrix} 5736 & -2868 \\ -2868 & 2868 \end{bmatrix} kN / m \quad 4-32$$

A concentrated mass of 3,600 kg is simulated on each storey resulting in natural vibration periods of 0.36 sec and 0.14 sec. The fundamental period of the two-storey shear frame is thus identical to the natural period of the SDOF-idealised steel MRF in Section 3.6. Equivalent viscous damping ratio of 5% is assumed for both modes of vibrations. The structure is also subjected to the 1978 Tabas earthquake ground motion, scaled to 8% amplitude to keep the maximum displacement at the top storey under 5 mm, close to the maximum displacement amplitude of the SDOF steel MRF. A 33.5 ms delay, calibrated against experimental data, is applied to the simulated force and displacement measurements at both DOF. The simulation employs the combination between the proposed delay compensation and Kalman filtering algorithm, and is conducted in “real-time” i.e. using a time scale of 1. Additionally, the

fictitious noises are set to have the same mean and standard deviations with those from the numerical verifications in Section 4.3.



a) Top storey (U2) displacement



b) Bottom storey (U1) displacement

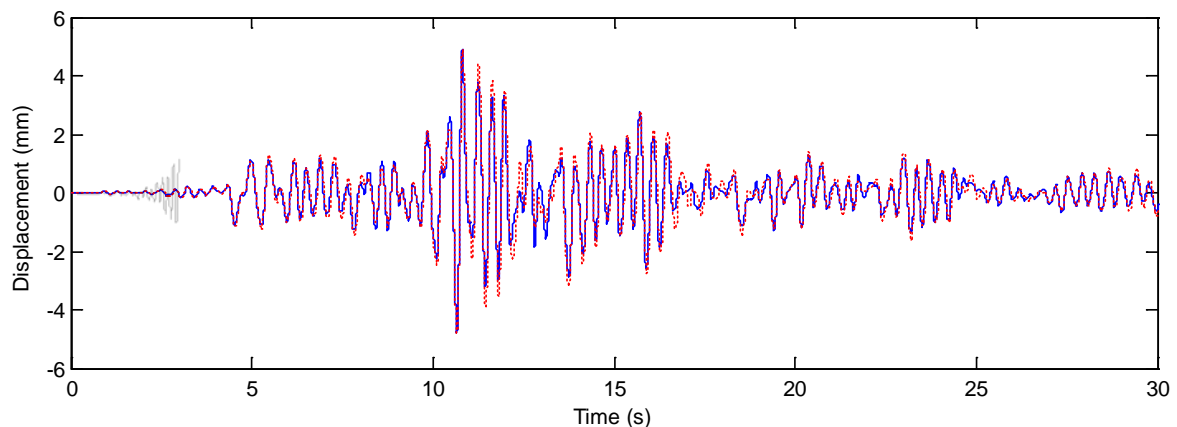
Figure 4-7 Simulated displacement response with combined delay compensation and Kalman filter application in the presence of actuator delay

Figure 4-7 shows the displacement responses of the two-storey shear frame for the first 30 seconds of the simulations. The figure shows an ideal displacement response of each storey without delay and fictitious noise, the simulation with compensated delay, labelled “Comp-Kalman”, and the simulation with only proposed delay compensation applied, labelled “Comp”. When only the proposed delay compensation applied, the displacement responses

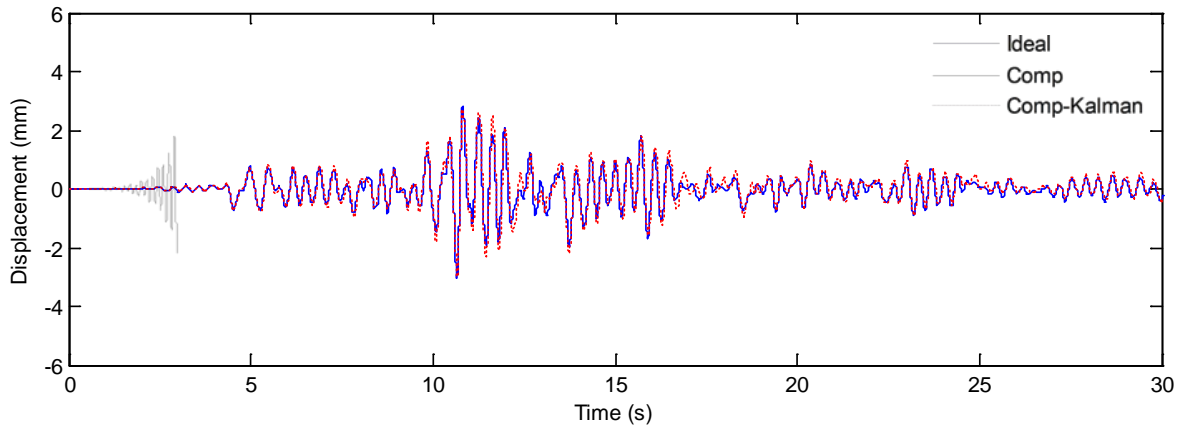
become unstable early into the simulation. The distinct differences between the ideal and the simulation with combined algorithms can be attributed to two factors:

- at 33.5 ms delay, the differences between the approximate energy error corrected by the proposed delay compensation, computed from Equation 3-9 to Equation 3-11, and the ideal magnitude will be large.
- Tangent stiffness estimation from measured data corrupted by noise.

The simulation with combined Kalman filter-proposed delay compensation requires tangent stiffness estimation so that the current research can be easily extended to nonlinear cases. For a linear elastic structure, the elastic stiffness of the structure can in fact be determined prior to the test. If the linear elastic stiffness is used if instead of the estimated tangent stiffness at each time step, the displacement time history tends towards the ideal result. This simulation result is shown in Figure 4-8.



a) Top storey (U2) displacement

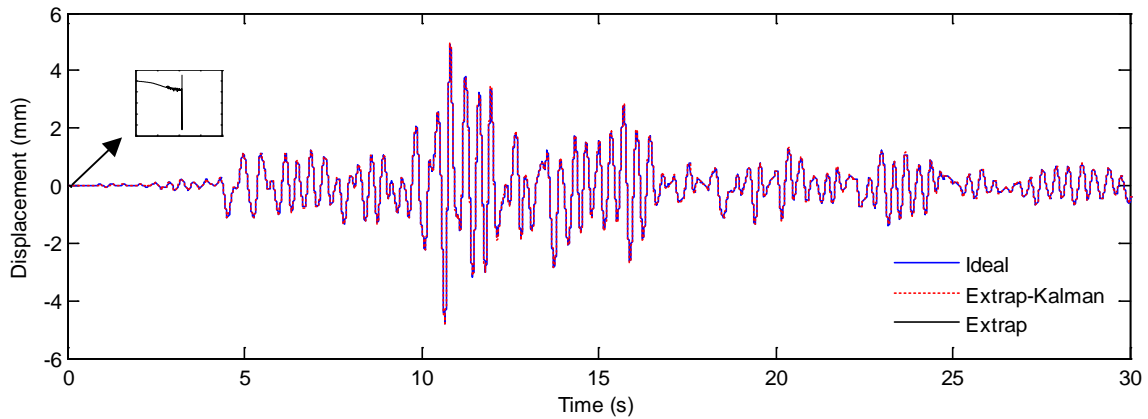


b) Bottom storey (U1) displacement

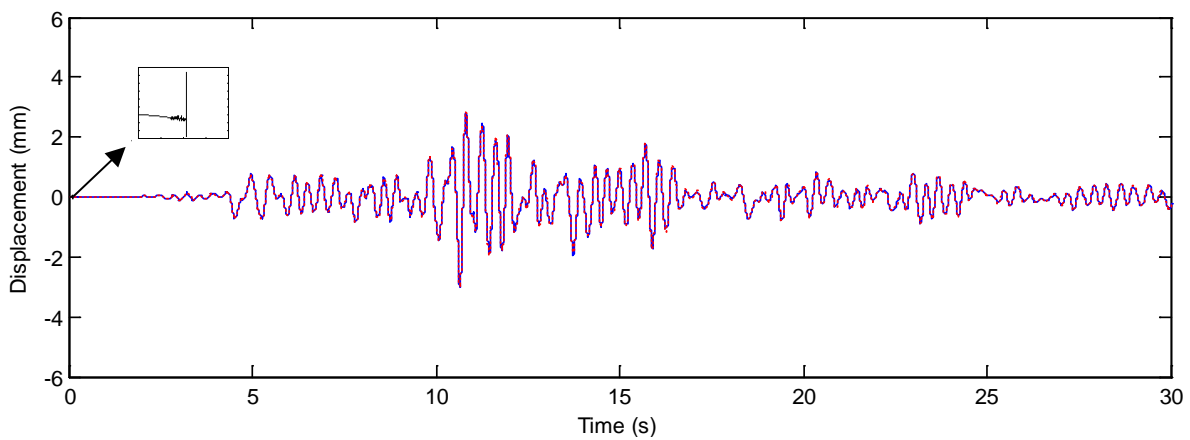
Figure 4-8 Simulation result using combined algorithms without tangent stiffness estimation update

The product of the natural frequency and the time delay magnitude,  $\omega_n t_d$  in this simulation is 1.5, which is 2.5 times the stability limit of the delay compensation-only application summarised in Table 3-2. The results demonstrate the capability of Kalman filter to increase the stability boundary of the proposed delay compensation method. The discrepancies between the results in Figure 4-8 for each DOF are mostly due to the large time delay magnitude rather than the simulated noises. The peak-to-peak value of the generated error signals, were less than 10% the peak displacement and restoring force, for both force and displacement measurement noises. Simulation results where only the effect of measurement noises at these magnitudes considered are very close to the ideal results, as demonstrated in [12].

For comparison, the Kalman filter algorithm is also integrated into the polynomial extrapolation method to mitigate actuator delay. Figure 4-9 shows the displacement responses of the simulations where third order polynomial extrapolation and Kalman filter (labelled “Extrap-Kalman”) are deployed. Ideal displacement responses are also plotted for comparison.



a) Top storey (U2) displacement



b) Bottom storey (U1) displacement

Figure 4-9 Displacement response from numerical simulations with delay utilising combined polynomial extrapolation-Kalman filter algorithm

It can be seen that the combination between polynomial extrapolation and Kalman filter yields better result than the combination between the proposed delay compensation and Kalman filter. Note that the simulation with the polynomial extrapolation method without Kalman filter also becomes unstable early into the simulation with 33.5 ms delay.

#### 4.4.2. Increasing simulation stability with modified command generation method

One of the requirements for a fast to real time hybrid simulation is that the actuator needs to continuously move without stop. The actuator servo-controller requires a new command signal from the test coordinator at the sample rate of the controller, even before a new

displacement target is available from the integration algorithm. One way to achieve this is to solve the equation of motion at the sampling rate of the controller, i.e. at 1 kHz as in the experimental validations in Section 3.6. The drawbacks of solving the equation of motion at such rate are placing burden in the test coordinator handling command generation algorithm especially during MDOF testing, compounding the effect of experimental errors from increased number of load steps, as well as amplifying the effect of noise due to smaller displacement increment magnitudes.

A better approach is for the actuator servo-controller to receive new target displacements at the update (sample) rate of the controller,  $\delta t$ , while the target displacement is generated at a larger time step of  $\Delta t$ . To synchronise the difference between  $\Delta t$  and  $\delta t$  sizes, the current hybrid simulation algorithm employs linear interpolation to generate command signal for the servo-controller. In discrete time implementation,  $\Delta t$  should be an integer multiplication of  $\delta t$ . The number of interpolation points  $N_{in}$  between the integration time steps is thus given by

$$N_{in} = \frac{\Delta t}{\delta t} \quad 4-33$$

At the current time step  $i$ , the displacement increment  $\Delta u_i$  imposed on the structure is the difference between the current and the target displacement at the previous time step. The new target displacement sent to the servo-controller at sub-step  $j$  of time step  $i$  is given by

$$u_i^j = \frac{j+1}{N_{in}} \Delta u_i + u_{i-1} \quad 4-34$$

where the interpolation index  $j = 0, \dots, N_{in}-1$  and the incremental displacement at time step  $i$ ,  $\Delta u_i = u_i - u_{i-1}$ .

The Kalman filter state matrices and vectors can be simplified because of the modification made in the actuator command generation algorithm. The state,  $z$ , and input,  $\bar{u}$ , vectors are now defined as

$$z = \left[ u_{m=1,j} \quad \cdots \quad u_{m=N_{DOF},j} \right]^T \quad 4-35$$

$$\bar{u} = \frac{1}{N_{in}} \left[ \Delta u_{m=1} \quad \cdots \quad \Delta u_{m=N_{DOF}} \right]^T \quad 4-36$$

And the Kalman filter state matrices are

$$\mathbf{A} = \begin{bmatrix} 1 & \cdots & 0 \\ \vdots & \ddots & \vdots \\ 0 & \cdots & 1 \end{bmatrix}_{(N_{state} \times N_{DOF}) \times N_{DOF}} \quad \mathbf{B} = \mathbf{A} \quad 4-37$$

$$\mathbf{C} = \begin{bmatrix} \mathbf{I} \\ K^e \end{bmatrix}_{(N_{msr} \times N_{DOF}) \times N_{DOF}} \quad 4-38$$

The two-storey shear frame structure is subjected to an impulse excitation to examine increasing stability limit of the proposed real-time hybrid simulation with delay compensation and modified command generation algorithm, owing to the application of Kalman filter. The same definition of stability limit as in Chapter 3 is used. Measurement noise is not simulated to eliminate associated uncertainties in determining the stability limit of the combined proposed delay compensation-Kalman filter algorithm.

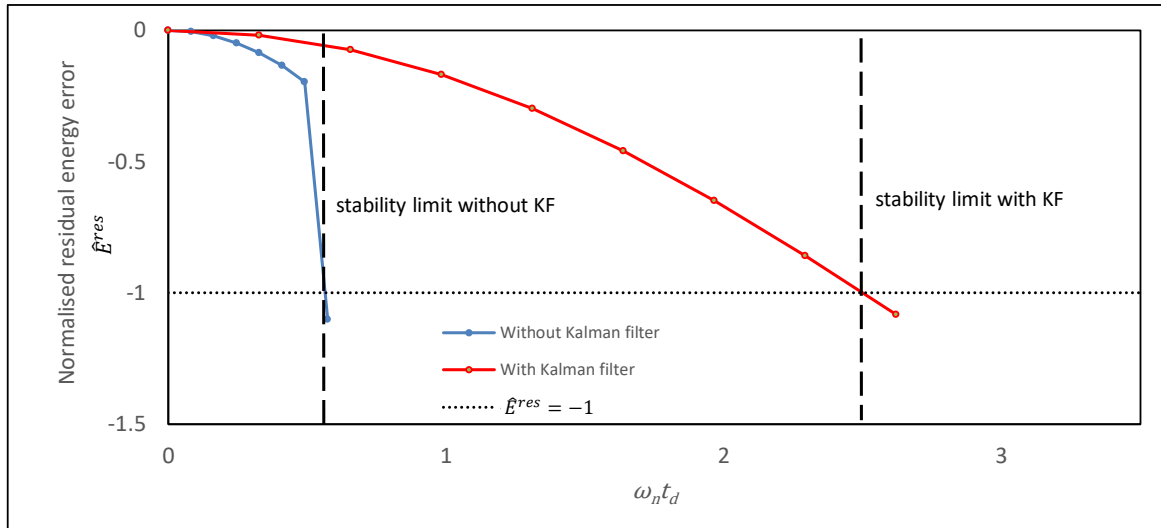


Figure 4-10 The relationship between normalised residual energy error and delay magnitude from parametric simulations with Kalman filter

Figure 4-10 show the stability limits for two different simulations. In simulations without Kalman filter, instability occurs at  $\omega_n t_d \approx 0.49$ . This limit is lower than the result presented in Section 3.7 due to the presence of a second, higher mode. With Kalman filter, the stability limit notably increases to about 2.5.

The stabilities of the simulations with Kalman filter are dependent to the selection of the noise covariance ratio  $\rho$ . The ratio determines whether measurements or the model predictions are given more weight when the filter algorithm updates the estimation of the current system states. A large  $\rho$  implies that the model of the system is given larger weight since according to Equation 4-13 this results in a small process noise covariance  $\mathbf{Q}$ . On the other hand, selecting a smaller  $\rho$  value implies an unreliable system model and decreases the stability limit of the delay compensation method since the delayed measurements are given more weight [50]. In the parametric study,  $\rho$  is selected equal to 10,000 so that the model of the system is given more weight. It should also be noted that setting  $\rho$  very large implies may result in the error covariance  $\mathbf{P}_i$  in Equation 4-9 becomes non-positive definite and the algorithm fails [55].

#### 4.5. Effectiveness of Kalman filter algorithm for inelastic systems

Since the hybrid simulation method is best utilised to investigate nonlinear behaviour of a structure, the effectiveness of the Kalman filter in nonlinear simulations is investigated. The following numerical simulations of hybrid tests evaluated the effect of measurement noises, the effect of actuator delay, as well as the Kalman filter effectiveness to improve simulation accuracy of inelastic systems.

##### 4.5.1. Numerical simulations of inelastic system

The same two-storey shear frame structure is used for the inelastic system simulation, where the inelastic behaviour is modelled following a Bouc-Wen force-displacement model [56, 57], defined as

$$\dot{u}_h(t) = \frac{1}{u_y} \left[ \dot{u}(t) - \gamma |\dot{u}(t)| |u_h(t)| |u_h(t)|^{\eta-1} - \beta \dot{u}(t) |u_h(t)|^\eta \right] \quad 4-39$$

$u_y$  : yield displacement

$u_h$  : hysteretic displacement

$\gamma, \beta, \eta$  : parameters that control the shape of the hysteretic curve

The restoring force of the structure can then be defined as

$$R(t) = \alpha K^e u(t) + (1 - \alpha) K^e u_y u_h(t) \quad 4-40$$

where  $\alpha$  is the ratio of post- to pre-yield stiffness,  $0 \leq \alpha \leq 1$ . A function was developed to solve the rate-dependent nature of Equation 4-39. The validity of the solver was verified by comparing a simulation result using the developed solver to a simulation result from SAP2000.

The validation can be found in Appendix B.

Table 4-1 listed the values of the parameters in Equation 4-39 to Equation 4-40 that produced the best replication to the SAP2000 [58] result. These values will be used throughout the simulations considering inelastic systems.

Parameters	Values
$\gamma$	0.45
$\beta$	0.55
$\eta$	2
$\alpha$	0

Table 4-1 The values of Bouc-Wen parameters for inelastic simulations

Figure 4-11 shows the resulting force-displacement relationship governed by the Bouc-Wen parameters listed in Table 4-1.

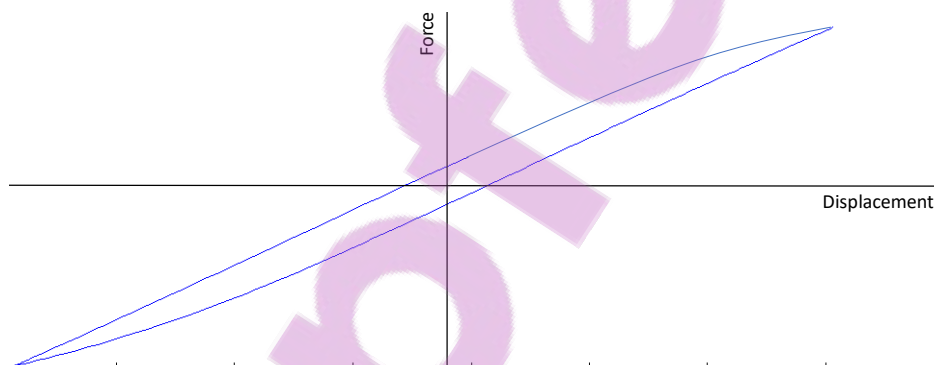


Figure 4-11 Resulting behaviour from Bouc-Wen relationship using parameters in Table 4-1

The Kalman filter algorithm can be utilised for inelastic systems through the Extended Kalman Filter (EKF) algorithm. When the dynamic model of the system is defined by a nonlinear function, the EKF algorithm linearizes the state transition and sensor algorithm around the most recent estimate and subsequently applies the standard Kalman filter equations. The procedure of the EKF algorithm can be described as follows [50]

$$z_i = \mathbf{f}(z_{i-1}) + \mathbf{B}\bar{u}_i + w_i \quad 4-41$$

$$y_i = \mathbf{h}(z_i) \quad 4-42$$

$$y_i^m = \mathbf{h}(z_i) + v_i \quad 4-43$$

The variables involved are identical to the standard Kalman filter described earlier, however the equations now contain nonlinear functions of the state variables  $\mathbf{f}(z_{i-1})$  and  $\mathbf{h}(z_i)$ , while  $y_i$  is the predicted output before considering measurements. These nonlinear functions are linearized around the corrected and predicted state, respectively, which is equal to finding the Jacobian matrices of the nonlinear functions with respect to the state variables.

$$\mathbf{F}(\hat{z}_i) = \left. \frac{\partial \mathbf{f}}{\partial z} \right|_{\hat{z}_i} \quad 4-44$$

$$\mathbf{H}(\hat{z}_i^-) = \left. \frac{\partial \mathbf{h}}{\partial z} \right|_{\hat{z}_i^-} \quad 4-45$$

In a discrete-time system, the EKF algorithm can be applied following these steps [51]

Initialization:

- Define initial estimated state:  $E[z_0]$  4-46
- Define initial estimated error covariance:  $\mathbf{P}_0 = E[(z_0 - \hat{z}_0)(z_0 - \hat{z}_0)^T]$  4-47

For  $i = 1, 2, \dots$

- State estimate prediction:  $\hat{z}_i^- = \mathbf{f}(\hat{z}_{i-1}) + \mathbf{B}\bar{u}_i$  4-48

- Covariance estimate prediction:  $\mathbf{P}_i^- = \mathbf{F}(\hat{z}_{i-1})\mathbf{P}_{i-1}\mathbf{F}(\hat{z}_{i-1})^T + \mathbf{Q}_{i-1}$  4-49

- Jacobian matrix update

$$\mathbf{H}(\hat{z}_i^-) = \left. \frac{\partial \mathbf{h}}{\partial \mathbf{z}} \right|_{\hat{z}_i^-} \quad 4-50$$

- Update filter gain:  $\mathbf{L}_i = \mathbf{P}_i^- \mathbf{H}(\hat{z}_i^-)^T (\mathbf{H}(\hat{z}_i^-) \mathbf{P}_i^- \mathbf{H}(\hat{z}_i^-)^T + \mathbf{R}_i)^{-1}$  4-51

- State estimate update:  $\hat{z}_i = \hat{z}_i^- + \mathbf{L}_i (y_i^m - \mathbf{h}(\hat{z}_i^-))$  4-52

- Covariance estimate update:  $\mathbf{P}_i = (\mathbf{I} - \mathbf{L}_i \mathbf{H}(\hat{z}_i^-)) \mathbf{P}_i^-$  4-53

- Jacobian matrix update

$$\mathbf{F}(\hat{z}_i) = \left. \frac{\partial \mathbf{f}}{\partial \mathbf{z}} \right|_{\hat{z}_i} \quad 4-54$$

Numerical simulations to demonstrate combined delay compensation-EKF algorithm for nonlinear systems in the presence of delay and measurement noises are presented in the following for the modified command generation algorithm case (Section 4.4.2). The EKF Jacobian matrices for the standard command generation algorithm (without interpolation) are presented in Appendix C.

The Jacobian matrices specific to the modified command generation algorithm are

$$\mathbf{F}(\hat{z}_i) = \mathbf{A} \quad 4-55$$

which is constant during a simulation, and

$$\mathbf{H} = \begin{bmatrix} \mathbf{I} \\ \mathbf{K}^t \end{bmatrix}_{(N_{msr} \times N_{DOF}) \times N_{DOF}} \quad 4-56$$

The Jacobian matrix  $\mathbf{H}$  contains the tangent stiffness matrix  $\mathbf{K}^t$  of the nonlinear structure. Several techniques are available for tangent stiffness estimation. Thewalt and Roman [46] employed a least square estimation method and the BFGS formula [59] to estimate the elastic and tangent stiffness matrix respectively to assess the accuracy of a hybrid simulation. This was only conducted post testing and therefore did not represent a validation. Another

implementation used a model based actuator delay compensation method with tangent stiffness matrix estimation utilising the Broyden formula [60]. The Broyden formula was simpler to implement and could be applied during testing.

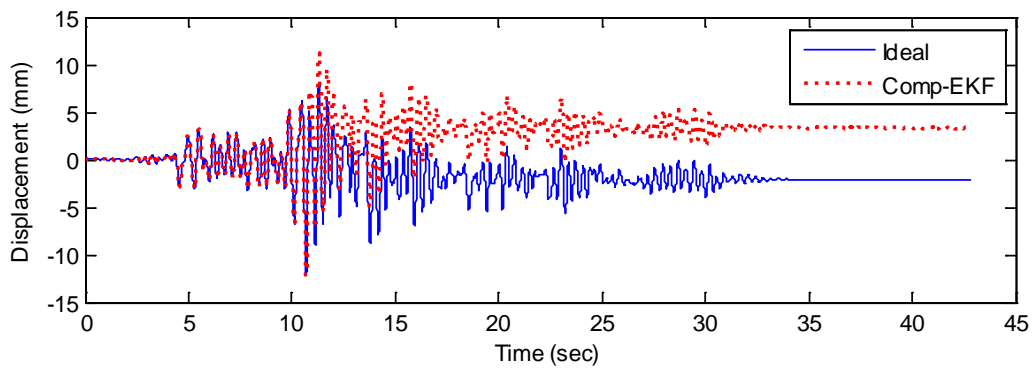
In the current research, the EKF algorithm utilises the method developed by Hung and El-Tawil [61], where the estimated tangent stiffness is obtained directly from the vectors of incremental forces and displacements. The method is equivalent to finding  $K^t$  that satisfies a linear relationship

$$\Delta R = K^t \Delta u \quad 4-57$$

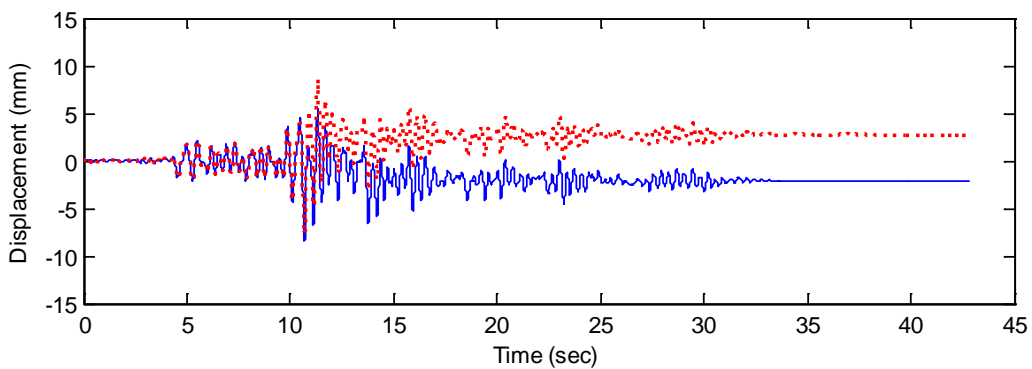
The minimum required number of data before every tangent stiffness estimation update is equal to the number of experimentally controlled DOF. However, to minimise the influence of measurement noises, more data points should be collected before every update and Equation 4-57 is solved using a least-square approach [61]. A more detailed explanation of the algorithm can be found in the original paper. In the numerical simulations in the current research, a data point is collected during each  $\delta t$  when the command is interpolated. This results in  $N_{in}$  data points collected between each tangent stiffness estimation update, where  $N_{in}$  is the total number of interpolation between integration time step  $\Delta t$ . It is assumed that the stiffness change within  $\Delta t$  is insignificant.

A moderately nonlinear simulation is conducted to demonstrate an overall performance of the combined delay compensation-EKF algorithm. The yield displacement of the structure is set to 6 mm, 15% of the peak response from the linear simulation in Case 1. The structure is subjected to 200% of the 1978 Tabas earthquake record, with a 33.5 ms simulated actuator delay.

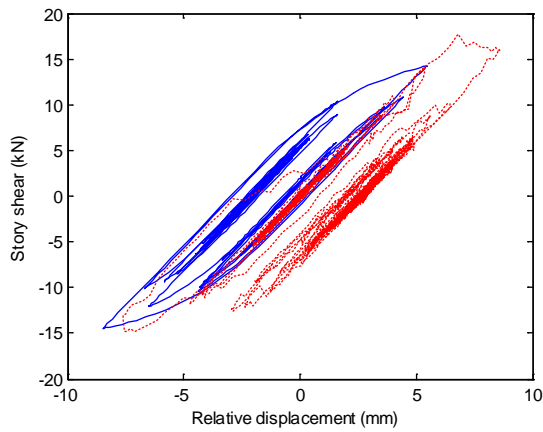
Figure 4-12a and Figure 4-12b show the top and bottom storey displacement time histories of the shear frame. Ideal response without fictitious noise and actuator delay is also presented for comparison, while the simulation result with only the proposed delay compensation method applied, although stable, is highly inaccurate and therefore is not shown for clarity. The simulation utilising the combined proposed delay compensation-Kalman filter algorithm results in erroneous residual drift. Figure 4-12c and Figure 4-12d show the hysteretic force-displacement relationships at both stories of the shear frame. The erroneous residual drifts at both stories can be seen as offsets in the hysteresis plots.



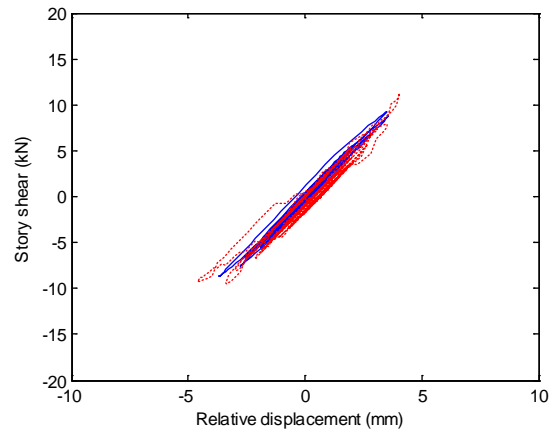
a) Top storey (U2) displacement



b) Bottom storey (U1) displacement



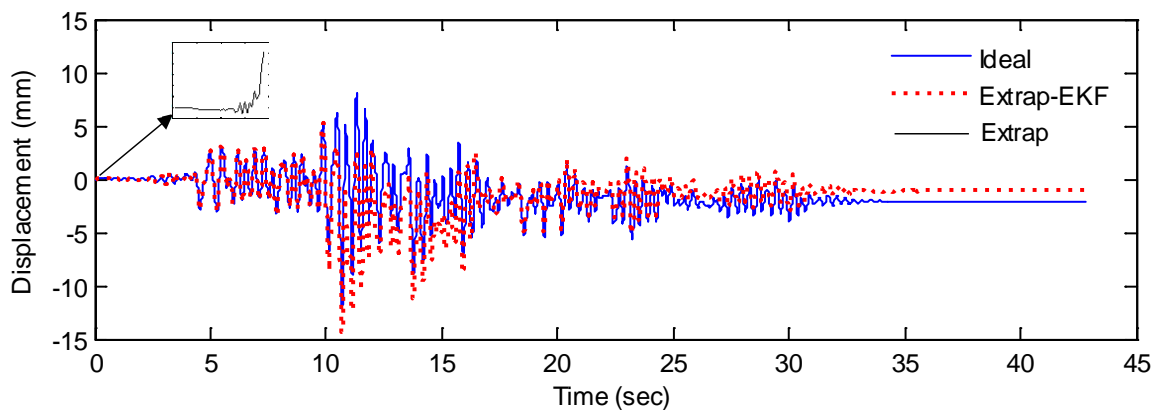
c) Storey shear – relative displacement relationship (U1)



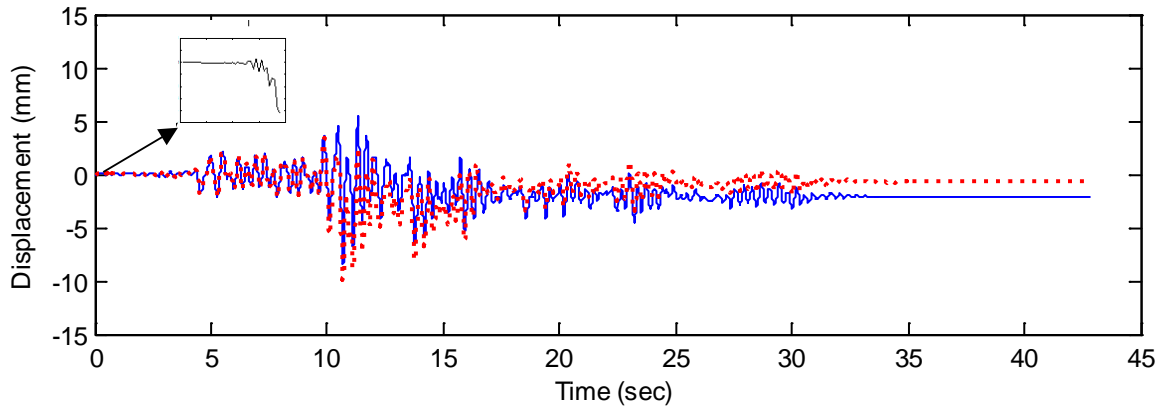
d) Storey shear – relative displacement relationship (U2)

Figure 4-12 Inelastic simulation result with combined proposed delay compensation and EKF algorithm

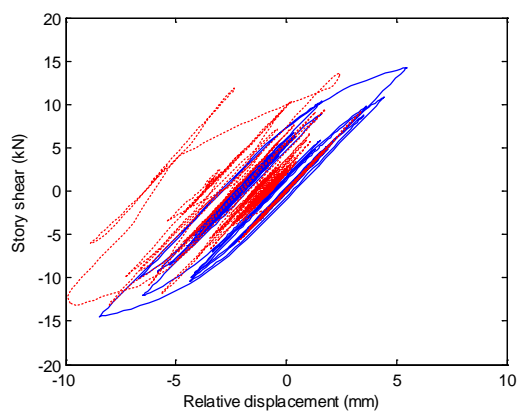
A simulation using combined algorithm between EKF and the polynomial extrapolation method is provided for comparison. All simulation parameters (delay and noise level) are identical with the previous simulation. Figure 4-13 shows the displacement time histories as well as hysteretic force-displacement relationships at both stories of the shear frame. The simulation result with only the polynomial extrapolation method applied becomes unstable early in the simulation as indicated in the figure as well.



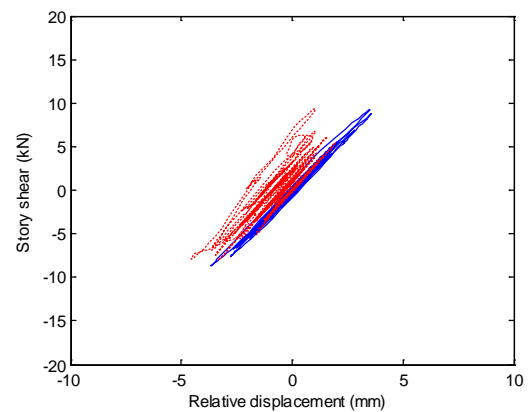
a) Top storey (U2) displacement



b) Bottom storey (U1) displacement



c) Storey shear – relative displacement relationship (U1)



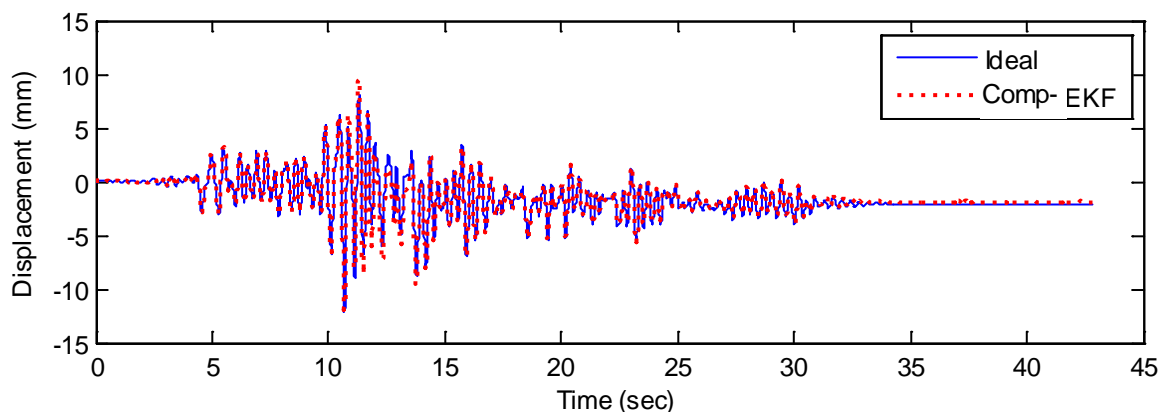
d) Storey shear – relative displacement relationship (U2)

Figure 4-13 Inelastic simulation result with combined polynomial extrapolation and EKF algorithm

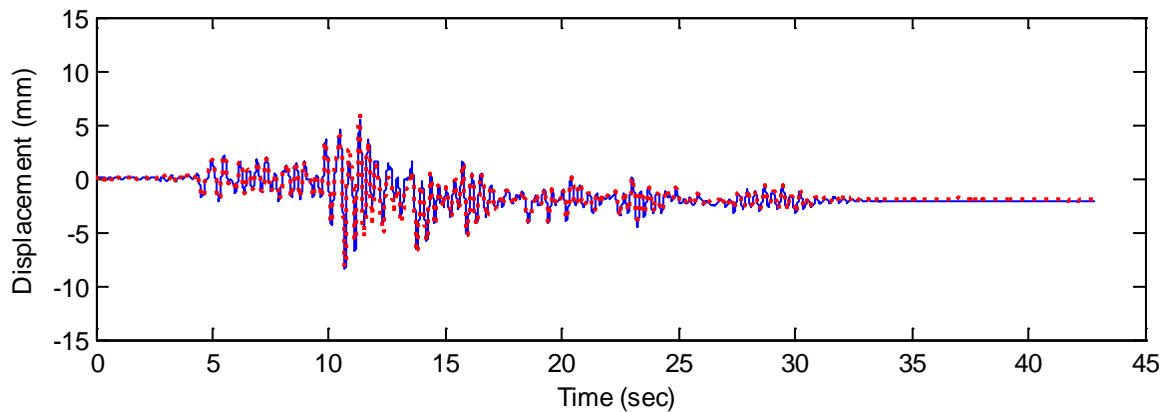
Figure 4-13 shows that the combined polynomial extrapolation-EKF algorithm also produce erroneous residual drift. The errors in the relative displacement at the top storey (Figure 4-13d) is larger in this simulation than the preceding one (Figure 4-12d), while at the bottom storey (Figure 4-12c and Figure 4-13c) the errors are on the same magnitude.

The inaccuracies in the inelastic simulations utilising either the combined proposed delay compensation-EKF or the combined polynomial extrapolation-EKF can be attributed to the fact that the EKF requires estimation of tangent stiffness of the experimental specimen from its measured force and displacement increments (Equation 4-57). In the combined proposed

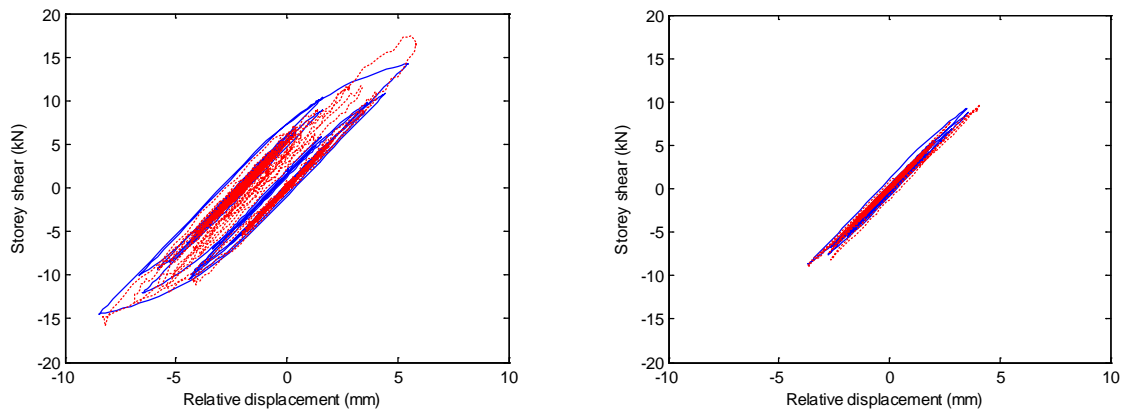
delay compensation-EKF algorithm, the measured force and displacement increments are delayed, leading to inaccurate tangent stiffness estimation at the magnitude of target displacement at the current step. In the combined polynomial extrapolation-EKF algorithm, although the target displacement is extrapolated to account for delay, over- or under-compensation will also result in inaccurate force and displacement increments, and hence inaccurate tangent stiffness estimation at the current target displacement. Thus, accurate tangent stiffness estimation is important whenever EKF is used regardless of the delay compensation method. To demonstrate this point, the simulation utilising combined proposed delay compensation-EKF algorithm is repeated with actual incremental restoring force and displacements. Figure 4-14 shows the simulation result performed in this condition. It can be seen that both displacement time histories as well as the hysteretic force-displacement at both stories match very well with the ideal simulation result. The remaining discrepancies are probably due: 1) instances when tangent stiffness is not updated due to current displacement increments being smaller than the prescribed threshold, and 2) linearising the nonlinear Bouc-Wen relationship (Equation 4-40) using Equation 4-57. It should be noted however that these simulations are unrealistic as the measured force and displacement increments are always delayed in real experiments with respect to the target displacement.



a) Top storey (U2) displacement



b) Bottom storey (U1) displacement



c) Storey shear – relative displacement relationship (U1)

d) Storey shear – relative displacement relationship (U2)

Figure 4-14 Inelastic simulation result with combined delay compensation and EKF algorithm: storey shear time histories

More recently, a variation of the standard Kalman filter, the unscented Kalman filter (UKF) has been developed. Since EKF requires calculating the Jacobian of the system at every time step, it requires the state and observation functions to be differentiable at the corresponding state. On the other hand, UKF does not require the Jacobian and therefore is more versatile in its application to highly nonlinear system or system with singular state point [62]. Researchers have since adopted UKF in hybrid simulation with substructuring [63, 64], where UKF is utilised to update parameters of the numerical substructure that is expected to behave

similarly (e.g. similar damage state) to the experimental substructure. In the current research, however, the actual experiment is envisioned to have no numerical substructure, i.e. the Bouc-Wen relationship is intended purely to simulate inelastic behaviour of a real specimen. Therefore, the restoring forces can only be obtained through measurement, and that the measurement equation in the Kalman filter algorithm can only be given by

$$R_{current} = R_{last} + k_{tangent}(u_{current} - u_{last}) \quad 4-58$$

It can be seen that linearization will always be required in the current research as the tangent stiffness term is a part of the numerical restoring force model. Therefore, in this research the performance of UKF, even if applied, will be no better than EKF as tangent stiffness estimate is still required at every step.

#### **4.5.2. Stability assessment for inelastic system**

Assessing the performance of the combined delay compensation-EKF algorithm in nonlinear simulations is more complicated. Unlike linear elastic simulation, the performance of the combined algorithms in nonlinear simulations do not seem to have a clear trend as long as  $\omega_n t_d$  is still within the stability limit.

The accuracy of a nonlinear simulation in the following parametric study is assessed using three different parameters; the rate of increase in dissipated energy, the maximum drift error ratio, and dissipated energy error ratio. Although none of the above parameters consider the accuracy of the entire displacement time history relative to an ideal simulation result, the last two parameters are the main concern in structural engineering design for earthquake resistant structures at the ultimate limit state, while the first parameter can be used as a direct indicator of the simulation stability.

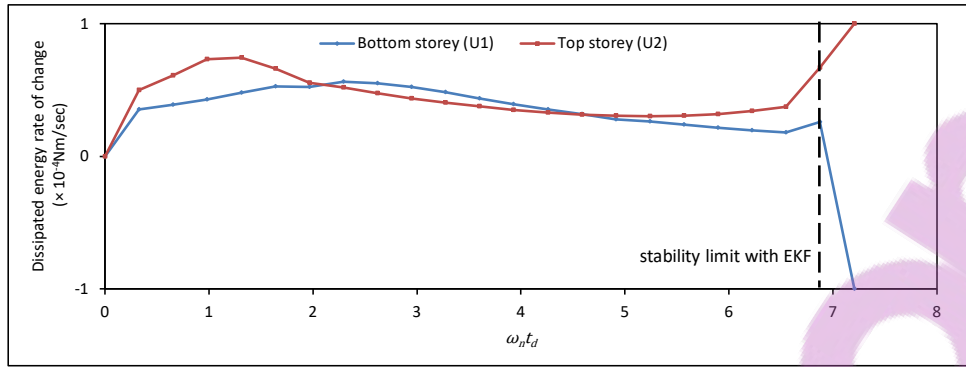


Figure 4-15 Parametric study result from inelastic simulations: dissipated energy rate of change

Figure 4-15 shows the rate of increase in cumulative dissipated energy from the relative movement at the bottom (U1) and top storey (U2) during free vibration phases from simulations using the combined delay compensation-EKF algorithm. When the magnitude of delay is large enough, the rate of additional energy into the structure from the negative damping effect will be larger than the rate of dissipated energy from viscous damping. This results in negative rate of increase in the cumulative dissipated energy, which is equivalent to the stability limit of system indicated by the dashed line in Figure 4-15.

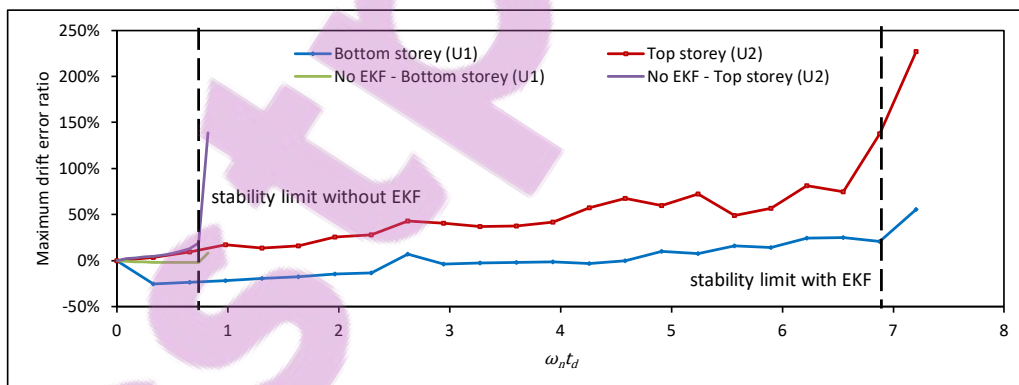


Figure 4-16 Parametric study result from inelastic simulations: maximum drift error ratio

Figure 4-16 shows the maximum drift error ratio on both storeys of the shear frame for increasing time delay magnitude. The maximum drift error ratio is the ratio between the difference of the maximum drift with error (i.e. time delay and measurement noise) to the

maximum drift in the ideal case and the maximum drift in the ideal simulation. The results are shown for simulations with the combined delay compensation-EKF algorithm as well as the results without EKF. Although inconsistent, the parameter shows an increasing positive error ratio as the magnitude of delay increases, suggesting that simulations produce larger displacements than the ideal results, especially the relative drift at the top storey (U2). The stability limits of both simulation types are indicated by the dashed lines, when sudden increases in the maximum drift error ratios occurred. Without EKF, the stability limit  $\omega_n t_d \approx 0.75$ . With EKF, the stability limit  $\omega_n t_d$  extends to  $\approx 6.8$ . This demonstrates that the tangent stiffness estimation method, albeit inaccurate at large delay, provides the necessary hysteretic energy dissipation which increases the stability limit.

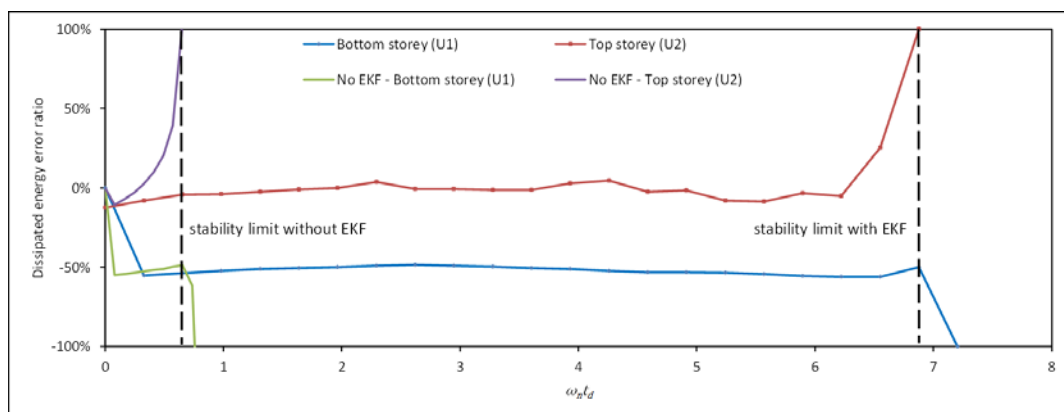


Figure 4-17 Parametric study result from inelastic simulations: dissipated energy error ratio

Figure 4-17 shows the dissipated energy error ratio, defined as the difference of the total dissipated energy at the end of excitation between the simulation with replicated error and the ideal one. Except for the dissipated energy resulting from the relative drift at the second storey from the simulation without the EKF algorithm, the parameter is insensitive to increasing delay magnitude. Sudden increases toward larger positive or negative magnitude occurred as the delay magnitude approaches the stability limit.

#### 4.6. Summary

A technique to improve the result of a hybrid simulation using a model based filtering algorithm called the Kalman filter is presented in this chapter. Numerical simulations showed that inherent noise in force and displacement measurements can affect the accuracies and stability of a MDOF hybrid simulation if there is strong coupling between the DOFs. For linear elastic structures, the application of the Kalman filter greatly improves the force feedback, where in the absence of the Kalman filter, it is completely obscured by noises. The removal of noises in the force feedback leads to improvement in the displacement responses.

This chapter also demonstrates the capability of Kalman filter to increase the stability of a fast-to-real-time hybrid simulation with actuator delay. A numerical simulation of a hybrid simulation of a two-storey shear frame with properties taken from the steel MRF in experimental validations in Chapter 3 shows that a combined proposed delay compensation-Kalman filter algorithm successfully maintained simulation stability as well as highly accurate (compared to the ideal result) in the presence of a 33.5-ms delay, even when the simulation is conducted in real time. It is shown that with the application of the Kalman filter, the stability of a real-time hybrid simulation can be maintained up to a time delay magnitude of 2.5 times larger than the stability limit in Chapter 3. Parametric studies using linear elastic simulations suggest that the application of the Kalman filter to the proposed delay compensation method increases the stability limit by four times.

The application of the Kalman filter to nonlinear simulation levels is also investigated utilising the Extended Kalman Filter (EKF) algorithm. Numerical simulations show that the effectiveness of the EKF algorithm in improving real-time, nonlinear hybrid simulation results depends on the degree of nonlinearity as much as on the magnitude of delay, due to the need

to continually update the tangent stiffness in the algorithm. A set of initial simulations show that inaccurate tangent stiffness estimations result in erroneous residual drift in the simulations with combined proposed delay compensation-EKF algorithm. Although unrealistic, it is shown that the simulation accuracies can be improved when tangent stiffness estimation utilises actual force and displacement increment. There is a need to develop a method to accurately estimate tangent stiffness of a real specimen from delayed force and displacement measurements before the combined algorithm can work more effectively.

Parametric simulations to assess the stability limit in inelastic case presented suggest that utilising the EKF algorithm produces rather inaccurate responses compared to the ideal results, with differences in the maximum drift error ratio and the total dissipated energy error ratio reaching as high as 50%. The inaccuracy in the maximum drift amplitude increases with increasing delay magnitude, while the inaccuracy in the total dissipated energy seems to be insensitive to increasing delay magnitude unless the stability limit has not been exceeded. Nevertheless, the simulations demonstrate the EKF algorithm, along with the intuitive tangent stiffness estimation method significantly increase the stability limit considering inelastic systems.



# Chapter 5

## Multi-axial Actuator Control

---

### 5.1. Introduction

A more realistic seismic simulation should consider the effect of this multidirectional load to the structure since real earthquake consists of multiple load components acting in different directions. However, compared to unidirectional tests, the number of experiments considering multidirectional loading is very limited.

A multiple actuator setup is necessary to replicate the response to multidirectional load as well as to impose accurate boundary conditions to the specimen. The challenge in imposing target displacements accurately to the structure in multidirectional tests is the interconnections between the specimen and the actuators that result in geometric change of the test setup. To ensure accurate test result, the displaced configuration of the actuators-specimen system must be accounted for by employing a nonlinear transformation procedure.

### 5.2. Prior research

Thewalt and Mahin [65] conducted a notable multi-directional hybrid simulation using a concrete block representing a rigid floor diaphragm. Assuming rigid in-plane behaviour the test controlled two translational and one torsional DOF at the centre-of-mass (COM) of the floor. These are the specimen global DOFs that are solved in the hybrid simulation coordinator. Due to physical limitation, each of these DOF may not always be possible to be controlled by a single actuator. Figure 5-1 illustrates the test setup configuration for that experiment, using three actuators that did not initially align with the three DOFs. A coordinate

transformation algorithm must be employed to transform the target displacements at the global DOFs ( $u_1, u_2, u_3$ ) to the required translational displacements at the actuators' DOFs ( $u_{A1}, u_{A2}, u_{A3}$ ). The restoring forces from the actuator load cells must also be transformed back into the global DOF before the simulation advances to the next time step.

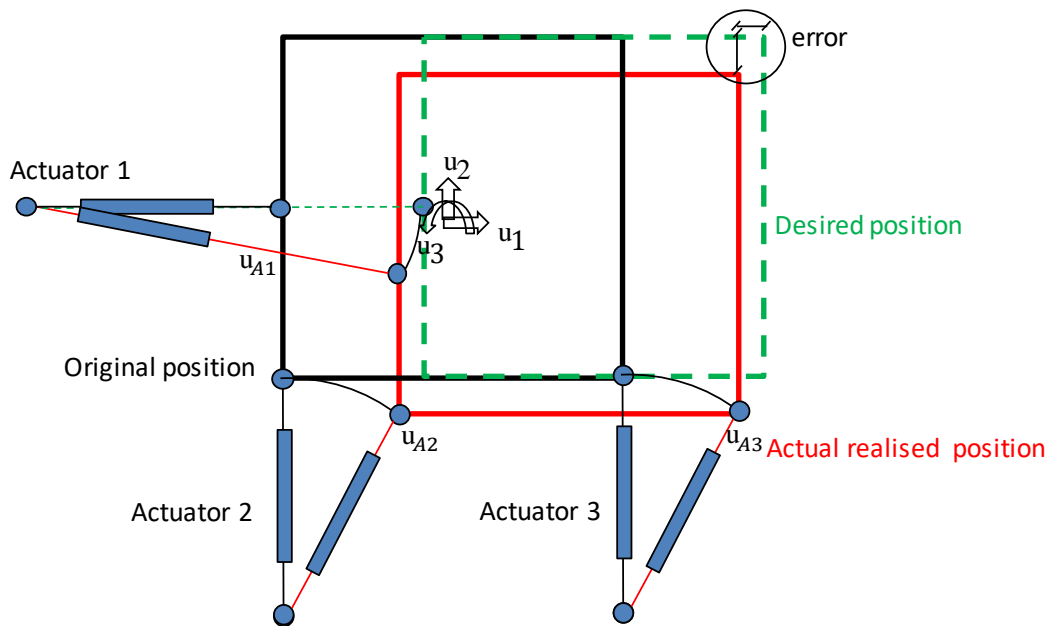


Figure 5-1 Geometric error due to finite actuator length in non-planar hybrid simulation [66]

In a multidirectional test, the coordinate transformation algorithm must be able to account for geometric error due to finite length of the actuators. Figure 5-1 illustrates that a displacement command in  $u_1$  will induce transverse displacement error in  $u_2$  due to arching motions of the actuators, resulting in misalignment between the specimen global DOF and the actuators' as the specimen displaces. Thewalt and Mahin [65] utilised external displacement transducers that were connected to the specimen from an isolated reference frame using 3.7 m long tubes to measure the global displacements of the structure. The relatively long tubes minimised the effect of position errors of the structure due to the transverse displacement errors.

Molina et al. [67] conducted an experiment on a large scale, three stories building with three DOF defined per floor level. Instead of relying on minimising transverse movement errors using physical test setup (e.g. displacement transducers with long tube), they employed a rigorous coordinate transformation algorithm between the structure global DOF and the required actuator displacements expressed using a set of nonlinear equations solved using iterative procedure. Liu and Chang [68] employed a “cost function” defined using the sum of the square difference between the target length of each actuator and the actual length after imposing the target displacement. The algorithm searched for a solution that minimised the cost function through an iterative optimisation technique. Tsai et al. [69] investigated the behaviour of a steel column reinforced using hybrid simulation on steel shear panels that controlled lateral, vertical, as well as rotational displacements. The challenge in the experiment was the difficulty to maintain constant axial load due to geometric effect, high axial stiffness of the steel shear panels, and flexibility of the transfer girder used to apply the required displacements at the top of the column. They adopted a mixed force-displacement correction technique to account for bending rigidity of the transfer girder in the coordinate transformation procedure. Obata and Goto [70] tested bridge piers subjected to NS and EW component of the 1994 Kobe earthquake in Japan. To minimise measurement related errors, they utilised a large numbers of observation points to solve the nonlinear coordinate transformation equations. The overdetermined set of equations defining the coordinate transformation algorithm was solved utilising the least-square method. Mercan et al. [71] developed a special configuration utilising actuators’ internal displacement transducers as well as external displacement transducers in multidirectional hybrid simulations on a rigid concrete slab. They modified the typical test setup in such a way that the test procedure eliminated the error associated with linearised approximation between the global and the

actuator DOF relationships as well as any iterative procedure in the coordinate transformation algorithm since the nonlinear transformation algorithm in the tests could be handled completely by well know trigonometric laws.

A sophisticated application of nonlinear transformation procedure between specimen's global and actuator's local coordinate system is adopted in the MAST system in Swinburne university [72]. The MAST system has a mixed-mode control feature that allows user to specify the deformation or load required for the desired direction of loading for to test specimen. The MAST control system also utilised force balance method to manage redundancy in the actuation system, since the system is over-constrained due to the more number of actuators available to impose 6 DOFs command to the test specimen. The force balance method ensure that the force is distributed equally among the driving actuators to prevent some portion of the actuators' forces opposing each other, which will limit the performance of the system.

This chapter presents a summary of multidirectional experiments conducted in The University of Auckland to simulate seismic demand on structures. Like the MAST system, the multidirectional system in The University of Auckland is able to control a specimen's deformation and/or load in a mixed-mode system, without redundancy in the actuators' load configuration. The experiments utilised the quasi-static and the hybrid simulation methods. Transverse displacement errors associated with geometric change in the test setup configurations were handled using nonlinear transformation (NLT) algorithms from literature that were adapted for specific tests. It was decided to develop our own NLT algorithm, as this enables us to study the path dependency effect, as a consequence to intrinsic actuator control and inter-timestep actuator path variations which can be found in Chapter 6.

### 5.3. Quasi-static tests on RC walls

The first set of experiments tested RC wall specimens using the quasi-static method. The wall specimens were 50% scale models of representative structural walls in multi-storey buildings. To include a different range of building heights, three aspect ratios of 2, 4, and 6 were selected. However, due to height restriction in the test facility, the heights of the wall specimens were further reduced, resulting in a final dimension of 2800 × 1400 × 150 mm for each wall. Since the *physical* aspect ratios of all wall specimens were 2, the experiments on walls with higher aspect ratio were accurate only if accurate boundary conditions were imposed during experiments.

These boundary conditions are illustrated in Figure 5-2. According to the equivalent static load principle, seismic load on a structure can be idealised as an inverted triangular load acting at each level where mass is concentrated, resulting in internal forces' distributions such as in Figure 5-2a. Figure 5-2b shows that when only the lower part of the structure is tested, external bending moments must be applied at the top of the structure to obtain equivalent distributions of internal forces to the full structure to represent the non-zero internal bending moments at that level, in addition to shear and axial loads.

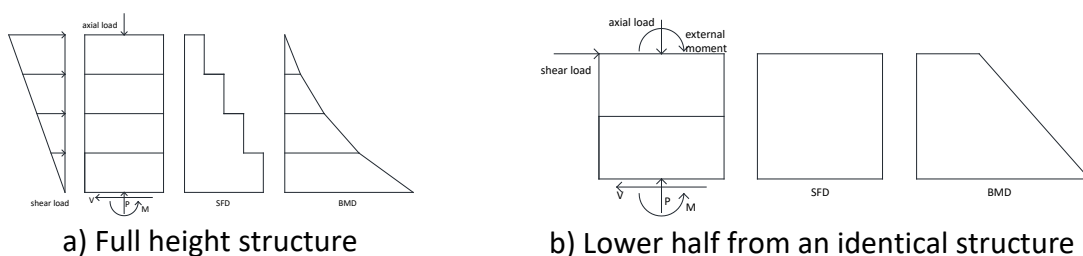
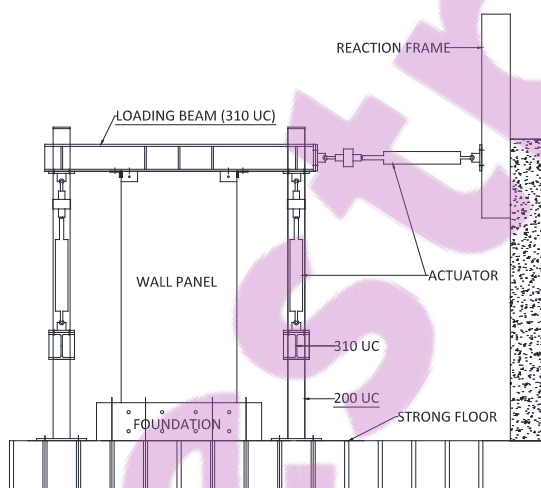


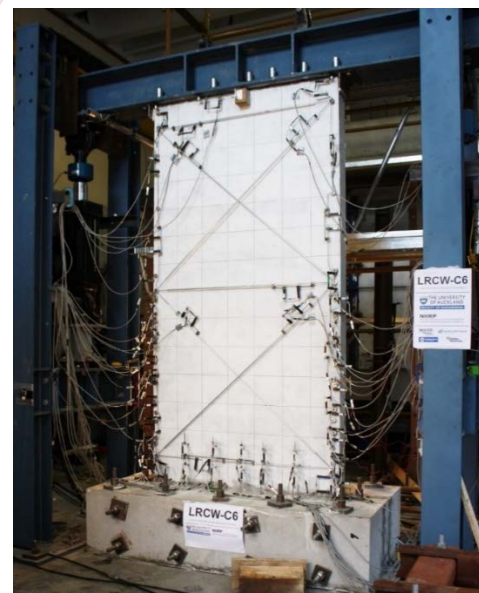
Figure 5-2 Schematic drawing of internal forces in the wall at a) full height and b) lower half of equivalent full height

### 5.3.1. Experiment setup

The required load combinations were imposed to the wall through a multi-actuator setup. Horizontal drifts were applied at the top of the wall using a manually operated actuator. A pair of servo-mechanical hydraulic actuators applied the required axial load and bending moment at the top of the wall. The combined shear, axial, and bending moment were applied through a 310 UC section acted as a rigid loading beam to ensure even distribution of these loads across the wall section. The horizontal actuator was secured to a reaction frame which in turn was fixed to a strong wall through post-tensioning. Each vertical actuator was bolted to a 310 UC section spanning across two 200 UC section columns. These columns were in turn fixed to the strong floor through post-tensioning. Each wall panel was fixed to the strong floor and clamped at the base between two concrete foundation blocks. The foundation blocks were in turn fixed to the strong floor. A schematic drawing of this setup is shown in Figure 5-3a while a photo of the actual test is shown in Figure 5-3b.



a) Schematic drawing



b) Actual setup

Figure 5-3 Schematic drawing of the quasi-static test setup

### 5.3.2. Loading protocol

Lu et al. [73] developed the horizontal drift protocol for the quasi-static test following the guideline outlined in ACI 374.2R-13 [74] and ACI ITG-5.1-07 [75]. Prior to cracking, the tests were conducted in force-controlled with incremental loads equivalent to 1/4, 1/2, 3/4 the load corresponding to theoretical cracking moment. The following cycles were conducted in displacement control consisting of three full cycles per drift amplitude. The resulting drift amplitudes were 0.2%, 0.25%, 0.35%, 0.5%, 0.75%, 1.0%, 1.5%, 2.0%, and 2.5% as the maximum inter-storey drift at the ultimate limit state per NZS1170.5 [76]. Figure 5-4 shows the loading protocol used during the quasi-static tests, where the load and displacement-controlled regions are indicated. During the load-controlled phase, the walls were loaded while the horizontal actuator's load cell readings were monitored as feedback. During the displacement-controlled phase, the walls' translational displacements were monitored using a string potentiometer.

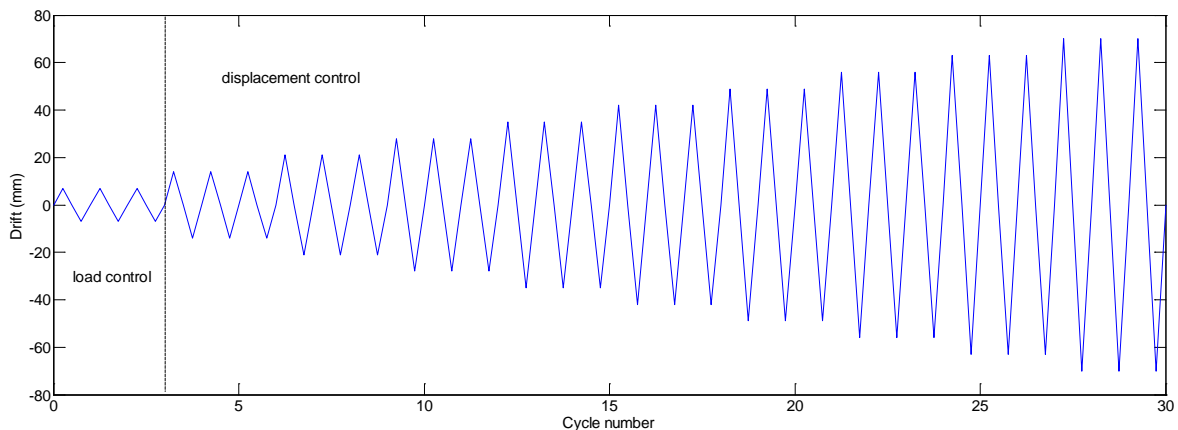


Figure 5-4 Translational displacement protocol for quasi-static experiments

The bending moments applied at the top of a wall are a function of the target aspect ratio during the test, dimension, and the required axial load. The relationship can be formulated as

$$Ar = \frac{M_t + Vh}{Vl_w} \quad 5-1$$

In Equation 5-1,  $Ar$  is the target aspect ratio,  $M_t$  is the required additional moment at the top of the wall,  $V$  is shear force,  $h$  and  $l_w$  are the wall's height and length, respectively. According to Equation 5-1, a target aspect ratio larger than the wall's physical aspect ratio can be achieved by applying the additional bending moment  $M_t$ . When  $M_t$  is equal to zero, the target aspect ratio reduces to the physical aspect ratio.

Rearranging Equation 5-1, the required moment  $M_t$  can be computed based on the shear load  $V$  and the target aspect ratio  $Ar$ .  $M_t$  is then applied at the top of the wall through the vertical actuators operating in load control, where the required load at each actuator is given in the following relationship

$$T_1 + T_2 = N \quad 5-2$$

$$T_1d_1 - T_2d_2 = M_t \quad 5-3$$

In Equation 5-2, Equation 5-3, and Figure 5-5,  $N$  is the required axial load,  $T$  and  $d$  are the required loads in the vertical actuators and the distance between the longitudinal axis of the vertical actuator to the center of the wall, respectively. Subscript "1" and "2" indicate the position of each vertical actuator relative to the horizontal actuator.

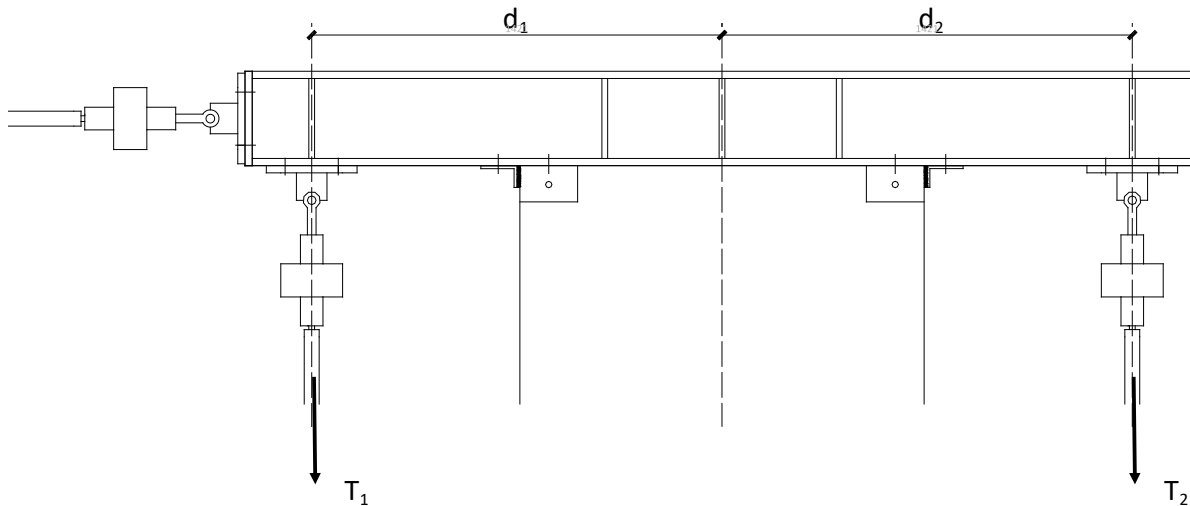


Figure 5-5 Free-body diagram of the wall-actuators setup

Rearranging Equation 5-1, 5-2, and 5-3 results in the target load for each vertical actuator as

$$T_1 = \frac{ArVl_w - Vh + Nd_2}{d_1 + d_2} \quad 5-4$$

$$T_2 = \frac{Nd_1 - ArVl_w + Vh}{d_1 + d_2} \quad 5-5$$

### 5.3.3. Transformation procedure

Figure 5-6 shows a typical displaced configuration of the actuators-wall system. Due to the finite length of each actuator, the motion of the horizontal actuator will induce rotational movements of the vertical actuators and vice versa. The readings from the displacement transducers (i.e. the string potentiometer for the horizontal actuator and the internal LVDT for the vertical actuators) as well as from the load cells are no longer aligned with the initial orientations used as the reference position for the applied load and displacement. These readings no longer reflect the actual displacements or the resistances of the wall in the assumed directions during testing. The differences can be significant especially if the wall experiences large displacements. To accurately achieve the intended combination of shear

force and bending moment, the orientation of each actuator at the displaced configuration of the test setup must be considered by applying the NLT algorithm.

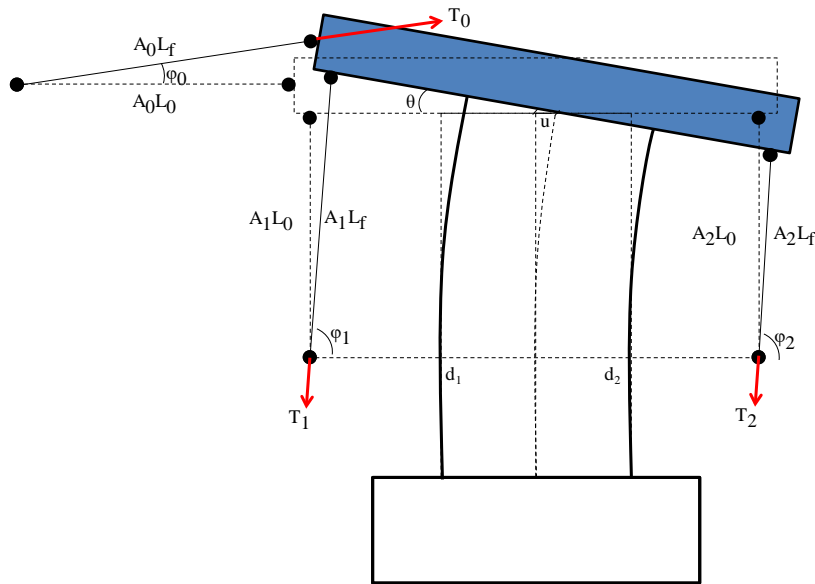


Figure 5-6 Typical displaced wall position during experiment

Referring to Figure 5-6, the current orientation of each actuator can be inferred from the initial and current lengths of each actuator. The current position of the wall in the initial orientation, defined by translation  $u$  and rotation  $\theta$  of a point at the top of the wall, can be evaluated by first defining a vector of multivariate equations  $s = \{S_0, S_1, \dots, S_{n-1}\}^T$  such that

$$S_0 : 0 = (A_0L_f)^2 - [(A_0L_0 + u + d_1(1 - \cos \theta))^2 + (d_1 \sin \theta)^2] \quad 5-6$$

$$S_1 : 0 = (A_1L_f)^2 - [(u + d_1(1 - \cos \theta) + D \sin \theta)^2 + (A_1L_0 - d_1 \sin \theta + D(1 - \cos \theta))^2] \quad 5-7$$

$$S_2 : 0 = (A_2L_f)^2 - [(u + d_2(\cos \theta - 1) + D \sin \theta)^2 + (A_2L_0 + d_2 \sin \theta - D(1 - \cos \theta))^2] \quad 5-8$$

The number of the multivariate equations is equal to the number of the actuators in the test setup. In Equation 5-6 to 5-8, the subscript "0" refer to the horizontal actuator while "1" and "2" refer to the vertical actuators.  $L_0$  refers to the original length of an actuator at zero

displacement position and  $L_f$  refer to the length of the actuator at the end of a time step. For example,  $A_0L_0$  and  $A_0L_f$  refer to the original and the length of the horizontal actuator at the end of a time step, respectively. The same conventions apply for the other actuators.  $D$  is the overall depth of the loading beam. The initial length of each actuator can be measured prior to each test and the change in the length of each actuator at the end of a time step can be inferred from the LVDT readings. The system of equations become overdetermined since the number of variables are less than the number of available equations. A least square method is employed to solve the system of equations.

However, the system of equations cannot be solved directly through linear algebra and an iterative procedure must be employed to find the approximate values of  $u$  and  $\theta$  that simultaneously satisfy Equation 5-6 to 5-8 to within some tolerance. The Newton-Raphson method [77] is adopted for this purpose, where such procedure involving multiple equations  $s = \{S_0, S_1, \dots, S_{n-1}\}^T$ , with multiple variables  $x = \{x_0, x_1, \dots, x_{m-1}\}^T$  can be formulated as

$$s(x) = 0 \quad 5-9$$

$$\delta x = -J^{-1}s \quad 5-10$$

$J$  is a Jacobian matrix consisting partial derivatives from Equation 5-6 to 5-8, defined as

$$J_{qp} = \frac{\partial s_q}{\partial x_p} \quad 5-11$$

At every iteration, the new values of  $x$  that satisfy the system of equations  $s$  are formulated as

$$x_{i+1} = x_i + \delta x \quad 5-12$$

The specific test setup in Figure 5-3 allowed direct monitoring of the wall's lateral displacement  $u$  from the string potentiometer. The unknown variables reduce to  $\theta$  only, as does the system of equations  $s$  which becomes

$$s = \begin{Bmatrix} S_1 \\ S_2 \end{Bmatrix} \quad 5-13$$

The resulting Jacobian matrix  $J$  is expressed as

$$J = \begin{bmatrix} \frac{\partial S_1}{\partial \theta} \\ \frac{\partial S_2}{\partial \theta} \end{bmatrix} = -2 \begin{bmatrix} (u + d_1)(d_1 \sin \theta + D \cos \theta) - (A_1 L_0 + D)(D \sin \theta - d_1 \cos \theta) + 2Z_1 \\ (u - d_2)(D \cos \theta - d_2 \sin \theta) - (A_2 L_0 - D)(d_2 \cos \theta - D \sin \theta) + Z_2 \end{bmatrix} \quad 5-14$$

The following substitute variables are defined

$$Z_1 = \frac{D^2 - d_1^2}{2} \sin 2\theta - Dd_1 \cos 2\theta \quad 5-15$$

$$Z_2 = (D^2 - d_2^2) \sin 2\theta \quad 5-16$$

Note that the Jacobian matrix in this case is not a square matrix due to an overdetermined system of equations, and the inverse of the Jacobian matrix in Equation 5-10 is replaced by  $J^\dagger$ , the pseudoinverse of  $J$ , defined as

$$J^\dagger = (J^T J)^{-1} J^T \quad 5-17$$

The iterations are repeated until a tolerance criterion is satisfied, for example  $\|s^k\| \leq \varepsilon$ , where  $k$  is an iteration index and  $\varepsilon$  is a specified tolerance. However, since the test coordinator runs

inside a controller board that requires new command signal within a constant time interval, the number of iterations must be limited. In the test coordinator for the quasi-static test, if convergence is not achieved after 10 iterations, the transformation algorithm will proceed using the last converged values. After solving for  $\theta$ , the orientation of each actuator can then be formulated as

$$\varphi_0 = \tan^{-1} \left( \frac{-d_1 \sin \theta}{A_0 L_0 + u + d_1 (1 - \cos \theta)} \right) \quad 5-18$$

$$\varphi_1 = \frac{\pi}{2} - \tan^{-1} \left( \frac{u + d_1 (1 - \cos \theta) + D \sin \theta}{A_1 L_0 - d_1 \sin \theta + D (1 - \cos \theta)} \right) \quad 5-19$$

$$\varphi_2 = \frac{\pi}{2} - \tan^{-1} \left( \frac{u + d_2 (\cos \theta - 1) + D \sin \theta}{A_2 L_0 + d_2 \sin \theta - D (1 - \cos \theta)} \right) \quad 5-20$$

In summary, the NLT procedure can be summarised into the following steps

- At the beginning of cycle  $i + 1$ , a new target displacement is applied at the top of the wall until the reading from the potentiometer shows the desired value  $u$ .
- The algorithm uses the measurements from the displacement transducers to obtain the current actuator lengths  $A_0 L_{f,i+1}$ ,  $A_1 L_{f,i+1}$ , and  $A_2 L_{f,i+1}$ . Equation 5-6 to 5-8 are assembled to solve for  $\theta$ . The algorithm then utilises the values of  $u$  and  $\theta$  to calculate the current orientation for each actuator  $\varphi_{0,i+1}$ ,  $\varphi_{1,i+1}$ , and  $\varphi_{2,i+1}$ .
- The measured load from the load cell on the horizontal actuator,  $T_{0,i+1}$  is used to calculate the required moment at the top of the wall  $M_t$  to maintain the desired aspect ratio  $Ar$  per Equation 5-1, where the wall shear load  $V$  is first obtained from  $T_{0,i+1}$  to consider the current horizontal actuator orientation.

$$V = T_{0,i+1} \cos \varphi_{0,i+1} \quad 5-21$$

- The desired loads from the two vertical actuators can be calculated from Equation 5-4 and 5-5, modified to consider the current vertical actuator orientations at the end of cycle  $i + 1$ , as given from the following relationships

$$R_1 = \frac{T_1}{\sin \varphi_{1,i+1}} \quad 5-22$$

$$R_2 = \frac{T_2}{\sin \varphi_{2,i+1}} \quad 5-23$$

- Repeat the procedure until the end of the test.

#### 5.3.4. Experiment results

The quasi-static test result of a wall with a target aspect ratio of 6 is presented in this section. The results are intended to validate the NLT procedure adapted for the specific purpose of the test, by demonstrating its ability to achieve the target aspect ratio while maintaining relatively constant axial load. Figure 5-7 shows the last three cycles of the applied displacements to the wall. In general, the wall did not attain the specified amplitudes in Figure 5-4 with sufficient accuracy, since the horizontal actuator was operated manually while monitoring the readings from the string potentiometer or the load cell.

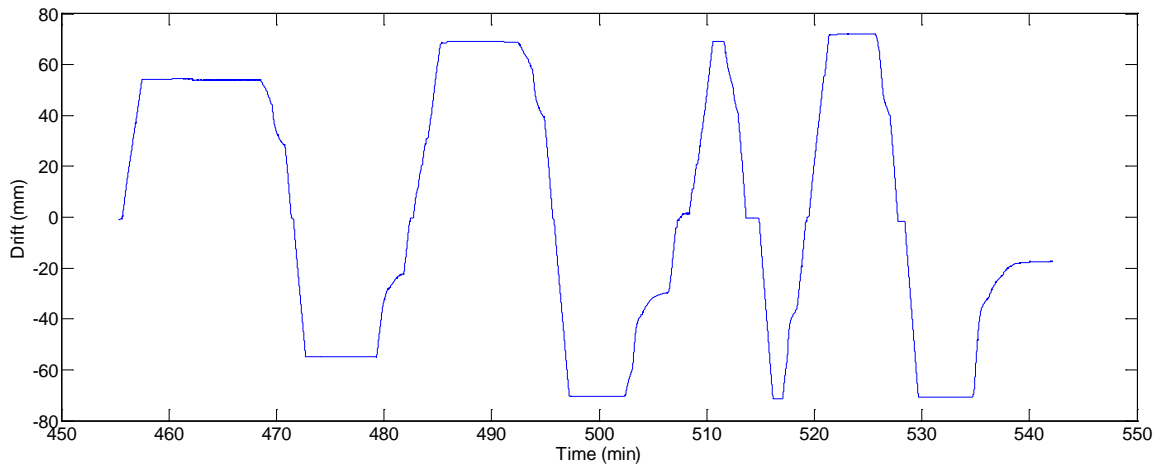


Figure 5-7 Last three cycles of actual wall displacement

Figure 5-8a and Figure 5-8b show 10-minute snapshots of the wall horizontal translations as it deflected from approximately 70 mm to -70 mm (Figure 5-8a) and from -70 mm to 70 mm (Figure 5-8b). Each figure also contains a secondary vertical axis indicating the number of iterations required to solve Equation 5-9 to Equation 5-12, showing that the algorithm failed to obtain converge  $\theta$  value after 10 iterations between the 495<sup>th</sup> and 496.5<sup>th</sup> minute (Figure 5-8a), as well as between the 518.5<sup>th</sup> and the 520<sup>th</sup> minute (Figure 5-8b). The convergence failure occurred as the wall displaced. Figure 5-8 also shows that most of the time convergences were achieved in one iteration, especially when the wall was held steady (i.e. the region in Figure 5-7 where displacement does not change). There were also instances where convergences were achieved in between one and ten iterations, which also occurred as the wall displaced. The failure to achieve convergence was probably due to a tight tolerance requirement, where it was set to  $\varepsilon = 10^{-6}$ .

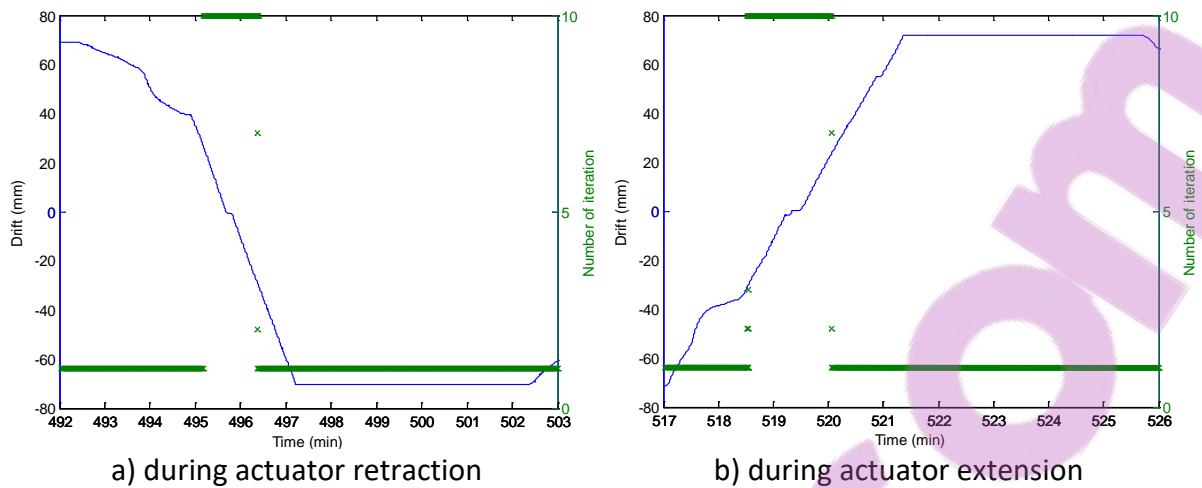


Figure 5-8 Wall drift and number of iteration required

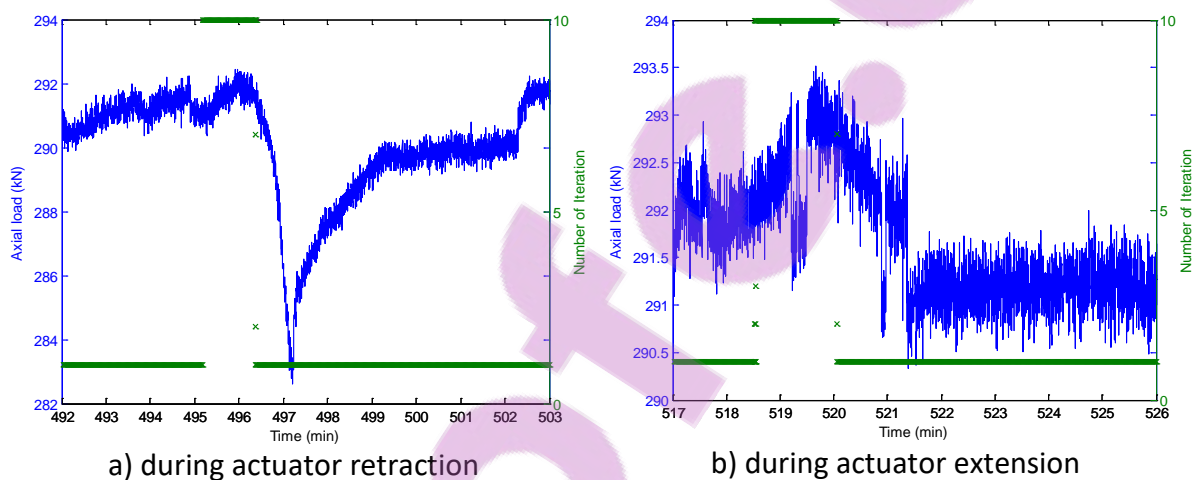


Figure 5-9 Actual axial force applied to the wall

Figure 5-9a and Figure 5-9b show the actual axial force applied to the wall. It can be seen that the desired axial load of 290 kN was satisfactorily achieved albeit a small offset. Comparing Figure 5-9a with Figure 5-8a, and Figure 5-8b with Figure 5-9b, it can be seen that the axial force drifted when the wall was displaced but stayed relatively constant as the wall was held steady. This was probably due to the the different rate of changes in the forces of the two vertical actuators.

Figure 5-10a and Figure 5-10b show the actual aspect ratio attained was about 6.24, very close to the targeted value. Comparing Figure 5-10a with Figure 5-8a and Figure 5-10b with

Figure 5-8b, it can be seen that the aspect ratio also drifted as the wall displaced and became relatively constant as it was held steady. There was, however, instances when the aspect ratio appeared to be constant even when the wall was displaced. These instances actually coincided with the period during which the iteration failed to converge such that the algorithm used the last converged values to evaluate the current orientations of the actuators, resulting in the short durations of constant aspect ratio.

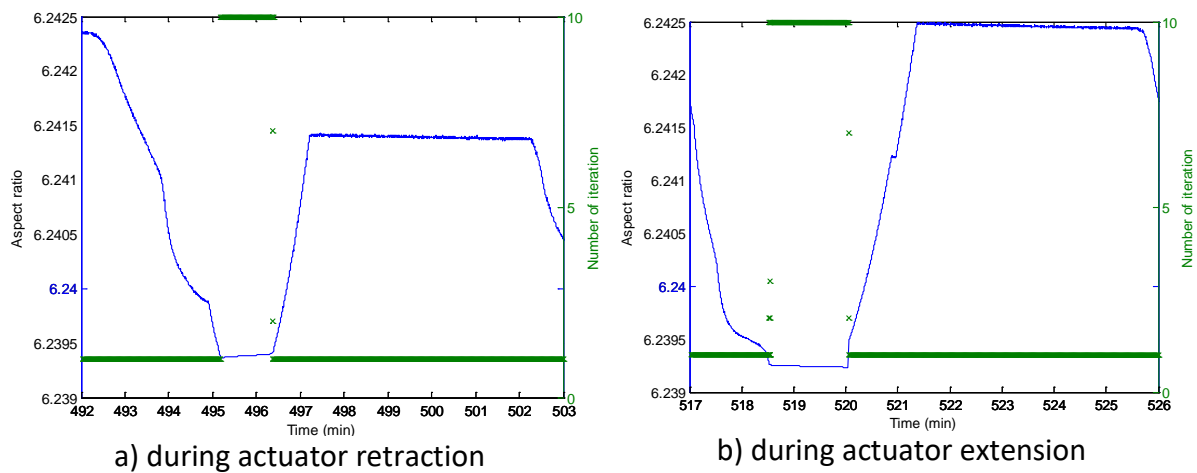


Figure 5-10 Actual aspect ratio of the wall

Figure 5-11 shows the orientations of the three actuators when the wall drifts corresponded to the magnitude shown in Figure 5-7. The changes of the horizontal actuator's orientation,  $\phi_0$ , relative to its initial orientation at the beginning of the test was slightly below two degrees, while the changes in the vertical actuators' orientations,  $\phi_1$  and  $\phi_2$ , relative to their initial orientations were up to eight degrees.

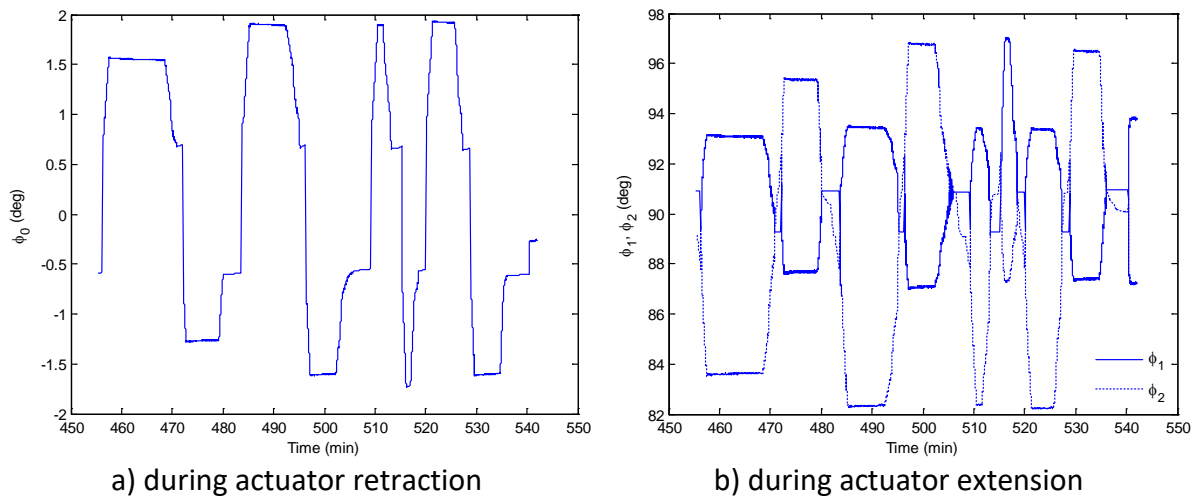


Figure 5-11 Change in the actuators' orientations during the wall cyclic displacement, a) horizontal and b) vertical actuators

Neglecting geometric changes during multi-axial test will lead to different apparent stiffness of the wall compared to its actual resistance. Additionally, if the load cell readings on the horizontal actuator are directly utilised in Equation 5-4 and 5-5 by neglecting the NLT procedure, it will lead to erroneous target loads for both vertical actuators. The force errors due to the change in the orientations of the actuators in Figure 5-11 are up to 0.05 kN in the horizontal actuator and up to 2.2 kN in the vertical ones.

In a quasi-static test, however, the wall horizontal displacements are completely predefined such that there are no cumulative errors due to unaccounted transverse displacements resulting from neglecting the NLT procedure, especially if the error magnitudes are relatively small compared to the magnitude indicated by the load cell readings. If the change in the actuators lengths are recorded during experiments, the NLT algorithm can even be applied to the recorded data after the experiments have concluded.

#### 5.4. Hybrid simulations on RC column

The second set of experiments utilised an RC column using the hybrid simulation method. The column was subjected to bidirectional action from earthquake records. The two main

objectives of the hybrid simulations: 1) to validate the adapted NLT algorithm for the specific tests, and 2) to investigate the effect of different displacement tracking strategies on the column's nonlinear behaviour. This chapter will focus on the first objective only.

#### 5.4.1. Experiment setup

Two servo-mechanical hydraulic actuators were connected directly to the specimen as shown in Figure 5-12. One actuator was fixed to strong wall while the other was fixed to a 350 × 350 H-shaped steel beams with 35 mm flange and web thickness designated as a reaction frame. The H-shape steel beam was in turn fixed to the strong floor by means of post-tensioning.

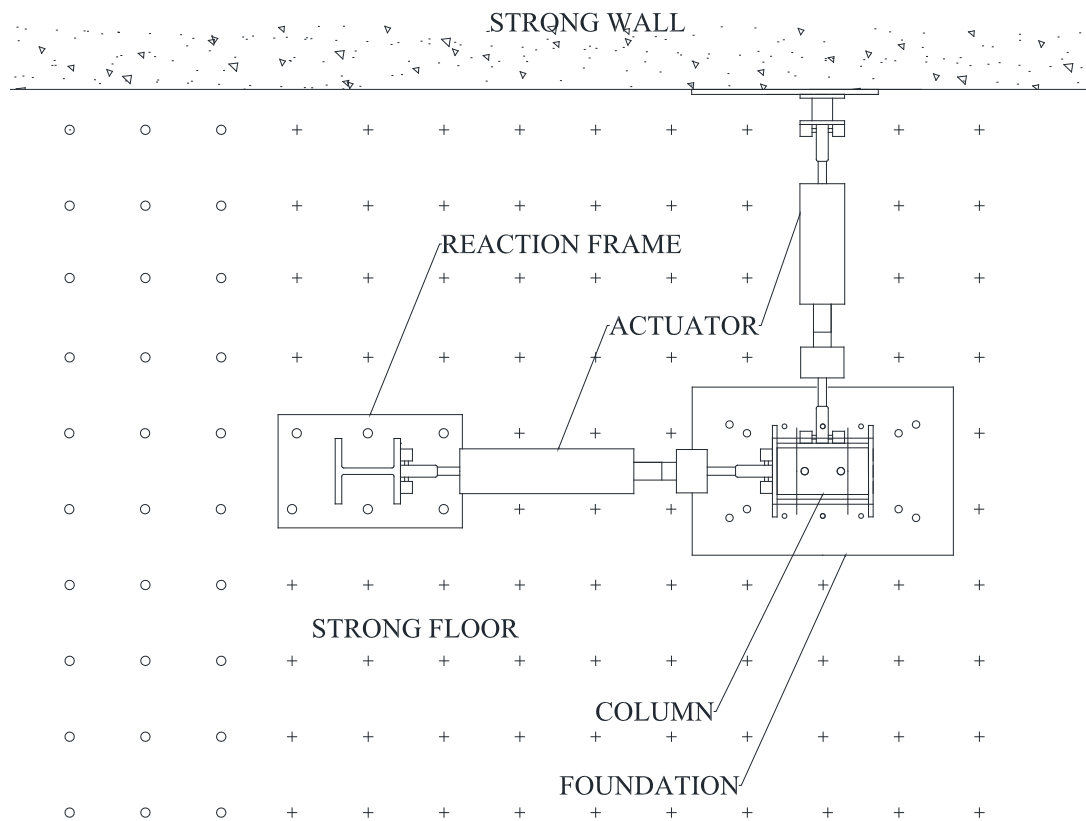


Figure 5-12 Schematic drawing of the bidirectional hybrid simulation setup plan view

#### 5.4.2. Transformation procedure

During the hybrid simulations, the column were subjected to target displacements computed by the test coordinator in the two perpendicular axes concurrently. The following NLT

algorithm refers to the schematic plan view of the test setup in its original position in Figure 5-13, noting the name of the variables involved in the transformation algorithm.

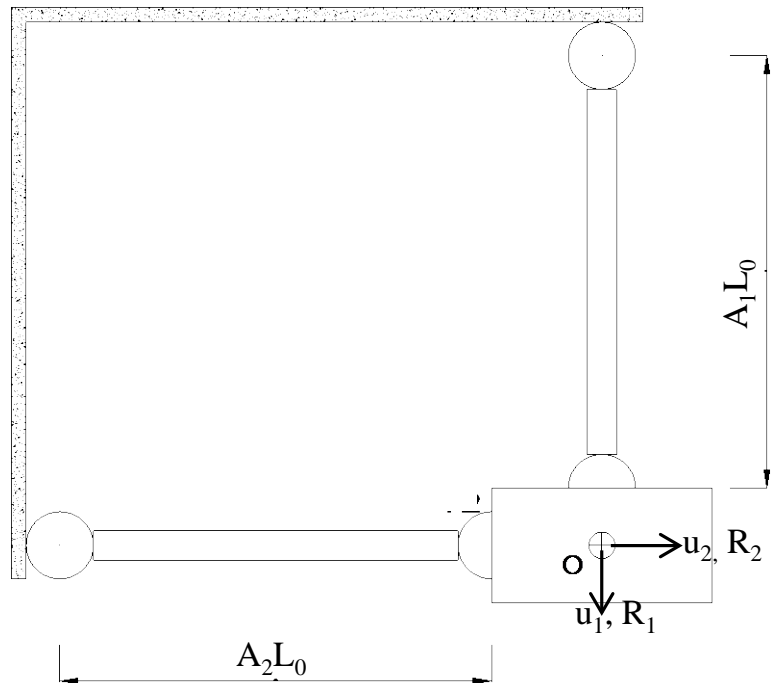


Figure 5-13 Schematic drawing of bidirectional hybrid simulation setup

$L_0$  is the initial length of an actuator in the original position of the test setup. Subscripts “1” and “2” denote the principal axes of the column, where axis 1 is parallel to weak axis. Thus  $A_1L_0$  is the initial length of the actuator parallel with the weak axis of the column in the original orientation of the test setup. The global DOF of the column is defined at the assumed location of the center of mass O.  $u_1$  and  $R_1$  are the displacement and the restoring force in the weak axis direction. The same conventions apply for the other axis. The initial length of each actuator is constant and can be measured at the beginning of a test.

To account for the arching motions of the actuators as the column displaces along both axes simultaneously, the computed displacement at every time step must be modified to account

for geometric change in the test setup relative to the original orientation. Figure 5-14 shows a typical displaced configuration of the column during a test.

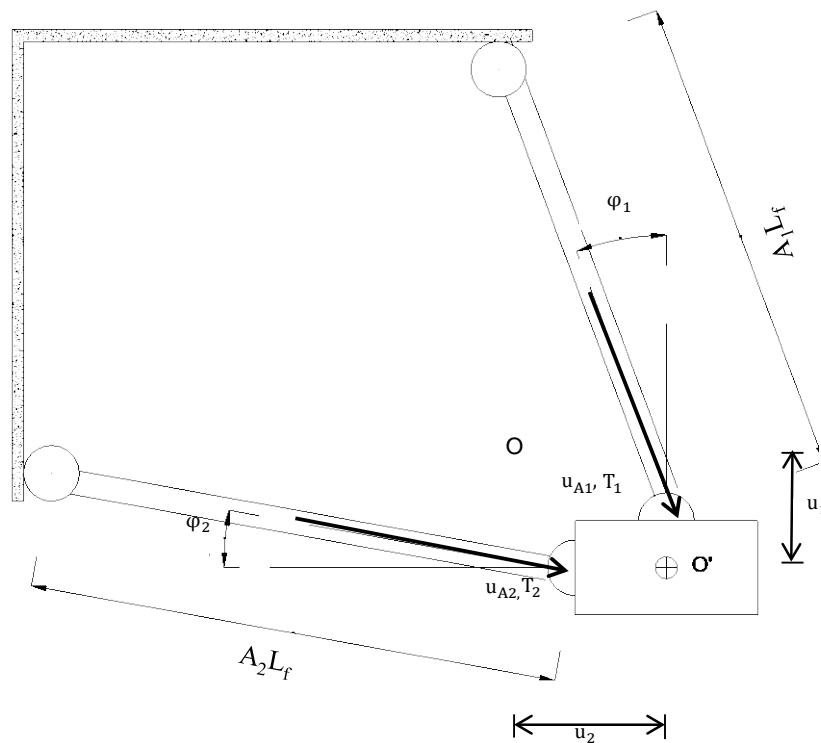


Figure 5-14 Typical displaced configuration of the column during experiment

In Figure 5-14, the current lengths of the actuators are  $A_1L_f$  or  $A_2L_f$ , are inferred from the actuators' LVDT. The actuator load cells indicate the restoring forces  $T_1$  and  $T_2$ , aligned to the current orientations of the actuators. The current orientation of each actuator is the rotation relative to its original orientation,  $\phi_1$  or  $\phi_2$ . The NLT solves for the current position of the column  $O'$  by seeking  $u_1$  and  $u_2$  using a couple of assumptions in the following:

- The column is rigid in the cross-section plane.
- Rotations of the actuators outside the plane of Figure 5-14 is negligible

The non-linear equations can be written as

$$S_1 : 0 = (A_1 L_0 + u_1)^2 + (u_2)^2 - (A_1 L_f)^2 \quad 5-24$$

$$S_2 : 0 = (A_2 L_0 + u_2)^2 + (u_1)^2 - (A_2 L_f)^2 \quad 5-25$$

The Newton-Rhapson procedure is adopted to iteratively solve for  $u_1$  and  $u_2$ . In this case, the Jacobian matrix  $J$  is defined as

$$J = \begin{pmatrix} \frac{\partial S_1}{\partial u_1} & \frac{\partial S_1}{\partial u_2} \\ \frac{\partial S_2}{\partial u_1} & \frac{\partial S_2}{\partial u_2} \end{pmatrix} = 2 \begin{pmatrix} A_1 L_0 + u_1 & u_2 \\ u_1 & A_2 L_0 + u_2 \end{pmatrix} \quad 5-26$$

The iteration process is terminated once convergence is achieved within some predetermined tolerance. The NLT in the hybrid simulations uses the most recent converged values if the iteration fails to find convergence after 10 iterations. Once  $u_1$  and  $u_2$  converge the rotation of each actuator relative to its original orientation can be calculated as

$$\varphi_1 = \tan^{-1} \left( \frac{u_2}{A_1 L_0 + u_1} \right) \quad 5-27$$

$$\varphi_2 = \tan^{-1} \left( \frac{u_1}{A_2 L_0 + u_2} \right) \quad 5-28$$

The restoring forces from the column  $T_1$  and  $T_2$  must be transformed to the restoring forces at the specimen's global DOFs  $R_1$  and  $R_2$ , which can be computed after solving for the current orientations of the actuators

$$\begin{Bmatrix} R_1 \\ R_2 \end{Bmatrix} = \begin{bmatrix} \cos \varphi_1 & \sin \varphi_2 \\ \sin \varphi_1 & \cos \varphi_2 \end{bmatrix} \begin{Bmatrix} T_1 \\ T_2 \end{Bmatrix} \quad 5-29$$

Similarly, the test coordinator must modify the target displacements from to account for the current orientation of each actuator. These displacements, noted as  $u_{A1}$  and  $u_{A2}$  in Figure 5-14, are computed according to the following relationships

$$u_{A1} = \frac{1}{\cos \phi_1} (u_1 + A_1 L_0 (1 - \cos \phi_1)) \quad 5-30$$

$$u_{A2} = \frac{1}{\cos \phi_2} (u_2 + A_2 L_0 (1 - \cos \phi_2)) \quad 5-31$$

### 5.5. Study on error accumulation

Position error as the result of neglecting transverse displacement errors during bidirectional hybrid simulations occur systematically. Although in the experiment displacement controls were rigorously handled using nonlinear transformation procedure to avoid the geometric position error, it is of interest to investigate possible cumulative position errors if transverse displacements were neglected. This can be assessed from the difference between the target displacements at the global DOF of the column  $u_1$  and  $u_2$ , and the command displacements for the actuators  $u_{A1}$  and  $u_{A2}$  after accounting for the current orientations. For simplicity, the subscripts "1" and "2" are omitted. Mathematically the difference can be formulated as

$$u^{er} = |u_A| - |u| \quad 5-32$$

The difference between the absolute values is used to automatically account for the displacement signs. Negative  $u^{er}$  indicates  $u_A$  is smaller than  $u$ , while the opposite is true for positive values. Since computed instead of measured displacements are used in the integration algorithm, which leads to the most favourable cumulative error propagation characteristic [1], Equation 5-32 does not explicitly contribute to cumulative error propagation since the global DOF of the specimen  $u$  is always used inside the numerical integration instead of the structural displacement at the actuator coordinate  $u_A$ .

However, displacement actuation error will affect the restoring force from the specimen the actuators measure at the current orientations. When transformation between the measured actuator loads  $T_1$  and  $T_2$  and the structure loads at the global DOF  $R_1$  and  $R_2$  does not exist, equivalent position errors arise. The difference can be formulated as

$$R^{er} = |T| - |R| \quad 5-33$$

Figure 5-15 shows the time histories of  $R^{er}$  from one of the hybrid simulations. The differences account for up to 3.29% relative to the maximum restoring force developed in the weak axis direction and up to 5.24% relative to the maximum restoring force in the strong axis direction.

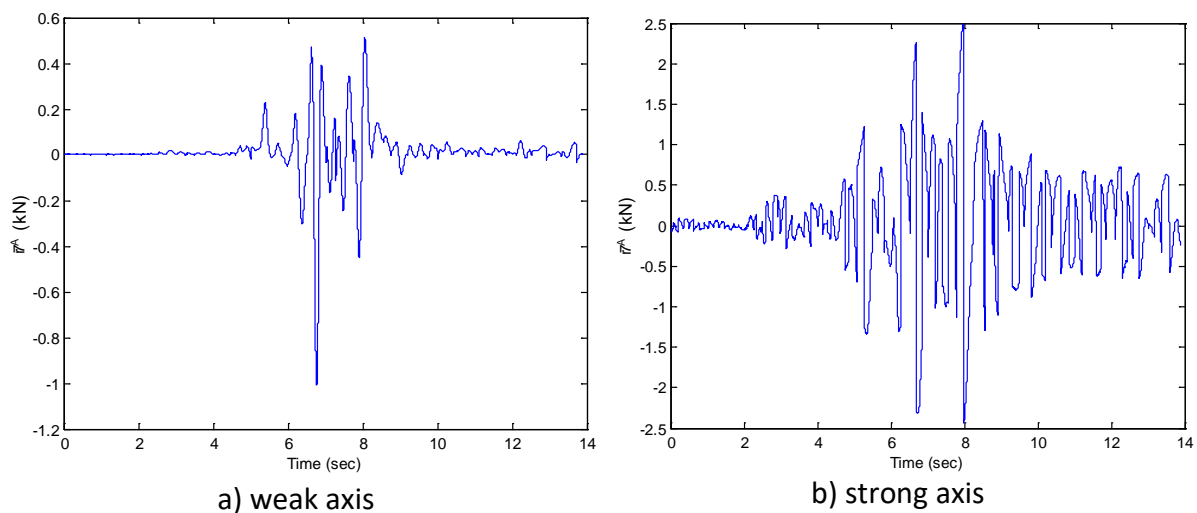


Figure 5-15 The time history of  $R^{er}$  for a selected hybrid simulation result along both axes of the column

$R^{er}$  in Figure 5-15 is equivalent to the column's response to error excitations which occurred systematically during the test. The effect of neglecting these differences can be studied by employing the same technique Shing and Mahin [1] used to study the cumulative error propagation effect in a hybrid simulation. The technique will be summarised in the following paragraphs.

Since computed instead of measured displacements are used inside the integration algorithm, the remaining source of errors comes from the force measurements from the specimen. Assuming a linear elastic stiffness  $k$ , the total error from force feedback at time step  $i$  can be formulated as

$$\mathbf{R}_i^{\text{er}} = k\mathbf{u}_i^{\text{er}} + \mathbf{R}_i^{\text{er},m} \quad 5-34$$

Equation 5-34 indicates that that the total error in the restoring force at every time step comes from an equivalent force error due to  $\mathbf{u}^{\text{er}}$  and from  $\mathbf{R}_i^{\text{er},m}$ , the force error associated with measurement alone. The total force error will in turn translates into an equivalent displacement error  $\mathbf{u}_i^{\text{e,Rr}}$

$$\mathbf{u}_i^{\text{er,R}} = \mathbf{k}^{-1}\mathbf{R}_i^{\text{er}} \quad 5-35$$

In a linear elastic system, cumulative error propagation depends on the dynamic characteristics of the structure and the numerical integration algorithm employed through its complex eigenvalues [1]. The eigenvalues of NEM employed during the hybrid simulations are formulated as

$$\lambda_{1,2} = \text{Re} \pm i \text{Im} \quad 5-36$$

where  $\text{Re} = 1 - \omega_n^2 \Delta t^2 / 2$  and  $\text{Im} = \sqrt{4 - (\omega_n^2 \Delta t^2 - 2)^2} / 2$ ,  $\omega_n$  is the natural frequency of the structure and  $\Delta t$  is the integration time step size. Equation 5-36 can be derived from the recursive form of the integration algorithm [1]. Subsequently the following two parameters can be defined

$$\bar{\omega} = \frac{\tan^{-1}(\text{Im}/\text{Re})}{\Delta t} \quad 5-37$$

$$D = \frac{2(\text{Re}-1)}{\text{Im}} \quad 5-38$$

Since cumulative displacement errors can be considered as the displacement response of a structure to some error excitations [1], any sequence of error signals can be decomposed into sinusoidal components at different frequencies using the discrete Fourier transformation procedure [78]. The maximum cumulative displacement error can be approximated through the following relationship

$$\left| \overline{u_{i+1}^{\text{er,R}}} \right|_{\text{max}} \approx 2 \sum_j H_j |c_j| \quad 5-39$$

$$H_j = \frac{1}{2} |D| \sqrt{\rho^2 + \gamma^2 - 2\rho\gamma \cos \phi} \quad 5-40$$

$$\gamma = \frac{\sin \bar{\omega} \Delta t \beta_j}{\cos \bar{\omega} \Delta t \beta_j - \cos \bar{\omega} \Delta t} \quad 5-41$$

$$\rho = \frac{\sin \bar{\omega} \Delta t}{\cos \bar{\omega} \Delta t \beta_j - \cos \bar{\omega} \Delta t} \quad 5-42$$

$$\phi_j = \bar{\omega} \Delta t (i+1)(1-\beta_j) \quad 5-43$$

$\left| \overline{u_{i+1}^{\text{er,R}}} \right|_{\text{max}}$  is the maximum cumulative equivalent displacement error up to time step  $i$  due to force measurement error  $R^{\text{er}}$  and  $H_j$  is the amplification factor of the cumulative error.  $\beta_j = \tilde{\omega}_j / \bar{\omega}$  is the ratio of the error excitation frequency  $\tilde{\omega}_j$  to the numerical natural frequency  $\bar{\omega}$  of the structure which contributes to the total cumulative error. In Equation 5-39  $c_j$  is the Fourier amplitude of  $u^{\text{er}}$  or  $R^{\text{er}}$  at frequency  $\tilde{\omega}_j$ .  $2|c_j|$  is the Fourier amplitude of  $\overline{u_{i+1}^{\text{er,R}}}$  at each contributing sinusoidal error component with frequency  $\tilde{\omega}_j$ . Since the systematic error is

amplified by the natural frequency of the structure itself, only a few frequencies with  $\beta_j$  close to unity need to be considered in Equation 5-39 while the contribution of other frequencies is negligible. The maximum cumulative displacement error can be computed by solving Equation 5-39 using a few known parameters during the test. For example, the parameters from the test result related to Figure 5-15 is summarised in Table 5-1. Note that the hybrid simulations are conducted on a 50-time scale, i.e. the natural periods of the column in each principal axis direction is 50 times larger than the natural periods of the same column tested in real-time.

Direction	$T_n$ (sec)	$\Delta t$ (sec)	k (kN/m)	$i$
weak axis	47	0.005	455.4	138000
strong axis	23.5		1821.8	

Table 5-1 Parameters of the specimens and numerical integrations used during hybrid simulations

$u^{er,R}$  must be transformed into the frequency domain first. Figure 5-16 shows a Fourier-transformed  $u^{er,R}$  at the weak axis.

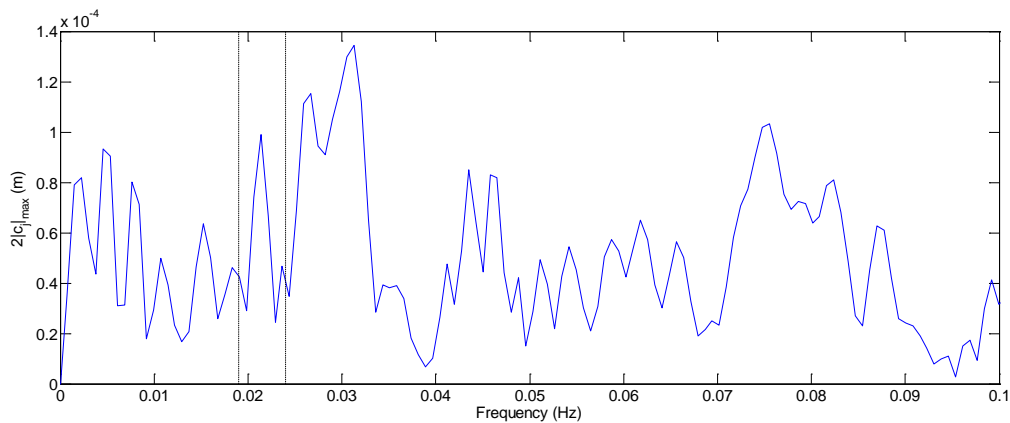


Figure 5-16 Fourier transformation of  $u^{er}$  in the weak axis direction

In Figure 5-16 the region between the dotted line represents the range of  $\beta_j$ 's that are accounted for when calculating  $\left| \overline{u_{i+1}^{er,R}} \right|_{max}$ . Table 5-2 summarises the computation result to determine  $\left| \overline{u_{i+1}^{er,R}} \right|_{max}$  from  $R^{er}$  in Figure 5-15.

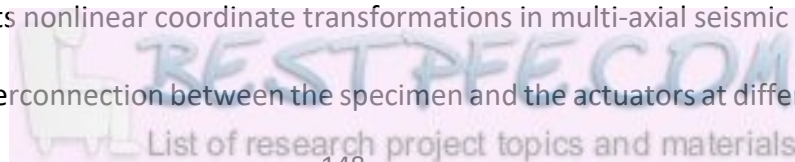
Direction	Total $\left  \overline{u_{i+1}^{er,R}} \right _{max}$ (mm)
weak axis	2.52
strong axis	8.08

Table 5-2 Summary of computation to determine total  $\left| \overline{u_{i+1}^{er,R}} \right|_{max}$  on both column axes

It should be noted that the values shown in Table 5-2 are computed assuming a linear elastic structure with elastic stiffness as specified in Table 5-1 for each direction of the column principal axes. Since the column experienced inelastic deformations and its stiffness changed, the result from Table 5-2 can only be interpreted as the expected cumulative displacement error for a corresponding linear system of the column which did not capture the effect of softening due to inelastic response. However, Shing and Mahin [1] have shown that for a displacement ductility less than 12, the expected cumulative error for an inelastic system is always less than that for the corresponding elastic system. From the hybrid simulation result it was found that the ductility of the column was 10 in the column weak axis direction, and 4 in the other. It is likely that the total cumulative displacement error considering the inelastic response will be less than the values tabulated in Table 5-2. Nevertheless, this analytical study should give an indication that a reasonably high cumulative displacement error can be expected if geometric effect in multi-directional test is neglected.

## 5.6. Summary

The chapter presents nonlinear coordinate transformations in multi-axial seismic simulations tests. Due to the interconnection between the specimen and the actuators at different planes,



transverse movement errors manifest whenever the specimen is actuated. Linear coordinate transformation procedure cannot consider these transverse displacements and to ensure accurate experiment result, nonlinear coordinate transformation between the desired displacements at the global DOF of the specimen and the corresponding displacement command to the actuators at the actuator DOF system must be employed. The transformation procedure must consider the current displaced configuration of the actuators-specimen setup.

Two different nonlinear transformation procedures are presented depending on the type of tests considered. In the quasi-static tests, the nonlinear transformation procedure is able to impose and maintain the correct boundary conditions. In the hybrid simulations, analytical study in the frequency domain to compute the cumulative displacement errors is employed to illustrate the effect of neglecting the nonlinear transformation procedure. The cumulative displacement error resulting from the frequency domain analysis is an upper-bound estimate since it does not consider the change in stiffness as the specimen experiences inelastic deformation, however it still gives a clear indication of the importance of the nonlinear transformation procedure to ensure accurate multi-axial testing.



# Chapter 6

## Displacement paths effect in hybrid simulations considering nonlinear response

---

### 6.1. Introduction

Most experimental seismic simulations today consider the response only to unidirectional ground motion although real earthquakes consist of multidirectional excitations. These multidirectional loads excite different principal axes of a structure, which may be sensitive to combined stresses resulting from deformations along the different axes. Most design standards regarding earthquake actions worldwide recognise the interaction between at least the two orthogonal horizontal components of an earthquake. For example, NZS1170.5 [76] requires that the design spectra for horizontal actions must be applied simultaneously in two orthogonal directions except for ductile structures. Eurocode 8 [79] permits independent analysis using two planar models for regular type structures, where section 4.3.3.5 of Eurocode 8 provides combination rules for these separate analyses. The analysis procedures provided by both standards assume the structure behaves elastically. It is explicitly stated in section 4.3.3.1 of Eurocode 8 while it is implied in NZS1170.5 through reduction factors for the elastic size hazard spectrum. However, in many cases structures deform nonlinearly during earthquakes. During inelastic response there are complex interactions between the responses along the principal axes of a structure or structural elements such that stiffness degradation in one axis can significantly reduce the same parameter in the other [80]. It is

important to gain deeper insight into inelastic structural response subjected to load from multiple axes through more experimental testing.

Since the cost of running a large-scale test on a shake table considering multidirectional excitations is very high, large scale tests on an expanded time scale such as using the quasi-static and the hybrid simulation method remains the most popular. The hybrid simulation method also reveals the information on the specimen's dynamic properties without the need of dynamic testing.

In cyclic experiments, there are an infinite number of possible deformation or load paths in a two-dimensional space to the specimen. It has been shown that different load paths lead to different inelastic behaviours [81], and consequently different energy dissipation capabilities. Additionally, it has also been shown that the energy dissipation characteristic may not always be proportionally related to the ultimate strength capacity for a given displacement path [80, 82]. So far, the effect of different load paths to the ultimate strength and energy dissipation capacity has only been studied under the quasi-static testing methods [80-82]. It is of interest to investigate its effect on a specimen subjected to actual ground motions. The randomness of an earthquake excitation may lead to significantly different energy dissipation capacity since inelastic deformations are history dependent.

This chapter presents the results of a series of bidirectional hybrid simulations. The focus of this chapter is the results of applying different displacement tracking strategies during the hybrid simulations. It will be shown that different displacement tracking strategies lead to different force and displacement amplitudes, but more importantly different energy dissipation magnitudes which confirm the dependency of these parameters to deformation path/history.

## 6.2. Test setup and specimen

The specimen used in the hybrid simulation series was an unbonded post-tensioned (PT) reinforced concrete (RC) column with asymmetrical cross-section. The column was designed to rock elastically under lateral loading. Furthermore, replaceable mild-steel bars were mounted externally to provide additional energy dissipations and to create plastic response. A rocking column was selected to ensure the specimen did not degrade significantly between experiments since the column was used for all hybrid tests. A rocking mechanism prevented the formation of plastic hinge and damage that usually occurs at the base of a monolithic column. The unbonded PT bars improved the stability of the rocking column, preventing it from toppling and giving rise to a stable positive post-uplift stiffness. The overall behaviour was essentially nonlinear elastic with small energy dissipation from the externally mounted energy dissipaters (EMD). The system was expected to produce a typical “flag-shaped” hysteretic curve for rocking structures [83].

The column specimen represented a 1:3 scale prototype bridge pier and was envisaged to be a part of a multi-span bridge system, such as shown in Figure 6-1. Since the boundary conditions at the abutments allows the bridge to sway in both longitudinal and transverse directions, bidirectional bending demand is warranted on piers supporting the bridge deck [84], thus seismic experiments on bridge piers should always consider at least bilateral loads. The Direct Displacement Based Design (DDBD) procedure is adopted for designing the bridge pier [85]. The DBDD procedure uses an equivalent single degree of freedom (SDOF) substitute structure with secant stiffness to the target displacement at the Maximum Considered Earthquake (MCE). The design procedure closely followed a similar column tested by Marriott [86].

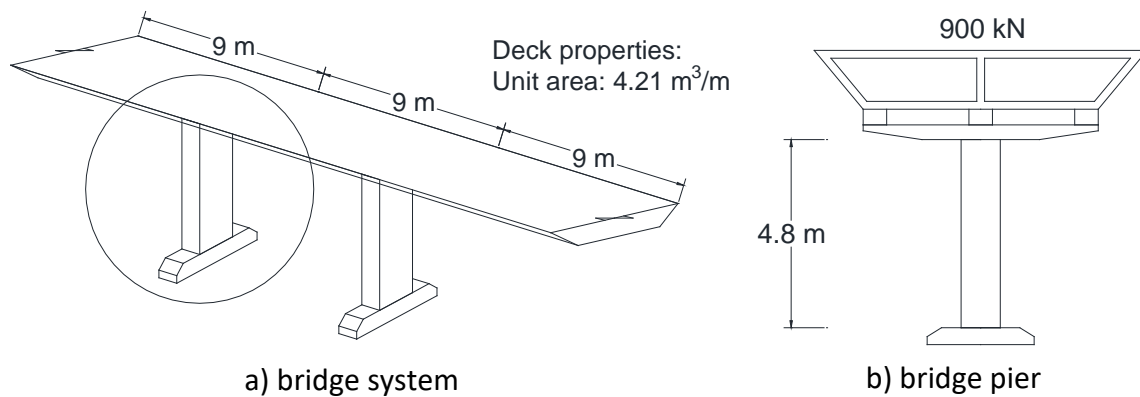


Figure 6-1 Multi-span bridge prototype

Table 6-1 presents a summary of the model and prototype column. The model column, herein referred to as the column, was detailed with 12 – D10 (10mm diameter, Grade 300 MPa, deformed bar) as longitudinal reinforcements, and three D10 rectangular hoops at 120 mm centres as transverse reinforcements. A concrete block was also casted for the column foundation. In the laboratory setup, the foundation block was fixed to the strong floor by means of post-tensioning. The column and the foundation block was clamped together through post-tensioning.

A 30x30x3 steel equal angle was casted into the perimeter at the base of the column to minimise damage during rocking impacts. Horizontal ducts were casted into the column base for steel brackets attachment. The steel bracket in turn held the replaceable EMD. Due to reinforcement congestions, chemical anchors were used to mount the steel brackets on the shorter column face. Concrete compressive as well as steel reinforcement tension test results can be found in Appendix D confirming the material qualities assumed during design. The test setup has been elaborated briefly in Chapter 5. The concrete column stood within the cavity in the middle of a steel base plate. The base plate prevented sliding upon rocking and provided anchorage of the EMD. Figure 6-2 shows the actual test setup as viewed from above. Figure 6-3 shows the setup detail at the column base, highlighting the locations of the EMD

and the steel brackets at both faces of the column, as well as the steel base plate. Schematic drawings of the column and foundation detailing, steel brackets, as well as a selection of photographs taken during specimen construction are shown in Appendix D.

	<b>Prototype</b>	<b>Model</b>
<b>Cross-section area</b>	1.1025 m <sup>2</sup>	1.225 × 10 <sup>5</sup> mm <sup>2</sup>
<b>Cross-section dimension</b>	1.05 × 1.05 m	490 × 250 mm
<b>Pier height</b>	4.8 m	1.6 m
<b>Participating deck gravity load</b>	900 kN	100 kN

Table 6-1 Properties of prototype and model of bridge pier

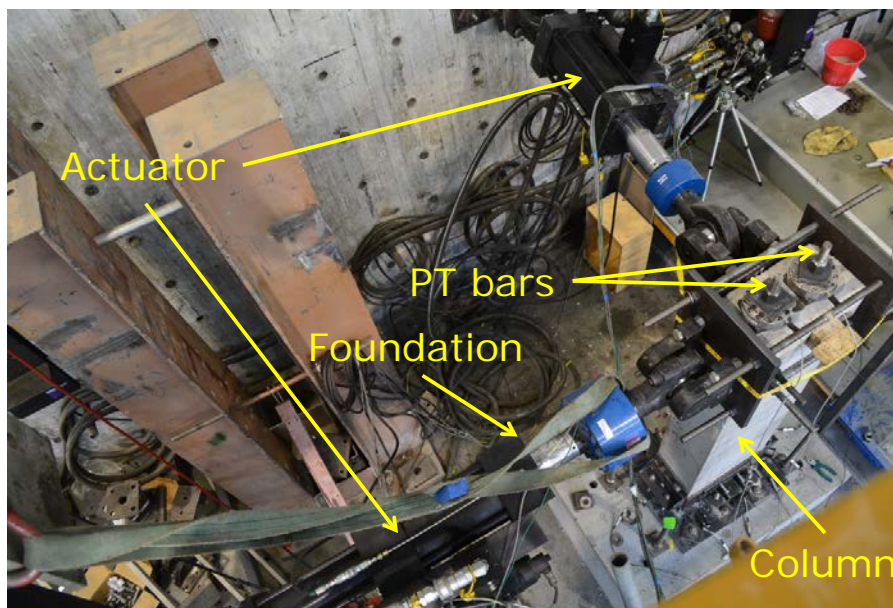


Figure 6-2 Bidirectional hybrid simulation setup as viewed from above

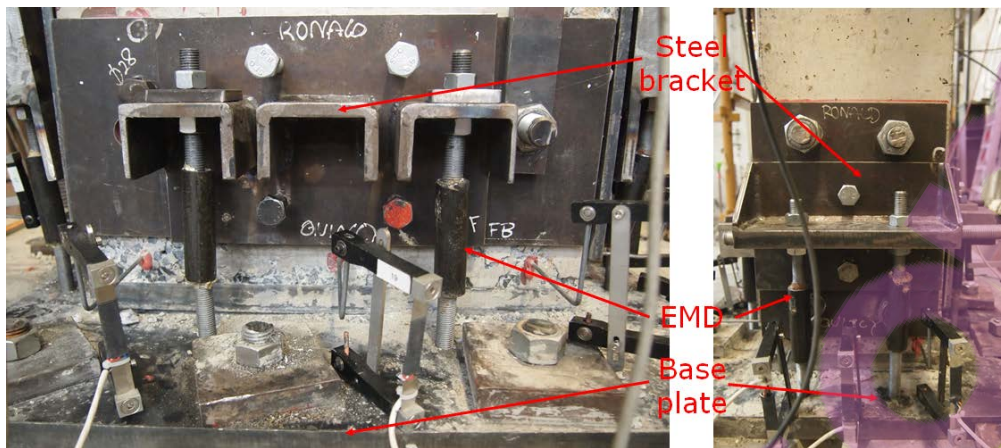


Figure 6-3 Column base detailing

### 6.3. Displacement tracking strategies

The rocking column was subjected to three different displacement tracking strategies along its principal axis directions. Referring to Figure 6-4, among infinite possible paths to move the column from Point 1 to Point 2, the experiments adopted a “staggering” pattern. In the first pattern (denoted I in Figure 6-4), the column was displaced along the strong axis (henceforth called the  $X$ -axis) while it was held steady in the weak axis (henceforth called the  $Y$ -axis) direction. Afterwards, the column was displaced along the  $Y$ -axis until reaching Point while the  $X$ -axis position was held steady. The second pattern (denoted II) was similar to Pattern I except the order of loading was reversed. In the third pattern (denoted III), the column was displaced along both axes simultaneously. Using different displacement tracking strategies in a hybrid simulation is analogous to using different load patterns under biaxial quasi-static tests. Since it is expected that displacement response amplitudes for these different tracking strategies are similar, the paths the column takes to reach these amplitudes influence how much energy is dissipated.

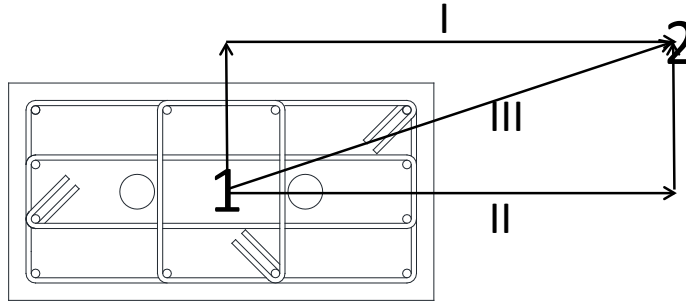


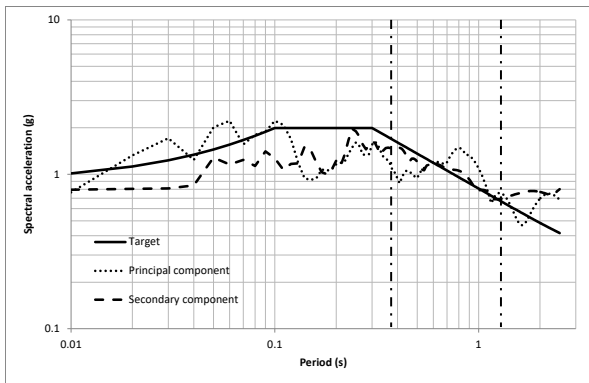
Figure 6-4 Plausible displacement paths for applying an in-plane displacement

#### 6.4. Loading regime

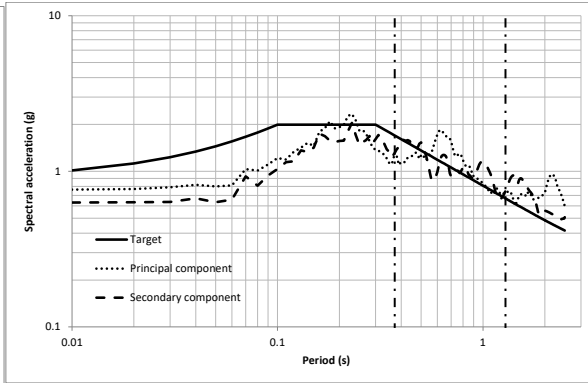
The experimental series was divided into two parts,

- A. Series of bidirectional hybrid simulations following three different loading strategies for each loading sub-step, and
- B. Series of quasi-static cyclic tests following four different loading patterns.

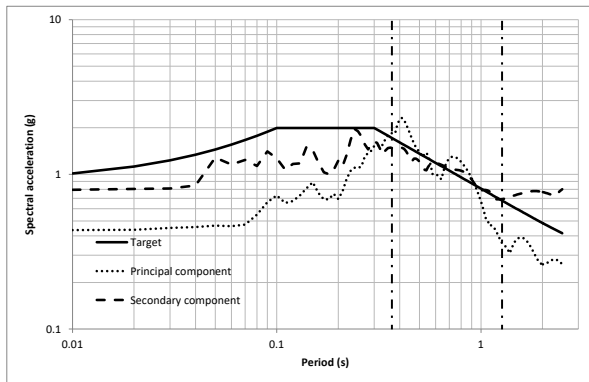
Five sets of earthquake ground motion were considered for the hybrid simulations in test series A. The selected records represented two seismic zones in the North Island New Zealand, specific for class C soil [87]. The earthquake records were selected and scaled based on the NZS1170.5 [76]. The seismic hazard parameters used to scale these records are summarised in Table 6-2. Figure 6-5 shows the site-specific target acceleration spectrum and the response spectra of the individual scaled earthquake records. The earthquake records were scaled to fit the target spectrum for the period range between  $0.4$  and  $1.3T_1$ , where  $T_1$  was the largest translational period in the direction of interest [76]. The range of the period where each ground motion was scaled to match the design spectra lies within the dotted vertical lines in each sub-figure of Figure 6-5. In this case  $T_1 = 0.94$  sec was the translational period at the Y-axis direction. For each set of ground motion, the test was repeated three times using the three different tracking strategies shown in Figure 6-4.



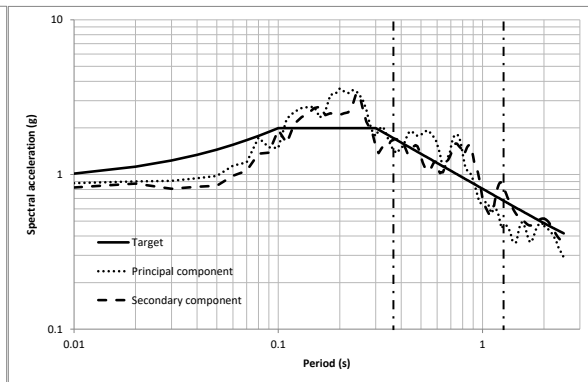
(a) 1979 El Centro



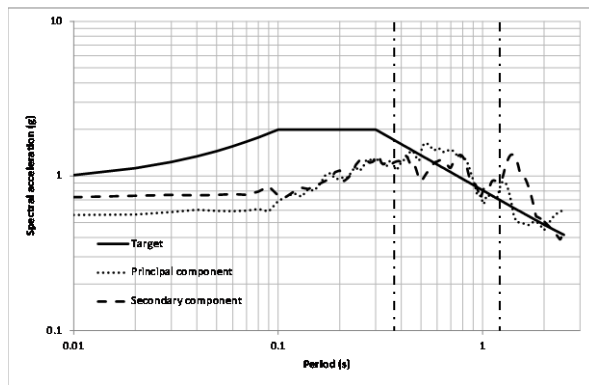
(b) 1999 Chichi



(c) 1999 Duzce



(d) 1978 Tabas



(e) 1999 Yarımcı

Figure 6-5 Scaled spectra of acceleration records used in test series A

Table 6-2 Seismic hazard parameters for earthquake record scaling

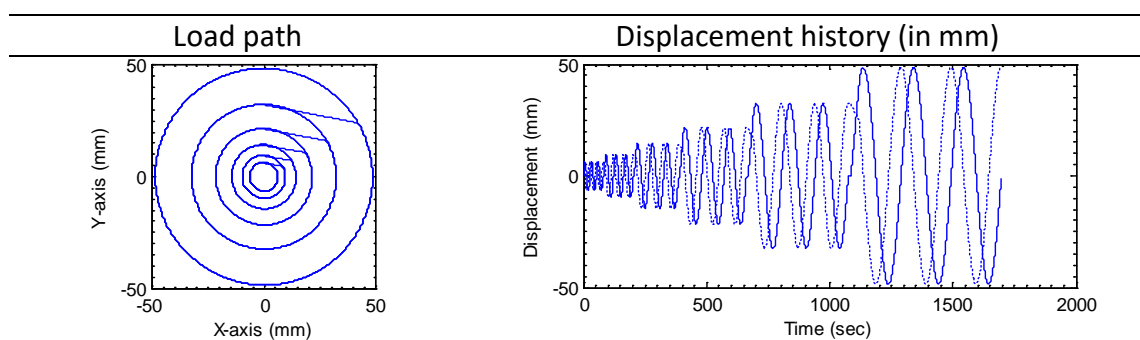
Site class	$Z$	$T_R$	$R$	$D$	$N(T_1, D)$	$S_P$	$PGA$
C	0.4	1/2000	1.7	8 km	Varies <sup>a</sup>	1	0.301

Note:  
Z: hazard factor



- $T_R$ : required annual probability of exceedance
- $R$ : return period factor
- $D$ : the shortest distance (in kilometres) from the site to a nearest fault
- $N(T_1, D)$ : near fault factor
- $T_1$ : fundamental period of structure
- $S_P$ : structural performance factor
- $PGA$ : peak ground acceleration
- <sup>a</sup>Varies depending on the fundamental period of the structure

The quasi-static tests in test series B consisted of six sets of cyclic deformations to the column for each of the four different loading patterns. These patterns were developed based on the ACI guidelines [75]. The sets of cyclic deformations were increasing in amplitudes as multiples of the yield displacement of the column, also known as the ductility factor ( $\mu$ ). Three cycles of loading were applied at each ductility level of  $\mu = \frac{2}{3}, 1, 1.5, 2.25, 3.5$  and  $5$ . Except for the linear pattern, where the rate of loading imposed was constant throughout the test, the rate of loading during the quasi-static tests varied. The actuators were limited to a 1.5 mm/s maximum rate of loading for all tests in test series B. The four loading patterns for the test series B are shown in Figure 6-6. The first column of this table indicates the load path for each pattern in both principal axes direction and the second column indicates the displacement time history in each axis. These patterns were (from top to bottom) linear, circular, diamond, and clover. Table 6-3 presents a summary of the different experiments considered in this study.



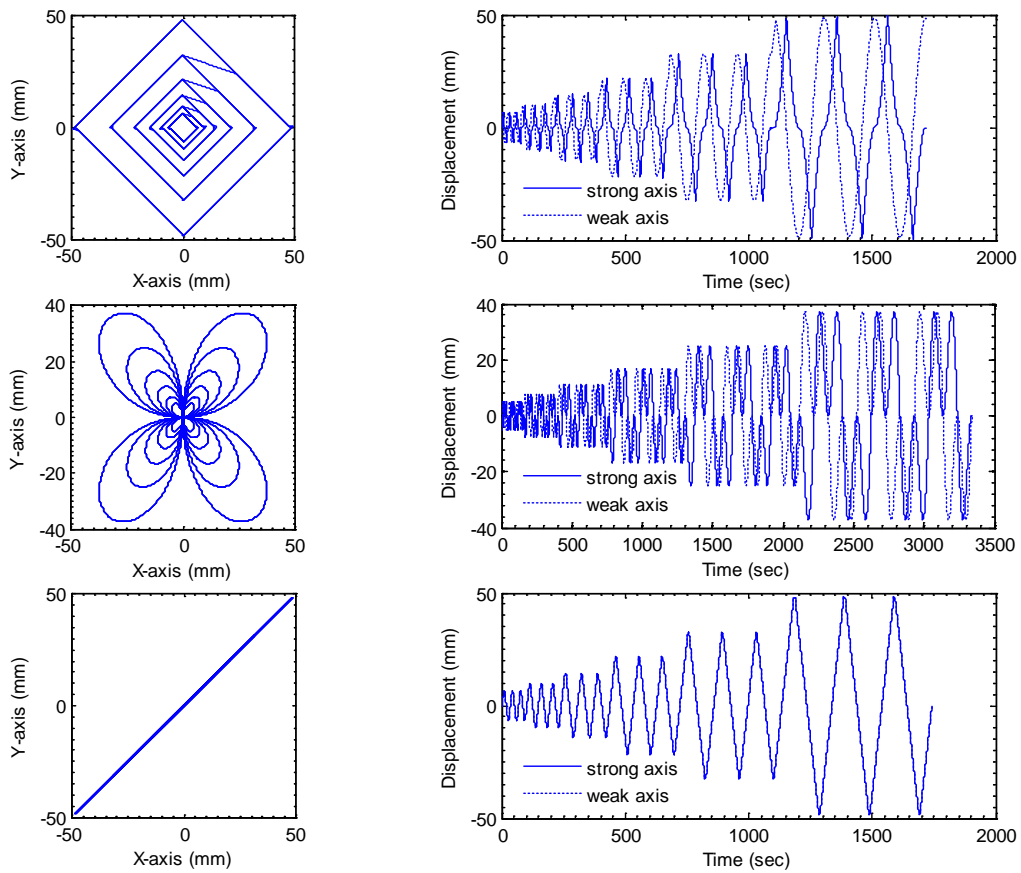


Figure 6-6 Quasi-static displacement patterns for test series B

Test series	Description	Displacement pattern			
A	Biaxial pseudodynamic test Scaled 1940 ElCentro	Pattern I	Pattern II	Pattern III	
	Biaxial pseudodynamic test Scaled 1999 Chi-Chi, Taiwan	Pattern I	Pattern II	Pattern III	
	Biaxial pseudodynamic test Scaled 1999 Duzce, Turkey	Pattern I	Pattern II	Pattern III	
	Biaxial pseudodynamic test Scaled 1987 Tabas 143, Iran	Pattern I	Pattern II	Pattern III	
	Biaxial pseudodynamic test Scaled 1999 Yarimca, Turkey	Pattern I	Pattern II	Pattern III	
B	Biaxial quasi-static test	Linear	Diamond	Circular	Clover

Table 6-3 Quasi-static displacement patterns for test series B

## 6.5. Experiment results and discussions

The results from test series B will be presented and discussed first. Beside the linear pattern, the quasi-static experiments subjected the structure to biaxial displacement patterns representative to the envelope of displacement time histories of a structure subjected to simultaneous earthquake excitation in two orthogonal directions. Both circular and diamond patterns represented the load paths that are 90° out-of-phase between the *X*- and *Y*-axis directions, i.e. increasing load in one direction accompanied decreasing one in the other direction.

Figure 6-7 presents individually the force-deformation response to the quasi-static cycles for each loading pattern, shown separately for each axis of loading. The force-deformation curves exhibited the expected flag-shaped behaviour of a self-centering system with hysteretic energy dissipation. The results showed that different loading patterns produced distinctly different strength and energy dissipation characteristics. It can be observed from Figure 6-7 that only the linear displacement pattern produced similar energy dissipations in the positive and negative directions for both axes of loading. The other patterns dissipated more energy in one direction than the other. This can be explained by the fact that the specimen was essentially loaded about a single bending axis under the linear displacement pattern, while the resultant bending axis was constantly changing in the other loading patterns. This behaviour was coupled with greater EMD extensions due to the different load paths, extra bending actions and consequently misaligned compressive load on returning cycles, leading to greater opportunities for dissipator buckling and hence accumulated plastic deformations in the displacement patterns other than the linear pattern, similar in concept to the

“ratcheting” phenomenon. Table 6-4 details the amount of energy dissipation in the different tests, in the different directions expressed as equivalent viscous damping.

Figure 6-8 presents the strength envelopes developed from the quasi-static tests. The figure shows that displacement paths indeed had a significant effect on the ultimate strength. In general, the diamond and circular patterns shows the lowest strength compared to the linear and clover patterns except in the positive  $X$ -axis direction. This was an expected behaviour considering the case when  $X$ -axis direction displacement was increased from zero to a peak value using the diamond displacement and circular patterns, the corresponding  $Y$ -axis displacement would decrease from the peak value to zero. This means there was less axial force, and consequently smaller restoring force in the column compared to the linear and clover pattern where displacements in both axes increased or decreased simultaneously resulting in larger axial force and hence larger restoring force in the column.

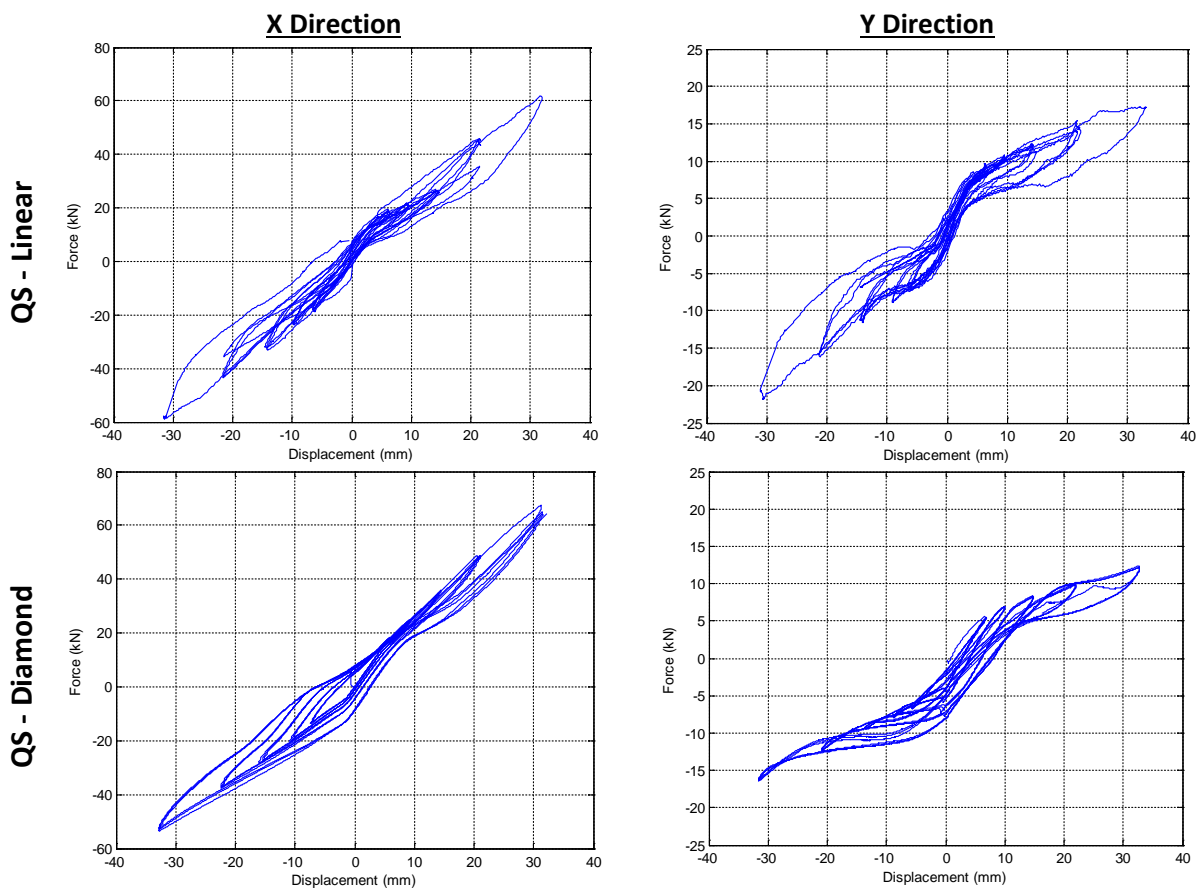
Figure 6-9 shows the variations of PT forces as a function of  $X$ - and  $Y$ -axis displacement directions under the different displacement patterns.

Figure 6-8 and Figure 6-9 reveal some interesting observations. The axial forces in the negative directions for the linear case on both axes were unusually high. This would explain why the strength in the negative  $X$ - and  $Y$ -axis directions were larger than in the positive directions. However, on the third cycle into +21 mm drift, there was an apparent stiffening in the positive  $X$ -direction which continued to the subsequent cycles. Although unexpected, the diamond pattern achieved higher strength than the linear pattern in the positive  $X$ -direction. This was probably due to the total axial force in this direction was slightly larger for the diamond pattern than that for the linear pattern. In the clover pattern, if the drift level considered was similar, the pattern always resulted in the largest strength, even compared to

the linear case. A closer inspection on Figure 6-9 reveals that for similar drift level, the total axial force in the clover pattern was the largest in both axes and directions, even compared to the negative directions for the linear case where the total axial force was unusually high. This was because for the same drift level in one axis, displacement in the other axis was always larger in the clover pattern than in the liner pattern (which was identical in both axes), resulting in a larger strain in the PT bars and larger increase in the axial force, in turn giving rise to larger strength in the column.

Test	X direction			Y direction			Combined
	Positive	Negative	Average	Positive	Negative	Average	
QS - Linear	6	9	7.7	3	3.6	3.3	11
QS - Diamond	1.5	3.3	2.8	3.3	1.1	2.7	7.4
QS - Clover	6.2	6.8	6.5	4.4	3.8	4.2	12
QS - Circular	2.2	6.3	5	4.4	3.3	3.8	10.7

Table 6-4 Equivalent viscous damping (%)



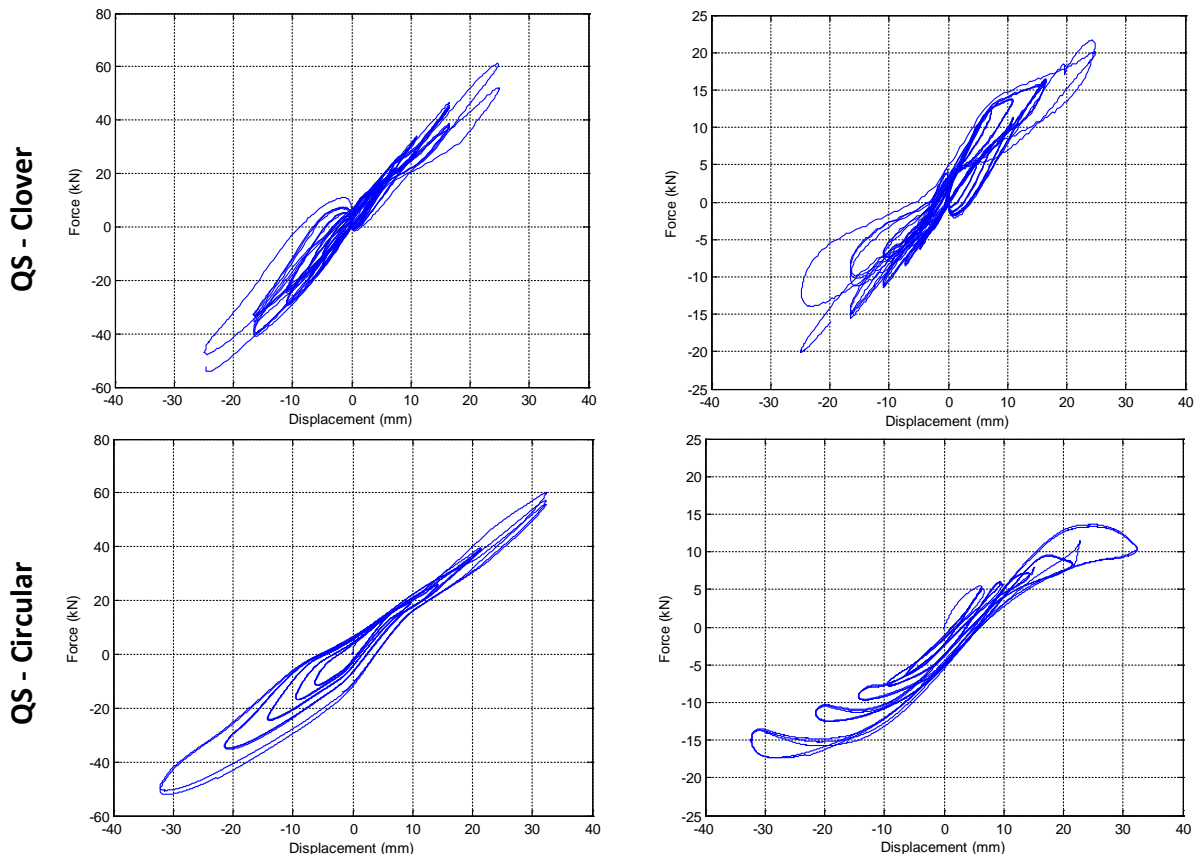


Figure 6-7 Quasi-static force-displacement response of the column under different loading patterns

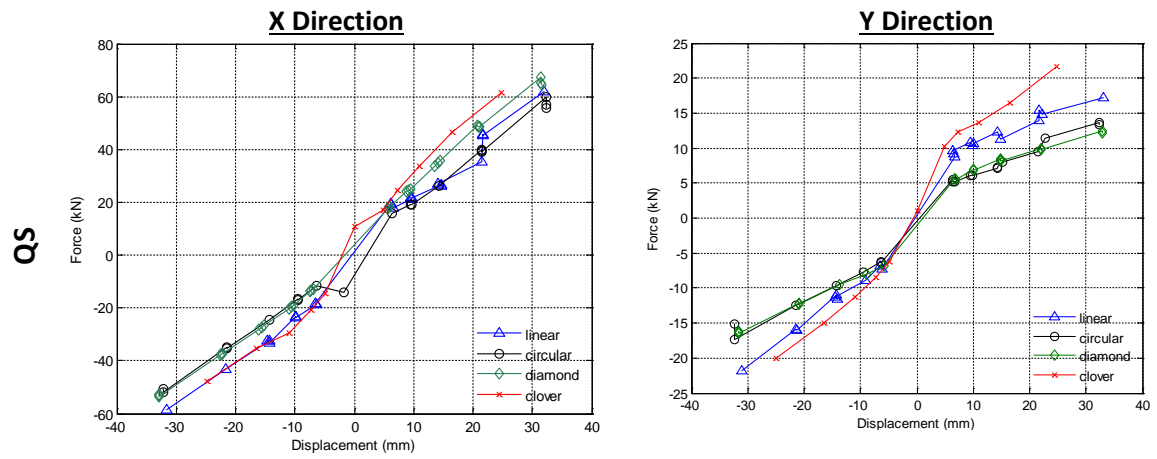


Figure 6-8 Quasi-static force-displacement envelope of the column under different loading patterns

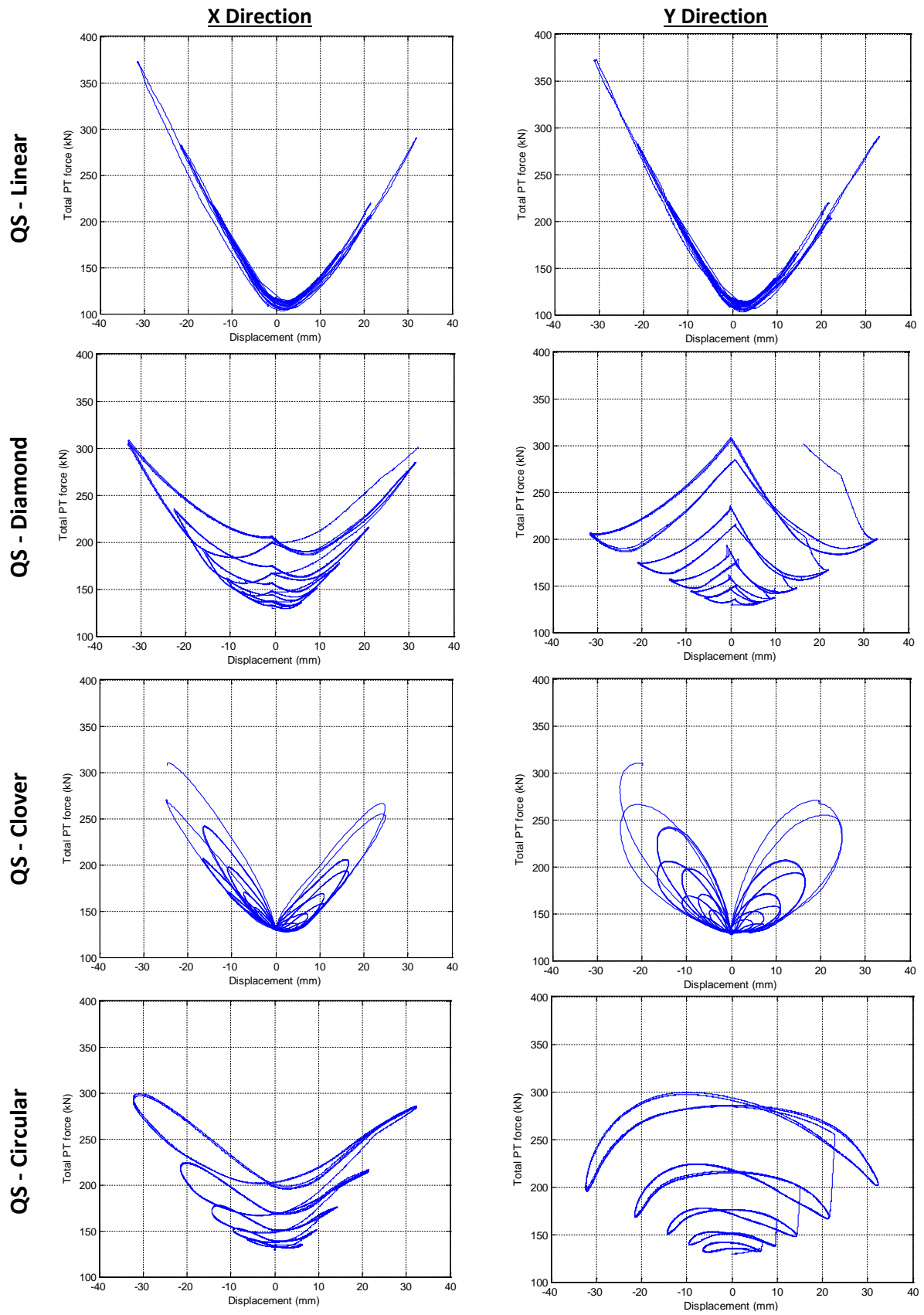
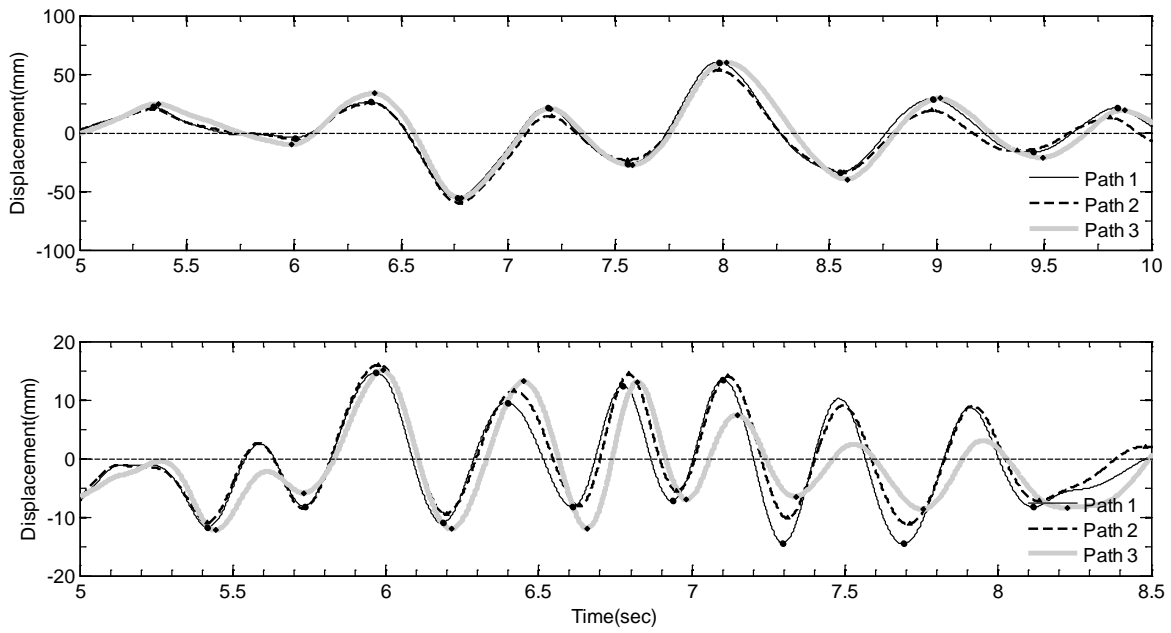
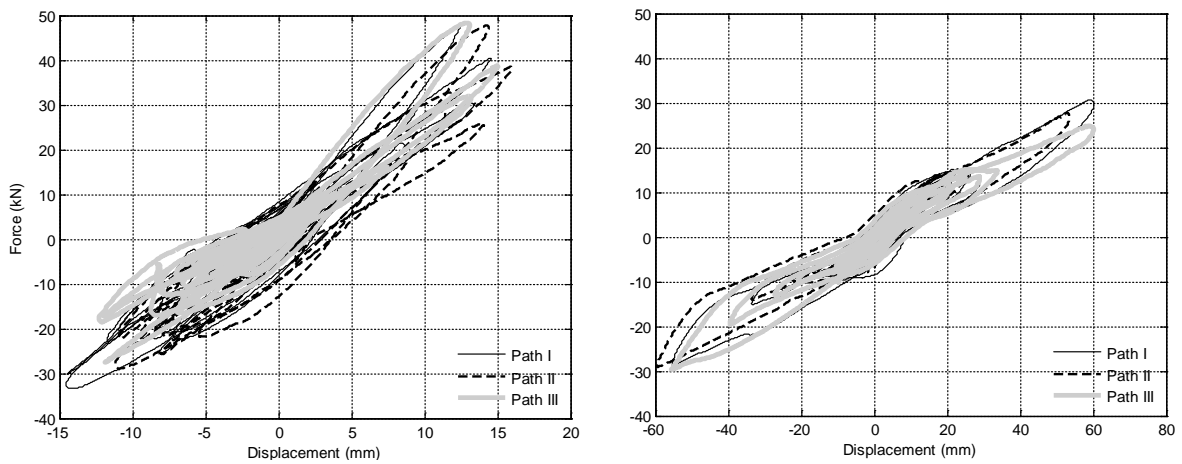


Figure 6-9 PT force-displacement history under different loading patterns

Displacement time histories of the column obtained from the hybrid simulations in test series B are shown Figure 6-10 to Figure 6-14. In each figure, several displacement amplitudes are indicated in a), while force-displacement relationships are indicated in b). Despite the similarities in the time history profiles for each earthquake record, there are phase and amplitude differences resulting from the differences in the displacement tracking strategies. It should be noted that the classical flag-shaped hysteretic curves did not develop, and that appreciable residual drifts were present. This was in part caused by a large crack at one corner of the column and therefore sliding, opening and closing of this crack dominated the hysteretic behaviour. The figures also highlighted poor performance of the EMD due to buckling and slippage. Figure 6-15 shows a buckled EMD during and after a test. There were two probable causes that contributed to the failure of the EMD. The first was bidirectional loading at the column led to large bending actions on the EMD. As the EMD motions were no longer predominantly axial, on compression cycles following tension cycles, concentrated rotation developed at the junctions where the anti-buckling grouted sleeve terminated. This resulted in significant eccentricity for the axial force which caused the EMD to buckle. Concentrated rotation occurred around the end of the milled-down portion as shown in Figure 6-15b. Although it has been shown through component testing and uniaxial cyclic assemblage test that the EMD yielded dependably in tension and compression [86], it was evident that the full performance was not attainable under bidirectional earthquake. It further highlights the importance of considering the effect of multidirectional load on such system.

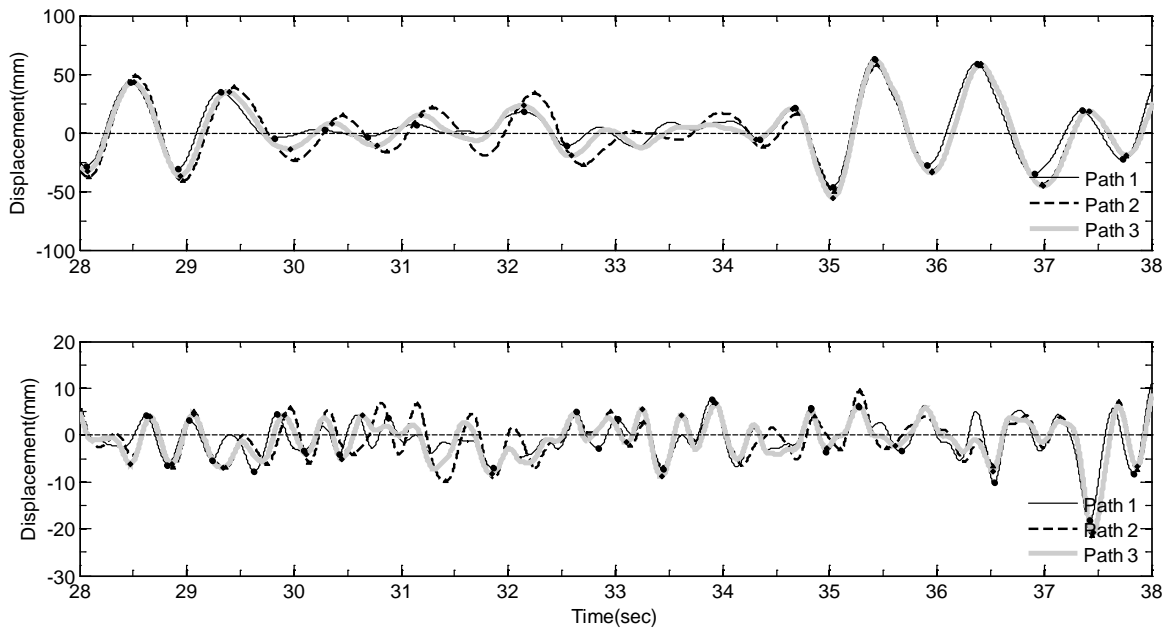


a) displacement time history, top: weak axis and bottom: strong axis

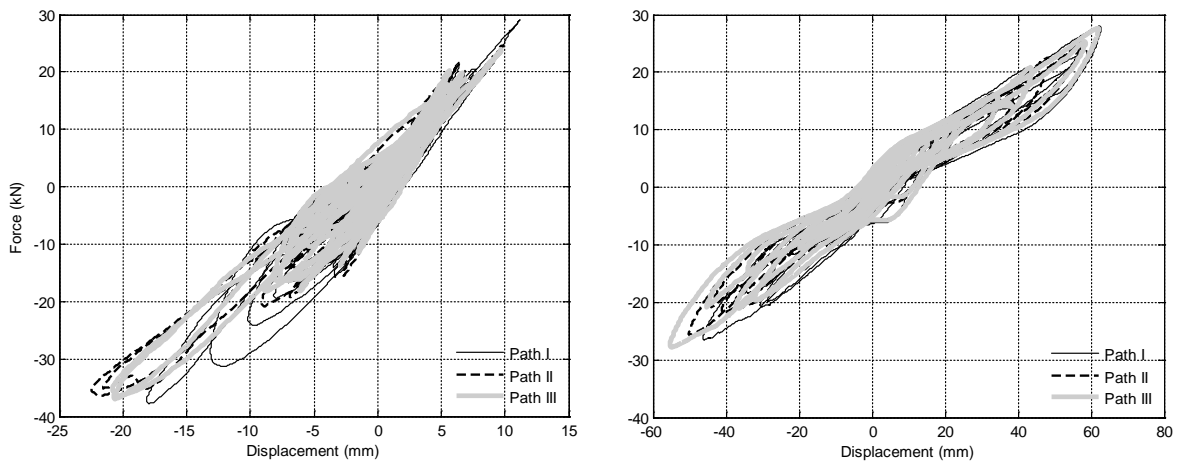


b) force-displacement relationship, left: strong axis and right: strong axis

Figure 6-10 hybrid simulation result using 1979 El Centro earthquake record

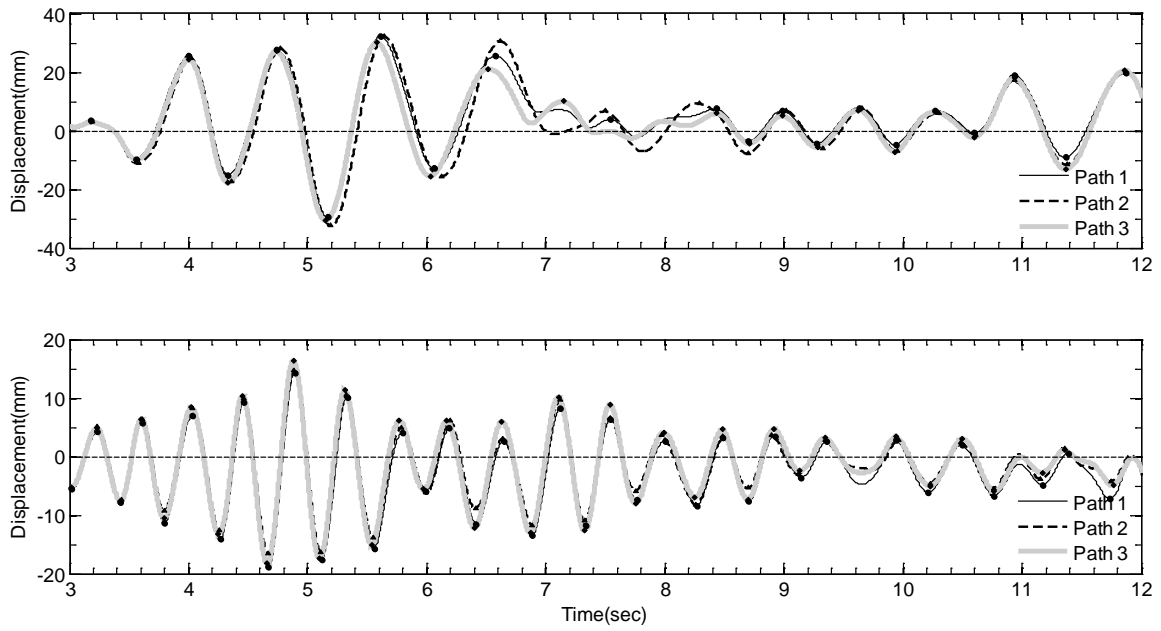


a) displacement time history, top: weak axis and bottom: strong axis

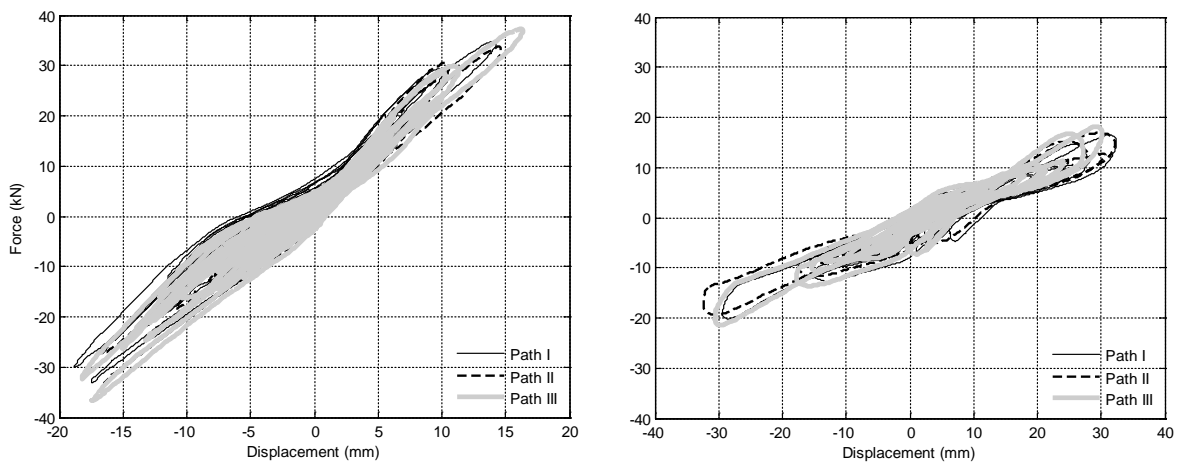


b) force-displacement relationship, left: strong axis and right: strong axis

Figure 6-11 hybrid simulation result using 1999 Chichi earthquake record

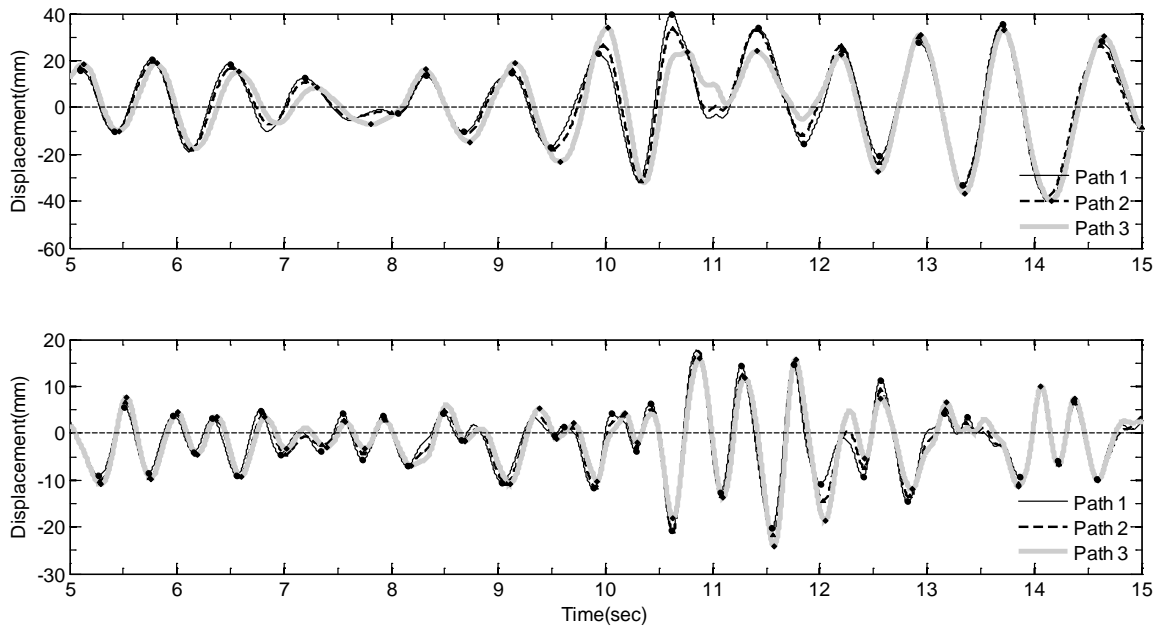


a) displacement time history, top: weak axis and bottom: strong axis

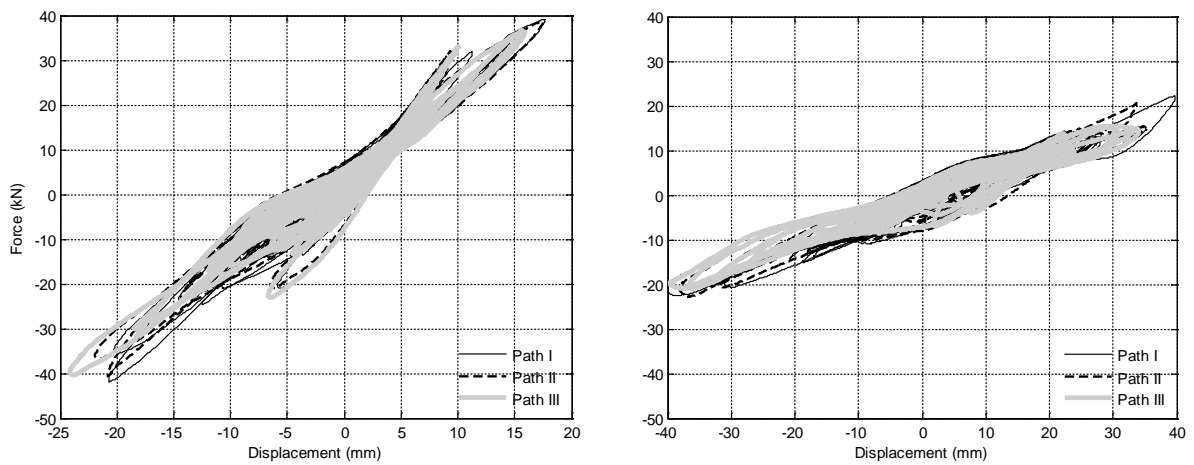


b) force-displacement relationship, left: strong axis and right: strong axis

Figure 6-12 hybrid simulation result using 1999 Duzce earthquake record

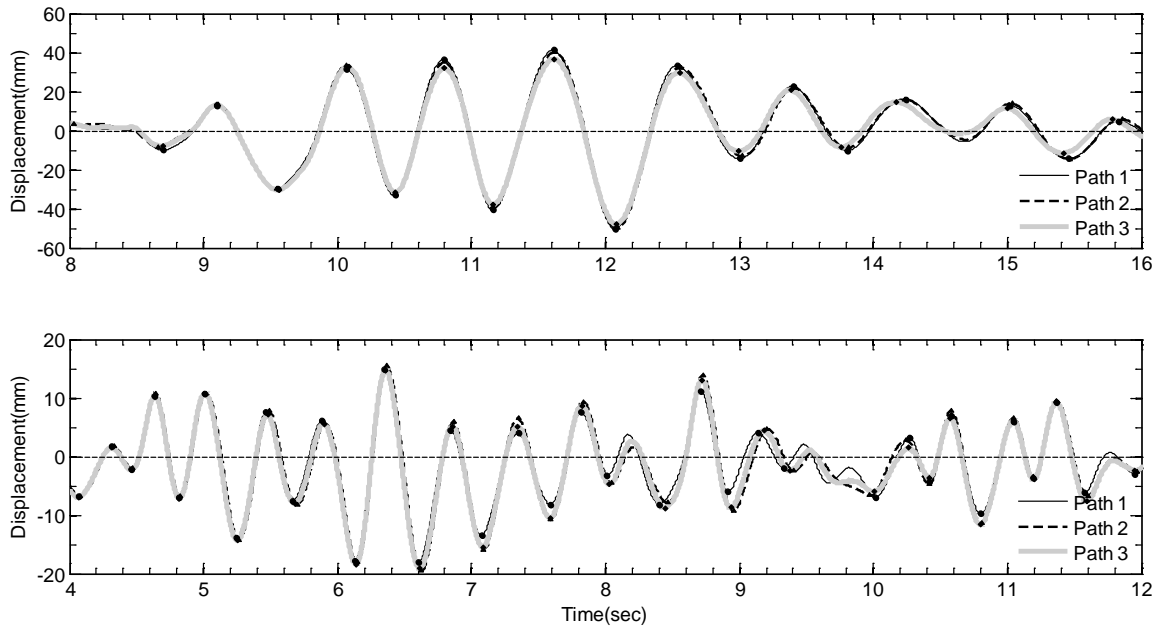


a) displacement time history, top: weak axis and bottom: strong axis

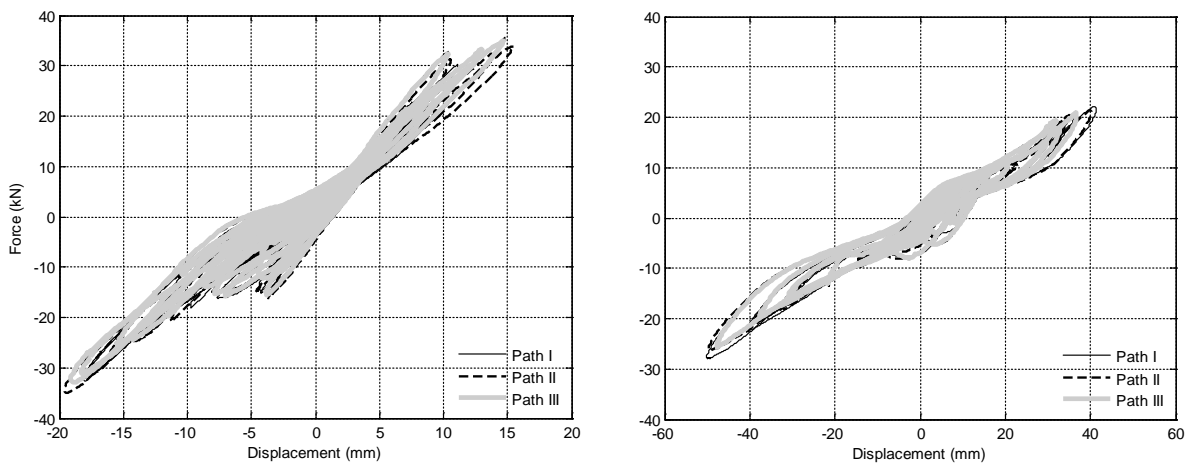


b) force-displacement relationship, left: strong axis and right: strong axis

Figure 6-13 hybrid simulation result using 1978 Tabas earthquake record



a) displacement time history, top: weak axis and bottom: strong axis

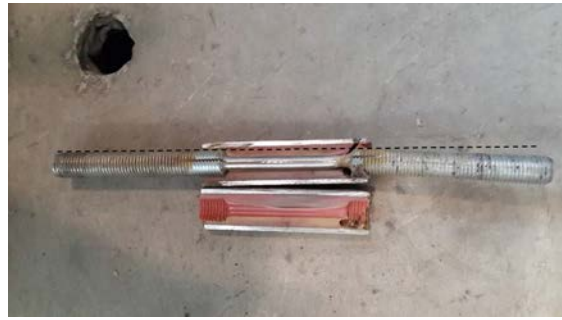


b) force-displacement relationship, left: strong axis and right: strong axis

Figure 6-14 hybrid simulation result using 1999 Yarımcı earthquake record



a) during experiment



b) anti-buckling cage splitted open

Figure 6-15 Buckled EMD

In the absence of reference results from full dynamic tests (e.g. shake table test), or idealised numerical simulations, the tracking strategy Path III can be thought as the ideal solution considering the shortest path is the most plausible. The amplitudes attained by the tracking strategies Path I and Path II can then be quantified in term of their differences relative to Path III. Mathematically, these amplitude differences can be represented as a normalised difference with respect to the amplitudes in Path III.

Table 6-5 provides a summary of the maximum displacements attained during each experiment using Path III, and the normalised differences with that attained from Path I and Path II experiments.

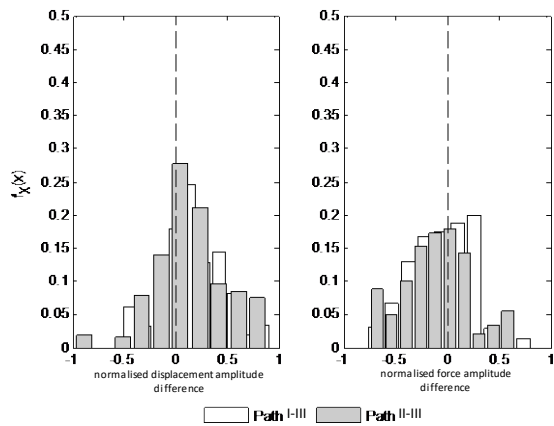
Earthquake record	Path III maximum displacement (mm)		Path I normalised difference (%)		Path II normalised difference (%)	
	Y	X	Y	X	Y	X
1979 Imperial Valley	60	15	1.7	-2.7	-1.1	6.5
1999 Chichi	62	21	1.3	-1.2	-5.3	7.9
1999 Duzce	31	18	-4	3.1	5.9	-5.4
1978 Tabas	40	24	1.2	-1.6	-4.2	-5.2
1999 Yarımcı	48	19	4.9	-5.3	4.1	2.5

Table 6-5 Normalised maximum displacement amplitude difference (%)

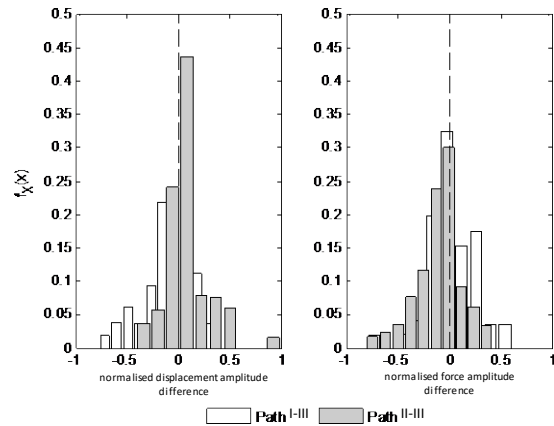
Table 6-5 shows that larger amplitudes were attained at least in one axis of the column in experiments using Path I or Path II. The largest difference was 8% from the 1999 Chichi earthquake experiment. On average, the results in Table 6-5 suggests that the increases in amplitudes were larger due to Path II compared to Path I. This can be explained by Figure 6-4 that shows that Path II deflects the column in the longer axis ( $X$ -axis direction) first, then the shorter axis. Using monolithic column analogy, Bousias et al. [81] demonstrated that in the nonlinear range, there is a phase lag between force and deflection resultants. Due to this lag, even when the displacement resultant was parallel with the  $X$ - direction, the restoring force would have a component in the  $Y$ -axis (weak axis) direction. This transverse force further softened the  $Y$ -axis even before the column moved along that axis. This mechanism also occurred during Path I but the transverse force introduced into the  $X$ -axis direction was smaller since the  $Y$ -axis was more flexible. Hence the resulting displacement amplitude increases were larger in Path II than Path I. Although Table 6-5 also indicates that both Path I and II could result in lower displacement amplitudes compared to Path III and the fact that the increase in displacement amplitudes was relatively negligible, it should be noted that Table 6-5 only shows the differences at the maximum amplitudes for each earthquake record. A better assessment would be to collate a larger number of the normalised amplitude differences for each earthquake record. The difference in the measured restoring forces can also be quantified in a similar way.

Collating the normalised amplitude differences for displacement and forces at each cycle in the earthquake time history allowed defining a probability density function (PDF). Figure 6-16 shows the PDF collated for each earthquake record for the differences between Path I and III, and the differences between Path II and Path III in term of displacement and force. In each

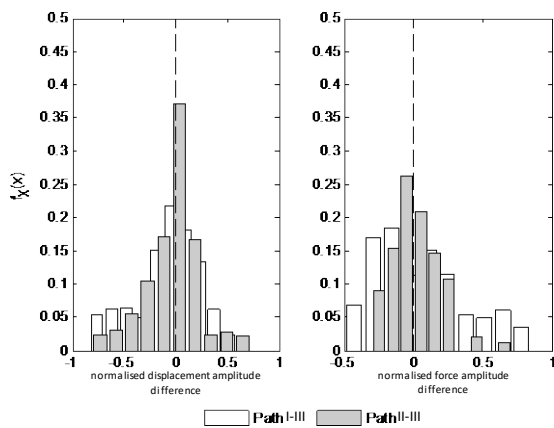
plot, a dashed line parallel with the vertical axis is drawn at zero. If different displacement paths, on average, produced the same displacement and force amplitudes, this would be indicated by the peak (median) of the density function coinciding with this line.



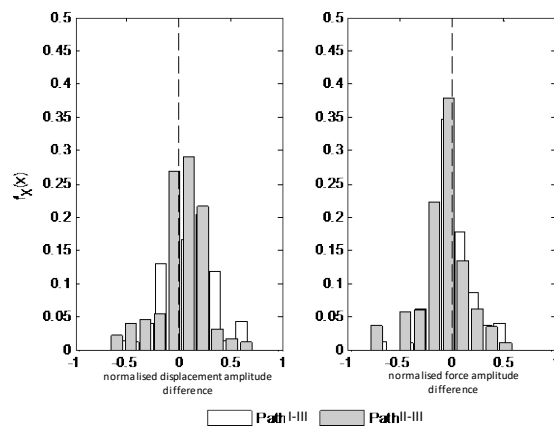
a) 1979 El Centro



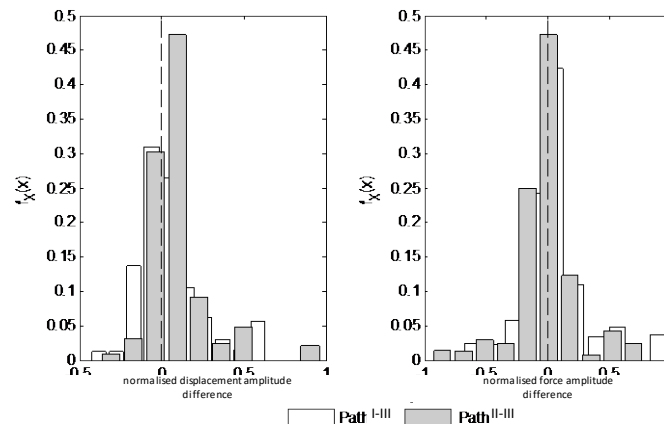
b) 1999 Chichi



c) 1999 Duzce



d) 1978 Tabas



e) 1999 Yarımcı

Figure 6-16 Distribution of normalised displacement and force amplitude differences from the hybrid simulations

Figure 6-16 shows that on average, the median of both the normalise displacement and force differences lay between 10 to 12%. This means the different displacement tracking strategies yield relatively good accuracy compared to the conventional path (Path III). It is interesting to observe from Figure 6-16 that most of the median values of the displacement amplitude differences are positives, and most of the median values of the force amplitude differences are negatives. During Path I or Path II experiments the column deflected a greater distance compared to Path III, providing greater opportunity for increased plastic deformation in the column. Consequently, it is likely that the column developed lower restoring forces which in turn led to these larger displacement amplitudes.

Figure 6-17 shows the biaxial bending moment trajectory developed in the column for each displacement path. On the trajectories, the instant of decompression are noted from the point where there is a sudden decrease in stiffness, creating interaction surface that separates the response of the column between rocking and non-rocking phase.

There is no significance difference observed in the resulting biaxial moment trajectory and the pair of decompression moments from the interaction surfaces obtained through the

different displacement tracking strategies. The negligible differences could be attributed to several causes, such as small differences in the initial post-tensioning force. Up to decompression, the response of a rocking structure is essentially linear elastic and identical to the response of a monolithic structure with equivalent sectional properties and geometry before reaching its yield limit state, known as the Monolithic Beam Analogy [88]. Therefore, the different displacement paths would have minimum effect in the non-rocking phase of the column response, and this was demonstrated by the resulting interaction surfaces. The figures indicated that the uniaxial decompression moment about the Y-axis was roughly 20 kNm, while the uniaxial decompression moment about the X-axis was roughly 10 kNm.

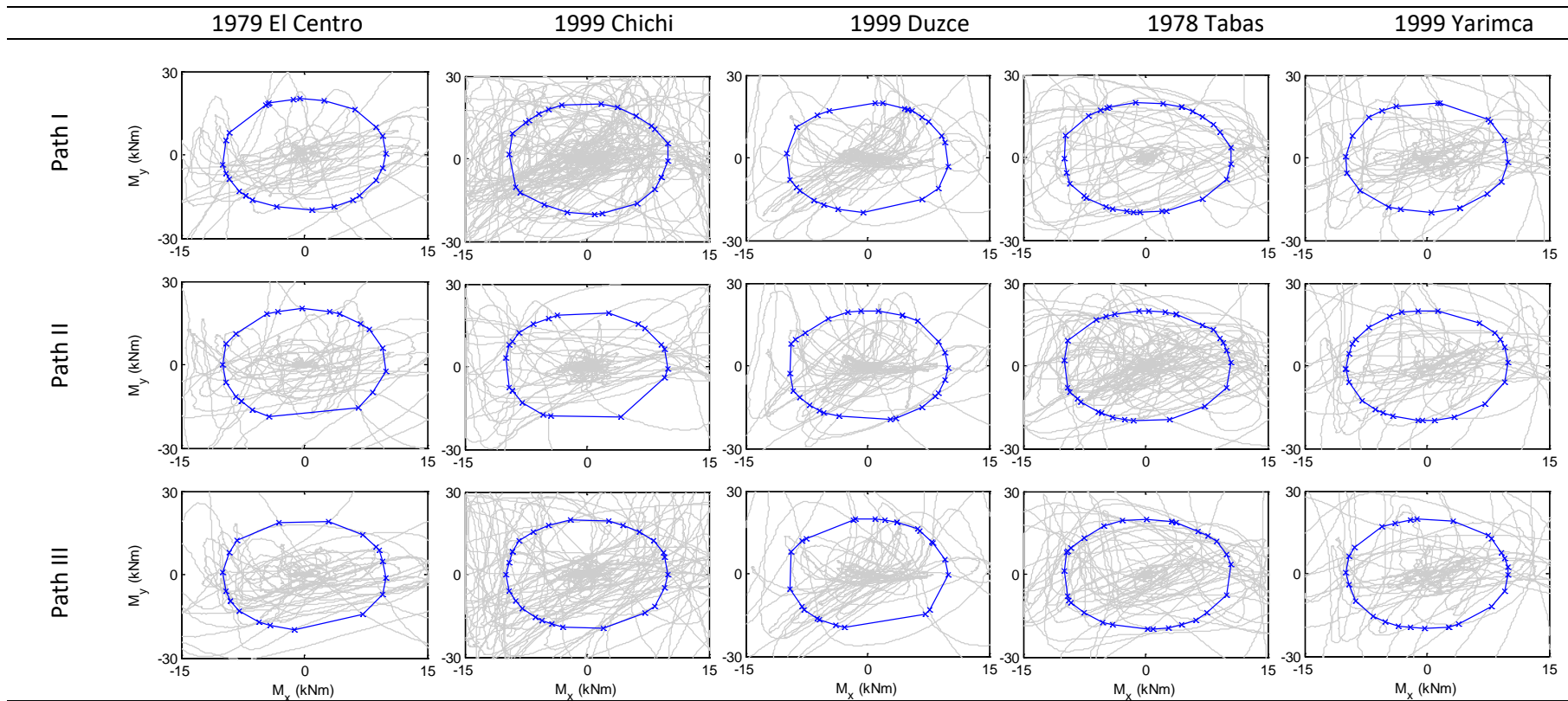
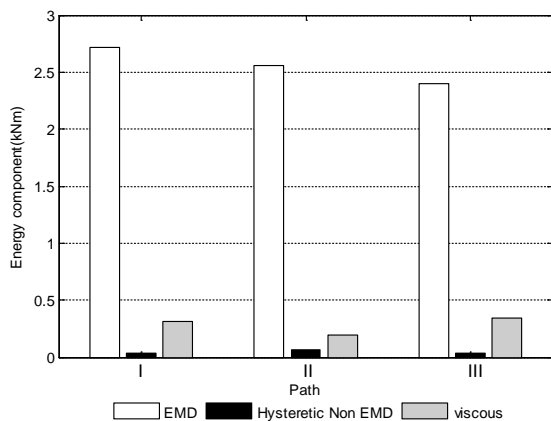
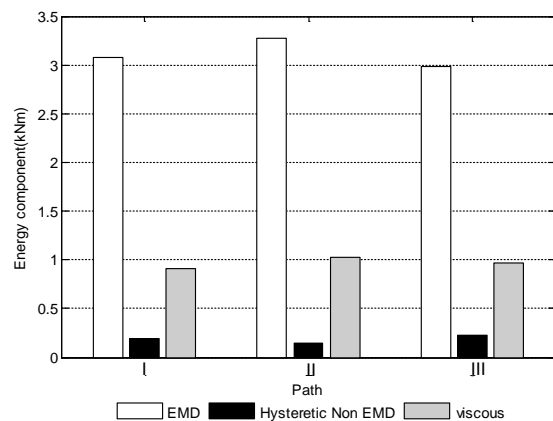


Figure 6-17 Biaxial moment trajectory and interaction surface at decompression

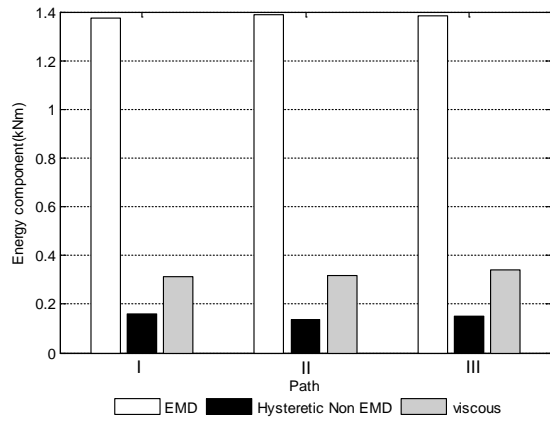
Separating the response of the column between rocking and non-rocking phase leads, it is of interest to distinguish the contribution of each component of the column response in dissipating the input energy from the earthquake excitation. Figure 6-18 shows the amount of dissipated energy by different mechanisms in the column relative to the input energy for each displacement tracking strategy. Note that the input energy will be different across the tracking strategies due to the differences in the resulting displacement histories. With the aid of the interaction curves derived earlier, hysteretic energy dissipations can be separated between those resulting from yielding of the EMD and other hysteretic mechanisms prior to decompression, such as sliding, opening and closing of concrete cracks, slip and friction, among others. A typical 5% critical damping ratio recognised by most building codes was specified for viscous damping in this study.



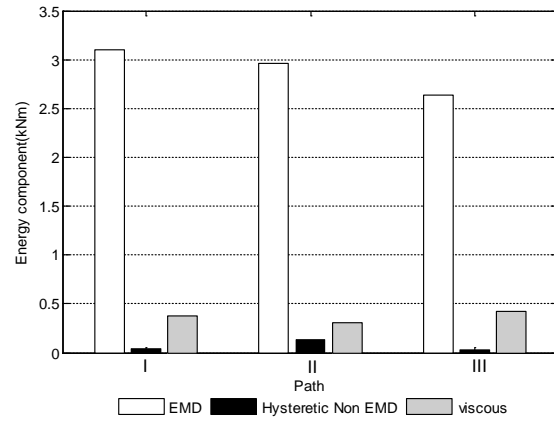
a) 1979 El Centro



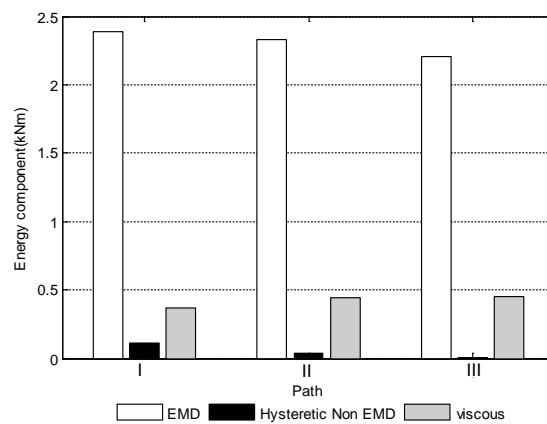
b) 1999 Chichi



c) 1999 Duzce



d) 1978 Tabas



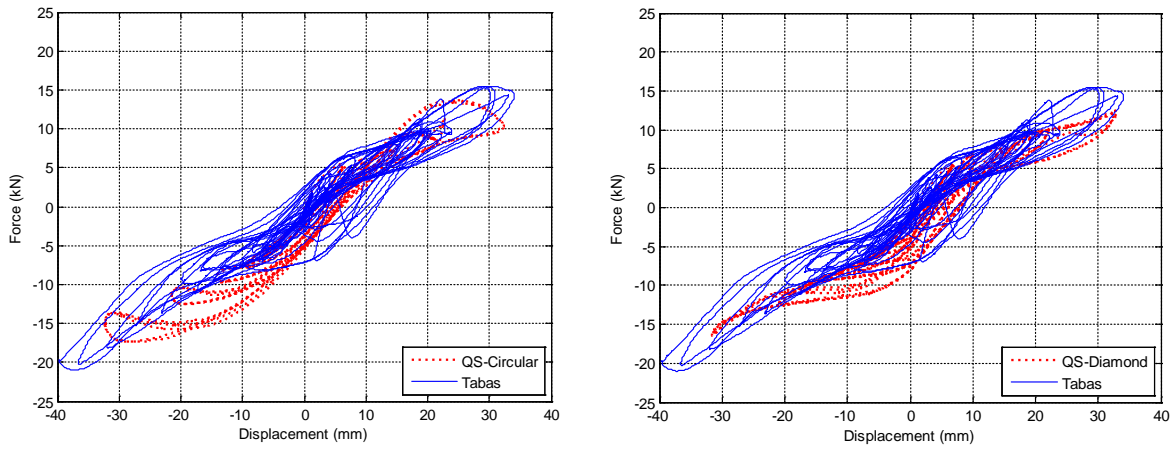
e) 1999 Yarmuca

Figure 6-18 Component of dissipated energy during hybrid simulations

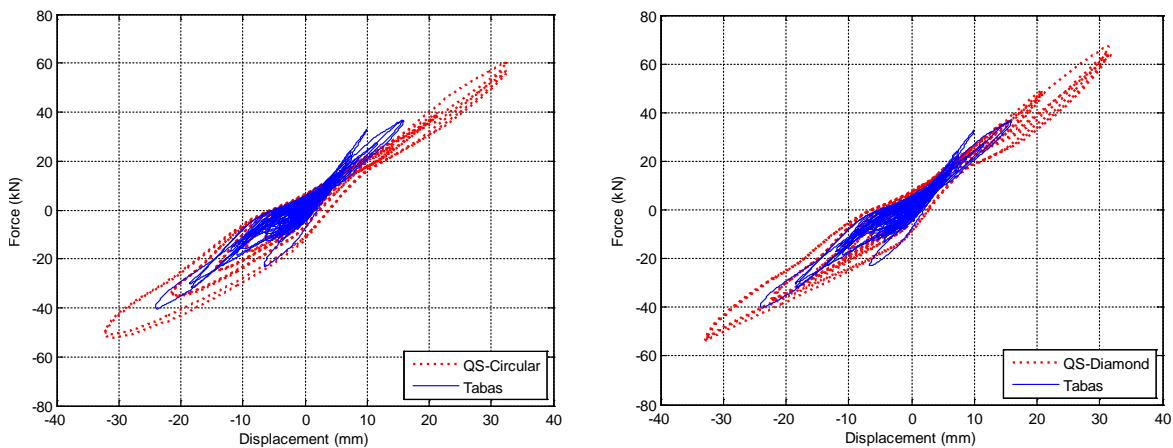
Figure 6-18 reveals that the amount of energy dissipations from EMD actions during Path III experiments was consistently less than the other two paths. Since during both Path I and Path II experiments the EMD experienced greater elongation and without so much loss of strength, they dissipated more energy. This is also consistent with the fact that the relative energy dissipated by viscous damping mechanism in Path III was consistently larger than those from the other two displacement tracking strategies, considering in Path I and Path II experiments the resulting effective stiffnesses of the column were lower, leading to smaller velocity.

During hybrid simulations, the column experienced more realistic load protocols compared to the quasi-static tests, so it is of interest to compare the hysteretic responses from both

methods. Figure 6-19 shows the hysteretic responses from the hybrid simulation using Tabas earthquake record compared to the hysteretic responses obtained through the quasi-static tests using circular and diamond patterns.



a) weak axis response



b) strong axis response

Figure 6-19 Comparison of hysteretic responses between experiments using quasi-static and hybrid simulation methods

It can be seen that unlike the responses from the quasi-static tests, the response envelopes from the hybrid simulation are asymmetrical, especially about the strong axis. This is a direct result of different load paths and it highlights the history-dependency of the column response. The weak axis responses indicate that the column experienced more pinching behaviour during the quasi-static tests, while more energy dissipations occurred during the

hybrid simulations as indicated by the “fatter” hysteretic curves. Although quasi-static tests are supposed to give the worst envelope of hysteretic behaviours of a structure such that for different loading histories, the responses should lie within the envelope, the research demonstrates that even for a very simple system, the assumption may not be valid. This phenomenon cannot be captured during the quasi-static tests since the load protocol is predefined.

## **6.6. Summary**

This chapter presents the results of quasi-static tests and hybrid simulations considering three-dimensional rocking response of an unbonded, post-tensioned RC column under bidirectional earthquake excitations. The main objective of the experiments was to investigate the effect of different tracking strategies when displacements were applied along the two principal axis directions of the column to the resulting energy dissipations.

Two set of experiments were conducted. In the bidirectional quasi-static experiments series, it was found that different bidirectional displacement patterns produced appreciably different amount of dissipated energy and strength envelopes. Similarly, hybrid simulations with different displacement tracking strategies demonstrated that applying displacements using the “staggering” pattern resulted in larger damage accumulation. These conclusions are drawn based on observing the larger displacement amplitudes, lower restoring forces, as well as larger hysteretic energy dissipations in experiments using the “staggering” pattern than those using the direct pattern.



# Chapter 7

## Hybrid simulation with substructuring on concrete wall

---

### 7.1. Introduction

Hybrid simulation with substructuring method allows only critical or not well understood parts of a structure to be physically tested while simulating other parts numerically. The loading history for the physical substructure in a hybrid simulation with substructuring is determined as the test progress, through solving the equation of motion utilising measured restoring forces from the physical substructure.

It is important that both numerical and physical substructures are simulated accurately. This entails accurate reproduction of loading and feedback from the physical substructure and accurate response simulation from the numerical substructure. Challenges arise when the physical substructure is not representative to the prototype structure, either due to modelling difficulties or experimental errors. Accurate modelling of the numerical substructure is thus important to ensure that the interaction between the two substructures results in a representative behaviour of the complete structure.

The experimental study in this chapter examines the effect of utilising physical substructure with incompatible behaviour. The aim of the tests is to test the hybrid simulation with substructuring ability to accurately reproduce the response of dissimilar specimen from the prototype using current best practices. The experimental study included three tests, namely 1) quasi-static cyclic testing to a predefined load pattern on a complete specimen, 2) hybrid

simulation on a complete specimen identically designed to the first test and 3) hybrid simulation where the complete specimen identically designed to the first and second test were divided into numerical and physical substructures.

The selected prototype structure was a flexure-dominant RC (reinforced concrete) wall with an aspect ratio of 2, detailed in accordance to the proposed amendments for minimum reinforcement detailing requirement for ductile wall in NZS 3101:2006 [89]. During the tests in 1) and 2) the walls were expected to exhibit flexure-dominant behaviour. The physical substructure used in experiment 3) was classified as a squat wall with an aspect ratio less than 2 which tend to fail in a mixed flexure-shear mode [2].

The results and discussions presented focuses on the comparison between the hybrid simulation without and with substructuring results including global response such as the force deformation relationship as well as local response such as the damage pattern.

## **7.2. Methodology**

The experimental project consisted of three different tests:

- Quasi-static cyclic test to a predefined loading pattern
- hybrid simulation using a ground motion record
- Hybrid test using a ground motion record

### **7.2.1. Experimental specimen**

Table 7-1 provides a summary of the precast RC walls' design and detailing used in the experimental project.

Shear span ratio	Axial load ratio	Material properties		Vertical reinforcement ratio (%)			Horizontal reinforcement ratio (%)	End stirrups (mm)
		$f'_c$ (MPa)	$f_y$ (MPa)	End region	Web region	Total		
2	3.5%	30	300	1.00	0.47	0.67	0.25	D6@60

Table 7-1 Summary of wall detailing

The dimensions of the walls were selected to represent 50% scale of typical RC walls in multi-storey buildings with a shear span ratio of 2. Table 7-2 provides dimension of the wall specimen for each test. The specimen for the hybrid simulation with substructuring (M7) had half the height of the others since it was designated as a physical substructure only.

Wall	Dimensions			Test type
	Height (mm)	Length (mm)	Thickness (mm)	
M5	2800	1400	150	Quasi-static
M6	2800	1400	150	Hybrid without substructuring
M7	1400	1400	150	Hybrid with substructuring

Table 7-2 Summary of wall specimen for each test

Figure 7-1a shows a schematic drawing of the wall specimen used in the quasi-static (M5) and the hybrid simulation without substructuring (M6), while Figure 7-1b shows a schematic drawing of the wall specimen used in the hybrid simulation with substructuring (M7).

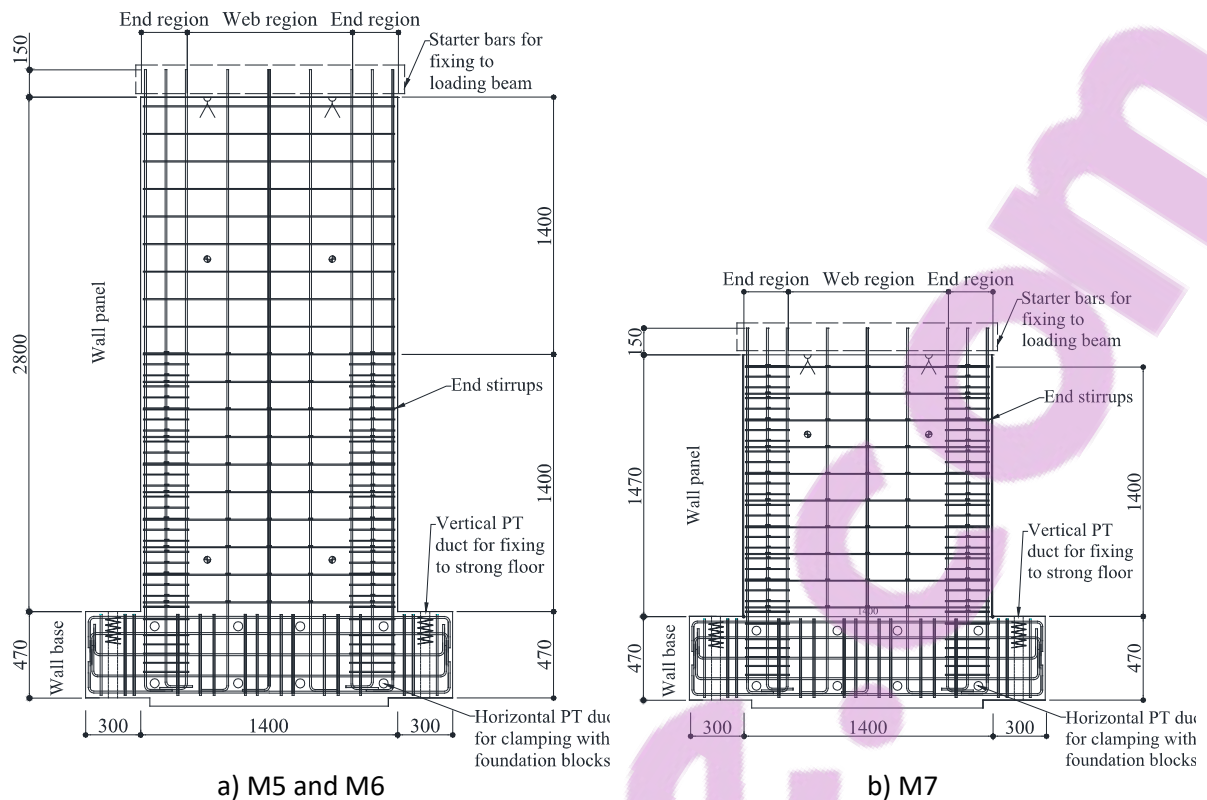


Figure 7-1 Schematic drawing of the wall specimens

Flexural-dominated wall specimens were selected as it was aligned with an interesting phenomenon of strain concentration that was observed during the 2011 Christchurch earthquakes. This research intended to see if the same phenomenon could be replicated using dissimilar specimen utilising hybrid simulation without substructuring method.

Detailed engineering drawings of the walls as well as a selection of photographs taken during the wall constructions can be found in Appendix E.

### 7.2.2. Loading protocol

The quasi-static test used a predefined displacement cycles identical to the one shown in Figure 5-4. The drift increments were 0.2%, 0.25%, 0.35%, 0.5%, 0.75%, 1.0%, 1.5%, 2.0%, and 2.5% with three cycles of loading for each amplitude.

Initially, the hybrid simulation on wall M6 intended to use the Christchurch Hospital (CHHC) ground motion during the 2011 Christchurch earthquake. Preliminary analysis was carried out using the quasi-static test result to select an appropriate scale factor for the earthquake record for wall M6 to attain maximum drift amplitude similar to that in the quasi-static test. However, during the actual hybrid simulation the record had to be scaled down since the specimen response was unexpectedly large. The resulting synthetic ground motion is shown in Figure 7-2 together with the original record for comparison.

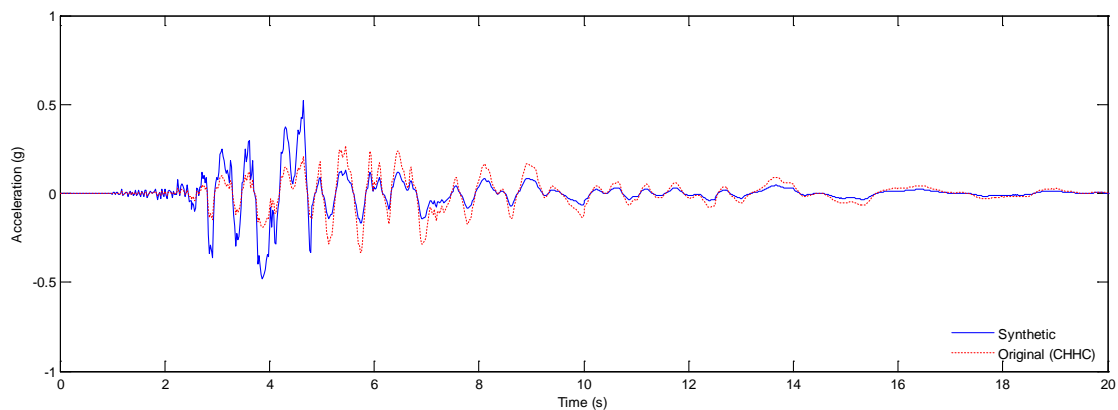


Figure 7-2 Comparison between the original (CHHC) and synthetic earthquake record

Figure 7-3 shows the 5% damped elastic response spectra of the synthetic and the original ground motion record. The elastic design spectra for Class D soil according to NZS1170.5 [76] is also shown in Figure 7-3 for comparison. The dashed line at 0.14 s marks the fundamental period of wall M6.

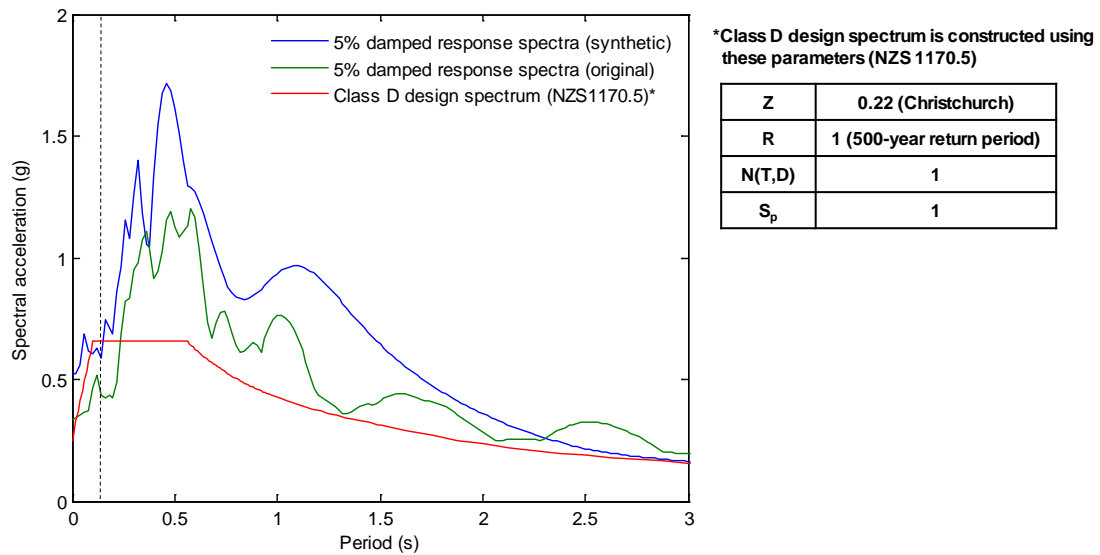


Figure 7-3 5% damped elastic response spectra for input ground motion

Since the objective of the experimental project is to replicate the behaviour of the wall M6 through testing dissimilar specimen (M7), the same synthetic record was used as the input ground motion for the hybrid simulation with substructuring.

### 7.2.3. Discrete parameters for the hybrid simulation with and without substructuring

Discrete parameter definitions were required for the hybrid simulation without and with substructuring. Figure 7-4 shows an idealised MDOF representation of the hybrid simulation specimen with horizontal translation  $u$  and rotational DOF  $\theta$ .

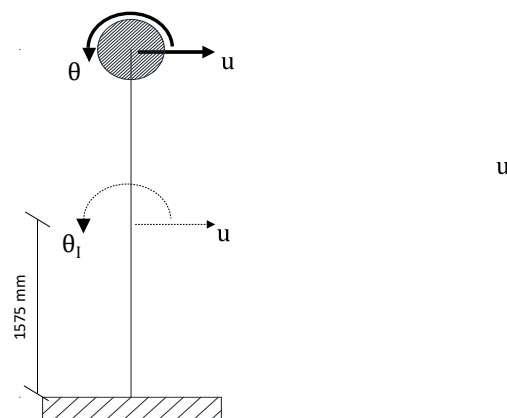


Figure 7-4 Idealised MDOF representation of the hybrid simulation without substructuring specimen

The resulting equation of motion is formulated as

$$M \begin{bmatrix} \ddot{u} \\ \ddot{\theta} \end{bmatrix} + C \begin{bmatrix} \dot{u} \\ \dot{\theta} \end{bmatrix} + \begin{bmatrix} V^m \\ M^m \end{bmatrix} = F \quad 7-1$$

In Equation 7-1,  $M$  is the mass matrix,  $C$  is the initial viscous damping matrix and  $F$  is the earthquake excitation vector. The mass matrix is formulated as

$$M = \begin{bmatrix} 30357 & 0 \\ 0 & 4788 \end{bmatrix} \text{N,m,s}^2 \quad 7-2$$

The first main diagonal element of the mass matrix is the sum between the axial load and the wall self-weight contributions. The second main diagonal element is the mass moment of inertia of the rotational DOF about the interface between the wall panel and the wall base (Figure 7-1).

The initial stiffness of wall M6 was experimentally determined by applying small displacement on one DOF while holding the other constant each time. The resulting stiffness matrix is

$$K = \begin{bmatrix} 77.8E6 & 51.3E6 \\ 60.4E6 & 185.8E6 \end{bmatrix} \text{N,m} \quad 7-3$$

This also dictated the highest natural frequency of the specimen which governed the time step size and the numerical integration method selection for the reason of stability. The resulting natural frequencies of wall M6 were 44.5 and 198.4 rad/sec. To avoid over- or under-estimation of initial viscous damping and to focus on replicating flexure-dominant behaviour at inelastic level response using dissimilar specimen, the hybrid simulation coordinator did not assign any initial viscous damping since small discrepancy in damping with the prototype structure will not affect the reliability of inelastic hybrid simulations [8].

Figure 7-5 shows an idealised MDOF representation of the hybrid simulation with substructuring specimen. In this test, the bottom half of the wall (Wall M7) was physically tested as the physical substructure and the top half of the wall is numerically simulated as the numerical substructure. These are represented by the solid and dotted lines respectively in Figure 7-5.

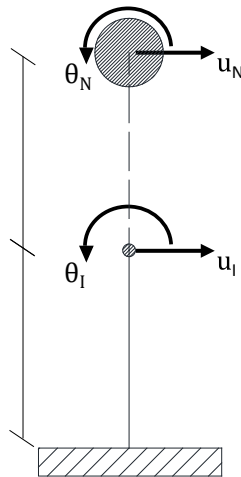


Figure 7-5 Idealised MDOF representation of the hybrid simulation with substructuring specimen

Translational and rotational DOF are specified for each node, where subscript “N” stands for “numerical” and subscript “I” stands for “interface”. The resulting equation of motion in by the hybrid simulation with substructuring is

$$M \begin{bmatrix} \ddot{\mathbf{u}}_N \\ \ddot{\boldsymbol{\theta}}_N \\ \ddot{\mathbf{u}}_I \\ \ddot{\boldsymbol{\theta}}_I \end{bmatrix} + C \begin{bmatrix} \dot{\mathbf{u}}_N \\ \dot{\boldsymbol{\theta}}_N \\ \dot{\mathbf{u}}_I \\ \dot{\boldsymbol{\theta}}_I \end{bmatrix} + K \begin{bmatrix} \mathbf{u}_N \\ \boldsymbol{\theta}_N \\ \mathbf{u}_I \\ \boldsymbol{\theta}_I \end{bmatrix} + \begin{bmatrix} 0 \\ 0 \\ \mathbf{V}^m \\ \mathbf{M}^m \end{bmatrix} = \mathbf{F} \quad 7-4$$

Equation 7-5 defined the mass matrix  $M$  as

$$M = \begin{bmatrix} 29978 & 0 & 0 & 0 \\ 0 & 691 & 0 & 0 \\ 0 & 0 & 757 & 0 \\ 0 & 0 & 0 & 1382 \end{bmatrix} \text{N, m, s}^2 \quad 7-5$$

There was no additional concentrated mass on the interface node so the mass was calculated based on the concrete self-weight contribution only. The mass moment of inertia of the rotational DOF at the interface node was the sum between the numerical and physical substructure contributions.

The restoring forces at the interface node was the superposition between the numerical restoring forces and the restoring forces measured directly from wall M7 as the physical substructure. Stiffness of the numerical substructure was formulated based on a numerical model whose result is calibrated against the hybrid simulation of wall M6. The resulting numerical substructure stiffness matrix is

$$K = \begin{bmatrix} 113.5E7 & -76.6E7 & -113.5E7 & -76.6E7 \\ -76.6E7 & 122.3E7 & 76.6E7 & -18.9E7 \\ -113.5E7 & 76.6E7 & 113.5E7 & 76.6E7 \\ -76.6E7 & -18.9E7 & 76.6E7 & 122.3E7 \end{bmatrix} \text{N,m} \quad 7-6$$

### 7.3. Test setup

The same test setup was used for all three different tests, with slight modifications for the hybrid tests. The setup was devised to permit the application of combined shear, axial and bending moment to the wall specimen. Figure 7-6 shows a schematic drawing of the setup for full size tests. A horizontal actuator at the top of the wall applied shear force. Axial load (or vertical displacement) and bending moment (or rotation) were applied through two vertical actuators. All loads were applied through a stiff loading beam. All actuators use servo-

control mechanisms. The wall was fixed to the strong floor by means of post-tensioning through the vertical PT ducts (see Figure 7-1). Two foundation blocks were placed on both sides of the wall base and each was fixed to the strong floor. The wall-foundation system was clamped together by grouting and post-tensioning. The longitudinal reinforcements inside the wall extended beyond the top of the wall and were secured to the top loading beam using high-strength grout to eliminate any slip between the wall and the loading beam.

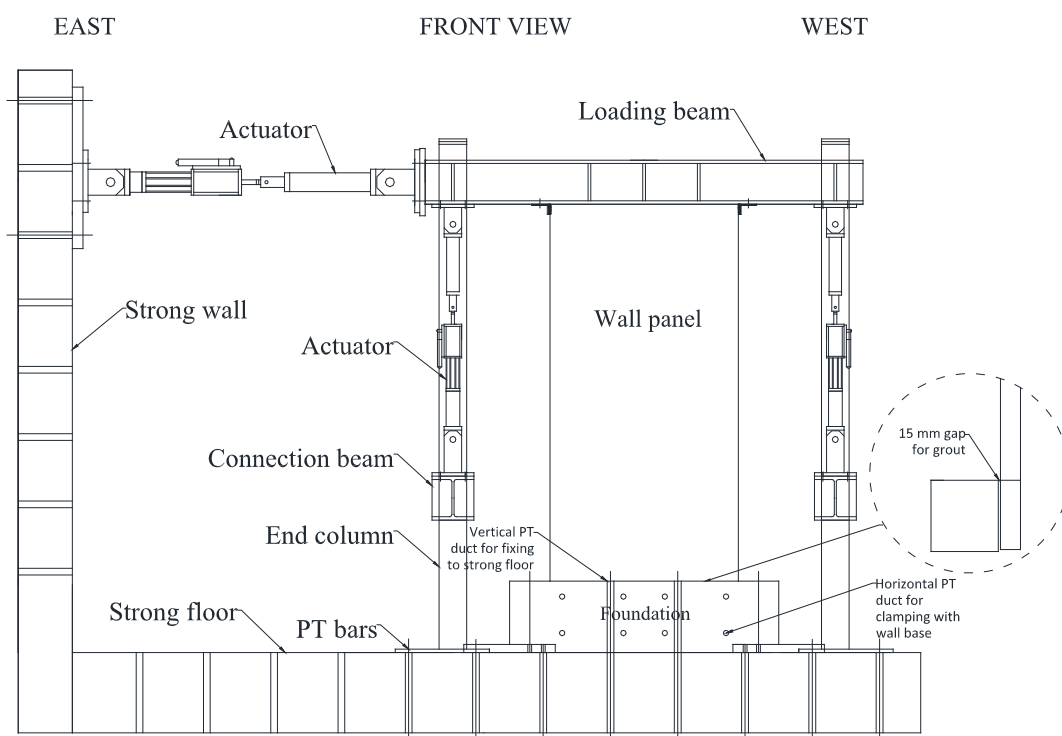
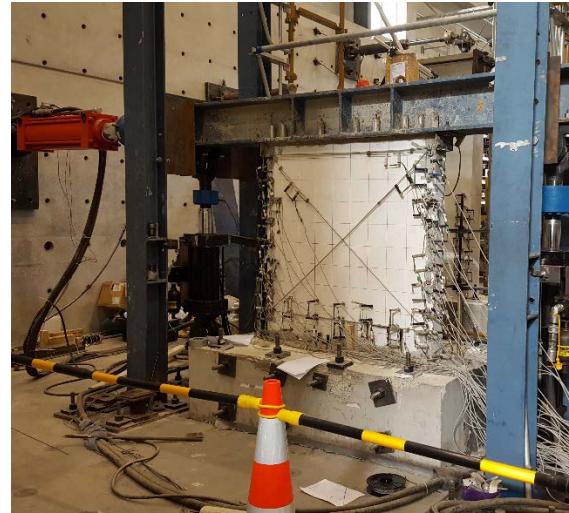


Figure 7-6 Schematic drawing of test setup

Figure 7-7a and Figure 7-7b show photographs of the test setup for two different wall set ups. The figures highlight the adjustments for accommodating the different wall heights. Figure 7-7c highlights the connection between the top of the wall and the loading beam.



a) Photo from actual test setup of the quasi-static and hybrid simulation without substructuring



b) Photo from actual test setup of hybrid simulation with substructuring



c) Connection between top of the wall and loading beam

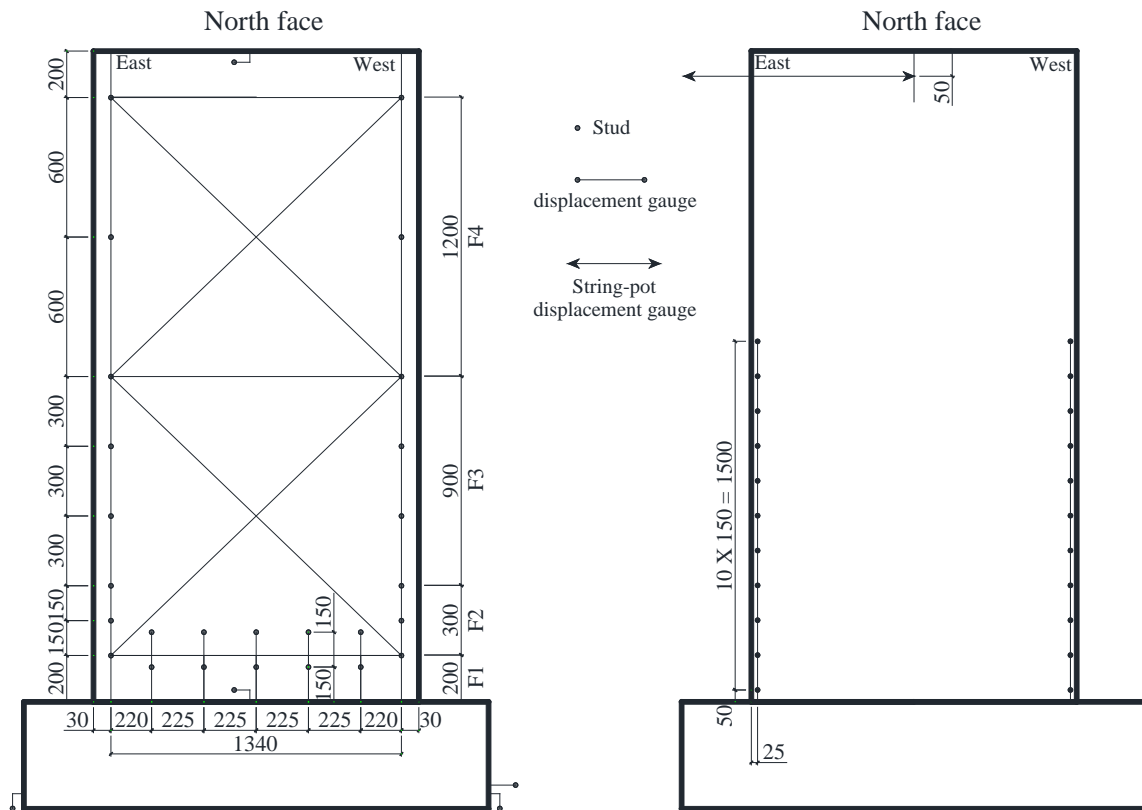
Figure 7-7 Photos from actual test setup

#### 7.4. Instrumentations

A dense array of instrumentations was used to monitor the global and local behaviours of the test walls. An LVDT inside the horizontal actuator measured the horizontal drift at the top of each wall while the load cell measured the shear forces. Small steel studs were embedded just under the concrete cover approximately 30 mm from the wall edges and displacement gauges were attached to these studs to measure local deformations at different sections

along the height of the wall. Nine displacement gauges were placed at each edge of the wall to measure axial strains and curvatures. Panel shear deformations were measured using displacement gauges arranged in a “X” configuration. Deformations in the plastic hinge region were measured by two rows of five displacement gauges along the wall length, extending 150mm and 300 mm above the wall-foundation interface. Studs were also welded directly to the corner longitudinal reinforcements, passing through recesses on the concrete cover. Displacement gauges were attached to these studs to measure average reinforcement strains at the extreme edges of the wall over a 150mm gauge length. Displacement gauges were also installed to measure strain penetrations at the wall-to-foundation interface, as well as any potential slips between the wall and the foundation, the wall and the loading beam, and between the foundation and the strong floor. String potentiometers were used to measure walls’ drifts externally at different locations depending on the type of the tests.

Figure 7-8 shows the schematic drawing of the instrumentation configurations. All instruments were installed on the North face of the wall; however, they are shown on separate diagrams in Figure 7-8a and Figure 7-8b for clarity. Figure 7-8a shows the displacement gauges used to measure the different types of concrete deformations described earlier, while Figure 7-8b shows the displacement gauges used to measure strains at the corner longitudinal reinforcements closest to the North face of the wall.



a) Instruments to measure concrete deformation

b) Instruments to measure steel reinforcement strain

Figure 7-8 Schematic drawing of instrumentations arrangement

Instrumentations for wall M7 were identical in configuration except only extended up to 1400 mm up from the top of the foundation. Figure 7-7a and Figure 7-7b show actual instrument installations of both type of wall specimens.

## 7.5. Implementation problems during tests

A few problems encountered during and after the hybrid simulation without and with substructuring that became an extra source of inaccuracies in the test results.

### 7.5.1. Faulty coordinate transformation algorithm

During the post-processing phase after all tests have been completed, faults were found in the hybrid simulation without and with substructuring algorithms. The faults lied in the

transformations between the outputs at global coordinate system ( $u, \theta$  in the hybrid simulation without substructuring and  $u_I$  and  $\theta_I$  in the hybrid simulation with substructuring) and the actuator coordinate systems ( $x_0, x_1, x_2$ ). The actuator coordinate system is illustrated in Figure 7-9, and the relationship between the global and the actuator coordinate system is given by

$$\begin{bmatrix} x_0 \\ x_1 \\ x_2 \end{bmatrix} = T_u \begin{bmatrix} u \\ \theta \end{bmatrix} \quad \text{or} \quad \begin{bmatrix} x_0 \\ x_1 \\ x_2 \end{bmatrix} = T_u \begin{bmatrix} u_I \\ \theta_I \end{bmatrix} \quad 7-7$$

$$T_u = \begin{bmatrix} 1 & 0 \\ 0 & -d_1 \\ 0 & d_2 \end{bmatrix} \quad 7-8$$

where  $T_u$  is the displacement transformation matrix.

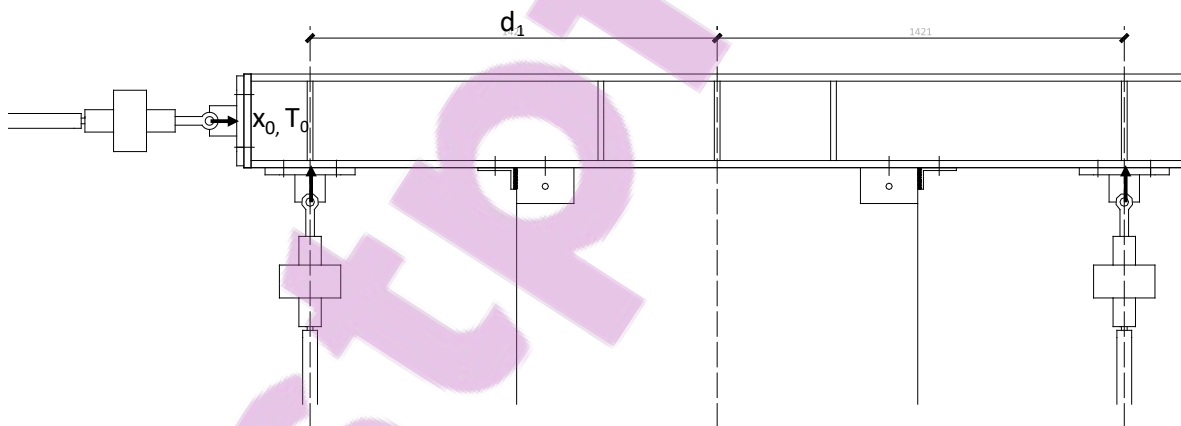


Figure 7-9 Actuator coordinate system

In the test setup, the vertical actuators were equidistant from the center line of the wall thus  $d_1 = d_2 = d$ . By mistake, an incorrect transformation matrix as Equation 7-9 was in fact adopted for the testing.

$$\mathbf{T}_u^* = \begin{bmatrix} 1 & 0 \\ 0 & \frac{-d}{2} \\ 0 & \frac{d}{2} \end{bmatrix} \quad 7-9$$

The force feedback transformation from the actuator coordinate system ( $T_0, T_1, T_2$ ) to the global coordinate system ( $V^m, M^m$ ) according to the normal relationship is as below.

$$\begin{bmatrix} V^m \\ M^m \end{bmatrix} = \mathbf{T}_R \begin{bmatrix} T_1 \\ T_2 \\ T_3 \end{bmatrix} \quad 7-10$$

$$\mathbf{T}_R = \mathbf{T}_u^T \quad 7-11$$

where  $T_R$  is the force transformation matrix. Another fault occurred in the force feedback transformation algorithm such that the actual force feedback transformation matrix became

$$\mathbf{T}_R^* = \begin{bmatrix} 1 & 0 & 0 \\ 0 & -d & d \end{bmatrix} \quad 7-12$$

Thus, the imposed rotations on both hybrid simulation without and with substructuring were only half of those computed by the numerical integration at every time step and the measured bending moments from half of the intended rotation were amplified by a factor of two when returned into the equation of motions.

Had the system been linearly elastic, this mistake would have produce no discernible difference in the final response prediction, as twice the restoring force from half the applied displacement is the same. In softening nonlinear system, however, it results in prolonged excursion in the linear state and the extra restoring bending moment feedback from doubling

half the elastic feedback. This results in stiffer system and more or less the same hysteretic energy dissipation.

Figure 7-10 shows a snapshot of bending moment time histories from the hybrid simulation with substructuring of wall M7, showing i) correct moment feedback, ii) the physically measured moment from half the rotation and iii) the incorrect moment feedback based on twice the measured moment. This figure shows that i) and iii) in fact are very close which would later explain why the experiments results were close to the reference result despite the errors.

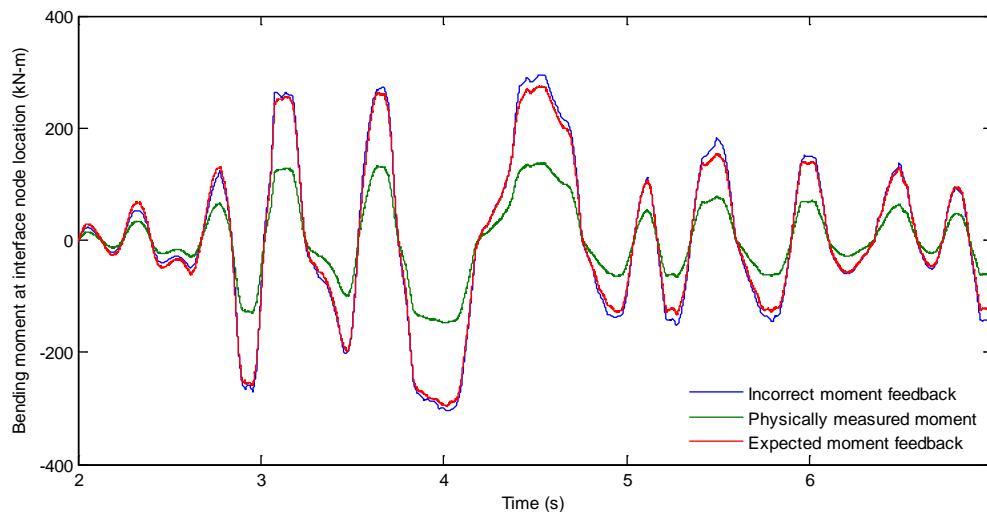


Figure 7-10 Comparison between physically measured, expected, and incorrectly fed back bending moment

### 7.5.2. Actuator behaviour

Prior to the hybrid simulation with substructuring, the wall was subjected to a low amplitude cyclic test and a free vibration test, both with a maximum amplitude of 0.3 mm (0.01% drift), which was well within the walls nominal elastic range. It was found during these tests that the horizontal actuator had notable delay and undershot at peak displacements, especially at small displacement amplitudes, due to poor tuning. Both errors introduced additional energy

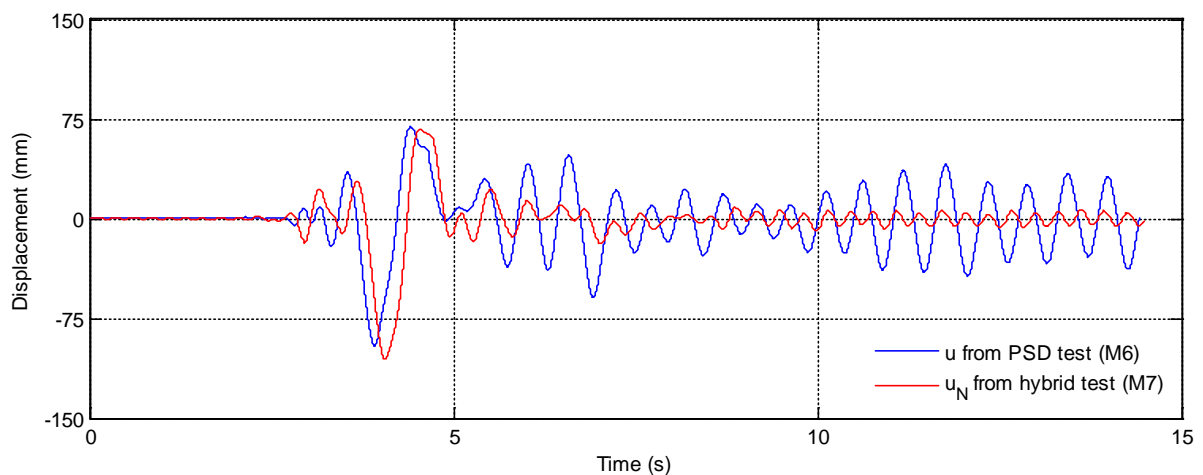
during the experiment. It was decided to use a time scale of 400 during both hybrid simulations to prevent instability.

## 7.6. Results and discussions on global responses

This section presents comparisons the results from hybrid simulation without and with substructuring in term of displacement time histories, force-deformation relationships, boundary load compliances, and energy dissipation characteristics.

### 7.6.1. Comparison of displacement time histories

Figure 7-11 compares the displacement time histories at the top of the prototype wall ( $u$  for the hybrid simulation without substructuring on wall M6 and  $u_N$  for the hybrid simulation with substructuring on wall M7) and at the locations of interface nodes  $u_I$  of both walls. The time axis in both figures has been scaled back to correspond to the original earthquake record time.



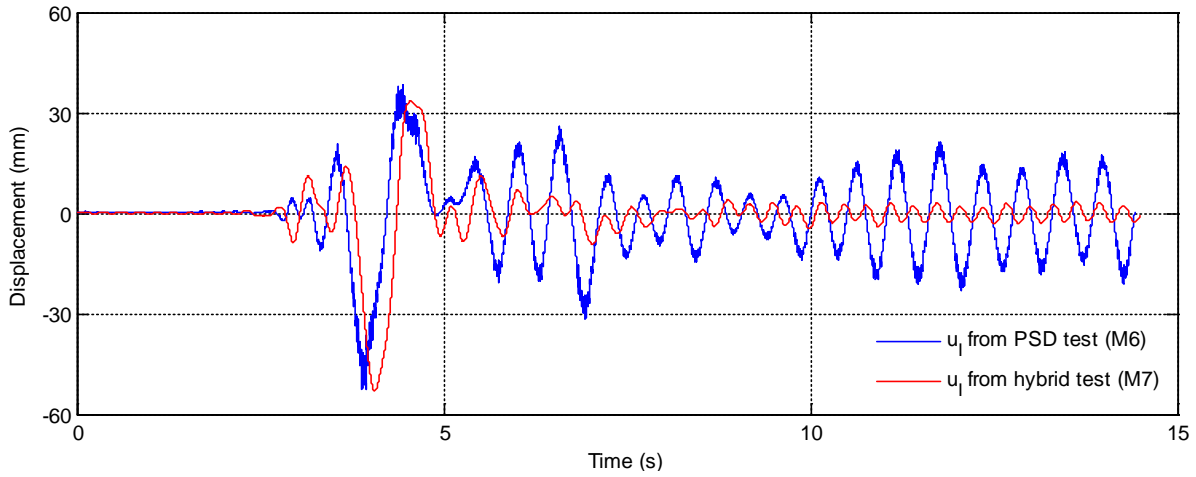


Figure 7-11 Comparison of displacement time histories at top of the wall (top figure) and at the location of interface node (bottom figure)

Table 7-3 and Table 7-4 provide a summary of comparisons between the maximum displacements attained at both tests in both positive and negative directions.

Comparison	Without substructuring (u)	With substructuring (u <sub>N</sub> )	Difference
Maximum positive displacement (mm)	72.1	67.5	-6.38%
Maximum negative displacement (mm)	-98.8	-106.1	+7.39%

Table 7-3 Comparison between u (without substructuring) and u<sub>N</sub> (with substructuring)

Comparison	Without substructuring (u <sub>I</sub> )	With substructuring (u <sub>I</sub> )	Difference
Maximum positive displacement (mm)	34.1	34.7	+1.76%
Maximum negative displacement (mm)	-45.9	-54.5	+18.74%

Table 7-4 Comparison of u<sub>I</sub>

The displacement time histories at the top and at the interface node locations show good agreement in term of amplitudes and profiles for the first 5 seconds, however the largest

difference in amplitude was as high as 18%, in the negative direction of  $u_i$ . The displacement time histories differed significantly between the two tests, due to the negative damping effect from actuator delay and undershot. The horizontal actuator tuning was improved to better follow the desired signals prior to running the hybrid simulation with substructuring, resulting in smaller displacement amplitudes of wall M7 after the first 5 seconds from reduced additional energy.

### 7.6.2. Comparison of force deformation relationships

Figure 7-12 shows the moment-displacement relationship obtained from both the hybrid simulation without and with substructuring. The difference between the maximum base moment magnitudes between the two tests were 4.5% in the positive direction and less than 1% in the negative direction. The results demonstrated that the hysteretic behaviours of the specimens from the tests without and with substructuring were similar, even in the presence of coordinate transformation errors in both tests (Section 7.5.1).

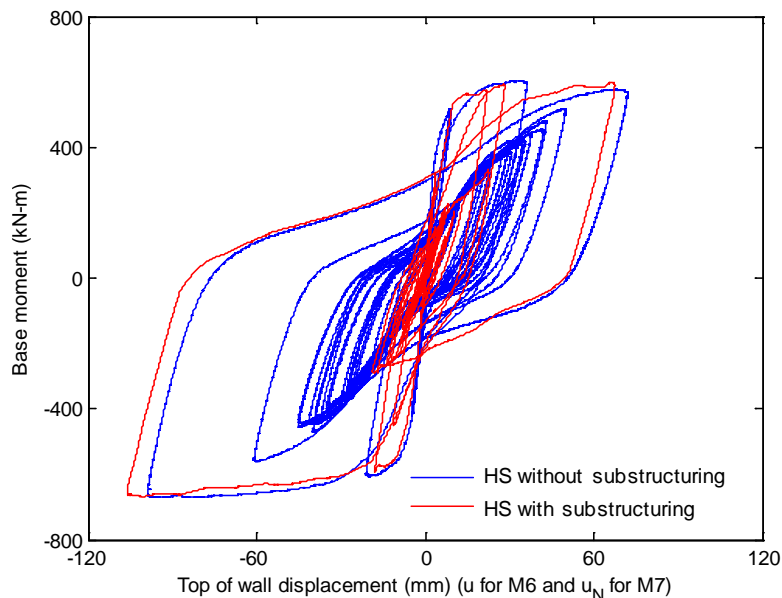


Figure 7-12 Wall base moment vs top of wall displacement for the test without and with substructuring

### 7.6.3. Replications of boundary conditions

The hybrid simulation without and with substructuring for this test series specified identical boundary conditions. These were replicated through a computer monitored combination of axial load and bending moment at the top of the wall specimens. It is important to confirm the boundary conditions were satisfied throughout the tests to ensure this is not the source of difference between the hybrid simulation without and with substructuring. Figure 7-13 shows the axial load time histories for the hybrid simulation without and with substructuring. In both tests, a constant 294 kN axial load as desired were well achieved despite the two vertical actuators working in displacement control. The maximum deviation from the desired magnitude was 4 kN or 1.4% for wall M6 (without substructuring) and 6 kN or 2% for wall M7 (with substructuring).

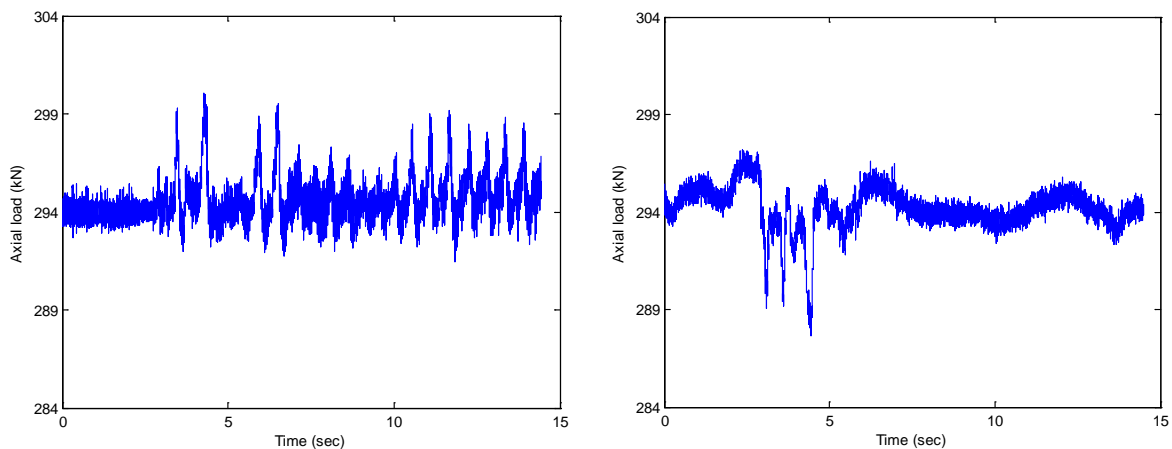


Figure 7-13 Axial load time histories from the hybrid simulation without substructuring (left) and the hybrid simulation with substructuring (right)

Figure 7-14 show the bending moment time histories of wall M6 (without substructuring) and wall M7 (with substructuring) at the interface node locations. The bending moment at the interface node location of wall M7 included the effect of the coordinate transformation error. The figure shows that in the first 5 seconds the bending moment at the interface node

locations of the two tested walls are similar, hence the similar displacement time history profiles from the two tests (Figure 7-11).

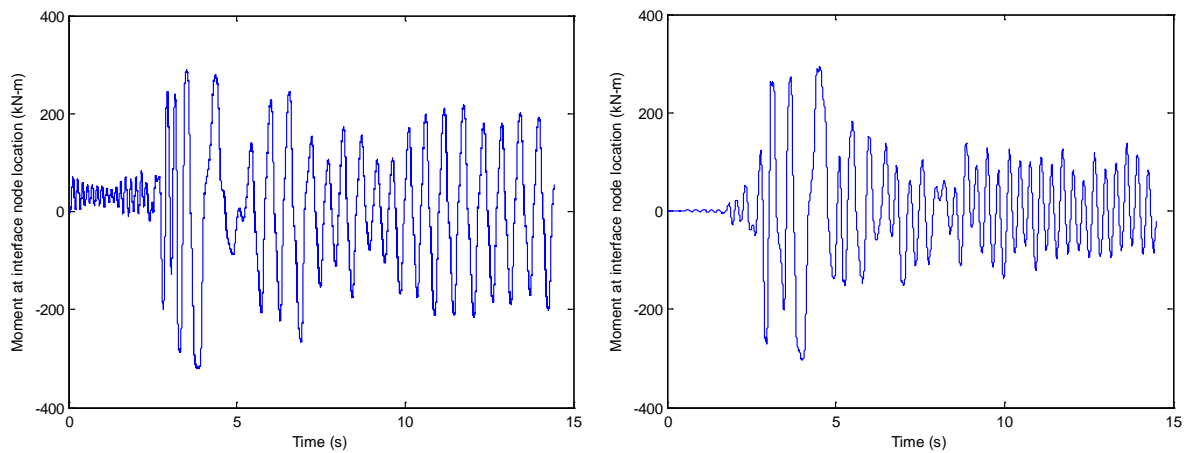


Figure 7-14 Bending moment time histories at interface node the hybrid simulation without substructuring (left) and the hybrid simulation with substructuring (right)

#### 7.6.4. Comparison of energy dissipation characteristics

For each test, hysteretic energy dissipation was calculated in proportion to the area under the force-deformation curve. The equivalent viscous damping  $\zeta_{eq}$  can then be derived from the hysteretic energy dissipation. For unsymmetrical loading protocol such as in hybrid simulations, Rodrigues et al. [90] suggested that the equivalent viscous damping be calculated from half-cycle force-deformation curves where a half-cycle is identified as the part of the force-deformation curve bounded by two consecutive points of zero forces. The equivalent viscous damping  $\zeta_{eq}$  is computed according to the following relationship:

$$\zeta_{eq} = \frac{A_{half-loop}}{\pi R_{max} u_{max}} \quad 7-13$$

where  $A_{half-loop}$  is the area under the open-loop, half force-deformation curve,  $R_{max}$  and  $u_{max}$  are the maximum force and deformation attained in the half-loop.

Figure 7-15 shows a snapshot of the restoring force time history from wall M6 (without substructuring) against real clock time. Several zero force crossings and local force maxima and minima, corresponding to the local displacement maxima and minima are highlighted as black and red circles. This serves to demonstrate the values that are used in Equation 7-13 to calculate the equivalent viscous damping at every half-cycle.

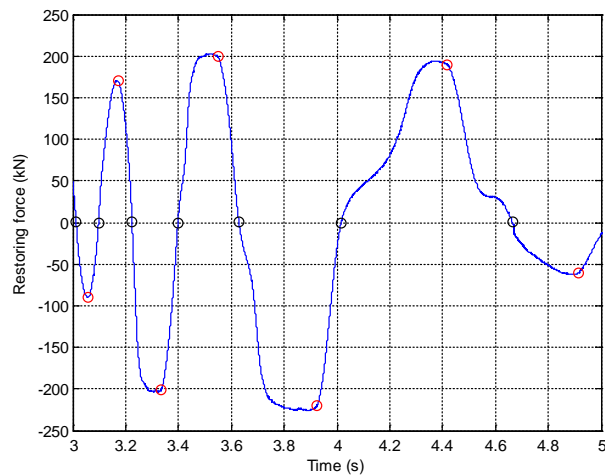


Figure 7-15 Example of force maxima and zero force point selections

Figure 7-16 shows the amount of dissipated energy per half-cycle of vibration as well as the cumulative dissipated energy up to the same number of half-cycles for the hybrid simulation without substructuring (wall M6) and with substructuring (wall M7). Up to 10 half-cycles, both tests shows similar cumulative dissipated energy at around 45 kN-m. From there onwards the test without substructure (wall M6) dissipated more energy than the test with substructure (wall M7) due to the much larger displacement amplitudes. This is consistent with the comparisons of the displacement time histories (Figure 7-11) where both tests produced similar results for the first 5 seconds of the simulations.

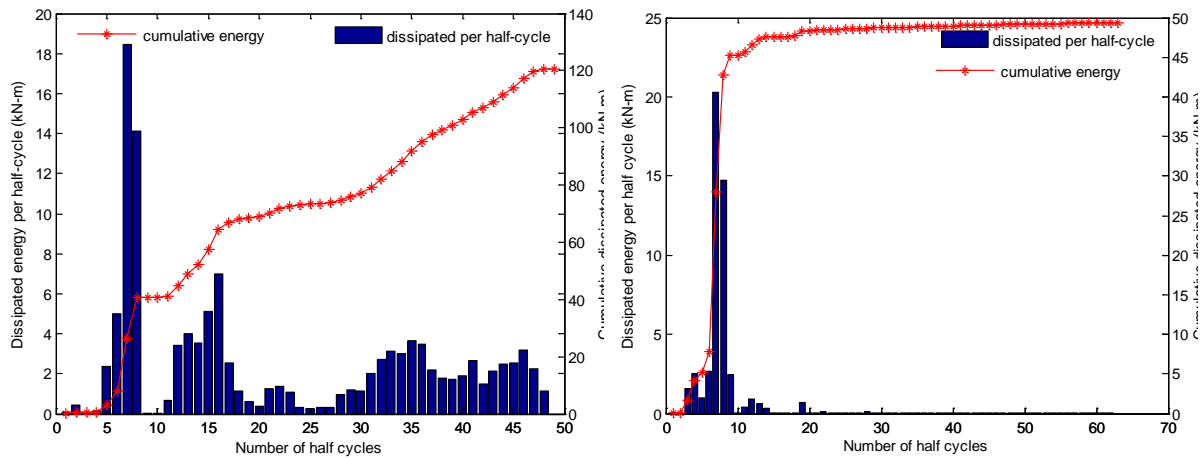


Figure 7-16 Comparison of dissipated energy between the wall M6 (left figure) and wall M7 (right figure)

Equation 7-13 indicates that the amount of equivalent viscous damping is related to the maximum displacement amplitude. It is common to derive the relationship between the equivalent viscous damping and displacement ductility. Displacement ductility is defined as the ratio of the maximum displacement to the displacement at first yield, such as yielding at the outer longitudinal reinforcement in RC wall structures. In these experiments, the instances of the first yield were experimentally measured using displacement gauges welded directly to the outer longitudinal reinforcements. The yield displacements were 3.12 mm for wall M6 (without substructuring) and 1.8 mm for wall M7 (with substructuring), measured at the interface node location. Different researchers have proposed different formulations for the equivalent viscous damping ratio for RC structures [90]. The current research recognises the formula by Grant et al. [91] for its general applicability where the relationship between the hysteretic component of an equivalent viscous damping and ductility is formulated as

$$\zeta_{hyst} = a \left( 1 - \frac{1}{\mu^b} \right) \left( 1 + \frac{1}{(T_e + c)^d} \right) \quad 7-14$$

where  $\zeta_{hyst}$  is the hysteretic component of equivalent viscous damping  $\zeta_{eq}$ ,  $\mu$  is the displacement ductility, and  $a, b, c$ , and  $d$  are empirical best-fit parameters. For concrete wall building, the Thin Takeda (TT) hysteresis rules are the most representative [92]. Table 7-5 listed the parameter values suggested by Priestley et al. [92] for TT hysteresis rules.

$a$	$b$	$c$	$d$
0.215	0.642	0.824	6.444

Table 7-5 Parameter values for Thin Takeda hysteresis rules

Equation 7-15 also indicates that  $\zeta_{hyst}$  is dependent to the effective period  $T_e$ , derived from the secant stiffness to the design displacement of the substitute structure in a Direct Displacement-Based Design (DBDD) approach. However, Priestley et al. [92] have shown that for effective periods between 1 to 4 seconds, which are common for regular structures such as wall and frame buildings, the influence of effective period is small for the different hysteresis rules, and neglecting the factor is conservative since it generates a lower estimate of damping.

In the experiments, rather than displacement ductility, the equivalent viscous damping experimentally derived using Equation 7-13 for each tested wall is correlated to the normalised displacement amplitudes attained during the experiment ( $u_{max}/u_{yield}$ ), noting that  $u_{max}/u_{yield}$  is also the definition of displacement ductility used in Equation 7-14. Accordingly, the relationship proposed by Grant et al. [91] can be plotted along with the experimental data for each wall in Figure 7-17 and Figure 7-18 where the term inside the second bracket in Equation 7-14 is omitted. A regression curve is also fitted for each experimental data using the same form as in Equation 7-14, excluding the effective period factor  $T_e$ . Table 7-6 listed

the parameters of the regression equations along with the coefficient of determination ( $R^2$ ) value.

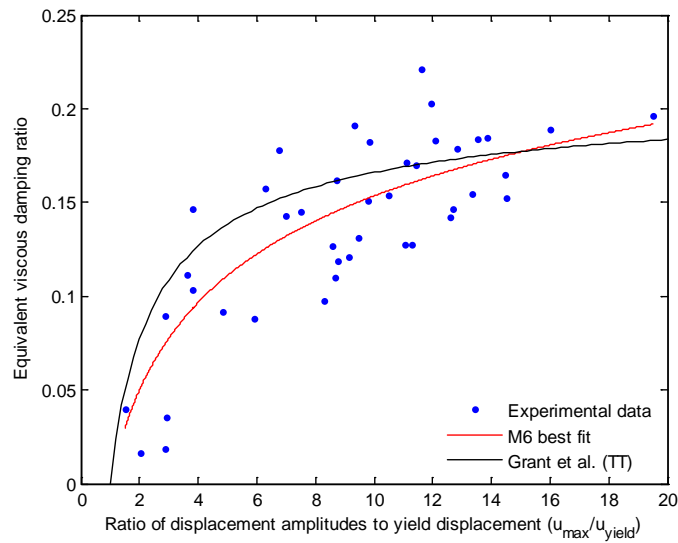


Figure 7-17 Relationship between  $\zeta_{eq}$  and  $u_{max}/u_{yield}$  for the hybrid simulation without substructuring (wall M6)

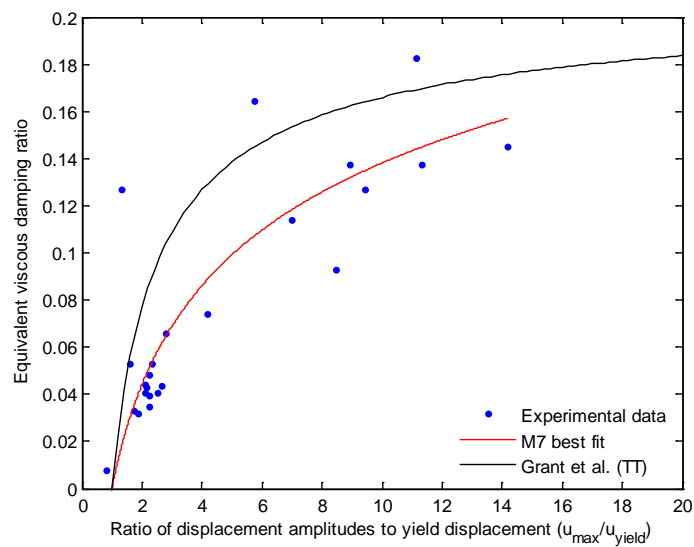


Figure 7-18 Relationship between  $\zeta_{eq}$  and  $u_{max}/u_{yield}$  the hybrid simulation with substructuring (wall M7)

Experiment	Regression parameters		$R^2$
	$a$	$b$	
M6	0.7457	0.1	0.66
M7	0.8475	0.077	0.64

Table 7-6 Regression parameters for experimentally derived  $\zeta_{eq}$

It can be seen from both figures that the energy dissipation property in both tests generally followed the equation proposed by Grant et al. [91].

## **7.7. Results and discussions on local responses**

The similarities between the hybrid simulation without and with substructuring results are also investigated on the local responses level of both walls. Beside damage patterns, the dense array of instrumentations allowed capturing and comparing local deformation components, curvature distributions, reinforcement strains, and plastic hinge lengths between the walls.

### **7.7.1. Comparison of damage patterns**

Figure 7-19 show wall M6 (without substructuring) and wall M7 (with substructuring) at the end of each test. In the left figure, the dashed line is drawn approximately on the same height as the top of wall M7. The effect of physically imposing smaller rotations (and hence bending moments) at the top of wall M7 manifested in fewer cracks forming up the height of wall M7 compared to wall M6. The cracks on wall M7 only extended up to a height roughly equal to the bottom 1/4<sup>th</sup> of wall M6 as indicated by the region inside the red box.

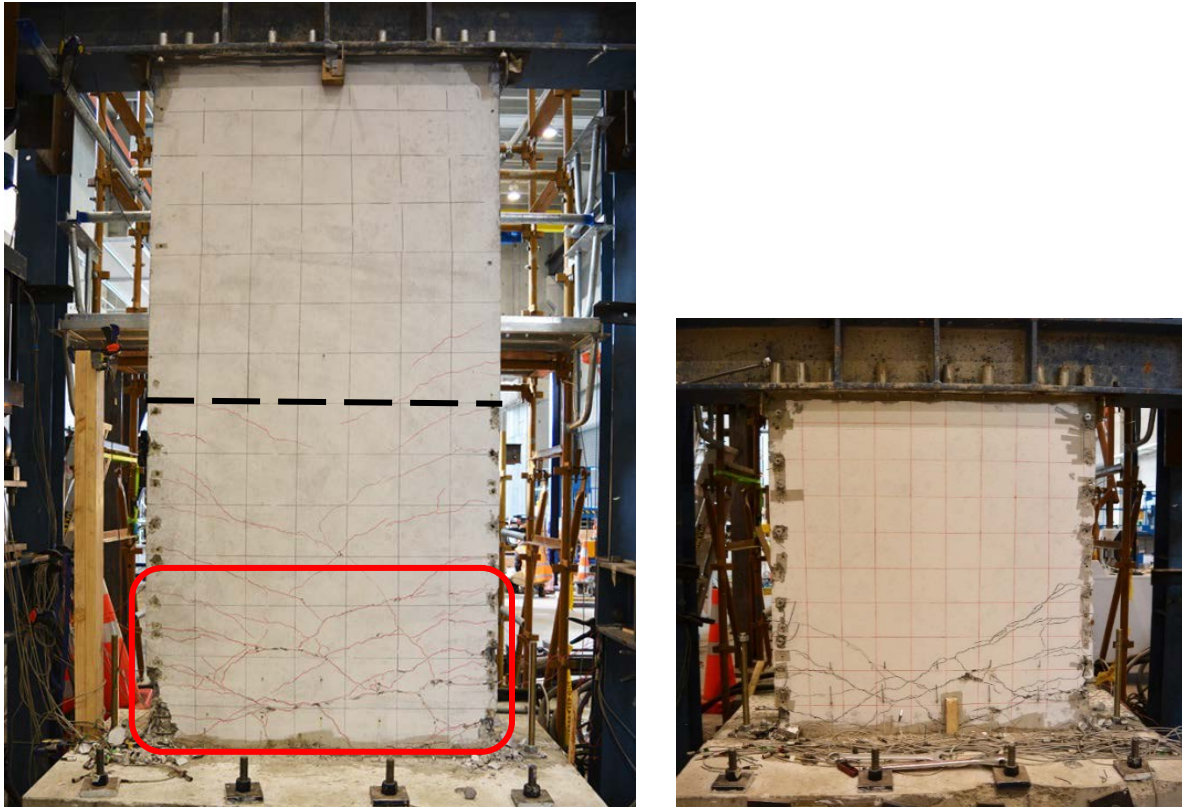


Figure 7-19 Final state of the hybrid simulated wall (left) and the hybrid tested wall (right)

Both walls exhibited flexure-shear cracks pattern indicated by the initially horizontal cracks forming at the edges of the walls followed by inclined cracks as they propagated to the web. A review of time-lapsed photography confirmed that there was no shear cracking in the web region on wall M7. The inclinations of the cracks on wall M7 were steeper due to the smaller bending moments applied to the wall from the coordinate transformation error. Since the average shear stresses on both walls were similar, smaller bending stresses would result in principal tensile stresses occurring at steeper angles.

#### **7.7.2. Comparison of deformation components**

The contributions of different sections of a test wall to the total lateral deformation were investigated by distinguishing four regions on the wall, F1, F2, F3 and F4, as shown in Figure 7-8. Curvatures were calculated from vertical deformations measured by the gauges along

the wall edges, and flexural deformations were obtained by double-integrating the curvatures. Shear deformations were directly derived from the displacement gauges in diagonal configurations according to the method proposed by Hiraishi [93]. Due to the difficulties in separating the contributions of strain penetrations to the walls' lateral deformations from the contributions of wide cracks at the base of the walls, reinforcement strain penetrations were not calculated separately but instead was included in F1. The contributions of the five displacement components at selected drift levels for each test are shown in Figure 7-20.

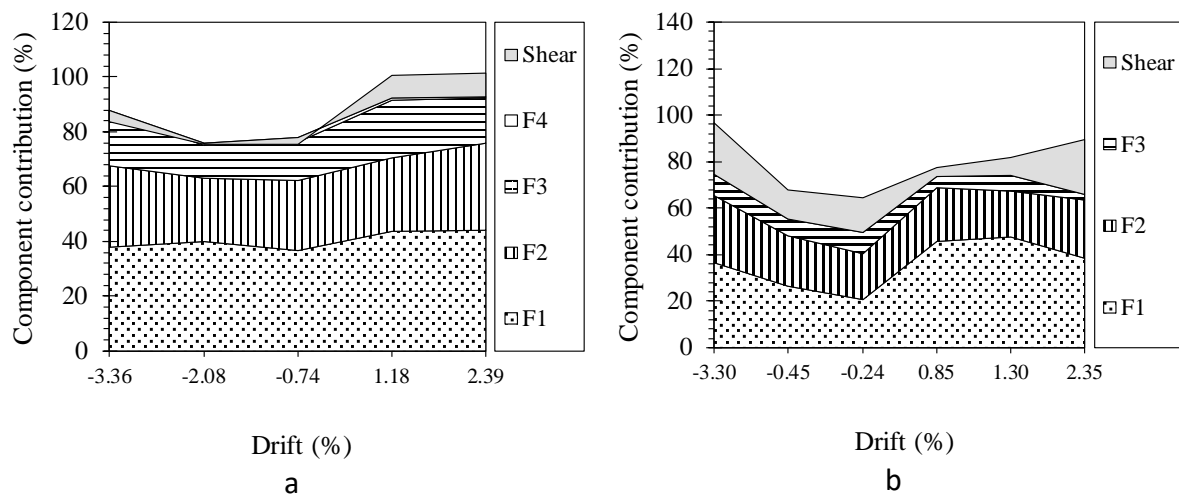


Figure 7-20 Deformation component contributions between a) wall M6 (without substructuring) and b) wall M7 (with substructuring)

Table 7-7 presents a summary of the deformation component F1 and F2 comparisons between the two test walls.

Component	Drift of wall M6 (without substructuring)		Drift of wall M7 (with substructuring)	
	-3.36%	+2.39%	-3.30%	+2.35%
F1	38%	44%	38%	40%
F1+F2	68%	76%	66%	66%

Table 7-7 Comparisons of F1 and F2 between the wall M6 (without substructuring) and wall M7 (with substructuring)

Table 7-7 suggests that the contributions of F1 were similar on both walls at comparable drifts. The lateral deformations of the walls were dominated by large cracks near the base. This is indicated by the total contributions of F1 and F2, that only accounted for 1/6<sup>th</sup> of the wall heights, being between 66% and 76% of the total lateral deformations of the walls.

There was a significant increase in the shear deformation contribution to the total lateral deformation of wall M7 (with substructuring) compared to wall M6 (without substructuring), which was accompanied by a significant decrease in the contribution of F3 to the total lateral deformation of M7. Since the steeper inclined cracks on wall M7 caused shear stresses resisted by shear reinforcements to become larger, shear reinforcement strains also increased which in turn widen the cracks on the surrounding concrete.

### 7.7.3. Comparison of curvature distributions

Figure 7-21 shows the curvature distribution profiles from the hybrid simulation without substructuring (wall M6) and the hybrid simulation with substructuring (wall M7) results.

The average curvatures at maximum drifts in each test are summarised in Table 7-8.

	Drift of wall M6 (without substructuring)		Drift of wall M7 (with substructuring)	
	-3.36%	+2.39%	-3.30%	+2.35%
Average curvature (km <sup>-1</sup> )	-68	+55	-69	+45

Table 7-8 Average curvatures at maximum drifts of the hybrid simulation without and with substructuring

Note that the average curvatures in wall M7 were measured up to a height of 1400 mm. At similar drifts, both walls developed similar curvature distributions especially near the base.

The curvature distributions were consistent with the deformation component contributions

shown previously in Figure 7-20 where the contributions of F2 to the total lateral deformations were similar for both tests. Due to the smaller bending moments physically applied to wall M7 as the result of the coordinate transformation error, Figure 7-21 shows that the average curvatures of wall M7 rapidly decreases toward zero compared to the average curvatures of wall M6.

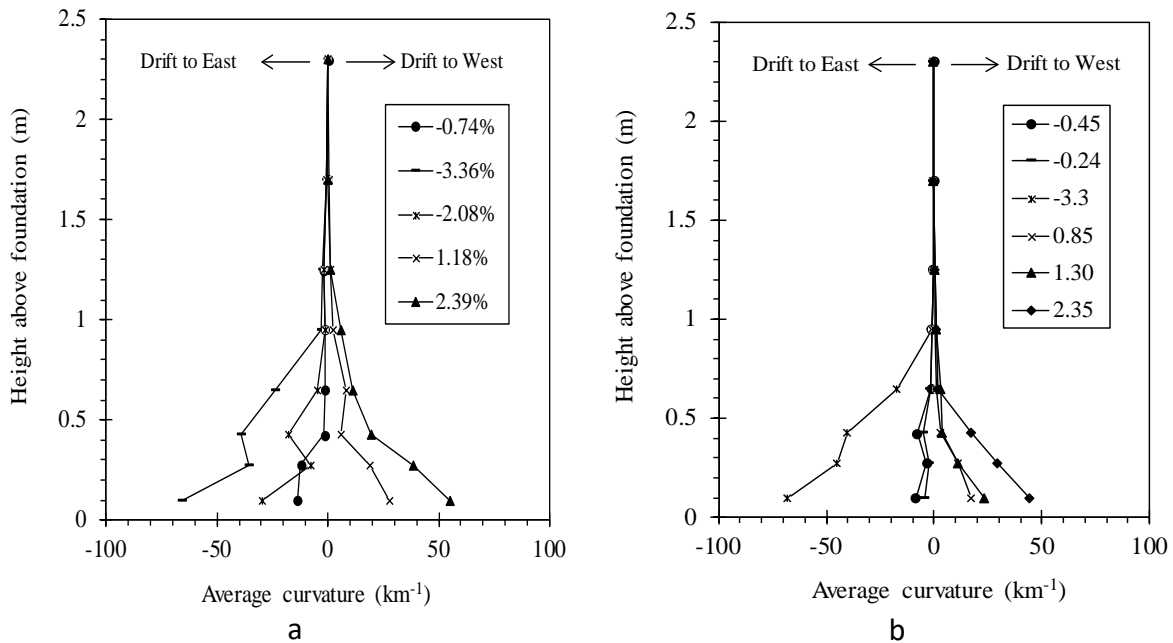
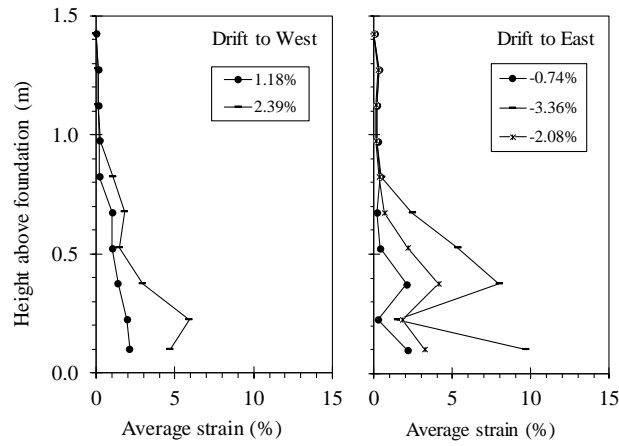


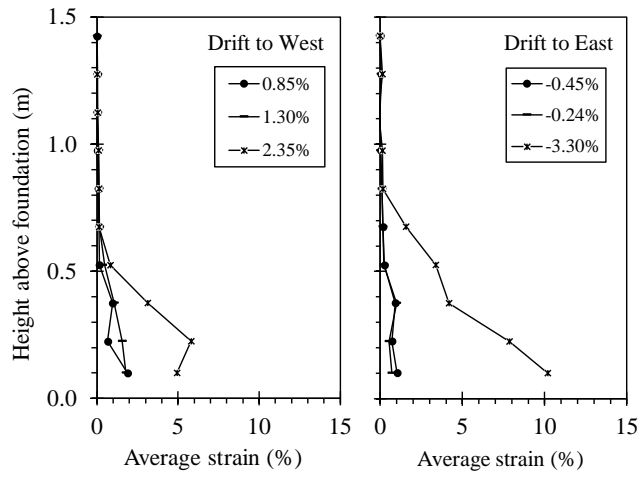
Figure 7-21 Curvature distributions obtained from a) wall M6 (without substructure) and b) wall M7 (with substructure)

#### 7.7.4. Comparison of average tensile strains

Figure 7-22 shows the average tensile strains along the corner longitudinal reinforcements of the walls. Strain measurements were compromised after reinforcements buckled, thus the strain values at drift levels after the occurrence of buckling are not shown in Figure 7-22. The figure shows that strains were distributed evenly over the height of the walls for the most part of both tests. This indicates ductile behaviours and matches with the observation that many cracks forming up the heights of the walls.



a)



b)

Figure 7-22 Average tensile strains from a) wall M6 (without substructuring) and b) wall M7 (with substructuring)

Table 7-9 shows the comparison of the longitudinal reinforcement strains at maximum drifts attained during the hybrid simulation without and with substructuring.

Parameter	Drift of wall M6 (without substructuring)		Drift of wall M7 (with substructuring)	
	-3.36%	+2.39%	-3.30%	+2.35%
Reinforcement strain (%)	9.9	4.8	10.2	5

Table 7-9 Longitudinal reinforcement strains at maximum drifts from the hybrid simulation without and with substructuring

The longitudinal reinforcement strains were similar for both tests at comparable drift levels. The strain profiles of wall M7 decrease toward zero earlier compared to wall M6, as in the curvature distributions, due to the erroneously small applied bending moment.

#### 7.7.5. Comparison of plastic hinge lengths

The ultimate displacements of RC structure can be usually predicted based on equivalent plastic hinge lengths. This is defined as the length over which plastic hinge rotations are assumed to occur. The plastic hinge rotation  $\theta_p$  can be calculated by integrating the curvatures obtained from the displacement gauge measurements, and the plastic hinge length  $l_p$  can then be computed according to the relationship given in Equation 7-16

$$\theta_p = (\varphi_m - \varphi_y) l_p \quad 7-15$$

where  $\varphi_m$  is the maximum curvature measured during the test and  $\varphi_y$  is the yield curvature calculated according to Priestley and Kowalsky [94]. The plastic hinge length  $l_p$  calculated for both test walls are plotted alongside the value of  $l_p$  specified in NZS3101:2006 [89] in Figure 7-23.

NZS 3101:2006 defines  $l_p$  as the smaller of i)  $0.15 M^*/V^*$ , where  $M^*$  and  $V^*$  are the design moment and shear action at ultimate limit state (ULS), respectively, and ii)  $0.5l_w$  where  $l_w$  is the wall length. For the test walls in the experiments with aspect ratios of 2, the plastic hinge length  $l_p$  according to NZS 3101:2006 is governed by  $0.15 M^*/V^*$  (420 mm). The measured plastic hinge length on each wall was different in different directions at similar drift level due to the different crack distributions in both directions. The average plastic hinge lengths were 468.15 mm for wall M6 (without substructuring) and 438.76 mm for wall M7 (with substructuring) indicating good correlations with NZS3101 prediction.

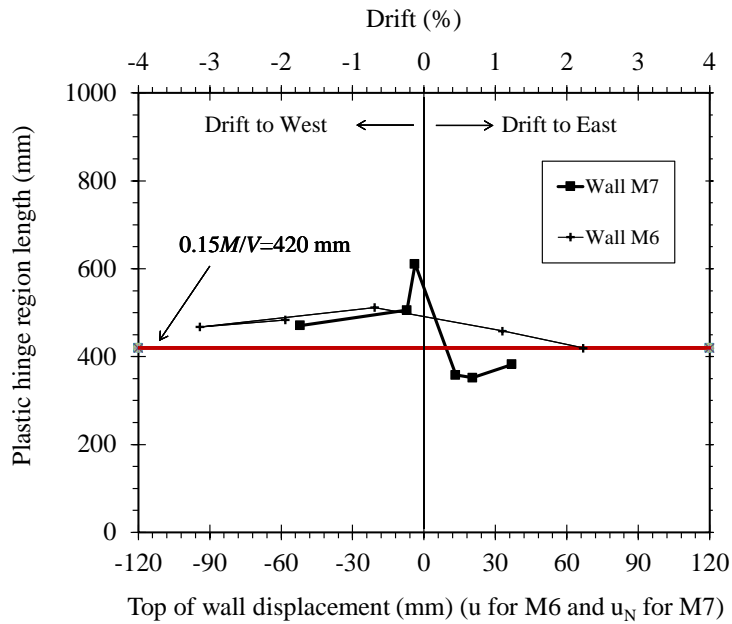


Figure 7-23 Comparison of plastic hinge lengths between wall M6 (without substructuring) and wall M7 (with substructuring)

## 7.8. Numerical validations

This section presents numerical models developed in SAP2000 as a benchmark to the hybrid simulation without and with substructuring results. The numerical models were separately developed for each type of test and the response of the model to the synthetic ground motion were compared to the displacement response obtained from the actual experiment.

### 7.8.1. Modelling of the wall from the hybrid simulation without substructuring

A macroscopic model consisting of an elastic frame element with a rotational spring element that connects the elastic frame and the ground was selected to capture the behaviour of wall M6 during the hybrid simulation. A schematic drawing of the model is presented in Figure 7-24.

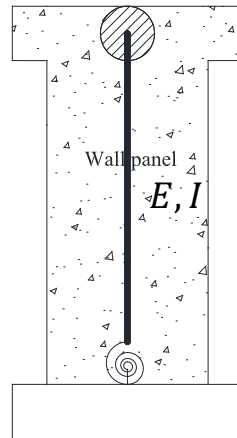


Figure 7-24 Schematic drawing of numerical model representing wall M6 (without substructuring)

Nonlinear behaviour was assumed to be completely defined by nonlinear moment-rotation relationships of the rotational spring element. The rotational spring was a Link object fixed in the X- and Z-axis of SAP2000 global coordinate system, where the nonlinear moment-rotation relationships were defined for rotation about the Y-axis. Table 7-10 lists the data points used to define the moment-rotation relationships for the Link element in the numerical model of M6. They were adjusted so that the numerical model achieves comparable strength during nonlinear static analysis to the ultimate strength from the quasi-static test (wall M5).

Rotation (rad)	Moment (kNm)
-0.0354	-580
-0.0175	-550
-0.003	-500
0	0
0.003	500
0.0175	550
0.0354	580

Table 7-10 Nonlinear moment-rotation relationships for Link element in M6 numerical model

The total effective height of the element was 3000 mm, very close to the actual height of wall M6 (hybrid simulation without substructuring) of 2975 mm. The rotational spring was defined

as a two-joint link element, 300 mm in length, which left 2700 mm as the length of the elastic frame member.

Concrete material was assigned to the elastic frame element with  $f'_c = 34.5$  MPa, close to the compressive strengths of the concrete materials from both walls determined from standard cylinder tests. The hysteretic behaviour of the rotational spring element was defined using the Pivot hysteresis rules [95]. The pivot hysteresis rules were controlled by three different parameters  $\alpha$ ,  $\beta$ ,  $\eta$ . These parameters are schematically shown in Figure 7-25 and were determined through trial and error and the values that resulted in the closest match to the experimental results are presented in Table 7-11.

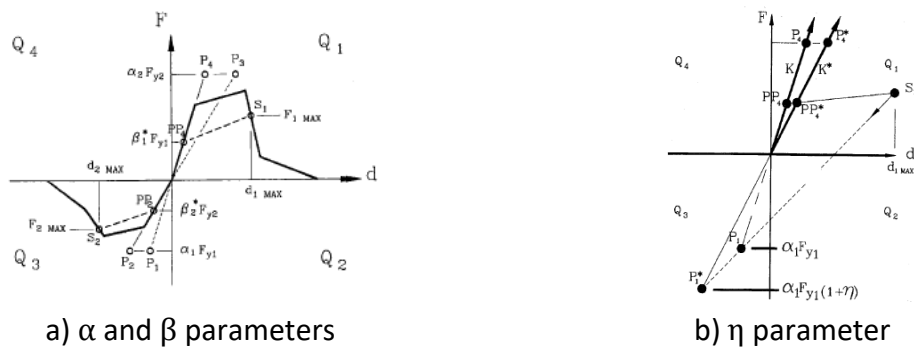


Figure 7-25 Schematic drawing of Pivot hysteresis rules parameters [92]

Parameters	Values
$\alpha_1$	2.5
$\alpha_2$	2.5
$\beta_1$	0.8
$\beta_2$	0.8
$\eta$	10

Table 7-11 Parameters for Pivot hysteresis rules in wall M6 (without substructuring) numerical modelling

In accordance with Equation 7-2, concentrated mass in the translational direction was also defined on the numerical model as an equivalent mass due to the axial load. The mass moment of inertia was also defined based on the wall's mass and dimensions.

Figure 7-26 shows the top wall displacement time histories from the SAP2000 model and the hybrid simulation, i.e. comparison of  $u$  from Figure 7-4. Figure 7-26 reveals that the SAP2000 numerical model accurately captures the experimentally measured displacement response of wall M6 especially in the first 5 seconds.

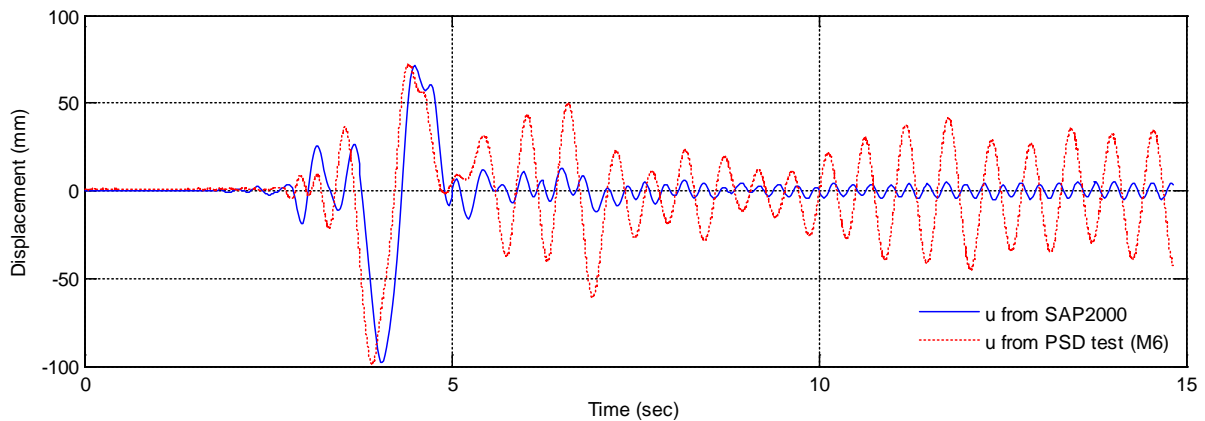


Figure 7-26 Time histories of  $u$  from the SAP2000 model and the hybrid simulation

The similarities between the two displacement responses degraded afterwards particularly in terms of displacement amplitudes. A possible explanation for the discrepancies is the previously mentioned actuator delay and undershoot. A numerical simulation in SAP2000 was conducted where the same numerical model was given a negative mass-and-stiffness proportional damping coefficients to test this assumption. Since it was observed that the actuator responses to command signals were at the least accurate at small displacement amplitudes, while on larger amplitudes these errors were negligible, the negative proportional damping was simulated only after 5.98 sec into the analysis. It was found that a critical damping ratio of -1.5% for the first and second elastic modes yielded a displacement time history as shown in Figure 7-27. Comparing the simulation results shown in Figure 7-26 and Figure 7-27 it was clear that the simulation with negative damping yielded better approximation of the hybrid simulation result both in amplitudes and oscillation frequencies.

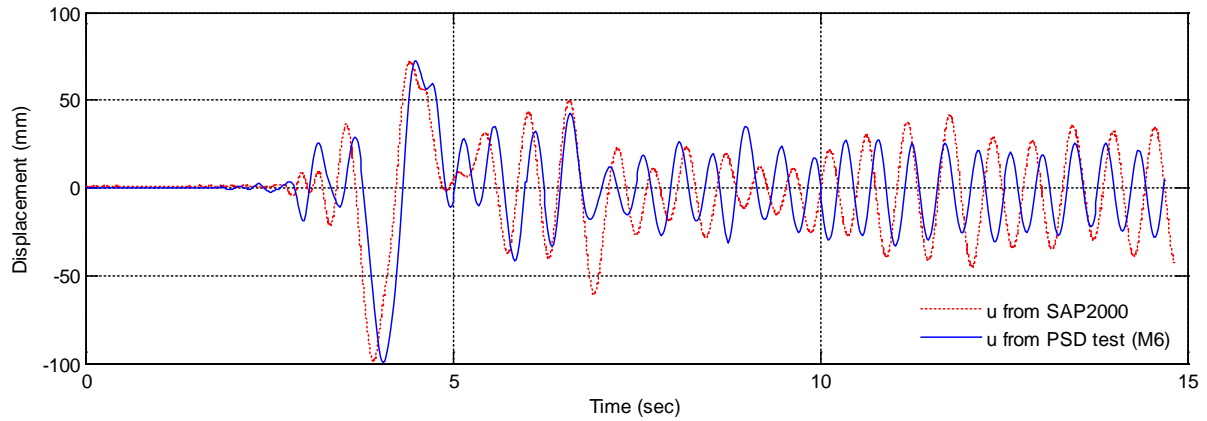


Figure 7-27 Time histories of  $u$  from the SAP2000 model with negative damping and the hybrid simulation

### 7.8.2. Modelling of the wall from the hybrid simulation with substructuring

The numerical model of wall M7 (with substructuring) consisted of two frame members connected by a joint representing the interface node. Figure 7-28 shows the schematic drawing of this numerical model. The numerical substructure was assumed to behave linear-elastically while all nonlinearities were assumed to concentrate in the physical substructure. The stiffness of the numerical substructure is given in Equation 7-6. Nonlinearities in this model was also assumed to be completely defined by the moment-rotation relationships of the rotational spring element. To enforce such condition, the frame element representing the physical substructure in the numerical model was made rigid by enforcing equal rotation constraint between the lower frame and the rotational spring elements.

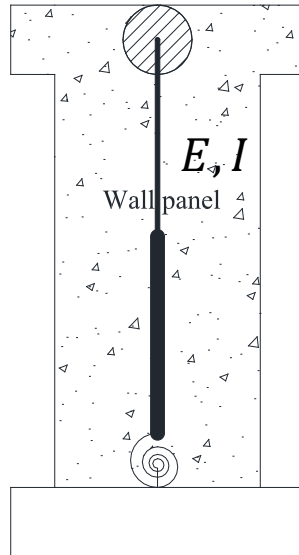


Figure 7-28 Schematic drawing of numerical model representing wall M7 (without substructuring)

Table 7-12 listed the parameters of the Pivot hysteresis rules that were determined through trial and error to produce the closest match between displacement responses from the model and the hybrid simulation result.

Parameters	Values
$\alpha_1$	3
$\alpha_2$	3
$\beta_1$	0.6
$\beta_2$	0.6
$\eta$	0

Table 7-12 Parameters for Pivot hysteresis rules in M6 numerical modelling

Figure 7-29 shows the displacement response time histories of the rigid element (i.e.  $u_1$  in Figure 7-5) of the numerical model and of the physical substructure (wall M7) from the hybrid simulation. Figure 7-29 reveals that the SAP2000 numerical model accurately captures the experimentally measured displacement response of wall M7 during the hybrid simulation particularly in the first 5 seconds. Note that unlike the numerical model of wall M6, the displacement response of the numerical model of wall M7 accurately captured the hybrid

simulation result at lower displacement amplitudes after the first 5 due to the properly tuned horizontal actuator.

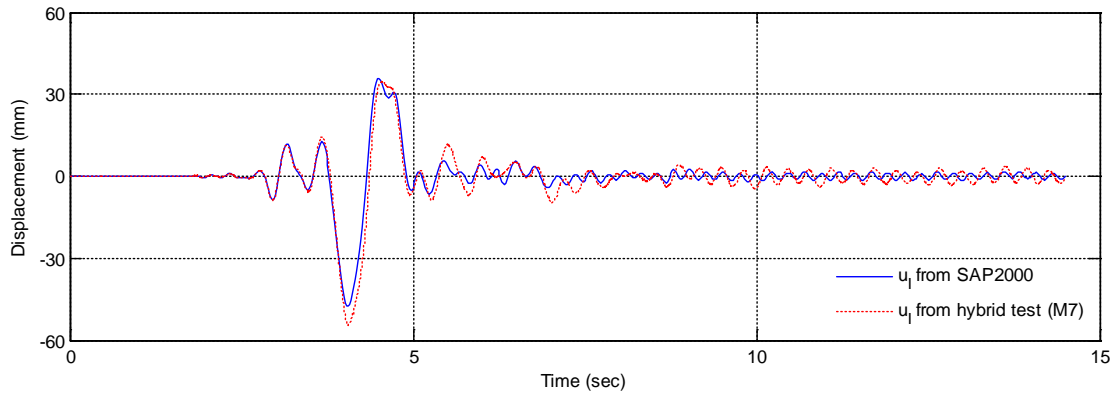


Figure 7-29 Time histories of  $u_1$  from the SAP2000 model and the hybrid simulation

## 7.9. Summary

This chapter presents experimental validations of the substructuring concept in the hybrid simulation method, to replicate a specimen's response as if the complete specimen is tested. The research aims to address the challenge that arises when the expected behaviour of the physical substructure is different from the complete structure, in this case is to replicate a flexure-dominant RC wall structure using a squat wall specimen with known shear-dominant behaviour. Due to errors in the coordinate transformation algorithms in both the hybrid simulation without and with substructuring coordinators, it is believed that the results of the experiments do not reflect the actual response of the prototype walls to the ground motion. However, comparison between the hybrid simulation without and with substructuring results also reveals insensitivity of the experiment results to the algorithm errors. In the presence of the errors, the hybrid simulation using squat wall as the physical substructure could closely replicate the flexure-dominant response of the complete wall specimen from the hybrid simulation in term of global force-deformation relationships as well as energy dissipation characteristics. Analysis into the data recorded from the array of instrumentations on each

tested wall still reveals different local behaviours such as different damage patterns that may be attributed to the algorithmic errors. Numerical simulations to validate the experimental results also seem to suggest that the experiments results may not be sensitive to the algorithm errors at all, since the simulations results match the experimental results with sufficient accuracy. The observations so far support the argument that the response of a complete specimen can be replicated through hybrid simulation using physical substructure with different expected behaviour.



# Chapter 8

## Conclusions

---

The hybrid simulation is a viable experimental method to simulate seismic response of structures. The method can replicate dynamic effects like in a shake table test while simultaneously offering the convenience of slow, large scale testing like in a quasi-static test. The reliability of a hybrid simulation result depends on minimising experimental errors. Experimental errors propagate and accumulate during a hybrid simulation, potentially lead to meaningless result. These errors, whether temporal or physical, are not exclusive to the hybrid simulation method but due to history dependency, they cannot be removed after the experiment has concluded. Some of the error sources can be minimised to negligible levels before the test. Others need special techniques to compensate for since they occur during the test.

The research presented in this thesis proposes methods to compensate some of the experimental errors that occur during a hybrid simulation. In particular, these errors include: 1) actuator delay due to inherent dynamics of control-actuator-specimen system, 2) high measurement noise, 3) position errors due to geometric change in multi-axial actuator-specimen setup, and 4) hybrid simulation with dissimilar physical substructure representation. The effect of displacement tracking strategies to energy dissipation characteristics in bidirectional hybrid simulations is also investigated.

Chapter 3 presents a new method to compensate for actuator delay in fast to real time hybrid simulation. Key findings from this chapter are as follows:

- There is inevitable delay in actuator response due to actuator dynamics, resulting in added energy into the specimen which can lead to instability. The proposed compensation method negates the added energy by introducing positive equivalent viscous damping of approximately the same magnitude. The method is intuitive since the hybrid simulation can be conducted without the need of displacement prediction or system identification.
- Numerical simulations and experimental validations of the proposed method were presented. For a small delay magnitude of 4 ms numerical simulations of the proposed method demonstrated excellent compensations for a linear elastic SDOF structure. During experimental validations, it was found that high measurement noise degraded the performance of the compensation method especially at small displacement increments. The use of adaptive gain addressed the noise problem. The gain controlled the timing at which the delay compensation operated based on displacement increment magnitudes.
- Parametric simulations using linear elastic SDOF structure showed that the stability limit of the proposed method depended on the natural period of the structure and the simulation time step size. It was found that the stability limit is smaller than those of existing delay compensation methods.

Chapter 4 investigates the application of Kalman filter to the hybrid simulation method through numerical simulations. The chapter presents the following key findings:

- Numerical simulations demonstrated that strong DOF coupling amplified the cumulative effect of measurement noise in the restoring force feedback to the displacement response. It was demonstrated that the Kalman filter algorithm was

capable to reduce noise without introducing time lag. The simulations with Kalman filter showed excellent agreement with ideal simulations results.

- Parametric simulations indicate that combining the delay compensation method proposed in Chapter 3 with the Kalman filter algorithm increased the stability limit of the compensation method by a factor of 5.
- The performance of the Extended Kalman Filter (EKF) algorithm for nonlinear simulations was less effective due to inaccurate estimations of tangent stiffness of the structure during simulations. The inaccuracies were the results of 1) estimating tangent stiffness from noisy force and displacement data, and 2) delay in the measured data causing the EKF algorithm to “track” different force-deformation curve from the ideal one.
- Parametric simulations showed that the EKF algorithm also significantly increased the stability limit of the proposed delay compensation method considering nonlinear behaviour. While simulation stabilities were successfully maintained, further research is required to improve accuracy of the simulation results.

Chapter 5 deals with techniques to accurately control multiple actuators in multi-axial experiments. Nonlinear Transformation (NLT) procedures were developed for this purpose. The procedures were adopted in experiments using the quasi-static and the hybrid simulation methods. The chapter presents the following key findings:

- Nonlinear transformation between the specimen DOF in the global coordinate system and the actuator coordinate system was required for multi-axial experiment. Linear transformation (i.e. simple matrix multiplication) does not consider the unavoidable

transverse movement of the specimen due to the connection between the specimen and the actuators at different loading axes.

- The applied NLT algorithm successfully maintained constant axial load and aspect ratio while aiming toward the required drift in the quasi-static tests. Experiment results showed that deviations of axial load and aspect ratio from the intended values were no more than 2.2% and 4% respectively.
- The importance of NLT procedure in multi-axial hybrid simulations was demonstrated through frequency domain analysis of force and displacement errors from a bidirectional hybrid simulation result. The analysis showed that a cumulative drift error as large as 0.75% at the end of experiment could result if NLT was not adopted during experiment. However, the frequency domain analysis result was an upper-bound estimate since it did not consider damping and yielding of the structure.

Chapter 6 investigates the effect of different displacement paths to energy dissipation characteristics of a bidirectional rocking column. The experiments were divided into quasi-static and hybrid simulation. In the quasi-static experiments, the column was subjected to bidirectional displacement patterns of linear, diamond, circular, and clover-shaped. In the hybrid simulations, for each set of two orthogonal ground motions, the column was subjected to three different displacement tracking strategies. The chapter presents the following key findings:

- Both experiments corroborated previous research which outlined maximum stress and energy dissipation capacity of nonlinear structure is dependent to the loading history.

- In quasi-static experiments, diamond and circular patterns resulted in the lowest strength envelope which was most likely due to the opposing nature of these patterns in the two orthogonal directions.
- In hybrid simulations, “staggering” displacement tracking strategies imposed additional damage accumulation on the column. The column appeared more flexible as the result, returning higher displacement amplitudes and lower forces compared to those resulting from the “direct” tracking.
- Longer deformation path resulted in higher ratio of hysteretic energy dissipation from externally mounted dissipators (EMD) compared to the total dissipated energy. Buckling was also detected in the EMD although it did not occur during component and uniaxial testing from previous research. It further highlights the importance of considering the effect of multidirectional load on such system.
- These results should inform structural designers to account for increased drift demand due to path dependency in bidirectional loading.

Chapter 7 presents hybrid simulation without and with substructuring on concrete walls. The chapter presents the following key findings:

- The tests aimed to validate the substructuring concept in the hybrid simulation method in the case where the physical substructure was expected to behave differently from the prototype structure. This was achieved using a squat wall as the physical substructure in the hybrid simulation with substructuring which had intrinsically shear-dominant behaviour to replicate flexure dominant behaviour of the prototype wall from the hybrid simulation without substructuring.

- Despite incorrectly formulated coordinate transformation algorithms on both tests, these errors seemed to have little impact since the result from the hybrid simulation with and without substructuring were very close in term of maximum force and displacement amplitudes. Numerical simulations were also able to closely replicate the results from both experiments, further suggesting insensitivity of the physical behaviours to the experimental errors.
- Unlike global responses, local responses such as crack patterns, deformation components, curvature distributions, and longitudinal reinforcement strains revealed different behaviours of the two specimens. It is still uncertain whether experimental errors including the incorrect transformation algorithm were the cause of the difference so further research is needed.

### **8.1. Future work**

Because of time limitation, not all aspects of the investigated topics can be addressed comprehensively in this study. This section presents a list of recommended future work that logically follows this study. The recommendations essentially surround the experimental validation for a combined Kalman filter-delay compensation algorithm, NLT procedures for multi-axial testing and hybrid simulation on concrete walls.

The combined Kalman filtered and the delay compensation method numerically simulated in this study should be experimentally validated. The study should examine linear and nonlinear, SDOF and MDOF systems and it should be extended to testing with numerical and physical substructures.

The accuracy of the NLT procedures should be validated in future studies by experimental results with ideal analytical solutions.

The hybrid simulation with substructuring method validation should be extended within wall structures and also into other specimen types. Related to the wall testing, future work should address the challenge when the physically tested wall has increasingly different behaviour from the prototype structure. For example, the length and thickness of the wall used as the physical substructure can be increased such that it can be expected to behave in pure shear without the substructuring technique. The hybrid testing versatility will be demonstrated if such physical substructure can replicate flexure dominant behaviour of a complete wall specimen with higher aspect ratio. There are also potential studies of hybrid simulation with dissimilar specimens for other prototype structures such as replicating the response of dual systems consisting of moment-resisting frame and wall structures as well as replicating floor slab-wall interactions.



# References

---

- [1] P.B. Shing, S.A. Mahin. Experimental error propagation in pseudodynamic testing. *Report No. UCB/EERC-83/12*. University of California, Berkeley, California, 1983.
- [2] C.A. Whyte, Hybrid simulation of the seismic response of squat reinforced concrete shear walls. *Ph.D. dissertation*, University of California, Berkeley, California, 2012.
- [3] R. Park. Evaluation of ductility of structures and structural assemblages from laboratory testing. *Bulletin of the New Zealand National Society for Earthquake Engineering*, **22** (3), 155-66, 1989.
- [4] G. Calvi, G. Kingsley. Problems and certainties in the experimental simulation of the seismic response of MDOF structures. *Engineering structures*, **18** (3), 213-26, 1996.
- [5] T.J. Hughes, *The finite element method: linear static and dynamic finite element analysis*. Courier Corporation, 2012.
- [6] C.A. Whyte, K.R. Mackie, B. Stojadinovic. Hybrid Simulation of Thermomechanical Structural Response. *Journal of Structural Engineering*, 04015107, 2015.
- [7] M. Nakashima, T. Akazawa, H. Igarashi. Pseudo-dynamic testing using conventional testing devices. *Earthquake engineering & structural dynamics*, **24** (10), 1409-22, 1995.
- [8] P.B. Shing, S.A. Mahin. Pseudodynamic test method for seismic performance evaluation: theory and implementation. *Report No. UCB/EERC-84/01*. University of California, Berkeley, California, 1984.
- [9] C.R. Thewalt, S.A. Mahin. Hybrid solution techniques for generalized pseudodynamic testing. *Report No. UCB/EERC-87/09*. University Of California, Berkeley, California, 1987.
- [10] H.E. Merritt, *Hydraulic control systems*. John Wiley & Sons, 1967.
- [11] MOOG Inc. Electrohydraulic Valves: A Technical Look.  
<http://www.moog.com/content/dam/moog/literature/ICD/Valves-Introduction.pdf>
- [12] G. Mosqueda, Continuous hybrid simulation with geographically distributed substructures. *Ph.D. dissertation*, University of California, Berkeley, California, 2003.
- [13] M. Ahmadizadeh, Real-time hybrid simulation procedures for reliable structural performance testing. University of New York, Buffalo, New York, 2007.
- [14] P.B. Shing, M.T. Vannan, E. Cater. Implicit time integration for pseudodynamic tests. *Earthquake engineering & structural dynamics*, **20** (6), 551-76, 1991.

- [15] A.H. Schellenberg, S.A. Mahin, G.L. Fenves. Advanced Implementation of Hybrid Simulation. University of California, Berkeley, 2009.
- [16] A.K. Chopra, *Dynamics of structures: Theory and Applications to Earthquake Engineering*. Ed. 3. New Jersey: Prentice Hall, 2007.
- [17] S.N. Dermitzakis, S.A. Mahin. Development Of Substructuring Techniques For On-line Computer Controlled Seismic Performance Testing. Earthquake Engineering Research Center, College Of Engineering, University Of California, Berkeley, California, 1985.
- [18] R. Severn. The development of shaking tables—a historical note. *Earthquake engineering & structural dynamics*, **40** (2), 195-213, 2011.
- [19] S. Dyke, B. Spencer Jr, P. Quast, M. Sain. Role of control-structure interaction in protective system design. *Journal of Engineering Mechanics*, **121** (2), 322-38, 1995.
- [20] J.A. Murcek, Evaluation of the effective force testing method using a SDOF model. *Master thesis*, University of Minnesota, Minnesota, 1996.
- [21] J. Dimig, C. Shield, C. French, F. Bailey, A. Clark. Effective force testing: a method of seismic simulation for structural testing. *Journal of Structural Engineering*, **125** (9), 1028-37, 1999.
- [22] J.C. Timm, Natural velocity feedback correction for effective force testing. *Master thesis*, University of Minnesota, Minnesota, 1999.
- [23] J. Zhao, C. French, C. Shield, T. Posbergh. Considerations for the development of real-time dynamic testing using servo-hydraulic actuation. *Earthquake Engineering and Structural Dynamics*, **32** (11), 1773-94, 2003.
- [24] C. Chen, Development and Numerical Simulation of Hybrid Effective Force Testing Method. *Ph.D. dissertation*, Lehigh University, Bethlehem, Pennsylvania, 2007.
- [25] N. Nakata. Effective force testing using a robust loop shaping controller. *Earthquake engineering & structural dynamics*, **42** (2), 261-75, 2013.
- [26] H.M. Hilber, T.J.R. Hughes, R.L. Taylor. Improved numerical dissipation for time integration algorithms in structural dynamics. *Earthquake engineering & structural dynamics*, **5** (3), 283-92, 1977.
- [27] C. Chen, J.M. Ricles. Development of direct integration algorithms for structural dynamics using discrete control theory. *Journal of engineering mechanics*, **134**, 676, 2008.
- [28] M. Nakashima, H. Kato, E. Takaoka. Development of real-time pseudodynamic testing. *Earthquake Engineering and Structural Dynamics*, **21** (1), 79-92, 1992.
- [29] M. Nakashima, N. Masaoka. Real-time on-line test for MDOF systems. *Earthquake Engineering and Structural Dynamics*, **28** (4), 393-420, 1999.

- [30] A.P. Darby, A. Blakeborough, M.S. Williams. Real-time substructure tests using hydraulic actuator. *Journal of Engineering Mechanics*, **125** (10), 1133-39, 1999.
- [31] R.-Y. Jung, Development of real-time hybrid test system. *Ph.D. dissertation*, University of Colorado at Boulder, Ann Arbor, Michigan, 2005.
- [32] T. Horiuchi, M. Inoue, T. Konno, Y. Namita. Real-time hybrid experimental system with actuator delay compensation and its application to a piping system with energy absorber. *Earthquake Engineering and Structural Dynamics*, **28** (10), 1121-41, 1999.
- [33] T. Horiuchi, T. Konno, T. Horiuchi, T. Konno. A new method for compensating actuator delay in real-time hybrid experiments. *Philosophical Transactions of the Royal Society of London. Series A: Mathematical, Physical and Engineering Sciences*, **359** (1786), 1893-909, 2001.
- [34] A.P. Darby, M.S. Williams, A. Blakeborough. Stability and delay compensation for real-time substructure testing. *Journal of Engineering Mechanics*, **128** (12), 1276-84, 2002.
- [35] J.E. Carrion, B. Spencer, Real-time hybrid testing using model-based delay compensation. *Proceedings of the 4th International Conference on Earthquake Engineering*, Taipei, Taiwan, 2006
- [36] M. Ahmadizadeh, G. Mosqueda, A. Reinhorn. Compensation of actuator delay and dynamics for real-time hybrid structural simulation. *Earthquake Engineering and Structural Dynamics*, **37** (1), 21-42, 2008.
- [37] J.E. Carrion, B. Spencer, B.M. Phillips. Real-time hybrid simulation for structural control performance assessment. *Earthquake Engineering and Engineering Vibration*, **8** (4), 481-92, 2009.
- [38] M. Wallace, J. Sieber, S. Neild, D. Wagg, B. Krauskopf. Stability analysis of real-time dynamic substructuring using delay differential equation models. *Earthquake engineering & structural dynamics*, **34** (15), 1817-32, 2005.
- [39] C. Chen, J.M. Ricles. Tracking error-based servohydraulic actuator adaptive compensation for real-time hybrid simulation. *Journal of Structural Engineering*, **136** (4), 432-40, 2010.
- [40] O. Mercan, Analytical and Experimental Studies on Large Scale, Real-time Pseudodynamic Testing. *Ph.D. Dissertation*, Lehigh University, Bethlehem, Pa., 2007.
- [41] P. Bonnet, C. Lim, M. Williams, A. Blakeborough, S. Neild, D. Stoten, C. Taylor. Real-time hybrid experiments with Newmark integration, MCSmd outer-loop control and multi-tasking strategies. *Earthquake Engineering and Structural Dynamics*, **36** (1), 119-41, 2007.
- [42] Y. Chae, K. Kazemibidokhti, J.M. Ricles. Adaptive time series compensator for delay compensation of servo-hydraulic actuator systems for real-time hybrid simulation. *Earthquake Engineering & Structural Dynamics*, **42** (11), 1697-715, 2013.

- [43] R. Christenson, Y.Z. Lin, A. Emmons, B. Bass. Large-scale experimental verification of semiactive control through real-time hybrid simulation *Journal of Structural Engineering*, **134** (4), 522-34, 2008.
- [44] T. Elkhoraibi, K.M. Mosalam. Towards error-free hybrid simulation using mixed variables. *Earthquake Engineering and Structural Dynamics*, **36** (11), 1497-522, 2007.
- [45] J. Liu, S.J. Dyke, H.-J. Liu, X.-Y. Gao, B. Phillips. A novel integrated compensation method for actuator dynamics in real-time hybrid structural testing. *Structural Control and Health Monitoring*, 2012.
- [46] C.R. Thewalt, M. Roman. Performance parameters for pseudodynamic tests. *Journal of Structural Engineering*, **120** (9), 2768-81, 1994.
- [47] G. Mosqueda, B. Stojadinovic, S.A. Mahin. Real-time error monitoring for hybrid simulation. Part I: Methodology and experimental verification. *Journal of Structural Engineering*, **133** (8), 1100-08, 2007.
- [48] G. Mosqueda, B. Stojadinovic, S.A. Mahin. Real-time error monitoring for hybrid simulation. Part II: structural response modification due to errors. *Journal of Structural Engineering*, **133** (8), 1109-17, 2007.
- [49] M. Ahmadizadeh, G. Mosqueda. Online energy-based error indicator for the assessment of numerical and experimental errors in a hybrid simulation. *Engineering Structures*, **31** (9), 1987-96, 2009.
- [50] J.E. Carrion, B. Spencer. Model-based Strategies for Real-time Hybrid Testing. *Report No. UILU-ENG-2007-1806*. University of Illinois at Urbana-Champaign, Champaign, Illinois, 2007.
- [51] M.J. Hashemi, Collapse simulation of multi-story buildings through hybrid testing with substructuring techniques. State University of New York at Buffalo, 2013.
- [52] M. Wallace, D. Wagg, S. Neild. An adaptive polynomial based forward prediction algorithm for multi-actuator real-time dynamic substructuring. *Proceedings of the Royal Society A: Mathematical, Physical and Engineering Science*, **461** (2064), 3807-26, 2005.
- [53] G. Vijayaraghavan, M. Brown, M. Barnes, *Practical grounding, bonding, shielding and surge protection*. Butterworth-Heinemann, 2004.
- [54] G. Magonette. Development and application of large-scale continuous pseudodynamic testing techniques. *Philosophical Transactions of the Royal Society of London. Series A: Mathematical, Physical and Engineering Sciences*, **359** (1786), 1771-99, 2001.
- [55] A. Mueller, Real-Time Hybrid Simulation with Online Model Updating. Western Michigan University 2014.

- [56] Y.-K. Wen. Method for random vibration of hysteretic systems. *Journal of the engineering mechanics division*, **102** (2), 249-63, 1976.
- [57] T.T. Baber, M.N. Noori. Random vibration of degrading, pinching systems. *Journal of Engineering Mechanics*, 1985.
- [58] E. Wilson, A. Habibullah. SAP2000 integrated finite element analysis and design of structures. *Analysis reference. Computers and Structures*, 1997.
- [59] J. Nocedal. Updating quasi-Newton matrices with limited storage. *Mathematics of computation*, **35** (151), 773-82, 1980.
- [60] C.G. Broyden. A class of methods for solving nonlinear simultaneous equations. *Mathematics of computation*, **19** (92), 577-93, 1965.
- [61] C.C. Hung, S. El-Tawil. A method for estimating specimen tangent stiffness for hybrid simulation. *Earthquake Engineering & Structural Dynamics*, **38** (1), 115-34, 2009.
- [62] W. Song, S. Dyke. Real-Time Dynamic Model Updating of a Hysteretic Structural System. *Journal of Structural Engineering*, **140** (3), 04013082, 2014.
- [63] M.J. Hashemi, A. Masroor, G. Mosqueda. Implementation of online model updating in hybrid simulation. *Earthquake engineering & structural dynamics*, **43** (3), 395-412, 2014.
- [64] G. Ou, A. Ozdagli, S. Dyke, A. Prakash. RTHS WITH CONCURRENT MODEL UPDATING ON A DISTRIBUTED PLATFORM.
- [65] C.R. Thewalt, S.A. Mahin. Non-Planar Pseudodynamic Testing. *Earthquake Engineering and Structural Dynamics*, **24**, 733-46, 1995.
- [66] S.A. Mahin, P.B. Shing, C.R. Thewalt, R.D. Hanson. Pseudodynamic test method: current status and future directions. *Journal of Structural Engineering*, **115** (8), 2113-28, 1989.
- [67] F. Molina, G. Verzeletti, G. Magonette, P. Buchet, M. Geradin. Bi-directional pseudodynamic test of a full-size three-storey building. *Earthquake Engineering and Structural dynamics*, **28** (12), 1541-66, 1999.
- [68] G.Y. Liu, S.Y. Chang, Bi-axial pseudodynamic testing. *Proceedings of the 12th World Conference on Earthquake Engineering*, Auckland, New Zealand, 2000
- [69] K.C. Tsai, H.Y. Wang, C.H. Chen, G.Y. Liu, K.J. Wang. Substructure Pseudo Dynamic Performance of Hybrid Steel Shear Panels. *Steel Structures*, **1**, 95-103, 2001.
- [70] M. Obata, Y. Goto. Development of multidirectional structural testing system applicable to pseudodynamic test. *Journal of Structural Engineering*, **133** (5), 638-45, 2007.

- [71] O. Mercan, J.M. Ricles, R. Sause, T. Marullo. Kinematic transformations for planar multi-directional pseudodynamic testing. *Earthquake Engineering and Structural Dynamics*, **38** (9), 1093-119, 2009.
- [72] M.J. Hashemi, R. Al-Mahaidi, R. Kalfat, G. Burnett. Development and validation of multi-axis substructure testing system for full-scale experiments. *Australian Journal of Structural Engineering*, **16** (4), 302-15, 2015/10/30, 2015.
- [73] Y. Lu, R.J. Gultom, R.S. Henry, Q.T. Ma. Cycling Testing of Reinforced Concrete Walls with Distributed Minimum Vertical Reinforcement. *Journal of Structural Engineering* 2015.
- [74] American Concrete Institute, ACI 374.2R-13. Guide for Testing Reinforced Concrete Structural Element under Slowly Applied Simulated Seismic Loads. Farmington Hills, Michigan, 2013
- [75] American Concrete Institute, ACI ITG-5.1-07. ACI ITG-5.1-07. Acceptance Criteria for Unbonded Post-Tensioned Precast Structural Walls Based on Validation Testing and Commentary. Michigan, USA, 2008
- [76] Standards New Zealand, Part 5: Earthquake actions - New Zealand. Structural Design Actions. Wellington, New Zealand, 2004
- [77] W.H. Press, S.A. Teukolsky, W.T. Vetterling, B.P. Flannery. Numerical recipes in FORTRAN 77, vol. 1. New York, NY: Press Syndicate of the University of Cambridge, 1992.
- [78] G. Dahlquist, A. Bjorck, N. Anderson, *Numerical Methods*. Prentice-Hall series in Automatic Computation. Prentice-Hall, 1974.
- [79] CEN, Eurocode 8: Design Provisions for Earthquake Resistance of Structures, Part 1.1: General rules, seismic actions and rules for buildings. 2013
- [80] E. Watanabe, K. Sugiura, W.O. Oyawa. Effects of multi-directional displacement paths on the cyclic behaviour of rectangular hollow steel columns. *Structural Engineering/Earthquake Engineering*, **17** (1), 69-85, 2000.
- [81] S.N. Bousias, G. Verzeletti, M.N. Fardis, E. Gutierrez. Load-path effects in column biaxial bending with axial force. *Journal of Engineering Mechanics*, **121** (5), 596-605, 1995.
- [82] F. Qiu, W. Li, P. Pan, J. Qian. Experimental tests on reinforced concrete columns under biaxial quasi-static loading. *Engineering structures*, **24** (4), 419-28, 2002.
- [83] J. Stanton, W.C. Stone, G.S. Cheok. A hybrid reinforced precast frame for seismic regions. *PCI journal*, **42** (2), 20-32, 1997.
- [84] D. Marriott, S. Pampanin, A. Palermo. Biaxial testing of unbonded post-tensioned rocking bridge piers with external replacable dissipaters. *Earthquake Engineering & Structural Dynamics*, **40** (15), 1723-41, 2011.

- [85] M. Priestley, G. Calvi, M. Kowalsky, Direct displacement-based seismic design of structures. paper presented at the 5th New Zealand Society for Earthquake Engineering Conference, Palmerston North, New Zealand, 30 March-1 April 2007.
- [86] D.J. Marriott, The development of high-performance post-tensioned rocking systems for the seismic design of structures. *Ph.D. Dissertation*, University of Canterbury, Christchurch, 2009.
- [87] C.A. Oyarzo-Vera, G.H. McVerry, J.M. Ingham. Seismic zonation and default suite of ground-motion records for time-history analysis in the North Island of New Zealand. *Earthquake Spectra*, **28** (2), 667-88, 2012.
- [88] S. Pampanin, M.N. Priestley, S. Sritharan. Analytical modelling of the seismic behaviour of precast concrete frames designed with ductile connections. *Journal of Earthquake Engineering*, **5** (03), 329-67, 2001.
- [89] NZS3101:2006, Concrete Structures Standard. Standards New Zealand, Wellington, New Zealand, 2006
- [90] H. Rodrigues, H. Varum, A. Arêde, A. Costa. A comparative analysis of energy dissipation and equivalent viscous damping of RC columns subjected to uniaxial and biaxial loading. *Engineering structures*, **35**, 149-64, 2012.
- [91] D.N. Grant, C. Blandon, M. Priestley. Modelling inelastic response in direct displacement-based design. 2005.
- [92] M.J. Priestley, G.M. Calvi, M. Kowalsky, *Displacement-Based Seismic Design of Structures*. Pavia: IUSS Press, 2007.
- [93] H. Hiraishi, Evaluation of shear and flexural deformations of flexural type shear walls. *Proceedings of the Proc. Of 8th WCEE*, 1984
- [94] M. Priestley, M. Kowalsky. Aspects of drift and ductility capacity of rectangular cantilever structural walls. *Bulletin of the New Zealand National Society for Earthquake Engineering*, **31** (2), 73-85, 1998.
- [95] R.K. Dowell, F. Seible, E.L. Wilson. Pivot hysteresis model for reinforced concrete members. *Structural Journal*, **95** (5), 607-17, 1998.



# Appendix A

## Implementation of proposed delay compensation method

---

The numerical verification in section 3.5 is implemented in MATLAB through the following

code

```
% Numerical verification of proposed delay compensation using variable
% damping correction

%% initialisation
% clear workspace
close all;clear;clc

% import ground motion
% ground motion should have time in the first column, value in the second
% column. Change as required
load('Tabas.mat'); % place ground motion in the same folder as script
t=udgg(:,1); % time vector, change variable name "udgg" as required
udgg=udgg(:,2); % value vector, change variable name "udgg" as required

% integration time step size
dt=t(2)-t(1); % constant time step size
Ndata=length(t); % length of data for for-loop purpose
g = 9.81; % gravity acceleration

%% structural properties

m=1000; % mass at floor level; kg (ton)
k=158000; % stiffness at each floor; N/m
ksi=0.02; % percentage of critical damping
c=2*ksi*(k*m)^0.5; % damping coefficient

%% set up analysis

% set up vector sizes for efficient computation
u=zeros(Ndata,1); % displacement
ud=u;udd=u;r=k*u; % velocity, acceleration, restoring force

% set up vector to monitor energy error
Sum_Eer=u; % sum of energy error by proposed method
Sum_EerTR=u; % sum of energy error by Thewalt and Roman (1994)
Sum_EerMo=u; % sum of energy error ny Mosqueda

F=-m*udgg; % external excitation, kN
udd(1)=1/m*(F(1)-c*ud(1)-r(1)); % acceleration response at t=0

%% run reference analysis without errors
```

```

% solved using NEM
for i=1:Ndata-1
    u(i+1)=u(i)+dt*ud(i)+0.5*dt^2*udd(i); % command displacement for
current time-step
    r(i+1)=k*u(i+1); % restoring force after displacement is applied
    udd(i+1)=1/(m+dt/2*c)*(F(i+1)-r(i+1)-c*ud(i)-dt/2*c*udd(i)); %
acceleration response
    ud(i+1)=ud(i)+dt/2*(udd(i) + udd(i+1)); % velocity
end

%% run analysis with simulated error
close all;
% set up vector sizes
ue=zeros(size(u)); % ue is command displacement for this simulation
um=ue; % um is measured displacement for this simulation, will be different
from ue due to simulated delay
ve=ue; % velocity response for this simulation
rm=k*um; % measured restoring force for this simulation, dependent on um
instead of ue
ae=ue;ae(1)=(1/m)*(F(1)-c*ve(1)-rm(1)); % acceleration response; initial
acceleration response
re=k*ue; % ideal restoring force

% delay simulation
mn=-0.01; % mean of random number, must be negative to simulate delay
% mean is proportional to the magnitude of delay
sd=0.001; % standard deviation of random number

% generate random number
simdelay=mn+sd*randn(Ndata,1);

clear i;
for i=1:Ndata-1
    ue(i+1)=ue(i)+dt*ve(i)+0.5*dt^2*ae(i);% command displacement
    um(i+1)=ue(i)+simdelay(i+1)*(ue(i+1)-ue(i));% feedback displacement
with delay
    rm(i+1)=k*um(i+1); % measured restoring force
    ae(i+1)=1/(m+dt/2*c)*(F(i+1)-rm(i+1)-c*ve(i)-dt/2*c*ae(i)); %
acceleration response
    ve(i+1)=ve(i)+dt/2*(ae(i)+ae(i+1)); % velocity response
end

%% run analysis with proposed delay compensation
close all;clc

% set up vector sizes
uc=zeros(size(u)); % ue is command displacement for this simulation
umc=uc; % um is measured displacement for this simulation, will be
different from uc due to simulated delay
vc=uc; % velocity response for this simulation
rmc=k*umc; % measured restoring force for this simulation, dependent on umc
instead of uc
ac=uc;ac(1)=(1/m)*(F(1)-c*vc(1)-rmc(1)); % acceleration response; initial
acceleration response
rc=k*uc; % ideal restoring force
cadd=uc; % required additional damping

for i=1:Ndata-1
    uc(i+1)=uc(i)+dt*vc(i)+0.5*dt^2*ac(i);
    umc(i+1)=uc(i)+simdelay(i+1)*(uc(i+1)-uc(i));% feedback displacement
with delay

```

```

rmc(i+1)=k*umc(i+1); % measured restoring force
% calculate ideal restoring force, cannot be done in real experiment
% especially in nonlinear cases
rc(i+1)=k*uc(i+1); % ideal restoring force

% calculation of strain energy and energy error from proposed method
Ee=0.5*(uc(i+1)+uc(i))*(rmc(i+1)-rmc(i)); % energy observed by
numerical integration (Equation 3-9)
Ebe=0.5*(umc(i+1)+umc(i))*(rmc(i+1)-rmc(i)); % actual energy in the
structure (Equation 3-10)
Eer=Ebe-Ee; % energy error (Equation 3-11)
Sum_Eer(i+1)=Sum_Eer(i)+Eer(i+1); % cumulative energy error

% calculation of strain energy and energy error from Thewalt-Roman
ETR=0.5*(rmc(i)+rmc(i+1)-rc(i)-rc(i+1))*(uc(i+1)-uc(i)); % Equation 3-5
Sum_EerTR(i+1) = Sum_EerTR(i)+ETR;

% calculation of strain energy and energy error from Mosqueda et al.
EeMo=0.5*(rmc(i+1)+rmc(i))*(uc(i+1)-uc(i)); % energy observed by
numerical integration (Equation 3-7)
EbeMo(i+1)=0.5*(rmc(i+1)+rmc(i))*(umc(i+1)-umc(i)); % actual energy in
the structure (Equation 3-8)
EerMo(i+1)=EeMo(i+1)-EbeMo(i+1); % energy error (Equation 3-6)
Sum_EerMo(i+1)=Sum_EerMo(i)+EerMo(i+1); % cumulative energy error

% calculate predicted velocity (Equation 3-15)
vp=vc(i)+dt*ac(i);

% calculate required additional damping (Equation 3-13)
% to avoid numerical error due to division by small amount, when the sum
% of velocities term become very small due, the required additional
% damping adopts the last calculated value
if sign(vc(i))==sign(vp)
    cadd(i+1)=-2*Eer/((vc(i)+vp)*(uc(i+1)-uc(i)));
else
    cadd(i+1)=cadd(i);
end

ac(i+1)=1/(m+dt/2*c)*(F(i+1)-rmc(i+1)-c*vc(i)-dt/2*c*ac(i)); %
acceleration response
vc(i+1)=vc(i)+dt/2*(ac(i)+ac(i+1)); % velocity response
end

```

A sample of SIMULINK application of the hybrid simulation coordinator with the proposed delay compensation method can be found in the following page.



Figure A-1 Root model

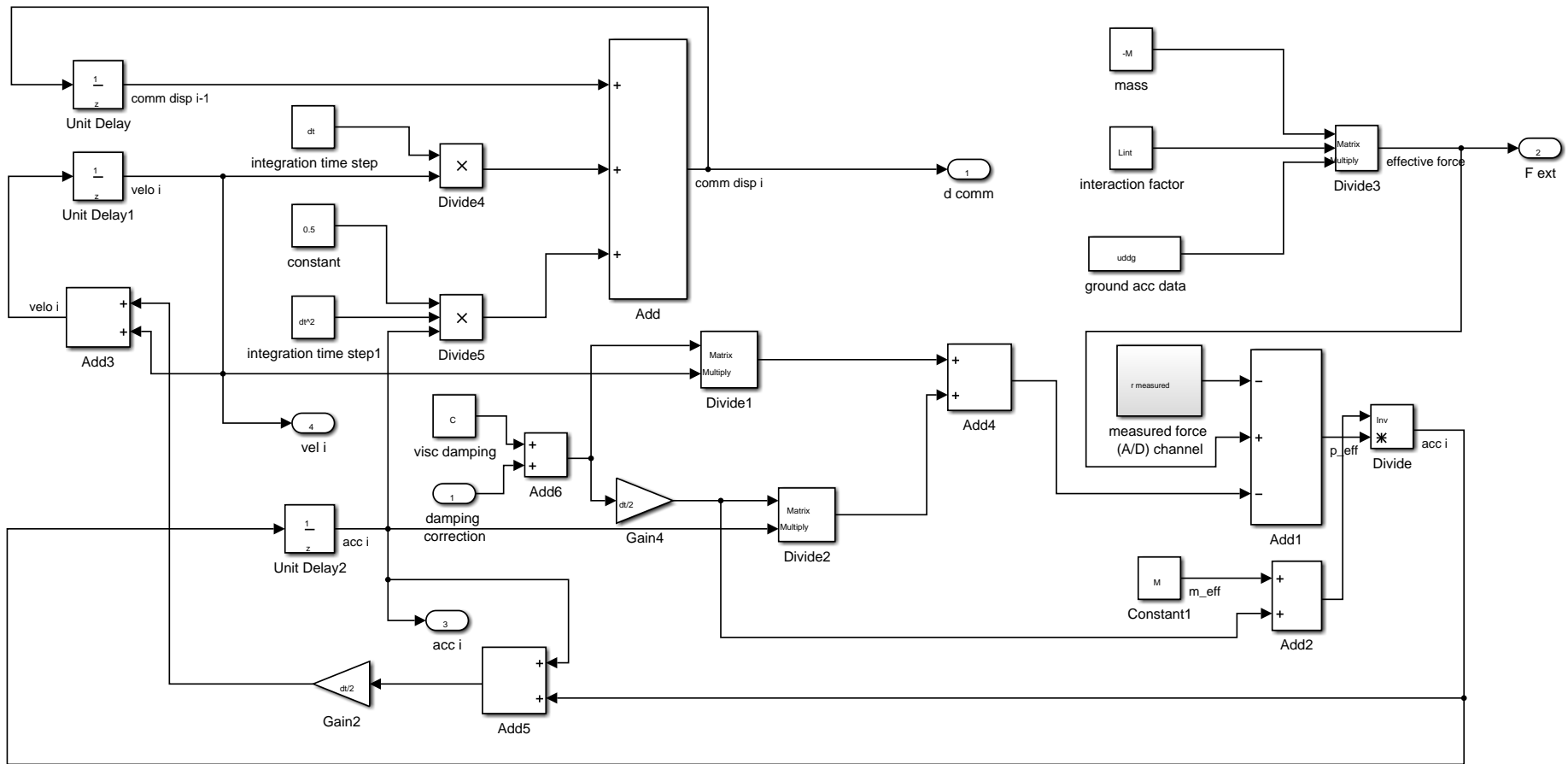


Figure A-2 "NEM integration" subsystem

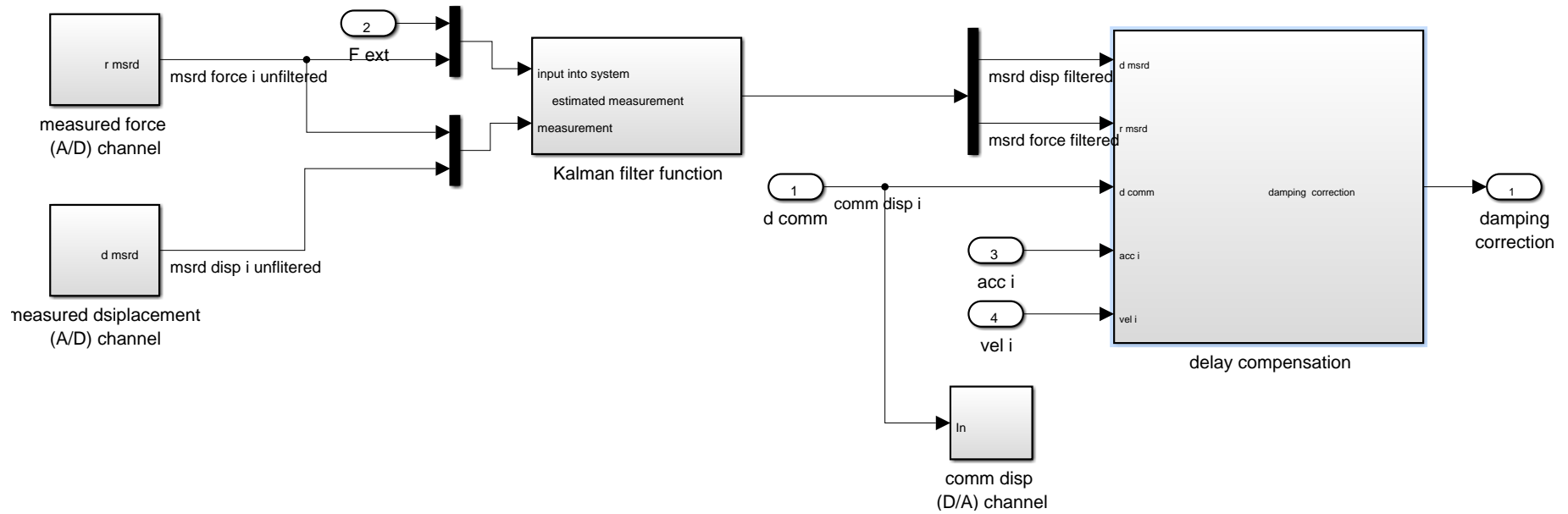


Figure A-3 "Experimental structure and compensation" subsystem

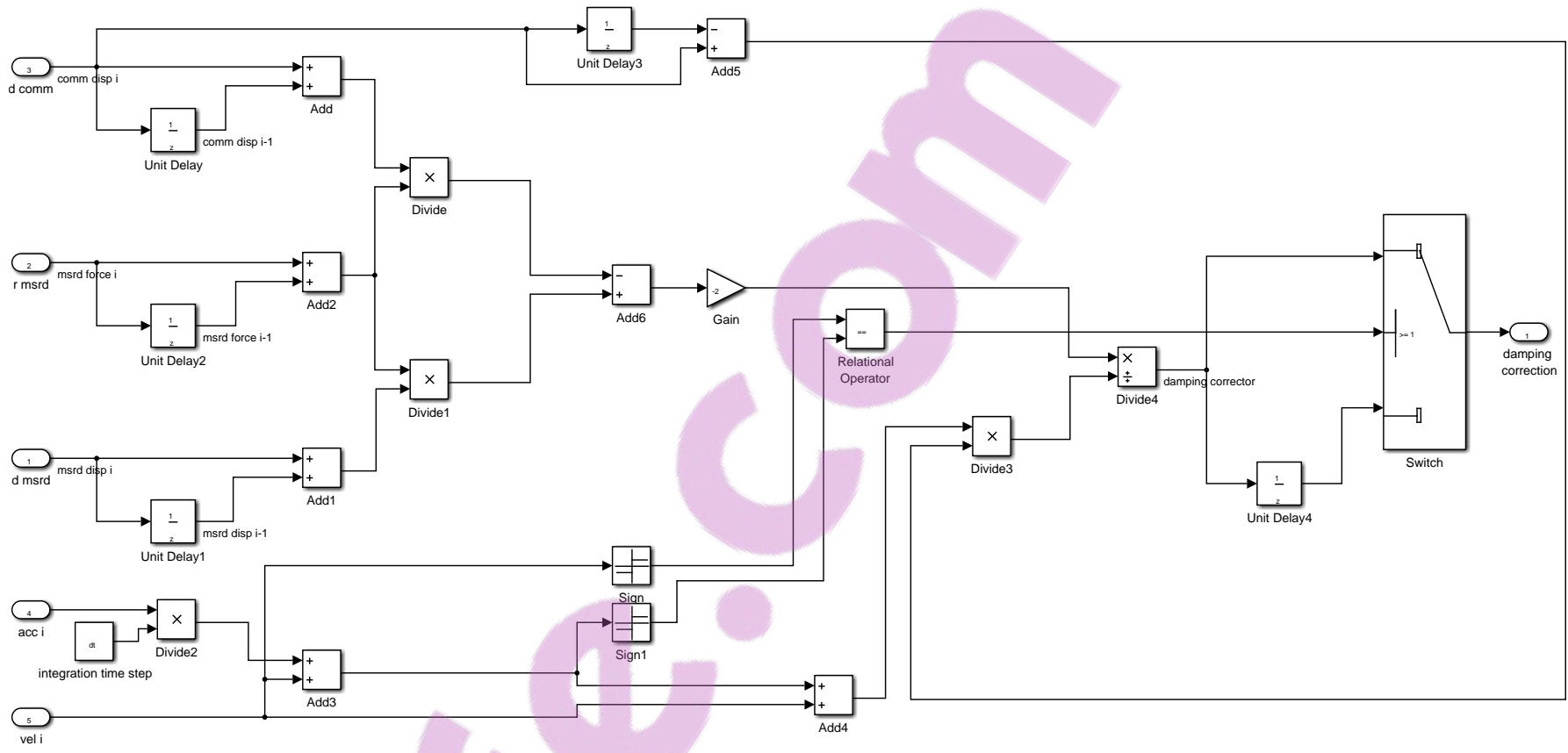


Figure A-4 Delay compensation subsystem

# Appendix B

## Bouc-Wen equation solver

---

The Bouc-Wen model for nonlinear force-deformation relationship is defined by the equations:

$$\dot{u}_h(t) = \frac{1}{u_y} \left[ \dot{u}(t) - \gamma |\dot{u}(t)| |u_h(t)| |u_h(t)|^{\eta-1} - \beta \dot{u}(t) |u_h(t)|^\eta \right] \quad \text{A-1}$$

$$R(t) = \alpha K^e u(t) + (1 - \alpha) K^e u_y u_h(t) \quad \text{A-2}$$

with the following variables

$u_y$  : yield displacement

$u_h$  : hysteretic displacement

$\gamma, \beta, \eta$  : parameters that control the shape of the hysteretic curve

$\alpha$ : the ratio of post- to pre-yield stiffness,  $0 \leq \alpha \leq 1$

The equations can be solved using fourth order Runge-Kutta method. The general purpose of the method is to solve an ordinary differential equation

$$\frac{dy}{dx} = f(x, y) \quad \text{A-3}$$

by changing  $x$  and  $y$  in small steps within a step size  $h$ , starting from initial conditions  $x = x_0$

and  $y = y_0$ .

Equation A-3 is solved using recurrence formulas defined as

$$y_{n+1} = y_n + h \frac{1}{6} (k_1 + k_2 + k_3 + k_4)$$

$$k_1 = f(x, y)$$

$$k_2 = f\left(x + \frac{h}{2}, y + \frac{h}{2}k_1\right)$$

$$k_3 = f\left(x + \frac{h}{2}, y + \frac{h}{2}k_2\right)$$

$$k_4 = f\left(x + \frac{h}{2}, y + hk_3\right)$$

The Bouc-Wen solver is implemented as a MATLAB function in the following script

```
function [f_r,Z1] =
bouc_wen(dt,u_bouc,ud_bouc,udd_bouc,dy,gamma,n,beta,Z,alpha,kspring)

% bouc-wen equation solver
% input:
% dt: time step size
% u_bouc: current displacement
% ud_bouc: predictor velocity
% udd_bouc: predictor acceleration
% dy: yield displacement
% gamma: bouc-wen parameter 1
% n: bouc-wen parameter 2
% beta: bouc-wen parameter 3
% Z: previous hysteretic displacement
% alpha: post-to-pre yield stiffness ratio
% kspring: pre-yield (elastic) stiffness
% output:
% f_r: restoring force
% Z1: current hysteretic displacement
vp=ud_bouc;
k1=1/dy*(vp-gamma*abs(vp).*Z.*abs(Z).^(n-1)-beta*vp.*abs(Z).^n);
vp=ud_bouc+0.5*dt*udd_bouc;
Za=Z+dt/2*k1;
k2=1/dy*(vp-gamma*abs(vp).*Za.*abs(Za).^(n-1)-beta*vp.*abs(Za).^n);
vp=ud_bouc+0.5*dt*udd_bouc;
Zb=Z+dt/2*k2;
k3=1/dy*(vp-gamma*abs(vp).*Zb.*abs(Zb).^(n-1)-beta*vp.*abs(Zb).^n);
vp=ud_bouc+dt*udd_bouc;
Zc=Z+dt*k3;
k4=1/dy*(vp-gamma*abs(vp).*Zc.*abs(Zc).^(n-1)-beta*vp.*abs(Zc).^n);
Z1=Z+dt/6*(k1+2*k2+2*k3+k4);
f_r=alpha*kspring*u_bouc+(1-alpha)*kspring*Z1*dy;
```

Numerical verification is conducted using a 2 DOF shear frame by comparing the analysis

result from the written MATLAB function and the analysis result from SAP2000.

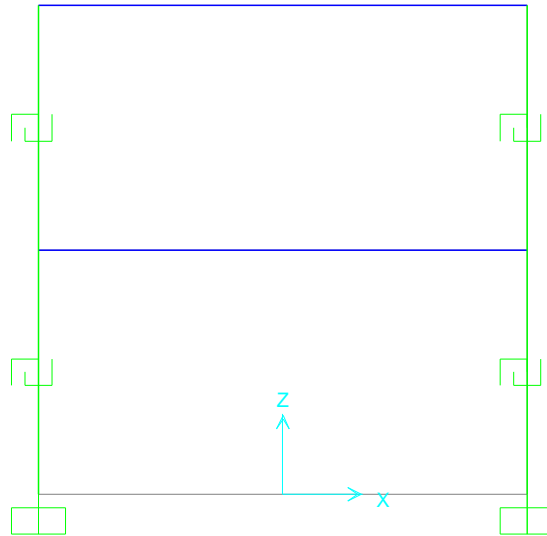


Figure B-1 2-DOF shear frame for Bouc-Wen MATLAB verification

Figure A-1 shows the 2 DOF shear frame where the beam at each storey is axially rigid. Nonlinear behaviour is completely provided by the frame's columns defined entirely by Link elements acting as shear springs, where Plastic (Wen) behaviour is selected as the nonlinearity type. The models were subjected to 1978 Tabas earthquake (Iran), scaled to 50 % amplitude. Since the Plastic (Wen) nonlinearity type in SAP2000 does not provide the option to specify the Bouc-Wen parameters defined in Equation A-1, these parameters are varied inside the MATLAB simulation.

Table A-1 shows the selected Bouc-Wen parameters that result in the closest approximation between the simulation results from MATLAB and SAP2000.

Figure A-2 shows comparison of force and relative displacement at each DOF of the shear frame model between MATLAB and SAP2000 simulation results. The results from both simulations are within reasonable similarity which confirm the validity of the MATLAB Bouc-Wen solver function.

$\alpha$	0
$\beta$	0.55
$\gamma$	0.45
$\eta$	2

Table A-1 Bouc-Wen parameters in MATLAB verification

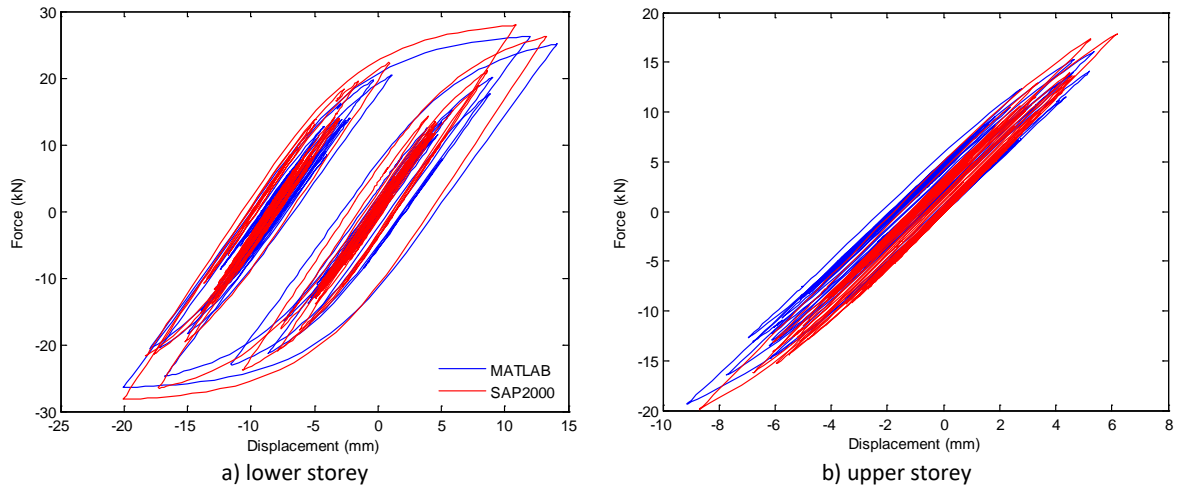


Figure B-2 Comparison of force and displacement for Bouc-Wen MATLAB verification

# Appendix C

## NEM state matrices for EKF

---

The EKF state matrices specific to the explicit Newmark integration algorithm (NEM) can be formulated following the relationship defined as

$$\mathbf{f}(\hat{\mathbf{z}}_i^-) = \mathbf{A}\hat{\mathbf{z}}_{i-1} + \mathbf{B}\bar{\mathbf{u}}_i \quad \text{B-1}$$

$\mathbf{A}$ ,  $\mathbf{B}$ ,  $\mathbf{z}$ , and  $\mathbf{u}$  are defined in Equation 4-18, 4-21, 4-27, and 4-28 respectively. According to Equation 4-44,  $\mathbf{F}(\hat{\mathbf{z}}_i)$  can be defined as

$$\mathbf{F}(\hat{\mathbf{z}}_i) = \mathbf{A} + \mathbf{B}\mathbf{Y} \quad \text{B-2}$$

$$\mathbf{Y} = \begin{bmatrix} 0 & \cdots & 0 \\ \vdots & \ddots & \vdots \\ 0 & \cdots & 0 \\ \hat{\mathbf{k}}_{m=1,n=1} & \cdots & \hat{\mathbf{k}}_{m=1,n=N_{\text{dof}}} \\ \vdots & \ddots & \vdots \\ \hat{\mathbf{k}}_{m=N_{\text{dof}},n=1} & \cdots & \hat{\mathbf{k}}_{m=N_{\text{dof}},n=N_{\text{dof}}} \end{bmatrix}_{(N_{\text{msr}} \times N_{\text{dof}}) \times (N_{\text{state}} \times N_{\text{dof}})} \quad \text{B-3}$$

$\hat{\mathbf{k}}_{m,n}$  is defined in Equation 4-26 where the stiffness terms are replaced by the terms from tangent stiffness matrix instead of the initial one. In addition, the term  $\mathbf{H}(\hat{\mathbf{z}}_i^-)$  from Equation 4-44 is identically defined by Equation 4-23, with the terms in  $\hat{\mathbf{k}}_{m,n}$  (Equation 4-26) are also replaced by the terms from tangent stiffness matrix.

# Appendix D

## Bidirectional hybrid simulation: material testing, specimen constructions, and construction drawings

---

### D.1. Material testing samples

Table D-1 lists the specified material properties used to fabricate the column and foundation for the bidirectional hybrid simulations specimen.

Material	$f'_c$ or $f_y$ (MPa)
Concrete	40
Grade 300E D10 steel reinforcement	300
Grade 300E D16 steel reinforcement	300

Table D-1 Specified material properties for bidirectional hybrid simulation specimen

Figure D-1 shows a sample of compressive tests on the concrete material. The compressive tests were conducted at the end of the bidirectional hybrid simulations series.

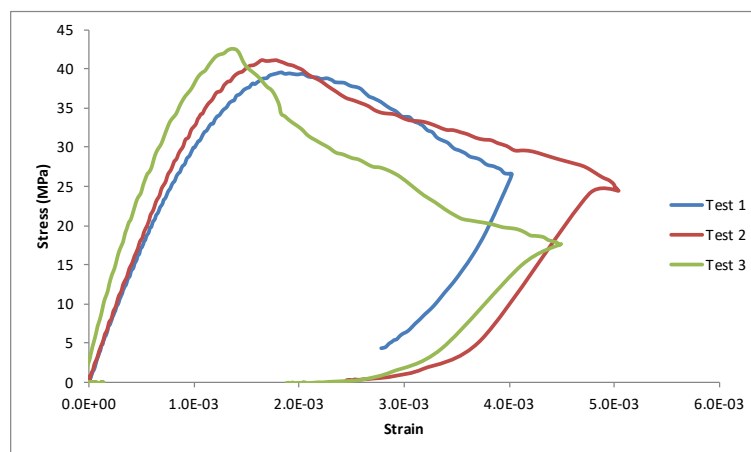


Figure D-1 Stress-strain curve from concrete compressive test

Table D-2 presents a summary of the concrete compressive tests. The specified design strength was achieved within reasonable accuracy.

No	Strength (MPa)	Dry weight (kg)	Submerged weight (kg)	Density (kg/m <sup>3</sup> )	Peak strain	Young modulus (MPa)
Test 1	39.6	3795	2063	2191.11	1.76E-03	2.48E+04
Test 2	41.1	3665	2135	2395.42	1.83E-03	2.84E+04
Test 3	42.5	3759	2163	2355.26	1.67E-03	3.22E+04
Average	41.07	3739.67	2120.33	2313.93	1.75E-03	2.85E+04

Table D-2 Concrete compressive test summary

Figure D-2 and Figure D-3 shows the results for the D10 and D16 tension tests series steel reinforcements respectively. The 300 MPa designed yield strength was achieved for both series.

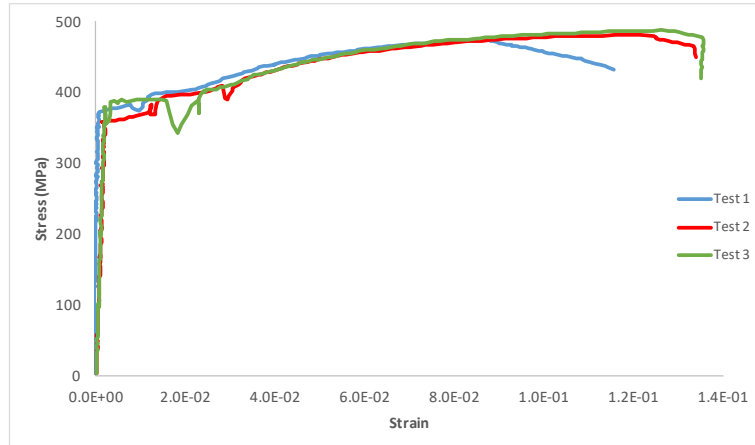


Figure D-2 Stress-strain curve from Grade 300E D10 tension test

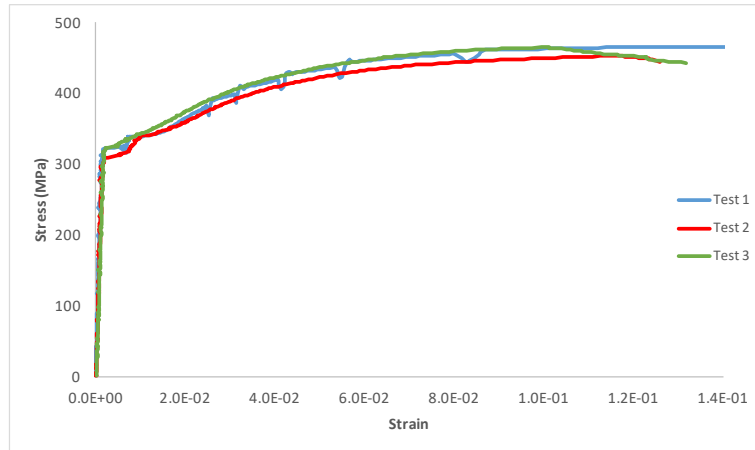


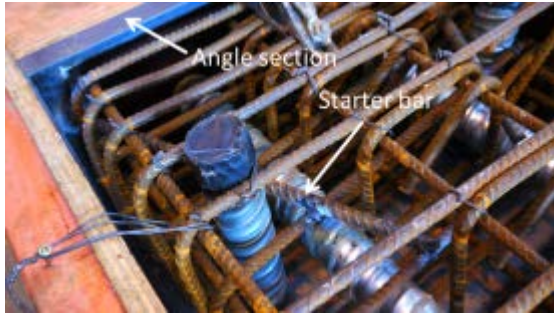
Figure D-3 Stress-strain curve from Grade 300E D16 tension test

## D.2. Specimen construction

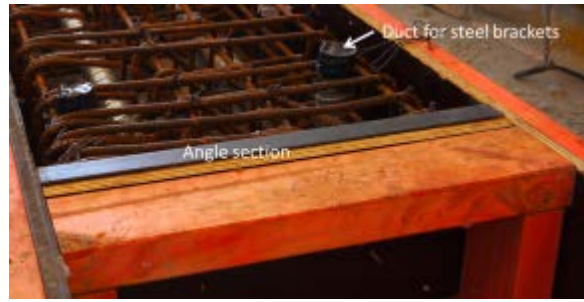
Figure D-4 and Figure D-5 show a selection of photos taken during the column specimen and foundation construction, respectively.



(a) Vertical ducts for PT bars



(b) Cast in place steel equal angle welded to main reinforcements

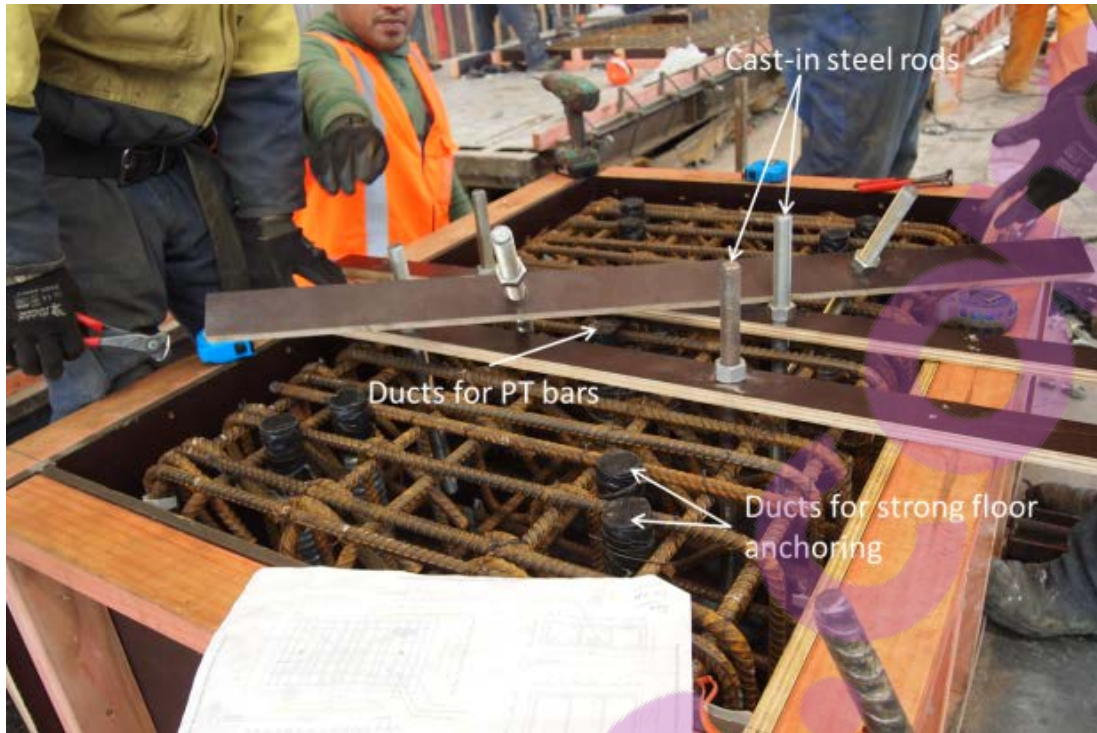


(c) Duct at column base for attaching steel bracket to column face



(d) Freshly casted column

Figure D-4 Photographs showing the construction sequence of the unbonded PT column



(a) Reinforcement arrangement of the concrete foundation block



(b) Casting of concrete into foundation block



(c) View of the cast-in steel bolt head after pouring

Figure D-5 Photographs showing the column foundation construction sequence

# Appendix E

## Wall hybrid test: material testing, specimen constructions, and construction drawings

---

### E.1. Material testing samples

Figure E-1 shows a sample stress-strain curve from the concrete compressive test on the concrete material of wall M6 (hybrid simulation). The compressive tests were conducted at the end of the hybrid simulation.

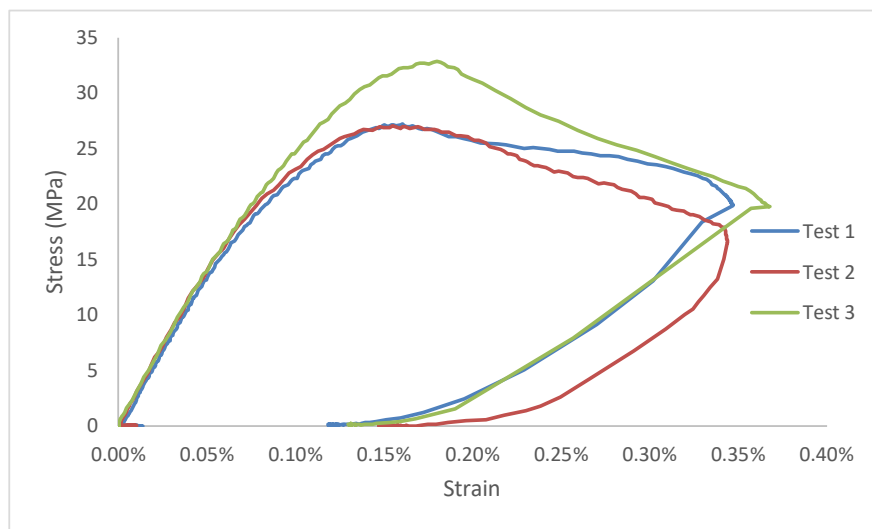
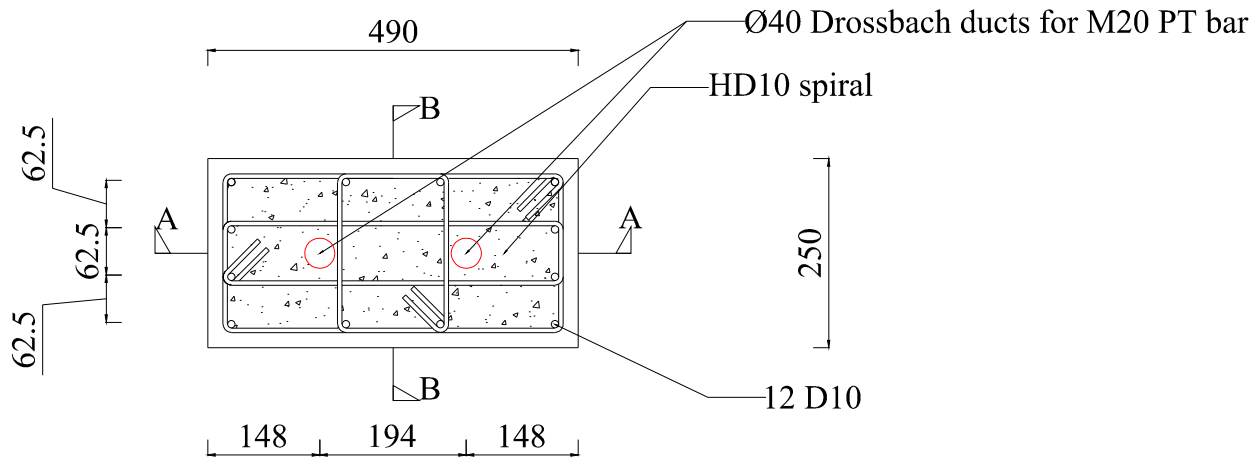
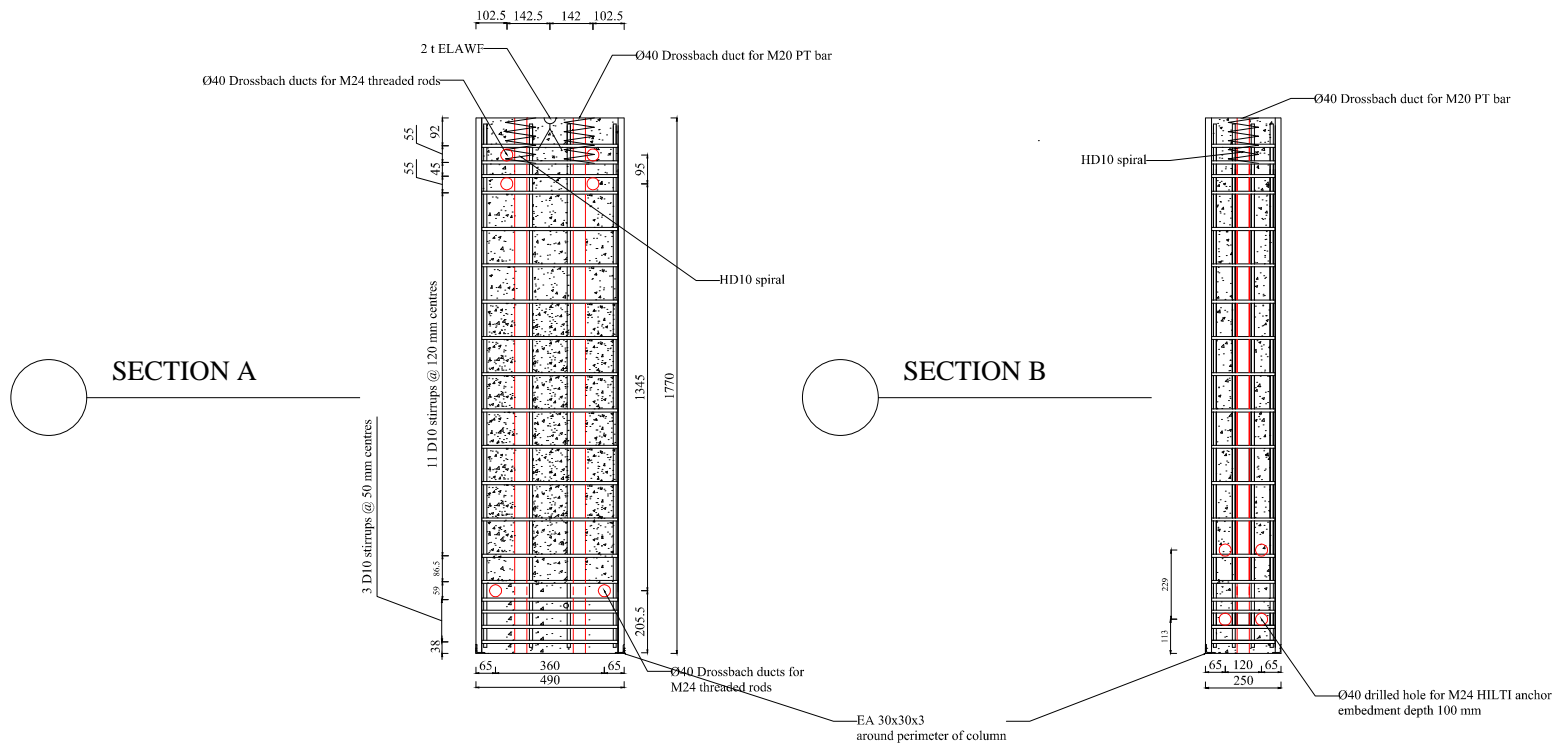


Figure E-1 Stress-strain curve from concrete compressive test of wall M6

Table D-1 to Table D-2 presents summaries of concrete compressive tests from the wall experiments. The specified design strengths of 30 MPa (Table 7-1) was achieved within reasonable accuracy.

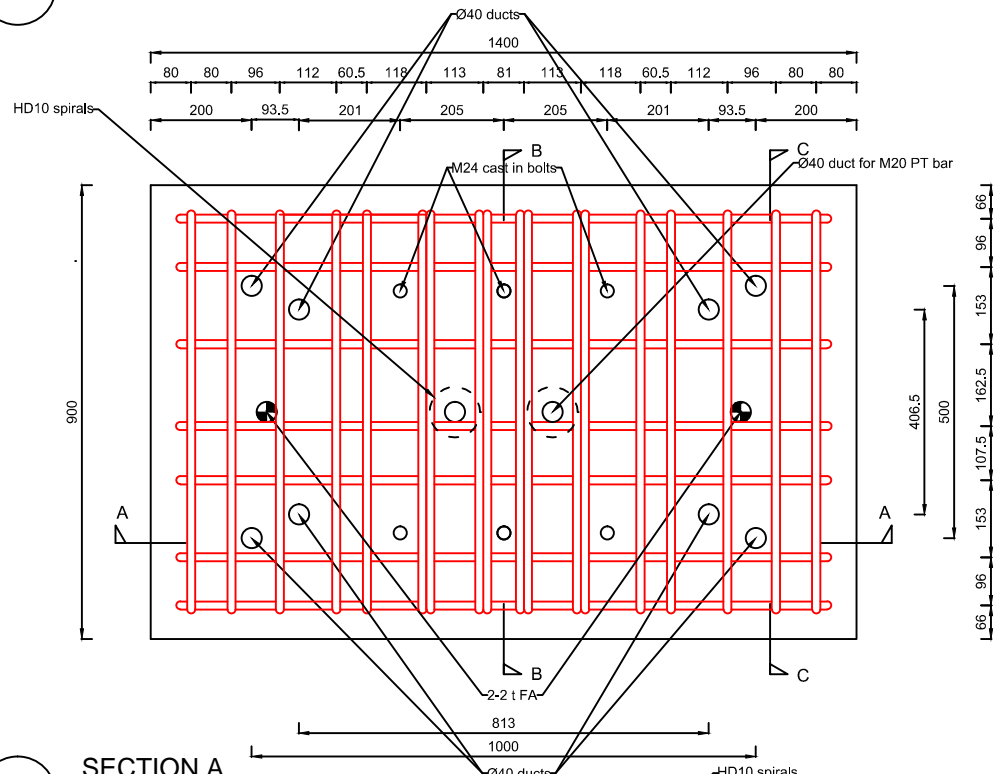


Drafter Ronald Gultom	
Title Cross section	
Revision date October 2016	
Scale 1:10	Paper size A4

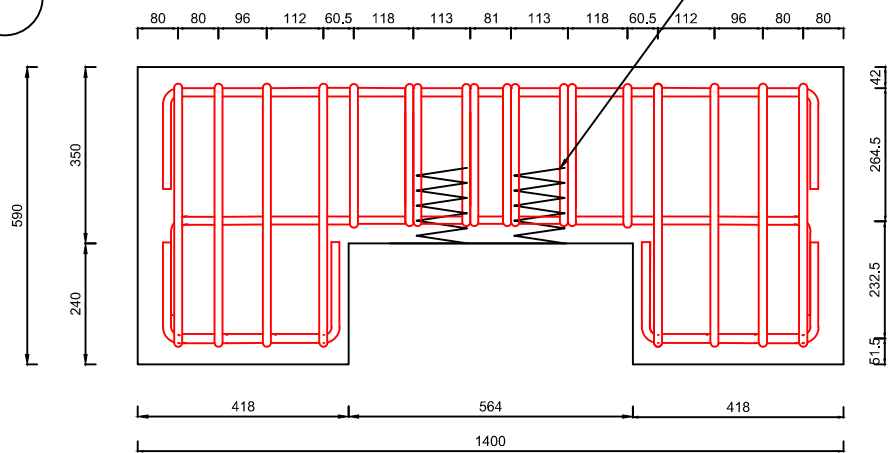


Drafter Ronald Gultom	
Title Elevation view	
Revision date October 2016	
Scale 1:25	Paper size A4

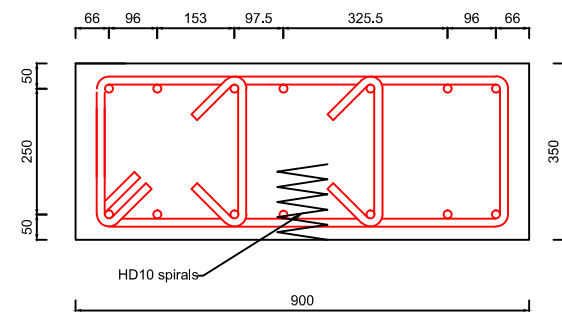
PLAN VIEW



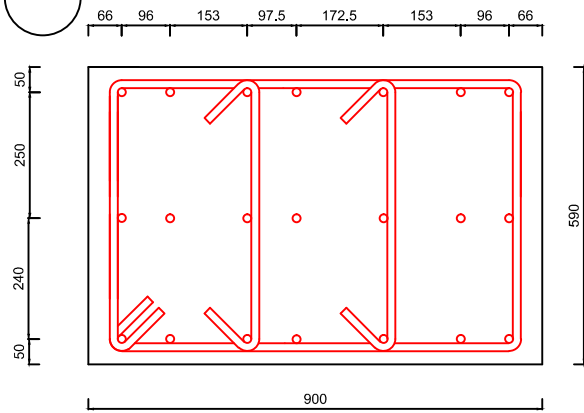
SECTION A



SECTION B

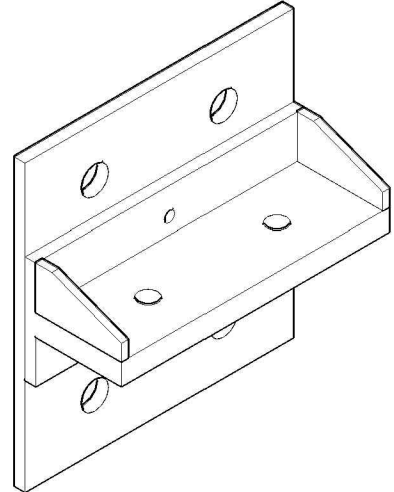
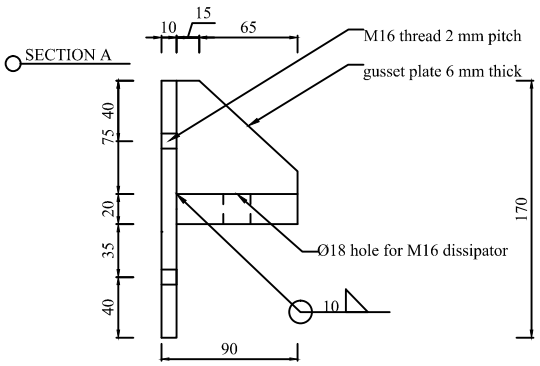
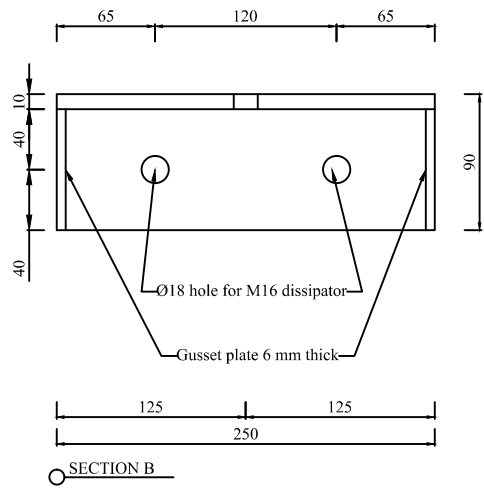
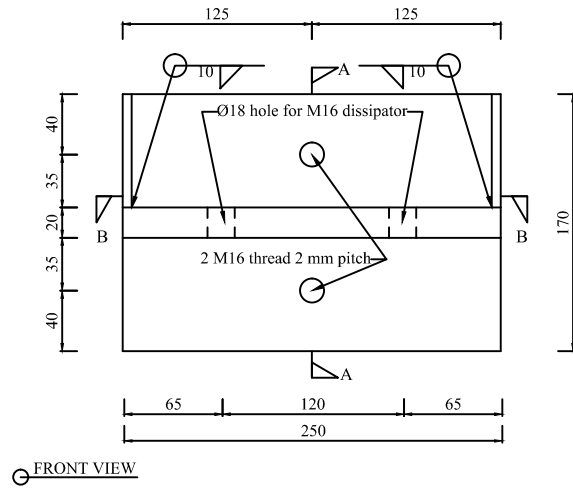


SECTION C



Drafter Ronald Gultom	
Title Foundation detail	
Revision date October 2016	
Notes  All longitudinal bar, stirrups, and ties are Grade 300E D16	
Scale  1:15	Paper size  A4





<p>Title Steel Bracket 2</p>	<p>Scale 1:5</p>	<p>Notes</p> <ul style="list-style-type: none"> <li>• All dimensions in mm unless specified otherwise</li> <li>• All steel plates <math>f_y = 350</math> MPa</li> <li>• All weld <math>f_y = 420</math> MPa</li> <li>• Make 2 of</li> </ul>	<p>Revision date October 2016</p>
<p>Drafter Ronald Gultom</p>	<p>Paper size A4</p>		

No	Strength (MPa)	Dry weight (kg)	Submerged weight (kg)	Density (kg/m <sup>3</sup> )	Peak strain	Young modulus (MPa)
Test 1	29.8	3760	2105	2271.90	0.18%	25500
Test 2	31.1	3680	2100	2329.11	0.18%	27400
Test 3	32.7	3710	2108	2315.86	0.14%	35300
Average	31.2	3716.667	2104.333	2305.6241	0.17%	29400

Table E-1 Wall M6 concrete compressive tests summary

No	Strength (MPa)	Dry weight (kg)	Submerged weight (kg)	Density (kg/m <sup>3</sup> )	Peak strain	Young modulus (MPa)
Test 1	27.2	3724	2159	2379.55	0.16%	26700
Test 2	27	3780	2108	2260.77	0.16%	27800
Test 3	32.8	3712	2104	2308.46	0.18%	27500
Average	29	3738.67	2123.67	2316.26	0.17%	27333

Table E-2 Wall M7 concrete compressive tests summary

Figure E-2 and Figure E-3 shows the results from the R6 and D10 steel reinforcement tension tests respectively. The 300 MPa (Table 7-1) designed yield strengths were satisfactorily achieved for both reinforcement types.

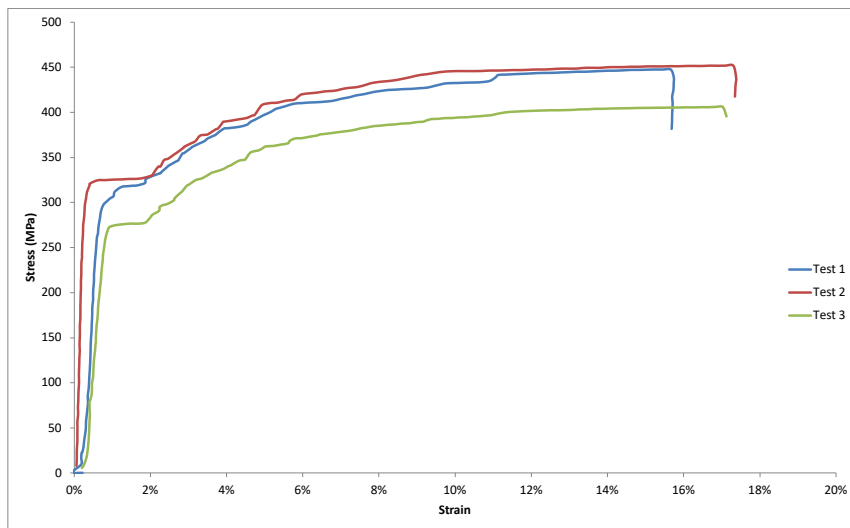


Figure E-2 Stress-strain curves from grade 300E R6 tension tests

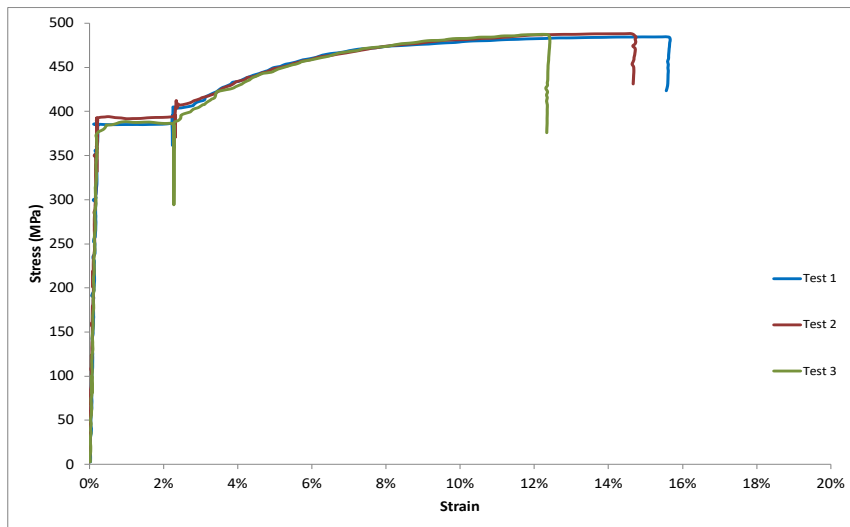
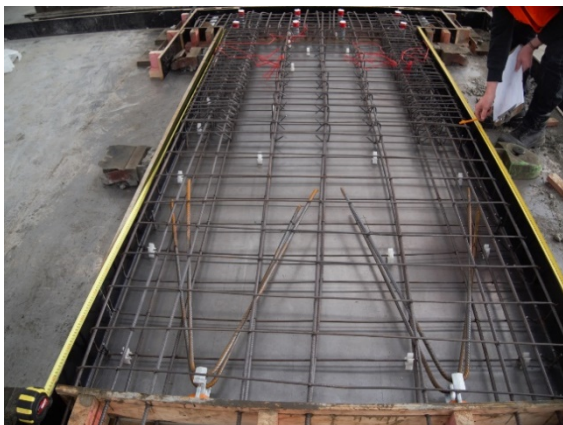


Figure E-3 Stress-strain curves from Grade 300E D10 tension tests

## E.2. Specimen construction

Figure E-4 shows a selection of photos taken during the walls construction. Detailing of wall M5 (tested quasi-statically) and M6 (tested pseudodynamically) were identical. Wall M7 was the half-height wall tested using the hybrid testing method.



a) As-built detailing of wall M5 and M6

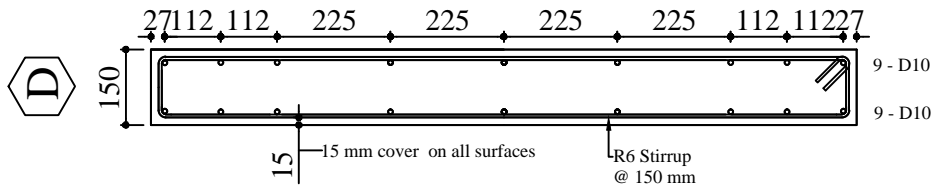
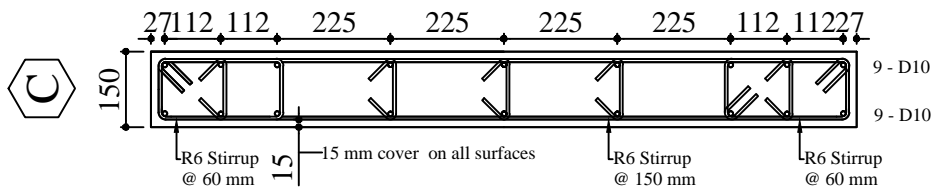
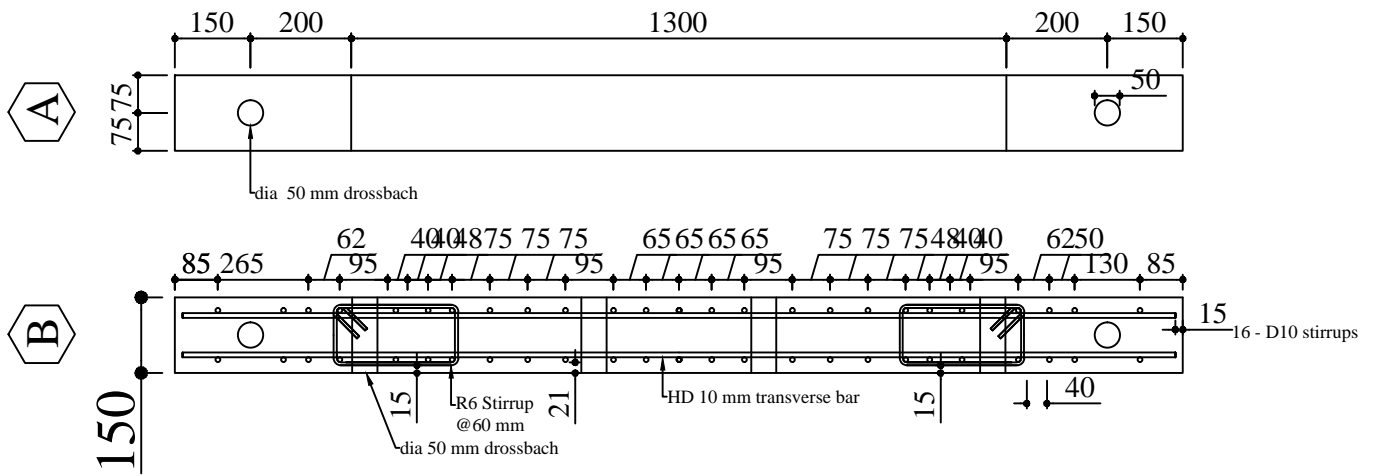


b) As-built detailing of wall M7

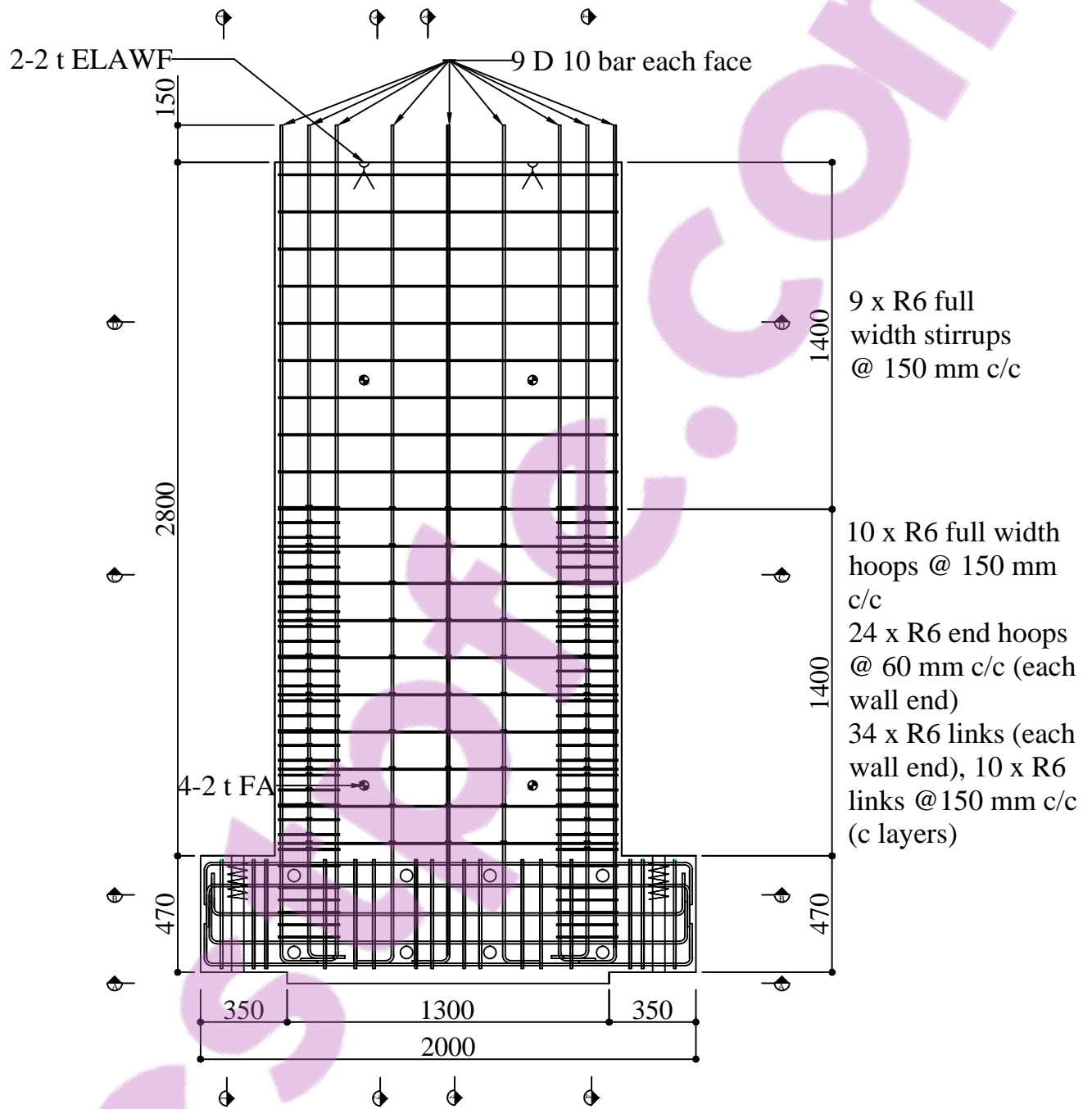


c) Fresh concrete pouring of wall M5

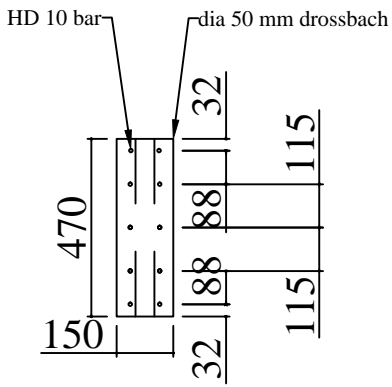
Figure E-4 Tested walls construction process



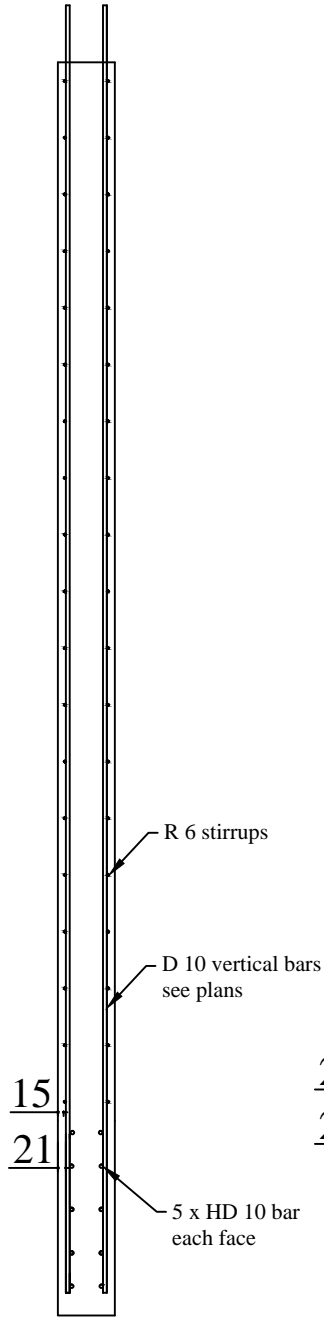
<p>Title</p> <p>Full height wall (detail - plan view)</p>	<p>Scale</p> <p>1:15</p>	<p>Notes</p> <ul style="list-style-type: none"> <li>All dimensions in mm unless specified otherwise</li> </ul>	<p>Revision date</p> <p>October 2016</p>
<p>Drafter</p> <p>Yiqiu Lu (original) Ronald Gultom (revised)</p>	<p>Paper size</p> <p>A4</p>	<ul style="list-style-type: none"> <li>Test type: Quasi-static and PSD</li> </ul>	



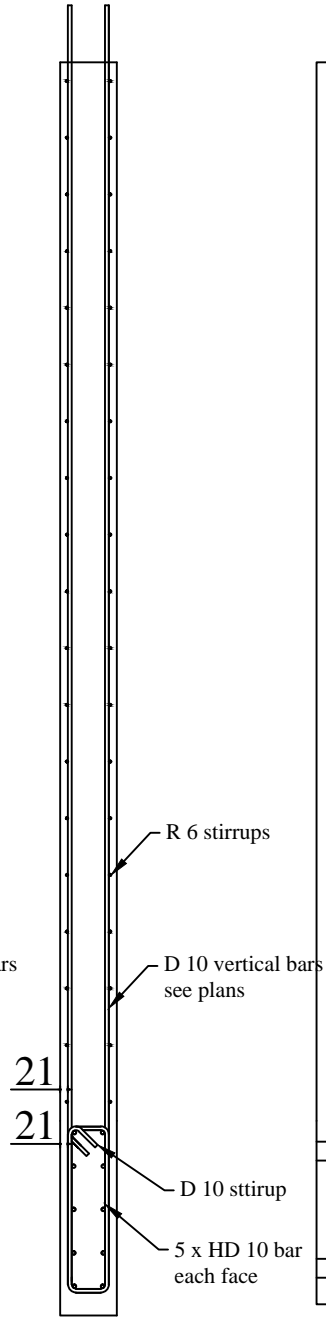
<p>Title</p> <p>Full height wall (elevation view)</p>	<p>Scale</p> <p>1:25</p>	<p>Notes</p> <ul style="list-style-type: none"> <li>All dimensions in mm unless specified otherwise</li> <li>Test type: Quasi-static and PSD</li> </ul>	<p>Revision date</p> <p>October 2016</p>
<p>Drafter</p> <p>Yiqiu Lu (original)</p> <p>Ronald Gultom (revised)</p>	<p>Paper size</p> <p>A4</p>		



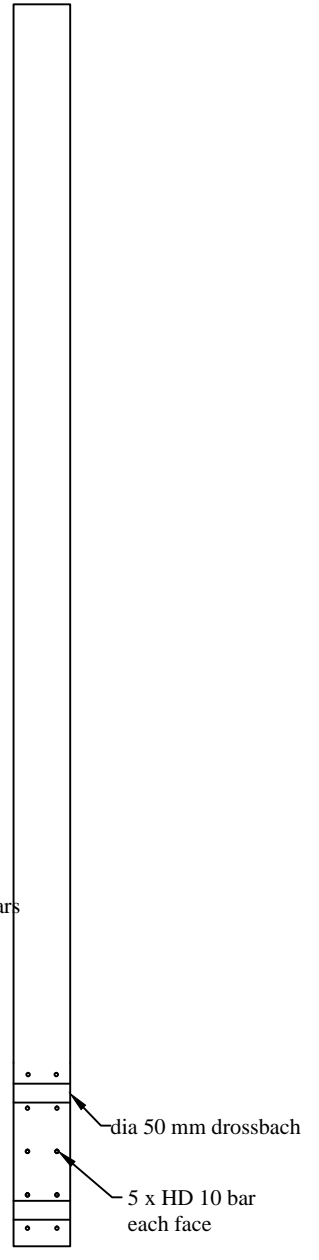
1



2

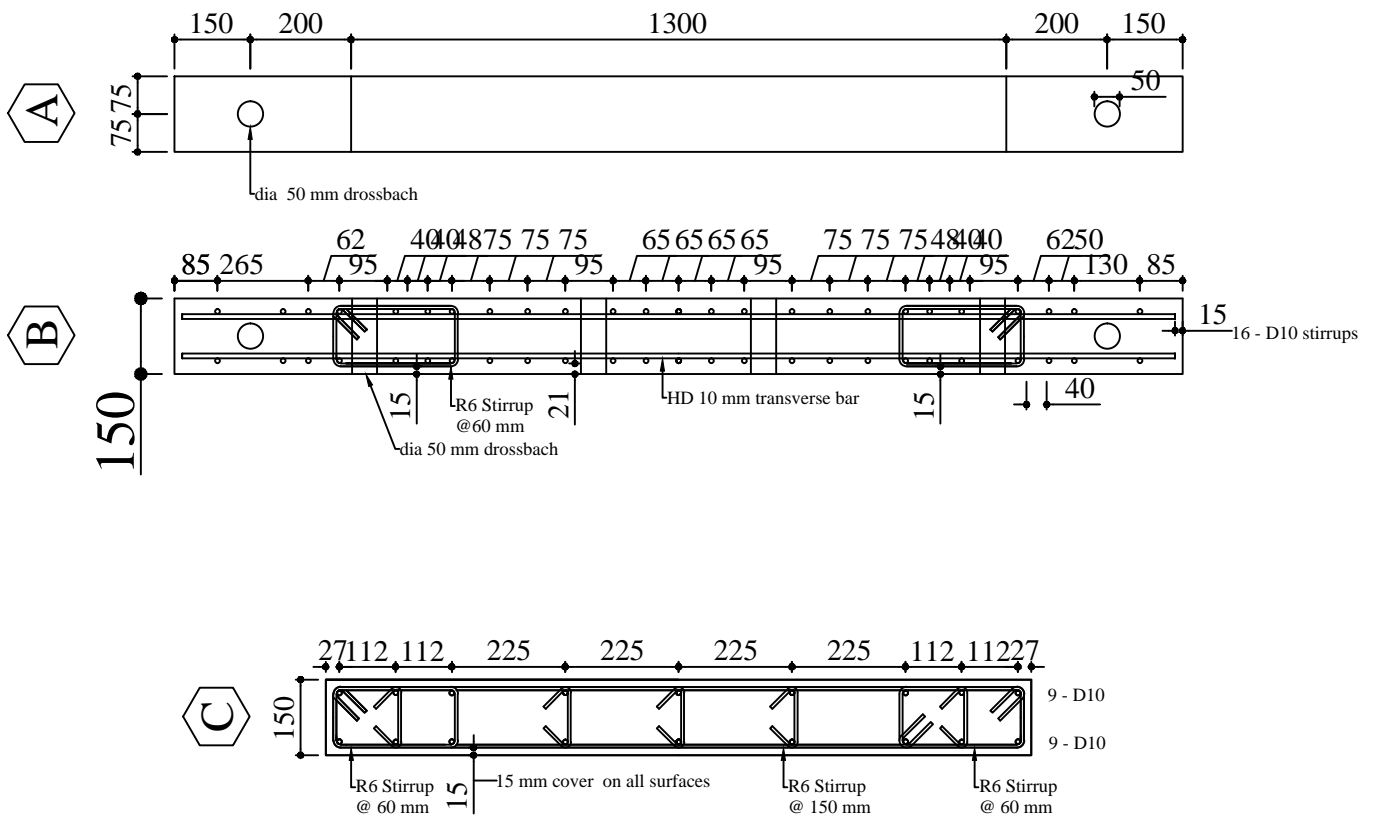


3

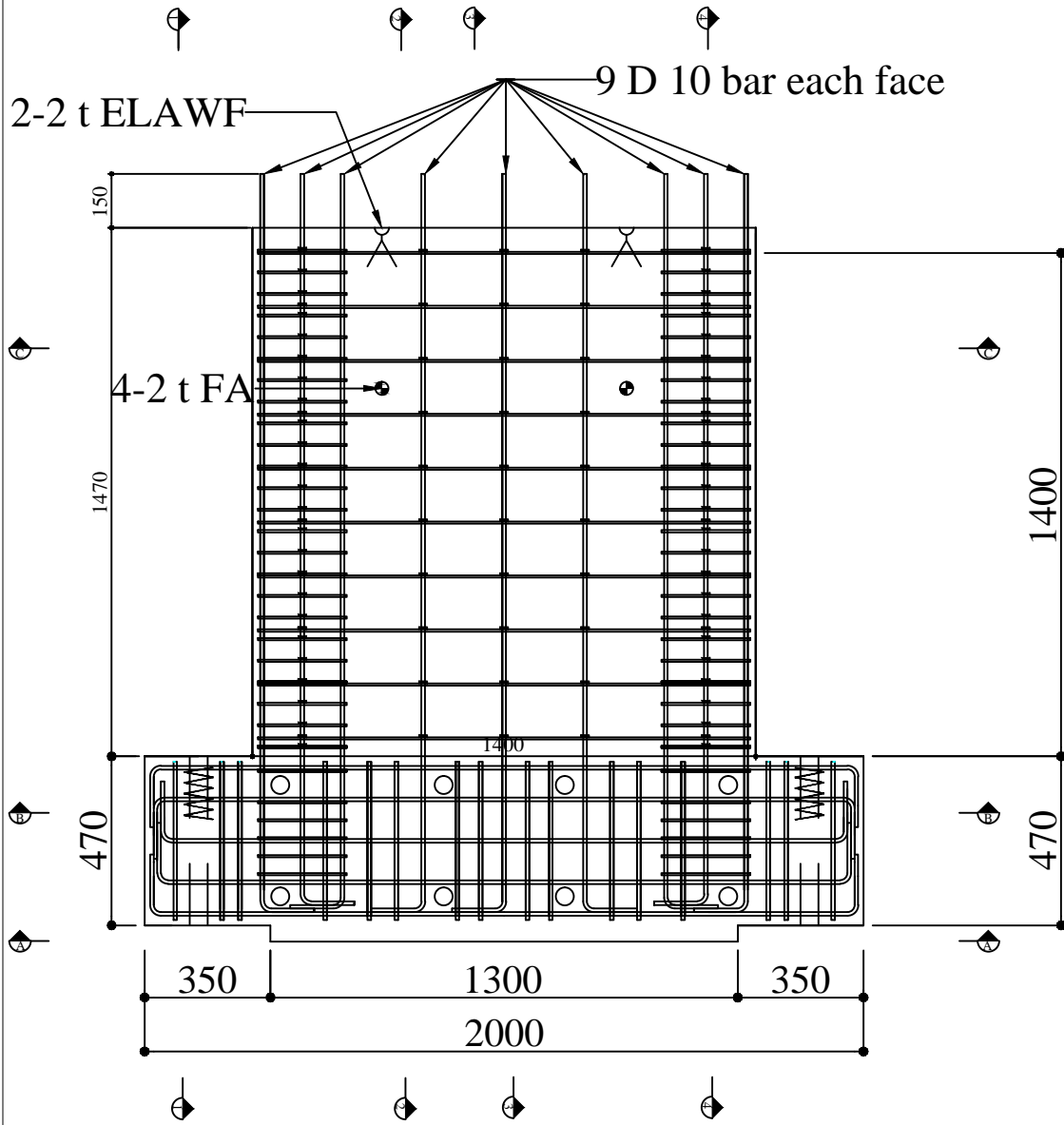


4

<p>Title</p> <p>Full height wall (detail - side view)</p>	<p>Scale</p> <p>1:20</p>	<p>Notes</p> <ul style="list-style-type: none"> <li>All dimensions in mm unless specified otherwise</li> <li>Test type: Quasi-static and PSD</li> </ul>	<p>Revision date</p> <p>October 2016</p>
<p>Drafter</p> <p>Yiqiu Lu (original) Ronald Gultom (revised)</p>	<p>Paper size</p> <p>A4</p>		

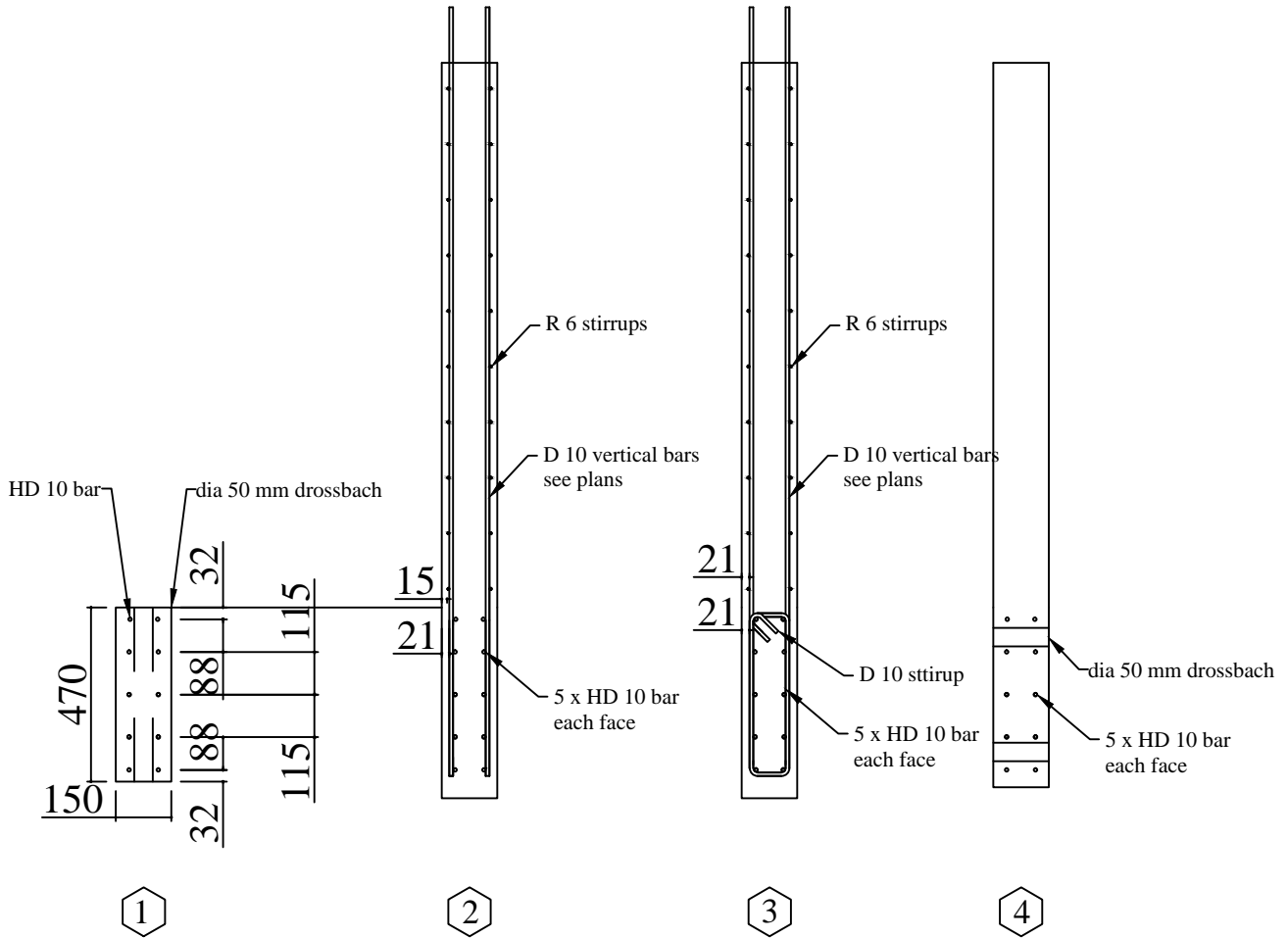


Title	Scale	Notes	Revision date
Half height wall (detail - plan view)	1:15	<ul style="list-style-type: none"> <li>All dimensions in mm unless specified otherwise</li> </ul>	October 2016
Drafter Yiqiu Lu (original) Ronald Gultom (revised)	Paper size A4	<ul style="list-style-type: none"> <li>Test type: Hybrid</li> </ul>	

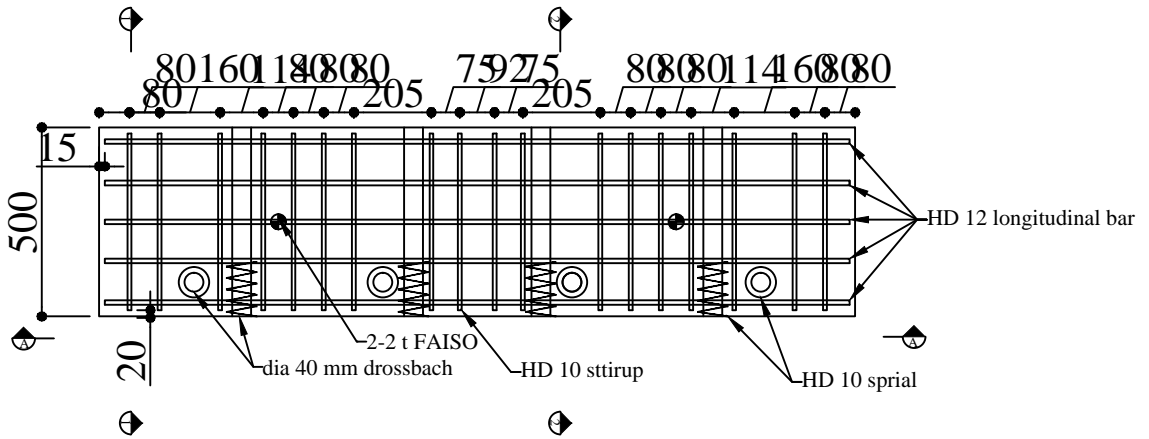


10 x R6 full width hoops @ 150 mm c/c  
 24 x R6 end hoops @ 60 mm c/c (each wall end)  
 34 x R6 links (each wall end), 10 x R6 links @ 150 mm c/c (c layers)

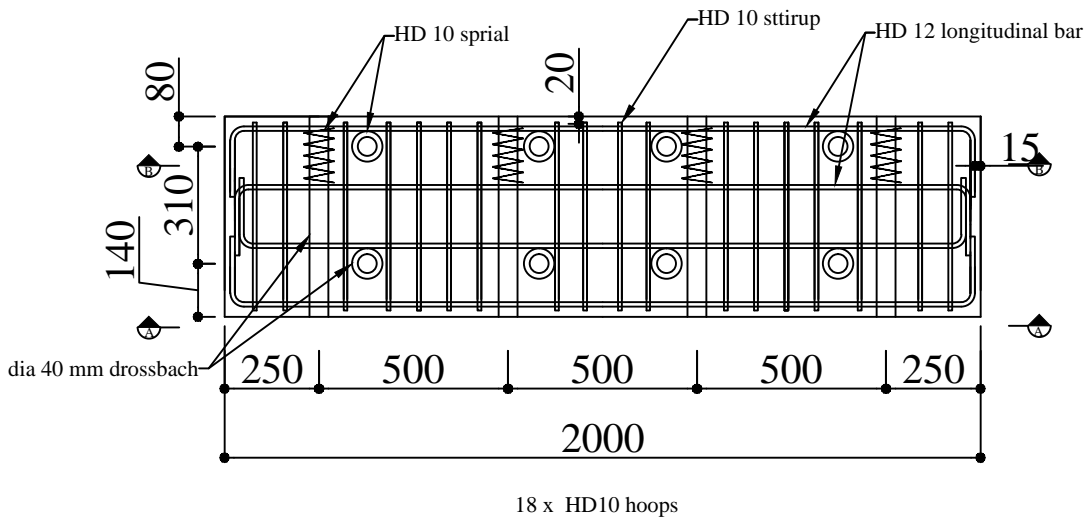
Title Half height wall (elevation view)	Scale 1:20	Notes <ul style="list-style-type: none"> <li>All dimensions in mm unless specified otherwise</li> <li>Test type: Hybrid</li> </ul>	Revision date  October 2016
Drafter Yiqiu Lu (original) Ronald Gultom (revised)	Paper size A4		



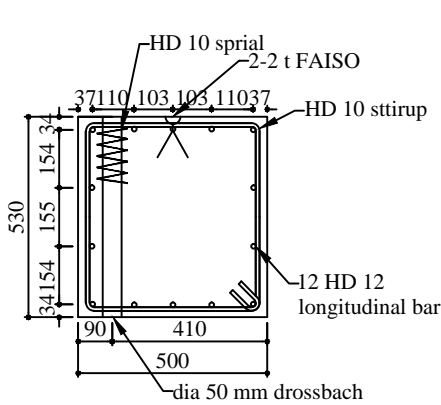
<p>Title</p> <p>Half height wall (detail - side view)</p>	<p>Scale</p> <p>1:20</p>	<p>Notes</p> <ul style="list-style-type: none"> <li>All dimensions in mm unless specified otherwise</li> <li>Test type: Hybrid</li> </ul>	<p>Revision date</p> <p>October 2016</p>
<p>Drafter</p> <p>Yiqiu Lu (original) Ronald Gultom (revised)</p>	<p>Paper size</p> <p>A4</p>		



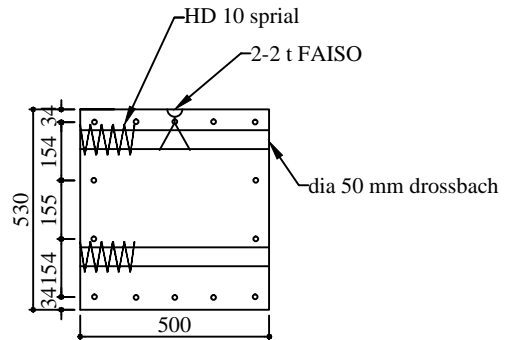
Plan



A



1



2

<p>Title</p> <p>Half foundation block (detail - all view)</p>	<p>Scale</p> <p>1:20</p>	<p>Notes</p> <ul style="list-style-type: none"> <li>All dimensions in mm unless specified otherwise</li> </ul>	<p>Revision date</p> <p>October 2016</p>
<p>Drafter</p> <p>Yiqiu Lu (original) Ronald Gultom (revised)</p>	<p>Paper size</p> <p>A4</p>	<ul style="list-style-type: none"> <li>2 of these blocks make a whole wall foundation</li> </ul>	